Deposition and modelling of lead zirconate titanate thin films on stainless steel for MEMS applications

Wachstum und Modellierung von Blei-Zirkonat-Titanat Dünnschichten auf Edelstahl für MEMS-Anwendungen
Zur Erlangung des akademischen Grades Doktor-Ingenieur (Dr.-Ing.)
Genehmigte Dissertation von Juliette Marie Alice Cardoletti aus Chamonix Mont-Blanc, Frankreich
Tag der Einreichung: June 2, 2021, Tag der Prüfung: September 7, 2021

1. Gutachten: Prof. Dr. Lambert Alff
2. Gutachten: Prof. Dr. Mario Kupnik
Darmstadt – D 17

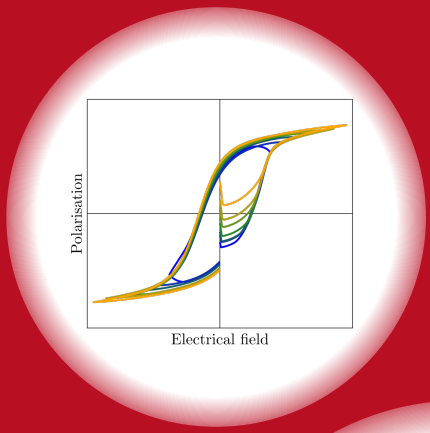

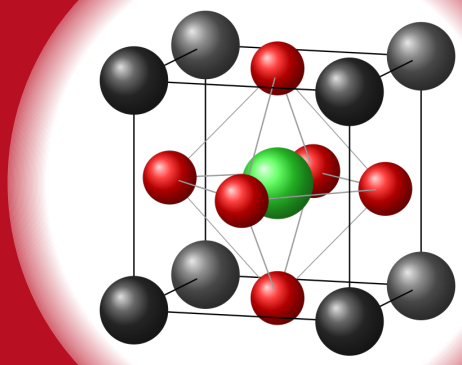

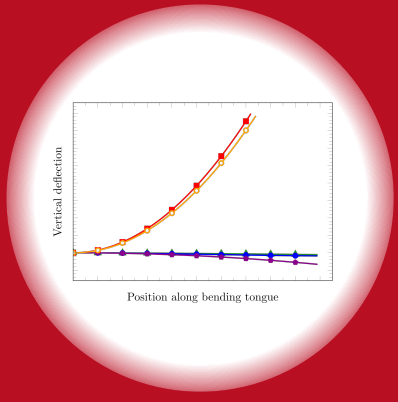

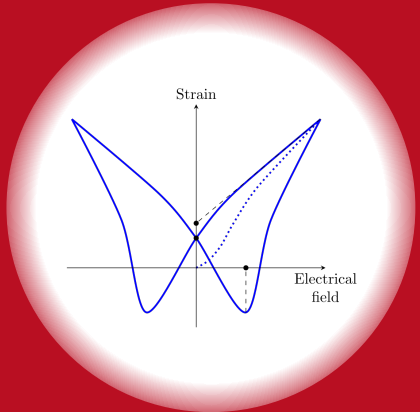

TECHNISCHE UNIVERSITÄT DARMSTADT

Materials and Earth Sciences Department

Institute of Materials Science

Advanced Thin Film Technology

Deposition and modelling of lead zirconate titanate thin films on stainless steel for MEMS applications
Wachstum und Modellierung von Blei-Zirkonat-Titanat Dünnschichten auf Edelstahl für MEMS-Anwendungen

Accepted doctoral thesis by Juliette Marie Alice Cardoletti

1. Review: Prof. Dr. Lambert Alff
2. Review: Prof. Dr. Mario Kupnik

Date of submission: June 2, 2021
Date of thesis defense: September 7, 2021

Darmstadt – D 17

Bitte zitieren Sie dieses Dokument als:
URN: urn:nbn:de:tuda-tuprints-196634
URL: http://tuprints.ulb.tu-darmstadt.de/id/eprint/19663

Dieses Dokument wird bereitgestellt von tuprints,
E-Publishing-Service der TU Darmstadt
http://tuprints.ulb.tu-darmstadt.de
tuprints@ulb.tu-darmstadt.de

Die Veröffentlichung steht unter folgender Creative Commons Lizenz:
Namensnennung – Nicht kommerziell – Keine Bearbeitungen 4.0 International
https://creativecommons.org/licenses/by-nc-nd/4.0/

This work is licensed under a Creative Commons License:
Attribution–NonCommercial–NoDerivatives 4.0 International
https://creativecommons.org/licenses/by-nc-nd/4.0/

Erklärungen laut Promotionsordnung

§8 Abs. 1 lit. c PromO

Ich versichere hiermit, dass die elektronische Version meiner Dissertation mit der schriftlichen Version übereinstimmt.

§8 Abs. 1 lit. d PromO

Ich versichere hiermit, dass zu einem vorherigen Zeitpunkt noch keine Promotion versucht wurde. In diesem Fall sind nähere Angaben über Zeitpunkt, Hochschule, Dissertationsthema und Ergebnis dieses Versuchs mitzuteilen.

§9 Abs. 1 PromO

Ich versichere hiermit, dass die vorliegende Dissertation selbstständig und nur unter Verwendung der angegebenen Quellen verfasst wurde.

§9 Abs. 2 PromO

Die Arbeit hat bisher noch nicht zu Prüfungszwecken gedient.

Darmstadt, June 2, 2021

J. Cardoletti

Declarations according to the doctoral regulations

§8 Par. 1 lit. c PromO

I hereby certify that the electronic version of my dissertation corresponds to the written version.

§8 Par. 1 lit. d PromO

I hereby affirm that no doctorate has been attempted at any time prior to this. In this case, more detailed information on the date, university, dissertation topic and result of this attempt must be provided.

§9 Par. 1 PromO

I hereby certify that this dissertation has been written independently and only using the sources indicated.

§9 Par. 2 PromO

The thesis has not yet been used for examination purposes.

A mes grands-parents maternels

La science n'a pas de patrie.
Science has no homeland.

Louis Pasteur
Inaugural speech of the Pasteur Institute
14 November 1888

Acknowledgements

First and foremost, I would like to thank **Prof. Lambert Alff** for believing in me and giving me the opportunity to carry out research in his group. I have been exceptionally fortunate to have his support and advice during the course of my doctoral studies. Under his guidance, I developed a strong interest for thin films and their fascinating properties. He gave me a chance to grow as a scientist and encouraged me to be more daring in front of professional challenges. I am thankful for the numerous opportunities he has offered me, whether it was an extensive stay as a research scholar in the United States to broaden my knowledge, to participate in international conferences or to get access to a wide range of experimental systems. I truly appreciate his accessibility, his feedback and encouragements to push my own boundaries further back.

I also express my sincere gratitude to **Prof. Susan Trolier-Mckinstry** for inviting me to stay in her research group at The Pennsylvania State University for six months. Her knowledge is invaluable and this work would not be what it is without her expertise. Her dedication to scientific research and teaching is tremendous and she deeply cares for people. In her group, I have learnt a lot about ferroelectrics and that a good scientist is above all a good person.

I would like to thank **Prof. Mario Kupnik** for kindly taking on the position of second reviewer. His time spend to review this dissertation is well appreciated. Besides him, I would like to acknowledge **Prof. Bai-Xiang Xu** and **Dr. Jurij Koruza** for their support by serving in my Ph.D. thesis committee and for the insightful discussions through the last few years.

I am grateful to **Dr. Philipp Komissinskiy** for sharing his knowledge of pulsed laser deposition and for his attention to detail which always makes me strive to improve my work. I am thankful for his feedback and the numerous hours he spent reviewing the articles we co-authored. I would also like to thank **Dr. Aldin Radetinac** for his scientific curiosity and his support at the beginning of my doctoral studies. His reminder that there should be a life outside of work was a great (and certainly needed) one.

This thesis could not have been completed without the support of many people who provided their help and technical expertise. I would like to thank **Gabi Haindl** and **Jürgen Schreeck** for their assistance in the laboratory. I am grateful to the electronics and mechanics workshops of the Institute of Materials Science, in particular to **Michael Weber** and **Jochen Rank** without whom the $e_{31,f}$ measurement system would never have been built. I also thank **Andreas Hönl** and **Stephan Diefenbach** for their help solving connection problems with a *P-E* loop tracer running on Windows NT.

From my stay at Penn State, I would like to acknowledge the Materials Research Institute staff from the Nanofabrication Lab. I thank notably **Kathy Gehoski** for teaching me photolithography, **Bangzhi Liu** for helping me with the SEM, **Bill Drawl** and **Andy Fitzgerald** for training me on several tools from the cleanroom. From the Materials Characterization Lab, I particularly give thanks to **Nichole Wonderling** and **Gino Tambourine** for their help with the XRD and for always answering my questions, and also to **Maria Dicola** for her help as I was struggling to polish stainless steel pieces.

I would like to thank **Marion Bracke** for her efficiency, the nice discussions we had and her useful tips on life in Darmstadt. I am grateful to **Sandie Elder** for always being kind, especially when I got sick. I would also like to acknowledge all the administrative staff, at the Technische Universität Darmstadt, at The

Pennsylvania State University and at the IDS-FunMat-Inno doctoral school for their assistance with the paperwork that my stay in the USA required.

Numerous thanks go to my co-workers past and present from the ATFT group for their support and friendship through the last few years. I am grateful to **Dr. Arzhang Mani** for giving me a chance during my master thesis and introducing me to the group. I would like to thank **Dr. Philipp Kehne** who, during that time, taught me how to use the PLD system (following a conversation with Prof. Alff on whether or not a "PLD crash course" could be taught, he did so in four days). I am grateful to **Dr. Alexey Arzumanov** for programming the $e_{31,f}$ measurement system and teaching me ion beam etching. I greatly appreciate the kindness of **Dr. Márton Major** and the time he gave to answer my questions, in particular about the analysis of XRD patterns. I would like to thank **Dr. Erwin Hildebrandt** for his help during the preparation of my stay at Penn State. Special thanks go to my fellow PLD users **Dr. Patrick Salg**, **Dr. Lukas Zeinar** and **Mahdad Mohammadi** for all their advice and the good times. I am thankful to **Thorsten Schneider** for the great discussions during the (anti)ferroelectrics meetings. I would like to acknowledge **Parastoo Agharezaei**, **Aaquib Shamim** and **Sadegh Yahyazadeh** whose work I guided and who helped me a lot. I am thankful to **Nico Kaiser** and **Tobias Vogel** for being wonderful office mates. I am especially grateful to **Dr. Shalini Sharma** and **Eszter Piros**, I am fortunate to enjoy their friendship. Not only did they have good advice but they made being away from home a much nicer experience than it could have been. I also acknowledge the support of the whole ATFT group including **Dr. Gennady Cherkashinin**, **Dr. Dominik Gölden**, **Dr. Jasnamol Palakkal**, **Dr. Stefan Petzold**, **Dr. Sareh Sabet**, **Dr. Vikas Shabadi**, **Dr. Sharath Ulhas**, **Supratik Dasgupta**, **Robert Eilhardt**, **Georgia Gkouzia**, **Jing-Jia Huang**, **Christian Lampa**, **Corinna Müller**, **Berthold Rimmler**, **Yating Ruan**, **Nils Schäfer**, **Seyma Topcu** and **Katrin Walter**.

I also own a lot to the STM group at Penn State. In particular to **Dr. Hong Goo Yeo** who taught me sol-gel deposition and whose guidance and experience with PZT thin films on nickel foils was very useful. I would like to thank **Dr. Julian Walker** for teaching me how to perform $e_{31,f}$ measurements and for the discussions on polarisation switching. I am also grateful to **Dr. Carl Morandi** for his valuable input on PZT thin films, notably on their growth by pulsed laser deposition. I am thankful to **Prof. Wanlin Zhu**, **Dr. Betul Akkopru-Akgun** and **Dr. Lyndsey Denis** for teaching me how to electrically characterise ferroelectric thin films. I would like to thank **Dr. Adarsh Rajashekhar** for guiding me through the different labs during my first weeks at Penn State. I am grateful for **Beth Jones**' constantly good mood and for the time she gave to teach me how to prepare PZT solution for sol-gel method. I would like to thank **Dr. Kathleen Coleman** for her help with $e_{31,f}$ measurements and for being a kind and cheerful cube mate. I am also glad to have had **Jared Carter** from Prof. Clive Randall's group and **Chris Cheng** as cube mates and would like to thank **Dr. Tianning Liu**, **Dr. Dixiong Wang** and **Leonard Jacques** for contributing to make my stay at Penn State a good one.

I am grateful to **Prof. Helmut Schlaak** and **Daniel Thiem** from the Department of Electrical Engineering and Information Technology of the Technische Universität Darmstadt for their collaboration and advice through the early stages of this work. I would like to thank **Prof. Barbara Malič** and **Silvo Drnovšek** from the Electronic Ceramics Department of the Jožef Stefan Institute in Slovenia for producing the PNZT lead zirconate target for pulsed laser deposition which enabled an important part of this work. I would also like to thank **Dr. Enrico Bruder** for performing the EBSD measurements reported in this work and **Ulrike Kunz** for preparing the sample with focused ion beam cutting. I would like to acknowledge **Prof. Wolfgang Donner** for his willingness to discuss the XRD patterns of my trickiest samples. I thank **Dr. Ali Nowroozi**, **Felix Nagler** and **Mao-Hua Zhang** for their help with the preparation of the LNO target for pulsed laser deposition. I would also like to thank **Dr. Marion Höfling**, **Dr. Lalitha Kodumudi Venkataraman**, **Alena Bell**, **Daniel Isaia** and **Heinz Mohren** for their help at various points of this work. I am also grateful to

Jean-Christophe Jaud for our discussions in French which cheered me up during my stay in Darmstadt. The formatting of this thesis would have been much more hazardous without the team behind the LaTeX templates package for the Technische Universität Darmstadt and their prompt answers to any questions which arose.

A large "Merci!" goes to **Birgit Franz** for her kindness and wisdom. She is well aware of the academia environment without being part of it and she lent me an attentive ear over the last few years. From the best landlady one could wish for, she has become a friend and I will dearly miss our conversations on weekends.

I would also like to thank my childhood friends, in particular **Mathilde**, **Maryne**, **Océane** and **Guillaume** for always being there. Having known most of them for over three quarters of my life is a privilege for which I shall always be grateful. I would certainly not be the person I am today without the **Club de Ski Nordique de la Vallée de Chamonix Mont-Blanc** with whom I trained for more than a decade before starting university. I am thankful to all its members, past and present, and particularly to the coaches **Florence**, **Christophe**, **Georges** and **Pek**. More than cross-country skiing, they taught me resilience.

Last but certainly not least, I would like to thank my family, especially my parents, my brother and my maternal grandparents. Each of them gave me their unconditional love and support. My mother **Nicole** has always been there for me, following my progresses and inviting me to go further. She taught me self-discipline and gave me the love of reading (despite how much I now read in English, I greatly appreciate her persistence to gift me books in French). My father **Patrice** has also been there with his own words and regardless of how much he understood what I was doing. He is still trying to teach me that sometimes it is okay not to care as much. Now that I have seen more of the world outside of the valley where I grew up, I am even more grateful to my younger brother **Théo** for his strongly voiced opinion that being a woman shall never be a synonym of weakness. It is a treasure to know that he cares and is always there when it matters the most. I am proud to call him my brother and delighted that keeping up with him is such a thrilling challenge. **Mala** might not be a relative but I have always considered her as a grandmother. She passed away long ago and it is only lately that I understood her most precious gift. Even if I am far from succeeding, I shall strive to listen without judgment, simply being there.

Georges and **Ginette**, my maternal grandparents, both passed away while I was preparing this thesis. Being raised at a time where a toolbox was not meant for women, they have always shown exceptional support along the path I chose. They taught me to always act at the best of my capabilities and were eager to share their knowledge. I would never forget the time I spent as a child poring over (sometimes a century old) books in my grandfather study nor the times where my grandmother told me, looking at a speech from the French President, to observe and articulate my own discourse. By their love, encouragements and presence, they have helped shape my life on a better path.

This manuscript is based on work supported by the Deutsche Forschungsgemeinschaft (DFG), under Grant number AL 560/19-1. A travel grant from the EIT RawMaterials IDS-FunMat- Inno is also acknowledged.

Note: The findings and conclusions in this thesis do not necessarily reflect the view of the funding agencies.

Abstract

Technological development is permanently advancing in the direction of miniaturisation and energy consumption reduction. One of the keys to this pathway lies in the integration of ferroelectric thin films into Micro-Electro-Mechanical Systems (MEMS) applications. For this purpose, due to its large piezoelectric response, lead zirconate titanate is the material of choice in industry. To broaden the range of applications, substrates less brittle than the currently favoured silicon must be implemented into MEMS. In this work, lead zirconate titanate thin films on stainless steel substrates were both experimentally investigated and modelled.

Lead zirconate titanate thin films of composition $PbZr_{0.52}Ti_{0.48}O_3$ were grown on AISI 304 stainless steel substrates by pulsed laser deposition with {001} texture to improve their piezoelectric response. As demonstrated using X-ray and electron backscatter diffraction, the texture engineering is achieved through a selection of two buffer layers, Al_2O_3 and $LaNiO_3$. The former buffer prevents the oxidation of the stainless steel substrate during deposition of the subsequent layers. The latter serves as both a bottom electrode and a growth template to promote the {001} texture of $PbZr_{0.52}Ti_{0.48}O_3$ thin films. The lead zirconate titanate thin films ferroelectric properties are improved through 2 mol.% Nb-doping, resulting in dielectric constants and losses at 1 kHz for a 200 nm thick film of 350 and below 5 %, respectively, before measurement of polarisation versus electrical field hysteresis. Following these measurements, the Nb-doped lead zirconate titanate thin films permittivity increases up to 430. With a thickness of 400 nm, the films exhibit a remanent polarisation of 16.5 $\mu C{\cdot}cm^{-2}$ and a coercive field of 92 $kV{\cdot}cm^{-1}$.

In the modelling, based on a ferroelectric switching criterion and the Euler-Bernoulli beam theory, it was investigated how the vertical deflection of ferroelectric bending tongues behaves with a load at their free end. The model developed here bridges the gap existing in literature between the modelling of ferroelectric switching and the mechanical description of linear piezoelectric structures. Furthermore, the ferroelectric switching criterion model is improved by the inclusion of strain saturation at high fields, which is inherent to ferroelectrics. The model includes parameters describing the geometry of the bending tongue, its mechanical and material properties, the crystallographic state and built-in strain of the ferroelectric thin film and the applied electrical field to determine the vertical deflection for MEMS applications based on ferroelectric bending tongues.

In summary, the technically relevant {001} texture of lead zirconate titanate thin films on stainless steel substrates has been successfully engineered. The thin films, especially with 2 mol.% Nb-doping, are excellent candidates for MEMS applications on non-brittle substrates, in particular in sensor technology. Furthermore, the model established in this work indicates that ferroelectric bending tongues made of lead zirconate titanate on stainless steel substrates can develop sufficient vertical deflection for MEMS applications.

Zusammenfassung

Die technologische Entwicklung schreitet permanent in Richtung Miniaturisierung und Reduzierung des Energieverbrauchs voran. Einer der Schlüssel zu diesem Weg liegt in der Integration von ferroelektrischen Dünnschichten in die Mikrosystemtechnik (Englisch: Micro-Electro-Mechanical Systems (MEMS)). Zu diesem Zweck ist Blei-Zirkonat-Titanat aufgrund seines großen piezoelektrischen Koeffizienten das Material der Wahl. Um den Anwendungsbereich zu erweitern, müssen Substrate, die weniger spröde sind als das derzeit favorisierte Silizium, in MEMS implementiert werden. In dieser Arbeit wurden Blei-Zirkonat-Titanat-Dünnschichten auf Edelstahlsubstraten sowohl experimentell untersucht als auch modelliert.

Die Blei-Zirkonat-Titanat-Dünnschichten der Zusammensetzung $PbZr_{0.52}Ti_{0.48}O_3$wurden auf AISI 304 Edelstahl-Substraten durch gepulster Laserabscheidung mit {001} Textur aufgewachsen, um ihr piezoelektrisches Verhalten zu verbessern. Wie mittels Röntgen- und Elektronenrückstreubeugung gezeigt werden konnte, wird die Texturoptimierung durch die Auswahl von zwei Pufferschichten, Al_2O_3 und $LaNiO_3$, erreicht. Die erste Pufferschicht verhindert die Oxidation des Edelstahlsubstrats während der Abscheidung der nachfolgenden Schichten. Die zweite dient sowohl als Bodenelektrode als auch als Wachstumsschablone zur Förderung der {001} Textur von $PbZr_{0.52}Ti_{0.48}O_3$-Dünnschichten. Die ferroelektrischen Eigenschaften der Blei-Zirkonat-Titanat-Dünnschichten werden durch 2 mol.% Nb-Dotierung verbessert, was im Rohzustand zu Dielektrizitätskonstanten und Verlusten bei 1 kHz für einen 200 nm dicken Film von 350 bzw. unter 5 % führt. Nach Messung der Hysteresekurve (elektrische Polarisation gegen das elektrische Feld) steigt die Permittivität der Nb-dotierten Blei-Zirkonat-Titanat Dünnschichten auf bis zu 430. Bei einer Dicke von 400 nm zeigen die Schichten eine remanente Polarisation von $16,5\ \mu C{\cdot}cm^{-2}$ und ein Koerzitivfeld von 92 $kV{\cdot}cm^{-1}$.

In der Modellierung wurde basierend auf einem ferroelektrischen Schaltkriterium und der Euler-Bernoulli-Strahlentheorie untersucht, wie sich die vertikale Auslenkung von ferroelektrischen Biegezungen mit einer Last an ihrem freien Ende verhält. Das hier entwickelte Modell überbrückt die in der Literatur bestehende Lücke zwischen der Modellierung des ferroelektrischen Schaltens und der mechanischen Beschreibung von linearen piezoelektrischen Strukturen. Darüberhinausgehend wird das Modell des ferroelektrischen Schaltkriteriums durch den Einbezug der Dehnungssättigung bei hohen Feldern, die den Ferroelektrika inhärent ist, verbessert. Das Modell enthält Parameter, die Geometrie der Biegezunge, ihre mechanischen und Materialeigenschaften, den kristallographischen Zustand, die eingebaute Verspannung der ferroelektrischen Dünnschicht sowie das angelegte elektrische Feld berücksichtigen, um die vertikale Auslenkung für MEMS-Anwendungen zu bestimmen, die auf ferroelektrischen Biegezungen basieren.

Zusammenfassend wurde die technisch {001} Textur von Blei-Zirkonat-Titanat-Dünnschichten auf Edelstahlsubstraten erfolgreich eingestellt. Die dünnen Schichten, insbesondere mit 2 mol.% Nb-Dotierung, sind hervorragende Kandidaten für MEMS-Anwendungen auf nicht-spröden Substraten, insbesondere in der Sensorik. Darüber hinaus zeigt das in dieser Arbeit aufgestellte Modell, dass ferroelektrische Biegezungen aus Blei-Zirkonat-Titanat auf Edelstahlsubstraten eine ausreichende vertikale Auslenkung für MEMS Anwendungen entwickeln können.

Table of contents

List of Tables

List of Figures

List of abbreviations and notations

The abbreviations employed in this manuscript are listed thereafter.

Abbreviation	**Description**
AC	Alternating Current
DC	Direct Current
EBSD	Electron Backscatter Diffraction
EDS	Energy-Dispersive X-ray Spectroscopy
IBE	Ion Beam Etching
IR	Infrared
LNO	Lanthanum Nickelate: $LaNiO_3$
MEMS	Micro-Electro-Mechanical Systems
P-E loop	Polarisation versus applied Electrical field curve
PLD	Pulsed Laser Deposition
PNZT	Nb-doped Lead Zirconate Titanate: $Pb_{1-\iota/2}\square_{\iota/2}(Zr_\gamma Ti_{1-\gamma})_{1-\iota}Nb_\iota O_3$
PZT or PZT $(\gamma \times 100)/(1-\gamma) \times 100)$	Lead Zirconate Titanate: $Pb(Zr_\gamma Ti_{1-\gamma})O_3$
RF	Radio Frequency
SEM	Scanning Electron Microscopy
SCLC	Space-Charge Limited Current
SS304	AISI 304 Stainless Steel
UV	Ultraviolet
XRD	X-Ray Diffraction
XRR	X-Ray Reflectivity

The principal notations appearing in the main body of the manuscript are listed thereafter. Notations relevant only to chapter 6 are listed in *List of notations specific to the modelling chapter*.

Notation	Variant(s)	Description
$\square$		Pb vacancy
2θ-θ scan		Out-of-plane XRD measurement
a	c	Lattice parameter
$\boldsymbol{D}$		Dielectrical displacement vector
d, e, g and h	d_{ij}, e_{ij}	Direct effect piezoelectric coefficients
$\boldsymbol{E}$	E	Electrical field vector (its amplitude)
$d_{33,f}$, $e_{31,f}$		Piezoelectric coefficients for thin films
E_c	$E_{c,-}$	Coercive field (negative coercive field)
$E_{c,shift}$		Internal bias field
$f_{(00l)}$	$f_{(00l)}{}^{\text{phase}}$	Lotgering factor (of given crystallographic phase)
hkl		Miller indexes
J		Leakage current density
k_B		Boltzmann constant
$n_{optical}$	$n_{optical,method}$	Optical dielectric constant (by given calculation method)
$\boldsymbol{P}$	P	Polarisation vector (its amplitude)
PNZT stack		PNZT/$LaNiO_3$/Al_2O_3/steel sample
P_r		Remanent polarisation
$\boldsymbol{P_s}$	P_s	Spontaneous polarisation vector (its amplitude)
P_{sat}		Saturation polarisation
PZT stack		PZT/$LaNiO_3$/Al_2O_3/Pt/steel sample
T	T_C	Temperature (Curie temperature)
$tan\ \delta$		Dielectric loss tangent
V_{AC}		AC voltage
ε_0		Electrical permittivity of free space ($\approx 8.854 \cdot 10^{-12}$ F·m^{-1})
ε_{ij}		Permittivity tensor
ε_r	$\varepsilon_{r,optical}$	Dielectric constant (optical dielectric constant)
κ_{ij}		Strain tensor
λ		Wavelength
$\boldsymbol{\sigma}$	σ	Applied stress (its amplitude)

List of notations specific to the modelling chapter

Due to the large number of abbreviations relevant only to the modelling of ferroelectric bending tongues, the notations introduced thereafter are specific to chapter 6 and its appendices (Appendices G and H).

Notation	Variant(s)	Description
$E_{\mathrm{Y},eff}$		Composite beam equivalent Young modulus
${E_{\mathrm{Y}}}^{i}$	${E_{\mathrm{Y}}}^{ferro}$	Young modulus of a layer (of ferroelectric layer)
I_{eff}		Effective second moment of area of composite beam
M_b	M_f	Bending moment due to the built-in (or ferroelectric) strain
n_{eff}		Effective neutral axis of composite beam
n^i		Mid-plane of a layer
q^L		Load applied at the free end of the bending tongue
q^W		Own weight of the bending tongue
t^i	t^{ferro}	Thickness of a layer (of ferroelectric layer)
${w_{eff}}^{i}$	${w_{eff}}^{ferro}$	Effective width of a layer (of ferroelectric layer)
x	x_l, x_m	Position on x-axis of bending tongue (length, beginning of end load)
$z(x)$	z_l, ${z_l}^{E}$, ${z_l}^{0}$	Vertical deflection of bending tongue (at free end, at free end with and without applied field)
κ_b	${\kappa_b}^{long}$	In-plane built-in strain (resulting longitudinal strain)
κ_f	${\kappa_f}^{long}$	In-plane ferroelectric strain (resulting longitudinal strain)
ν_{eff}		Equivalent Poisson ratio for a composite beam

1. Introduction and motivations

Discovered a century ago, the field of ferroelectrics underwent a substantial development since World War II, when the need for capacitors arose. Today, ferroelectrics are omnipresent in modern society; their main markets, as capacitors and for piezoelectric applications, represent an annual value of $6 billion and $1 billion, respectively. While the capacitors market is fully mature with trillions of barium titanate-based multilayer ceramic capacitors produced annually, piezoelectric applications still offer a wide range of progress for new opportunities [1–3].

Ferroelectrics possess large dielectric coefficients granting them a high volumetric efficiency for dielectric charge storage. Furthermore, their unique properties provide them with high piezoelectric coefficients, opening the possibility for efficient low-voltage actuators, and switchable polarisation, which, through poling, can produce net piezoelectric response [1].

The versatility of ferroelectric materials allows them to be employed in numerous fields for a wide-scope of applications, ranging from ultrasound imaging (medical ultrasound imaging, sonar [1, 2, 4]) through non-volatile memory (ferroelectric random access memory [5, 6]), energy harvesters (thermal and mechanical [7–9]), optical components (wave-guides, modulators, adjustable optics [10–12]), electrical components (resonators, filters [13]), pyroelectric devices (heat detectors, infrared-imagers [14–16]) to robotics (piezoelectric Micro-Electro-Mechanical Systems (MEMS), ink-jet printing, ultrasonic motors [4, 17–19]).

Future technological developments, notably wearable sensors and the Internet of Things, are strongly dependent on solving two issues: **miniaturisation** and **energy consumption reduction** [8, 20]. The former entails the need to integrate functional materials into MEMS and the progressive transition towards Nano-Electro-Mechanical Systems [4, 18]. The latter is a vital imperative, both environmentally and economically, impacting societies and their legislation. Within the framework of the *European Green Deal* and through the *European Climate Law* proposed in March 2020, the European Union aims to reduce energy consumption to reach climate-neutrality by 2050, affecting for instance the direction of research for decades to come [21].

Through their piezoelectric applications, ferroelectrics can contribute to energy consumption reduction as key components for self-powered sensors, actuators with low driving voltage and energy harvesters [4, 17]. **The continuous progress of ferroelectrics integration into MEMS applications is decisive for the implementation of future technologies.**

Particularly, the dimensions of ferroelectric thin films make them better suited than bulk ceramics for integration as functional materials into MEMS. Not only do the dimensions promote miniaturisation but thinner films lead to higher applied electrical field at a given voltage [17]. However, in industry, ferroelectric thin films are generally deposited on silicon substrates, which have a limited toughness. To expand the range of potential applications of ferroelectric thin films, the use of less brittle substrates, better suited for demanding mechanical applications is necessary. With manufacturing and processing methods already well established in industry, a relatively good resistance to corrosion and a comparatively high toughness, stainless steel is an ideal substrate candidate [22].

Lead zirconate titanate, with its large piezoelectric coefficient, have long imposed itself as the choice material for transducers, sensors, and actuators design [17]. Despite its lead content, shaped into the

simplest piezoelectric MEMS device that is a bending tongue, it remains an excellent proof-of-concept candidate for deposition on the unconventional substrate that is stainless steel.

Nonetheless, MEMS efficiency depends on several factors besides the choice of materials. Modelling is an economical method to probe the influence of some parameters, such as MEMS geometry or applied electrical field. Therefore, this thesis shall endeavour to both model and deposit lead zirconate titanate thin films on stainless steel for MEMS applications.

This chapter aims to give an overview of the deposition methods of lead zirconate titanate thin films on various substrates. Afterwards, it proposes a literature review of the modelling of both piezoelectric bending tongues and ferroelectric behaviour. This chapter also states the purpose of this thesis and introduces the thesis structure.

1.1. Literature review: state of the art

This section presents the state of the art regarding lead zirconate titanate thin films grown by different methods on a variety of substrates with a particular focus on metallic substrates. Then, it introduces the existing models describing piezoelectric bending tongues and those representing ferroelectric behaviour.

1.1.1. Overview of lead zirconate titanate thin films in literature

Since the first study on lead zirconate - lead titanate solid solutions seventy years ago, numerous investigations have been carried out on the compound nowadays known as lead zirconate titanate, both on its bulk form and as thin films [23]. Lead zirconate titanate is a ferroelectric solid solution of formula $Pb(Zr_{\gamma}Ti_{1-\gamma})O_3$ (PZT) whose perovskite structure and properties are described in sections 2.1.5 and 2.2.1, respectively.

A wide array of deposition methods has been used to grow PZT thin films, historically starting with physical vapour deposition methods in the early 1980s [24]. The first PZT depositions were performed by sputtering, either ion beam sputtering [25, 26], Radio Frequency (RF) magnetron sputtering [27] or Direct Current (DC) magnetron sputtering [28, 29]. Almost a decade later, the growth of PZT thin films by chemical vapour deposition methods was investigated using chemical solution deposition, notably sol-gel processes [30–32] and metal-organic-decomposition [33]. Additionally, metal-organic-chemical vapour deposition also proved to be a reliable method for PZT films deposition [34–36]. Pulsed Laser Deposition (PLD) of PZT thin films was also established around the same period [37, 38].

Forty years after the growth of the first PZT thin films, novel depositions methods are still investigated, such as aerosol deposition [39]. Nowadays, chemical solution deposition and metal-organic-chemical vapour deposition methods are largely used in sensor and integrated circuit industries, respectively. The former, when aimed at small-scale production, is the less expensive method despite requiring post-annealing to crystallise the film. The latter process offers a good conformal coverage, as needed for integrated circuits [24].

The choice of substrates for PZT thin films is mostly dependent on applications, most of them requiring a parallel-plate capacitor structure with top and bottom electrodes. In order to remain electrically conductive and to avoid oxidation, the electrodes must be thermally and environmentally stable during PZT thin films deposition. Besides electrodes oxidation, it is often necessary to prevent substrate oxidation by

applying buffer layers between substrates and thin films. Furthermore, PZT thin films are susceptible to interdiffusion from substrates which can also be prevented by appropriate buffer layers [24]. These constraints limit the possibility of materials on which PZT thin films can be deposited.

As a result, while PZT can be grown on numerous substrates, e.g. silicon, single crystal oxides or glass, the most common choices of electrodes are platinum and some metallic oxides, e.g. RuO_2 or $SrRuO_3$ [17, 40–44]. The electrode material often plays a part in the diffusion barrier, along with additional buffer layers. For example, with a Si substrate, the most frequent combination of electrode and buffer layers is PZT/Pt/Ti/SiO_2/Si [24]. However, the electrode by itself is rarely a sufficient diffusion barrier, e.g. oxygen can migrate through a platinum electrode [45].

Regarding lead zirconate titanate thin films deposited on metallic substrates, the number of pertinent reports is more limited. These investigations mainly focus on chemical solution deposition procedures applied on various metallic substrates [46–50]. Recently, several reports on the growth of {001}-oriented lead zirconate titanate thin films on Ni foils have been published [8, 51–54]. Growth of lead zirconate titanate films on flexible Ni-Cr substrates have also been reported [55].

The case of stainless steel substrates has been approached by several authors reporting PZT thin films of various textures deposited by sol-gel process [56–59], electron beam evaporation technique [60], electrochemical reduction [61] or RF magnetron sputtering [22, 62–67]. A noteworthy report presents {001}-oriented Nb-doped lead zirconate titanate thin films grown by RF magnetron sputtering on stainless steel substrates [68].

This is of particular relevance as crystallographic orientation is another aspect of PZT thin films which is crucial to MEMS applications. Indeed, an improvement of lead zirconate titanate films piezoelectric response can be engineered by promoting a {001} texture [17]. **There are, however, no compelling reports demonstrating tetragonal {001}-textured lead zirconate titanate films grown directly on stainless steel by pulsed laser deposition.**

1.1.2. Modelling of piezoelectric bending tongues and ferroelectric behaviour, a review

When modelling ferroelectrics MEMS, two aspects have to be taken into consideration. The first is the mechanical system itself, including its linear piezoelectric response when subjected to an applied electrical field. The second is the ferroelectric behaviour, i.e. the possibility to switch the polarisation direction between discrete crystallographically allowed orientations by applying an external electrical field [17].

As linear piezoelectric structures have been extensively studied, this review focuses on systems composed of bending tongues (cantilevers or wider beams) based on piezoelectric ceramics. However, to date, bending tongue-based devices have been modelled without simulating the ferroelectric switching occurring in grains [69–72].

On the other hand, ferroelectric switching has been described through various micromechanical models. Particularly, polarisation switching in single or multicrystals has been studied through phase-field models, which require no switching criteria [73–75]. Nonetheless, to model polycrystalline ferroelectrics, micromechanical approaches are more efficient in view of the large amount of grains they encompass. A number of micromechanical models are self-consistent estimates [76] while others, e.g. Hwang, Lynch and McMeeking's model, take hysteretic polarisation-field and strain-field behaviour into account [77].

The above-mentioned model by Hwang et al. estimates the response of a bulk ferroelectric ceramic subjected to both mechanical and electrical external loads. The bulk ferroelectric response is calculated from the

strain and polarisation for an individual grain, resulting from an applied electrical field and applied stress. The model postulates that when the loading level is larger than a work energy criterion, polarisation switching occurs. The individual grains being assumed to display a statistically random orientation, their response is averaged to estimate the bulk response. Over time, to take more physical aspects into account, Hwang's model has been extended in various directions, including mean-field approach, and numerically implemented with the finite-element method [78–84].

The modelling of piezoelectric/metal/piezoelectric actuators by the finite-element method and the laminated beam theory, taking into account static electromechanical displacement and polarisation switching, is noteworthy, although it only concerns three-point-loaded actuators [85]. **Therefore, to describe a ferroelectric bending tongue, it remains necessary to bridge the gap between the mechanical and ferroelectric approaches.**

1.2. Statement of purpose

The issues of miniaturisation and energy consumption reduction are critical for the continuous advancement of technology. Therefore, technological innovations are dependent on the integration of ferroelectrics into MEMS applications. However, some fundamental questions arise:

1. How to incite the growth of tetragonal {001}-oriented or textured lead zirconate titanate thin films on steel substrates by pulsed laser deposition to engineer a larger piezoelectric response?
2. Are the ferroelectric properties of lead zirconate titanate thin films on steel substrates suitable for piezoelectric MEMS applications?
3. How to calculate the accessible vertical deflection of ferroelectric bending tongues, taking into account both their linear piezoelectric structure and ferroelectric switching?

The first purpose of this work is to establish a procedure to grow {001}-textured lead zirconate titanate thin films on stainless steel substrates by pulsed laser deposition. This method encompasses substrate preparation, buffer layers selection and deposition. The chosen buffer layers aim to prevent oxidation of the steel substrates during thin films deposition and to act as a growth template to direct the lead zirconate titanate thin films into a {001} orientation. The phase and crystallographic orientation of the thin films are both ascertained using notably X-ray diffraction.

The second aim of this work is to characterise the dielectric, piezoelectric and ferroelectric properties of {001}-textured lead zirconate titanate thin films on stainless steel substrates to assess their potential for piezoelectric MEMS applications. For this purpose, characterisation techniques previously not implemented in the research group are set up. The effect of Nb-doping on lead zirconate titanate thin films is analysed and the deposition parameters are tuned to optimise the films properties.

The third objective of this thesis is to develop a model which describes the vertical displacement of ferroelectric bending tongues with a load at their free end to replicate MEMS applications. This model relies on both the ferroelectric switching criterion established by Hwang et al. [77] and the Euler-Bernoulli beam theory. The model intends to calculate bending tongues vertical deflection as a function of the applied electrical field while taking into account the physical characteristics of bending tongues, e.g. geometry, material properties, load at the free end, crystallographic state, etc. It provides insight into the relative importance of the different contributions controlling the vertical deflection to allow an optimisation of bending tongues characteristics.

1.3. Thesis structure

Chapter 2 outlines the fundamentals that lay the foundations of this thesis, starting with the characteristics of piezoelectrics and ferroelectrics. It also introduces lead zirconate titanate and other materials pertinent to this work. Additionally, the chapter discusses thin film growth theory.

Chapter 3 introduces the different sample configurations involved in this work and the procedures to prepare the samples, from substrate preparation and thin film deposition methods to electrodes patterning. It also describes the methods to characterise the structure of thin films.

Chapter 4 presents the various experimental setups and procedures, previously not implemented in the research group, which are used in this thesis to characterise the samples ferroelectric properties, including dielectric permittivity and piezoelectric coefficient.

Chapter 5 describes and discusses the experimental results obtained with heterostructures produced and characterised according to the methods and processes introduced in chapters 3 and 4. The texture and ferroelectric properties of lead zirconate titanate thin films deposited on stainless steel substrates are investigated along with the effect of Nb-doping on the properties of these thin films.

Chapter 6 describes the modelling of ferroelectric bending tongues loaded at their free end to understand the influence of some parameters on the vertical deflection. Equations of the model are introduced and the results are illustrated with examples.

Chapter 7 provides answers to the statement of purpose of this thesis and summarises the main conclusions of this work. Its outlooks are outlined, along with and potential future work.

2. Fundamentals

This chapter examines the literature pertinent to the work done in this thesis. Section 2.1 introduces ferroelectric materials along with dielectricity, piezoelectricity and pyroelectricity. This section also discusses the perovskite structure in relation to ferroelectricity. Afterwards, section 2.2 gives an overview of the materials relevant to this thesis, including lead zirconate titanate as the selected ferroelectric material, the various buffer layer materials and AISI 304 stainless steel as the substrate of choice for this work. Subsequently, section 2.3 introduces thin film growth theory and crystallographic structure of thin films.

2.1. Ferroelectric materials: dielectrics, piezoelectrics and pyroelectrics

All ferroelectric materials are pyroelectrics which, themselves, are part of the piezoelectric class. Piezoelectric materials belong to the preeminent class of dielectrics [86]. Therefore, it is necessary to understand ferroelectricity in relation with these other phenomena as shown in this section.

Through this section, the physical properties of crystals will be defined in a *Cartesian coordinates system* with a point O for origin and three base vectors $\boldsymbol{e}_1$, $\boldsymbol{e}_2$ and $\boldsymbol{e}_3$. These base vectors are orthogonal in pairs ($\boldsymbol{e}_i \perp \boldsymbol{e}_j$ for $i \neq j$ with $i, j = 1, 2, 3$) and of unit length ($\|\boldsymbol{e}_1\| = \|\boldsymbol{e}_2\| = \|\boldsymbol{e}_3\| = 1$). The scalar product of any of these two base vectors is equal to [87]:

$$\boldsymbol{e}_i \cdot \boldsymbol{e}_j = \delta_{ij} \qquad \text{with } i, j = 1, 2, 3, \tag{2.1}$$

where δ_{ij} is the Kronecker symbol defined by:

$$\delta_{ij} = \begin{cases} 1, & i = j \\ 0, & i \neq j. \end{cases} \tag{2.2}$$

In this thesis, both the Einstein convention summation over repeated indices and the reduced matrix notation for tensor properties, also known as Voigt notation, are employed [88, 89].

2.1.1. Dielectrics and electrostriction

Dielectric materials are insulators that can be polarised by the application of an external electrical field, $\boldsymbol{E}$. The dielectric polarisation is due to the electrical charges shifting slightly out of their equilibrium positions under the influence of the electrical field. The ability of a dielectric to polarise under the applied field is called *electrical susceptibility*, described by the dielectric susceptibility tensor χ_{ij}, and is defined as the constant of proportionality between the polarisation density vector, also called *polarisation*, $\boldsymbol{P}$, and the applied electrical field by [90, 91]:

$$P_i = \varepsilon_0 \chi_{ij} E_j, \tag{2.3}$$

where ε_0 is the electrical permittivity of free space with $\varepsilon_0 \approx 8.854 \cdot 10^{-12}$ F·m^{-1}. The permittivity tensor, ε_{ij}, and the relative permittivity or dielectric constant of a material, $\varepsilon_{r,ij}$, are defined by:

$$\varepsilon_{ij} = \varepsilon_{r,ij}\varepsilon_0 = (\chi_{ij} + \delta_{ij})\,\varepsilon_0. \tag{2.4}$$

The electrical displacement vector, $\boldsymbol{D}$, is linked to the polarisation vector and to the applied electrical field by [90, 91]:

$$D_i = \varepsilon_0 E_j + P_i = \varepsilon_0 \varepsilon_{r,ij} E_j. \tag{2.5}$$

Under an alternating electrical field, a dielectric material tends to dissipate some energy due to the movement of its electrical charges, generating heat. This lost energy is known as *dielectric loss* and is quantified with the loss tangent, $tan\ \delta$, defined as [92]:

$$tan\ \delta = \frac{\varepsilon''}{\varepsilon'}, \tag{2.6}$$

where ε' and ε'' are the real and imaginary components of the permittivity, respectively.

In any material, including dielectrics, *electrostriction* is the fundamental electromechanical coupling defined as a mechanical deformation due to an applied electrical excitation [91]. Electrostriction is a quadratic effect expressing the dependence, at zero stress values, of the induced strain tensor, κ_{ij}, on the electrical stimulation or on an induced dielectric displacement [93]. These relations are expressed respectively by:

$$\kappa_{ij} = M_{ijkl} E_k E_l, \tag{2.7}$$

$$\kappa_{ij} = Q_{ijkl} D_k D_l, \tag{2.8}$$

where M_{ijkl} and Q_{ijkl} are the fourth rank tensors electrostriction coefficients. It should be noticed that electrostriction can be neglected at lower stress and strain values, with regard to the linear effect of piezoelectricity described in the following section [93].

2.1.2. Piezoelectricity

Direct piezoelectric effect is displayed by a material when, being mechanically deformed, it generates a change in electrical polarisation proportional to the deformation. Oppositely, the *converse piezoelectric effect* corresponds to the application of an external electrical field on the material giving rise to strain in the material [94, 95]. These two effects are illustrated in Figure 2.1.

In 1880, Jacques Curie and Pierre Curie were the first to experimentally demonstrate the existence of *piezoelectricity* in several materials, e.g. tourmaline, quartz or topaz [96]. Piezoelectricity corresponds to a linear relation between electrical and mechanical states in crystals which do not possess a centre of symmetry [94, 95].

Piezoelectricity emerges in a material from its crystal structure: for electrical polarisation to appear when an external mechanical force is applied, the crystal must have a symmetry sufficiently low [97]. As they are polarisable, i.e. can develop charges on their surfaces, all piezoelectrics are also dielectrics [98]. While 32 crystal classes exist, only 21 are non-centrosymmetric, potentially allowing piezoelectricity. However, the crystal class 432, while not possessing a centre of symmetry, does not display piezoelectricity due to additional symmetry elements. Therefore, the 20 crystal classes producing the piezoelectric effect are the following: 1, 2, m, 222, $2mm$, 3, 32, $3m$, 4, $\bar{4}$, 422, $4mm$, $\bar{4}2m$, 6, $\bar{6}$, 622, $6mm$, $\bar{6}2m$, 23, $\bar{4}3m$ [99]. For

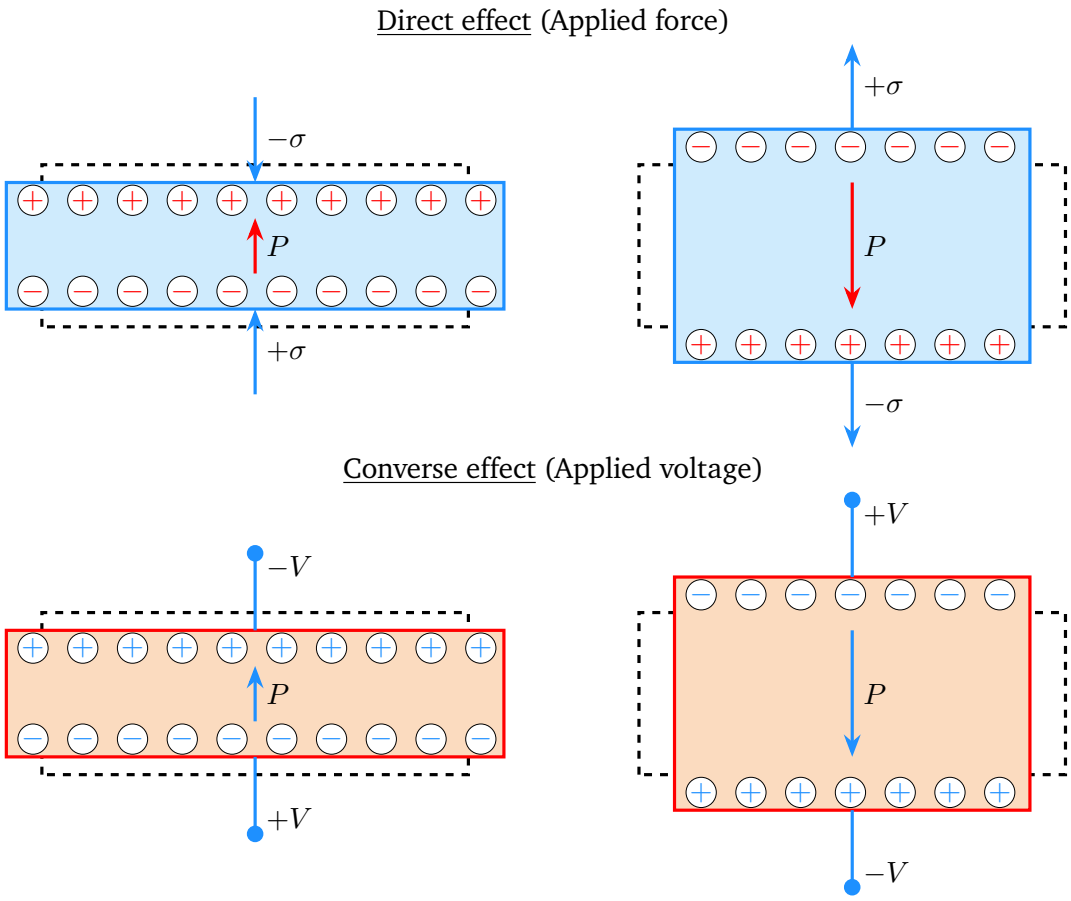

Figure 2.1.: Schematic representation of the direct (top schematics) and converse (bottom schematics) piezoelectric effects on a piezoelectric crystal. The dashed lines indicate the shape of the crystals before stress, $\pm\sigma$, or voltage, $\pm V$, (generating a polarisation, P) are applied. The blue colour indicates applied quantities and the red colour highlights induced polarisation and strain. The $\oplus$ and $\ominus$ symbols represent qualitatively positive and negative electrical charges, respectively. Adapted from [95].

each of these space groups, the non-zero components of their piezoelectric coefficient tensors and their relationship can be found in literature [89, 100].

It should be noted that the linearity of the piezoelectric response is only valid at low applied stress and field levels. At higher levels, electrostriction becomes non-negligible (see section 2.1.1) and, in the case of ferroelectrics, domain wall motion contributes to the non-linearity of the response (see section 2.1.4) [101]. Therefore, the relations given below (Equations (2.15) and (2.16)) are only valid in the linear range of the piezoelectric response of the material under consideration.

The piezoelectric response of a material is described by a series of coefficients known as *piezoelectric coefficients*. The coefficients d, g, e and h correspond to the direct effect while the coefficients d^*, g^*, e^* and h^* correspond to the converse effect. The piezoelectric coefficients are defined by the following

equations [102]:

$$d = +\left(\frac{\partial D}{\partial \sigma}\right)_{E,T}, \qquad d^* = +\left(\frac{\partial \kappa}{\partial E}\right)_{\sigma,T}, \tag{2.9}$$

$$g = -\left(\frac{\partial E}{\partial \sigma}\right)_{D,T}, \qquad g^* = +\left(\frac{\partial \kappa}{\partial D}\right)_{\sigma,T}, \tag{2.10}$$

$$e = +\left(\frac{\partial D}{\partial \kappa}\right)_{E,T}, \qquad e^* = -\left(\frac{\partial \sigma}{\partial E}\right)_{\kappa,T}, \tag{2.11}$$

$$h = -\left(\frac{\partial E}{\partial \kappa}\right)_{D,T}, \qquad h^* = -\left(\frac{\partial \sigma}{\partial D}\right)_{\kappa,T}, \tag{2.12}$$

where σ is the applied stress, κ is the induced strain and T is the temperature. The variables kept constant are indicated by the subscripts.

Due to thermodynamics, the piezoelectric coefficients for the direct effect are equal to their respective counterparts for the converse piezoelectric effect [102].

From the experimental approach, it should be noted that when the stress is kept constant, i.e. $\sigma = cst$, the piezoelectric sample is said to be in a *mechanically free* state [90]. It is difficult to realise this condition experimentally as the sample must be held without generating stress, e.g. in nodes of vibration [103]. Contrarily, when the strain is kept constant, i.e. $\kappa = cst$, the piezoelectric is in a *mechanically clamped* state [90]. It can be achieved experimentally by maintaining the sample in an infinitely stiff neighbourhood [103]. Analogue states can be expressed electrically: *electrically free* and *electrically clamped* states are obtained by keeping the electrical field strength constant, i.e. $E = cst$, or by maintaining the electrical flux density constant, i.e. $D = cst$, respectively [90]. Experimentally, the electrodes collecting the charges must be shortened in the first case and must be kept in an insulating environment in the latter [103].

The coefficients d and e both refer to electrically free states and to mechanically free and clamped states, respectively. The coefficient d is known as *piezoelectric charge constant* and describes the relation between the dielectric displacement and the stress. It is expressed in C·N^{-1}. The coefficient e characterises the relation between the dielectric displacement and the strain. Its unit is C·m^{-2}. Conversely, the coefficients g and h apply to electrically clamped states with mechanically free and clamped states, respectively. The coefficient g or *piezoelectric voltage constant* and the coefficient h describe the relation between the electrical field and the stress or the strain, respectively. Their respective units are C^{-1}·m^2 and C^{-1}·N [90, 103].

Piezoelectric coefficients are third rank tensors and therefore contain 27 components. However, as the coefficients, e.g. d_{ijk}, are symmetrical in i and j, the number of independent components is limited at 18 [89, 103]. This allows the use of the Voigt notation to simplify piezoelectric coefficients into a matrix notation. The coefficients d_{ijk} and e_{ijk} and their matrix notations $d_{i\mu}$ and $e_{i\mu}$ follow, respectively, the relations [103]:

$$\begin{pmatrix} d_{111} & d_{122} & d_{133} & 2d_{123} & 2d_{113} & 2d_{112} \\ d_{211} & d_{222} & d_{233} & 2d_{223} & 2d_{213} & 2d_{212} \\ d_{311} & d_{322} & d_{333} & 2d_{323} & 2d_{313} & 2d_{312} \end{pmatrix} \cong \begin{pmatrix} d_{11} & d_{12} & d_{13} & d_{14} & d_{15} & d_{16} \\ d_{21} & d_{22} & d_{23} & d_{24} & d_{25} & d_{26} \\ d_{31} & d_{32} & d_{33} & d_{34} & d_{35} & d_{36} \end{pmatrix}, \tag{2.13}$$

and

$$\begin{pmatrix} e_{111} & e_{122} & e_{133} & e_{123} & e_{113} & e_{112} \\ e_{211} & e_{222} & e_{233} & e_{223} & e_{213} & e_{212} \\ e_{311} & e_{322} & e_{333} & e_{323} & e_{313} & e_{312} \end{pmatrix} \cong \begin{pmatrix} e_{11} & e_{12} & e_{13} & e_{14} & e_{15} & e_{16} \\ e_{21} & e_{22} & e_{23} & e_{24} & e_{25} & e_{26} \\ e_{31} & e_{32} & e_{33} & e_{34} & e_{35} & e_{36} \end{pmatrix}. \tag{2.14}$$

The coefficients g and h follow the same rules as the coefficients d and e, respectively.

In practice, the conditions for mechanically and electrically free or clamped states are rarely met. Therefore, the elastic and dielectric linear equations of state for piezoelectric are written as:

$$D_i = d_{i\mu}\sigma_\mu + \varepsilon_{ik}E_k \text{ (direct effect)} \qquad \kappa_\lambda = d_{k\lambda}E_k + s_{\lambda\mu}\sigma_\mu \text{ (converse effect)}, \tag{2.15}$$

and

$$D_i = e_{i\lambda}\kappa_\lambda + \varepsilon_{ik}E_k \text{ (direct effect)} \qquad \sigma_\mu = -e_{k\mu}E_k + c_{\lambda\mu}\kappa_\lambda \text{ (converse effect)}, \tag{2.16}$$

where $s_{\lambda\mu}$ is the elastic compliance and $c_{\lambda\mu}$ is the elastic stiffness [103]. Equations of state for the coefficients g and h can also be written but are not relevant to this work.

It should be noted that the piezoelectric coefficients described above refer to bulk coefficients. In the case of piezoelectric thin films, the boundary conditions to which the film is subjected needs to be taken into account [104]. Indeed, for the majority of MEMS applications, piezoelectrics are integrated into a composite structure. This imposes a mixed boundary condition as the piezoelectric layer is clamped to another elastic body whose properties are often predominant in the composite [17, 24].

Therefore, the piezoelectric coefficients $e_{31,f}$ and $d_{33,f}$ relate to thin films clamped to rigid substrates in the $(\boldsymbol{e}_1, \boldsymbol{e}_2)$ plane and with unconstrained off-plane motion in the $\boldsymbol{e}_3$ direction. $e_{31,f}$ and $d_{33,f}$ describe the transverse effect, i.e. the in-plane stress as a function of the applied field, and the longitudinal effect, i.e. the thickness change as a function of the applied field, respectively. The $e_{31,f}$ and $d_{33,f}$ coefficients for thin films are defined as follow: [17, 24].

$$e_{31,\mathrm{f}} = \frac{d_{31}}{{s_{11}}^E + {s_{12}}^E}, \tag{2.17}$$

$$d_{33,f} = d_{33} - \frac{2{s_{13}}^E}{{s_{11}}^E + {s_{12}}^E}, \tag{2.18}$$

where ${s_{11}}^E$, ${s_{12}}^E$ and ${s_{13}}^E$ are the s_{11}, s_{12} and s_{13} elastic compliances at constant electrical field, respectively.

2.1.3. Pyroelectricity

Within the piezoelectric classes, ten point groups, presenting a unique polar axis, are characteristic of pyroelectrics: 1, 2, m, $2mm$, 3, $3m$, 4, $4mm$, 6 and $6mm$. Known as the *polar classes*, they exhibit a spontaneous polarisation, i.e. non-zero electrical polarisation in zero applied electrical field, which is temperature dependent [103]. The term *polar axis* refers to the direction of the spontaneous polarisation [105].

Similar to piezoelectricity, pyroelectricity displays direct and converse effects, referred to as *pyroelectric effect* and *electrocaloric effect*, respectively. The pyroelectric effect corresponds to a change in spontaneous polarisation due to a change in temperature. Conversely, the electrocaloric effect describes a change in temperature originating from an applied electrical field [103].

The relation between the change in spontaneous polarisation vector, $\boldsymbol{P_s}$, and the change in temperature, T, is described by the vector of pyroelectric coefficients, $\boldsymbol{p}_i$ [98]:

$$\boldsymbol{p}_i = \frac{\partial \boldsymbol{P}_{\boldsymbol{s},i}}{\partial T}. \tag{2.19}$$

2.1.4. Ferroelectricity

A system is *ferroelectric* if it is insulating and possesses at least two stable or metastable states of different spontaneous polarisation between which it is possible to switch under an applied electrical field. The ability to switch from one state to another is due to the field-to-polarisation coupling through which an applied electrical field varies the states relative energy [106].

Ferroelectricity was identified experimentally for the first time in Rochelle salt in 1920 by Valasek [107,108]. However, Rochelle salt or sodium potassium tartrate tetrahydrate of chemical formula $NaKC_4H_4O_6 \cdot 4H_2O$ was the only known ferroelectric material for more than a decade after being discovered, leading ferroelectricity to be known as *Seignette-electricity* from the name of the company preparing Rochelle salt until the early 1940s [86].

Ferroelectric materials are pyroelectrics in which the polarisation switching is accessible through very small lattice distortions. In case substantial lattice reconstruction is needed to change the orientation of the spontaneous polarisation, the material is pyroelectric without being ferroelectric as the large energetic requirements for polarisation switching are likely to result in dielectric breakdown [103].

Polarisation itself has long been challenging to define until the beginning of the 1990s. In the case of a finite system, the Clausius-Mossotti model can be applied and the task is simple enough. Indeed, the dipole moment corresponds to the polarisation and can be calculated as the volumic charge density. However, difficulties arise when considering polarisation as the bulk property of an infinite crystal [109].

The first obstacle emerges when attempting to choose a dipole in a periodic continuous distribution. It is not possible to separate such a distribution in localised contributions without ambivalence: a dipole could either be composed by $\oplus - \ominus$ (positive - negative) or $\ominus - \oplus$ (negative - positive) electrical charges combinations and selecting one of the options would arbitrarily define the polarisation direction [109,110]. Another complication derives from the nature of the bonding inside the ferroelectric. In real materials, e.g. in typical ferroelectric oxides, as opposed to a perfect modelled material, the bonding is a mixture of ionic and covalent characters. As such, the ions are sharing the electronic charge which is delocalised, making impossible the utilisation of the Clausius-Mossotti model [109].

The *modern theory of polarisation*, developed by Resta, King-Smith and Vanderbilt [111–113], arises from a change of perspective on the problematic: it aims to define the change in polarisation and no longer reach the absolute value of polarisation [109]. This theory relies on Berry phases and Wannier functions. For more details, the reader is referred to [112–115].

Previous attempts to define polarisation based on a charge distribution proved to be flawed as they failed to differentiate bulk contributions from surface ones. The modern theory of polarisation not only provides a definition separating bulk from surface contributions, independently of both the shape and location of the unit cell, but it also produces a unique solution for the polarisation. Assuming that any charge pumped to the surface of the dielectric cannot be conducted away, the change in polarisation is defined by [109]:

$$\Delta \boldsymbol{P} = \int \mathrm{d}t \frac{1}{V_{cell}} \int_{cell} \mathrm{d}\boldsymbol{r}\ \boldsymbol{j}(\boldsymbol{r}, t), \tag{2.20}$$

where $\Delta \boldsymbol{P}$ is the change in internal polarisation, V_{cell} is the volume of the unit cell, t is the time, $\boldsymbol{r}$ is the position vector and $\boldsymbol{j}$ is the current density vector.

Ferroelectrics ability to switch their spontaneous polarisation between discrete states at lower temperatures is due to the instability of the transverse optical lattice vibration mode at high temperature. As the

temperature decreases, the phonon frequency diminishes until it reaches zero at the Curie temperature, T_C. This vibration mode is called *soft mode* and leads to a crystal structure with lower symmetry when the atomic position freezes at T_C [103, 116, 117].

In terms of thermodynamics, the transition from the higher symmetry phase, called *paraelectric* phase, to the lower symmetry ferroelectric phase is described by the Landau-Devonshire theory. The thermodynamic state of a bulk ferroelectric system in equilibrium can be described by the temperature, polarisation, electrical field, strain and stress variables. In practice, electrical fields and elastic stresses are the physical quantities applied on ferroelectrics. Therefore, polarisation and strain are considered as "internal" variables [118].

It should be noted that the Landau-Devonshire theory is intended to handle poled bulk ferroelectrics and that for unpoled ferroelectrics the Levanyuk-Ginzburg criterion should be used. For more details on the latter, the reader is referred to [118].

Based on the fundamental postulate of thermodynamics, the Helmholtz free energy density, $\mathcal{F}_P$, of a ferroelectric depends on ten variables: the temperature, the three components of polarisation and the six components of stress. According to the Landau-Devonshire theory, assuming that for a free non-polarised and non-strained crystal the origin of energy is zero, the free energy as a function of polarisation, truncated at the sixth term, can be written as:

$$\mathcal{F}_P = \frac{1}{2}a_0\left(T - T_0\right)P^2 + \frac{1}{4}bP^4 + \frac{1}{6}cP^6 - EP, \tag{2.21}$$

where T_0 is the paraelectric-ferroelectric transition temperature at which $a_{iso} = a_0\left(T - T_0\right)$ changes sign, a_{iso} is the reciprocal isothermal permittivity at constant stress in the non-polar phase and b and c are coefficients that are assumed to be independent of temperature. The coefficient a_0 is positive for all known ferroelectrics and the coefficient c must be positive to ensure stability when $P \to \infty$ [118, 119].

Therefore, the order of the transition between the paraelectric and the ferroelectric phases, whose free energy densities are represented in Figure 2.2, is characterised by the sign of the coefficient b [118, 119].

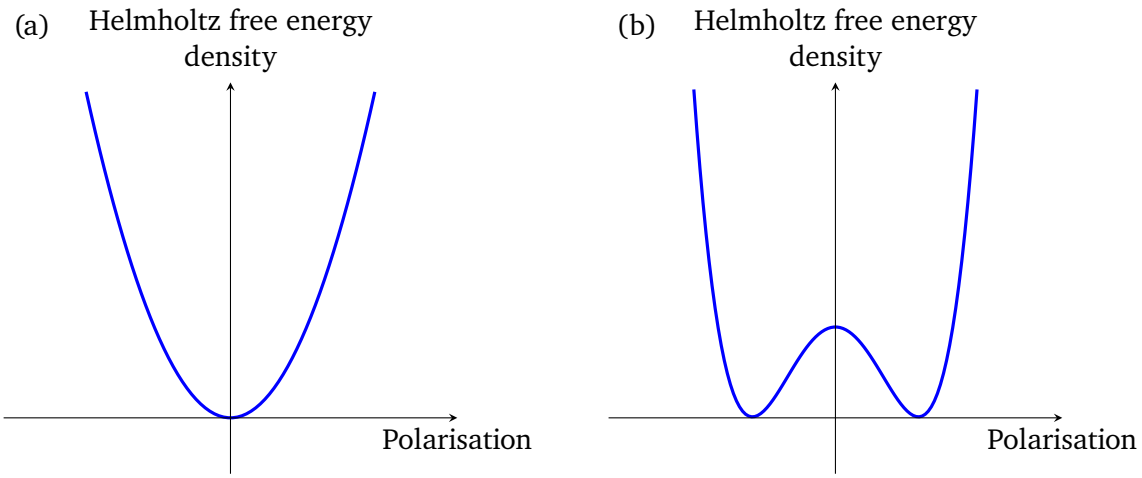

Figure 2.2.: Helmholtz free energy density, $\mathcal{F}_P$, versus polarisation, P, for (a) paraelectric ($T \gg T_0$) and for (b) ferroelectric ($T \ll T_0$) phases. Adapted from [118].

A second-order transition from the paraelectric to the ferroelectric phase occurs at the temperature $T_0 = T_C$ if the coefficient b is positive. In that case, the free energy density changes continuously between the two

states represented in Figure 2.2 and the spontaneous polarisation also evolves continuously as shown in Figure 2.3 (a). The electrical susceptibility presents a discontinuity at T_0 [103, 118, 119].

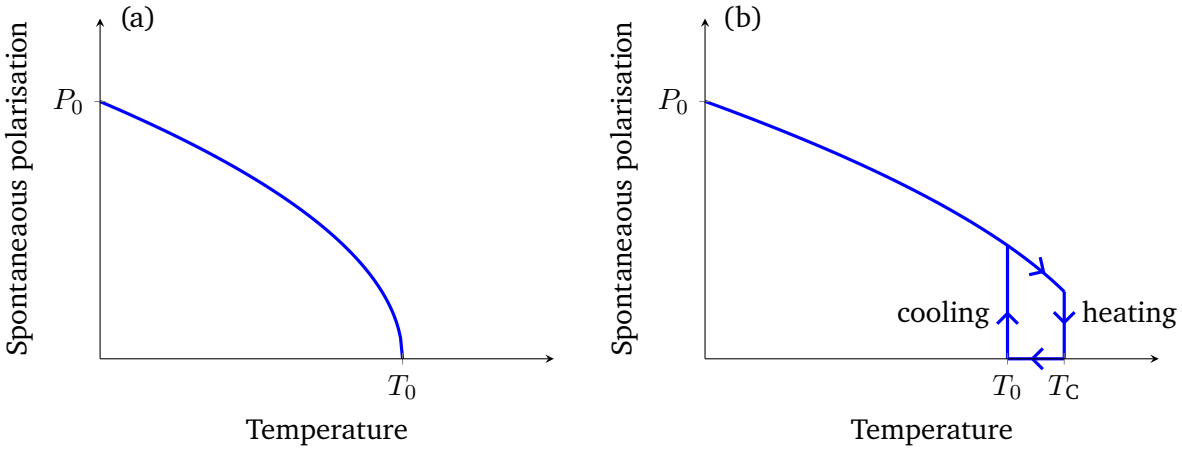

Figure 2.3.: Spontaneous polarisation, P_s, as a function of temperature, T, for (a) a second-order phase transition and (b) a first-order phase transition representing the thermal hysteresis associated with finite heating and cooling rates. The spontaneous polarisation maximum, P_0, is indicated, along with T_0 and the Curie temperature, T_C. Adapted from [118,120].

In the case where the coefficient b is negative, a discontinuous first-order phase transition occurs at T_C. Indeed, as b is negative, the free energy density can reach two secondary minima at non-zero polarisation along with the minimum at zero polarisation. At the Curie temperature, these two minima at non-zero polarisation become configurations with lower energy than the paraelectric phase. It follows that the spontaneous polarisation drops to zero at T_C, as represented in Figure 2.3 (b). The susceptibility reaches a finite value at T_C with $T_C > T_0$ for first-order transitions [103, 118, 119].

Due to the free energy density presenting three energetically degenerate minima at T_C, the first-order phase transition between the paraelectric and ferroelectric phases varies depending on whether it is approached during heating or during cooling, as shown in Figure 2.3 (b) [118, 120].

Close to the ferroelectric transition, when it is approached from the paraelectric phase, i.e. $T > T_0$, both the electrical susceptibility and the dielectric permittivity follow the Curie-Weiss behaviour. The Curie-Weiss law for the permittivity can be expressed as:

$$\varepsilon_r = \frac{C_W}{T - T_0}, \tag{2.22}$$

where C_W is the material specific Curie-Weiss constant [103, 118]. It should be noted that a ferroelectric might reach its melting point before reaching its transition temperature [106].

Another approach to describe the ferroelectric transition is to consider the lattice displacements due to the electronic polarisation. The lattice displacements are finite below T_C but can either vanish or remain above T_C. In the former case, the transition is called *displacive* and the dipole moments below T_C are due to ions spontaneous displacement, while in the latter case, where the symmetry-breaking distortions are randomly oriented above T_C, the transition is considered as *order-disorder* [103, 118]. The order of magnitude of the Curie-Weiss constant differs for *displacive* and *order-disorder* transitions. A Curie-Weiss constant of

the order of 10^5 K is characteristic of a *displacive* transition and can be found, for example, in perovskite ferroelectrics. Conversely, *order-disorder* transitions, common in the presence of hydrogen bonds, present a Curie-Weiss constant of the order of 10^2 to 10^3 K [103, 120].

As described above, ferroelectrics are able to switch between states of different spontaneous polarisation under an applied electrical field. Following the Landau-Devonshire theory, this process implies a hysteresis in the polarisation versus applied electrical field curve, also known as *P-E* loop [118]. Since ferroelectrics are also piezoelectrics, a hysteresis is also present in the elastic strain versus applied electrical field curve, called *butterfly* loop, due to its shape [121]. The typical *P-E* loop and *butterfly* loop for an ideal single-crystal when the applied electrical field is parallel to the spontaneous polarisation are represented in Figure 2.4 (a) and (c), respectively. The positive applied electrical field under which the polarisation is reversed from one state to another, known as *coercive field*, E_c, is indicated [120]. The figure also shows the saturation polarisation, P_{sat}, corresponding to the linear extrapolation at zero applied field of the maximum polarisation which can be reached at high field. Its counterpart is the saturation strain, κ_{sat}.

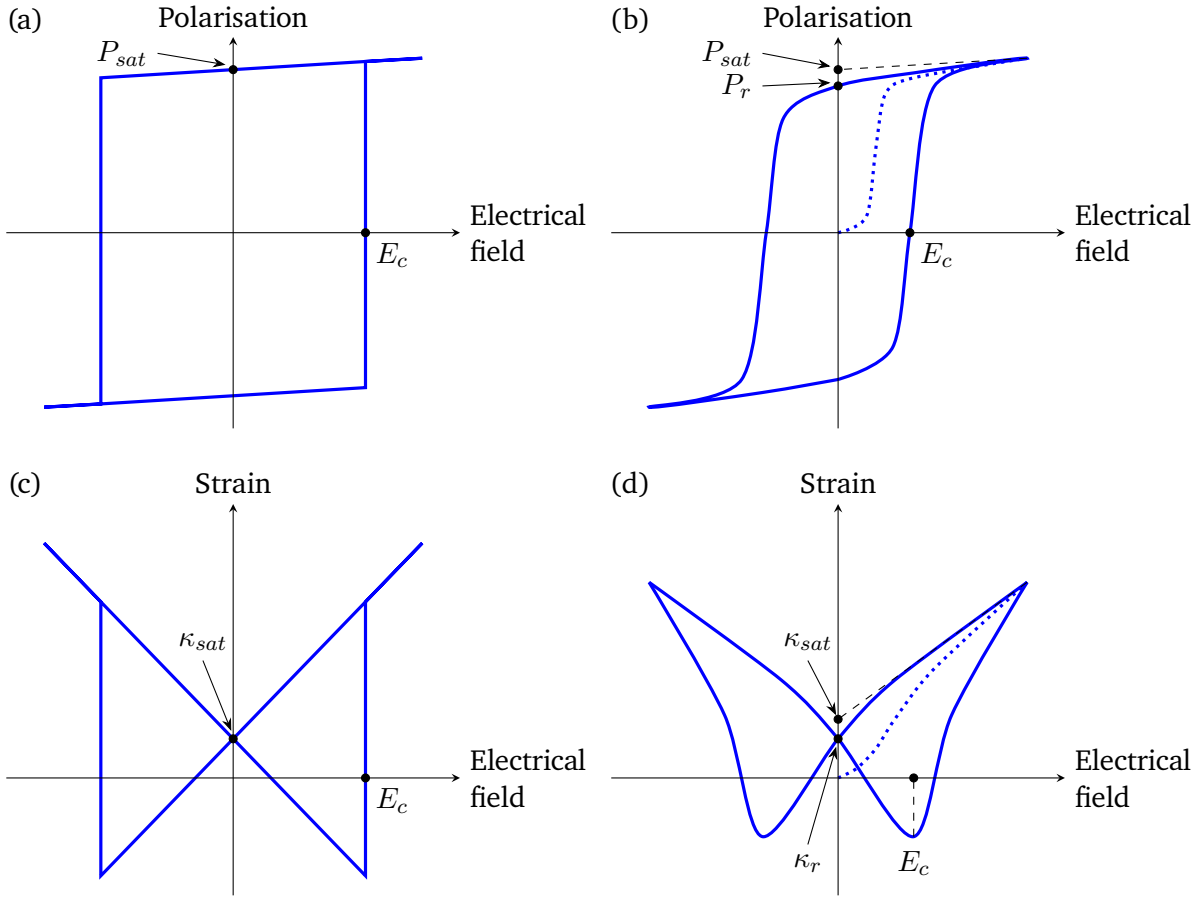

Figure 2.4.: Typical hysteresis loops for ferroelectrics. Polarisation, P, and elastic strain, x, versus applied electrical field, E, hysteresis loops for (a) and (c) an ideal single-crystal when the applied electrical field is parallel to the spontaneous polarisation and (b) and (d) a polycrystalline sample, respectively. The saturation polarisation, P_{sat}, the remanent polarisation, P_r, the coercive field, E_c, the saturation strain, κ_{sat} and the remanent strain, κ_r are indicated. Adapted from [120].

The shape of the ferroelectric hysteresis loops for polycrystalline samples, presented in Figure 2.4 (b) and (d), as well as for non-ideal single-crystals, is due to the existence of ferroelectric *domains*. Domains are regions within which the polarisation is oriented in a given direction. They are separated from each other by *domain walls*. The apparition of *domain structures* in ferroelectrics aims to minimise the system free energy by balancing the electrical field energy reduction and the domain walls energy [103, 120].

It should be noted that while the number of domains depends on several parameters, e.g. crystal size and applied forces, the type of domains, i.e. the directions in which the polarisation can be oriented, are limited by the crystal symmetry [120]. For example, in a tetragonal crystal, the polarisation can take six distinct directions, as shown in Figure 2.5.

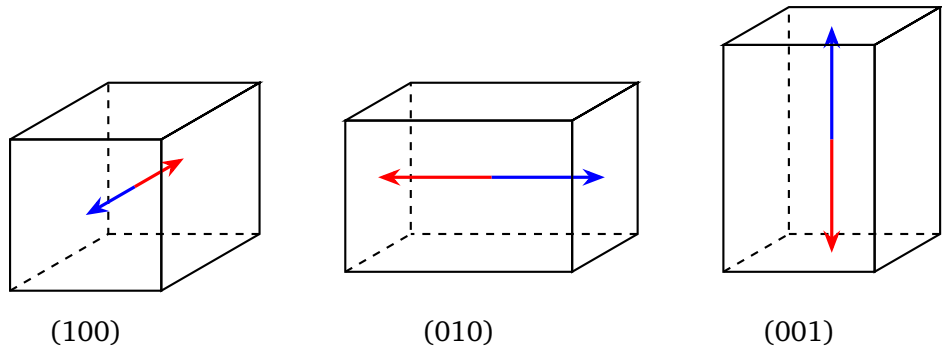

Figure 2.5.: Schematic representation of the accessible polarisation directions in a tetragonal crystal along (100), (010) and (001) orientations.

Domain walls are named by the angle between the polarisation of their two neighbouring domains [120]. In the case of a tetragonal crystal, due to the six accessible directions of polarisation, two sorts of domain wall exist: $180°$ and $90°$ domain walls, the latter also referred to as non-$180°$ domain wall [118]. A schematic representation of ferroelectric domains with either $180°$ or non-$180°$ domain walls is shown in Figure 2.6. The dielectric response is impacted by both $180°$ and non-$180°$ domain walls, while the piezoelectric response is dependent only on non-$180°$ domain walls. This is due to all domain walls being ferroelectrically active, while only non-$180°$ domain walls are ferroelastically active [122].

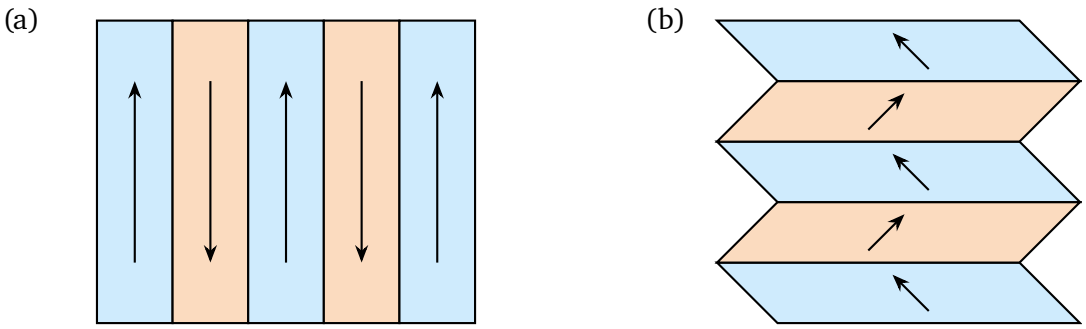

Figure 2.6.: Two dimensional schematic representation of ferroelectric domains in a crystal with (a) $180°$ domain walls and (b) non-$180°$ domain walls. Adapted from [123] and [124], respectively.

Due to their multiple-domains states, the net polarisation of ferroelectric crystals is generally zero or very limited. The re-orientation, under a unipolar applied electrical field, of the domain polarisations to create

a single-domain state leads to an increase in the net polarisation, as can be observed in Figure 2.4 (b). During this *ferroelectric switching* process, above the coercive field, E_c, the domain polarisations align themselves as closely as possible with the applied field direction. The process of applying an electrical field on a ferroelectric to create a net polarisation is known as *poling* [120]. The poling axis, along which the electrical field is applied, is conventionally called axis *3* [125].

Once the applied field is released, some domain polarisations might reverse to their original state due to elastic interactions. This phenomenon, known as *back-switching*, reduces the net polarisation to the remanent polarisation, P_r, a value below the saturation polarisation [120]. The remanent polarisation and its counterpart, the remanent strain, κ_r, are indicated in Figure 2.4 (b) and (d).

It should be noted that the piezoelectric response of ferroelectrics is due to both intrinsic and extrinsic contributions. The intrinsic contribution is due to the lattice contributions while the extrinsic contribution arises from domain wall motion or from phase boundary motion [122,126]. It is the irreversibility of domain wall motion that generates the hysteretic behaviour of *P-E* loops. The contribution to the piezoelectric response of the irreversible domain wall motion can be quantified under low applied electrical fields by the Rayleigh law [127]. As ferroelectrics undergo ageing, domain walls move towards more energetically stable positions, leading to energy losses and to a decrease of permittivity [128].

2.1.5. Perovskite structure and ferroelectric materials

Numerous materials display ferroelectric properties ranging from oxides (compounds of $LiNbO_3$ family, boracites or hexagonal manganites, e.g. $YMnO_3$), through layered oxides (Ruddlesden-Popper transition-metal oxides or Aurivillius phases, e.g. Bi_2WO_6 or $SrBi_2Ta_2O_9$) to polymers (polyvinylidene fluoride) and plastic crystals (tetramethylammonium bromotrichloroferrate(III)) [106, 129, 130].

However, a vast number of piezoelectric applications (see chapter 1) relies on ferroelectric materials with a perovskite structure [8, 18, 63]. The benefits of using ferroelectrics for piezoelectric applications are their large piezoelectric response and the possibility to pole these materials to create a net polarisation [106,131]. In particular, $BaTiO_3$ and PZT, the most widely used ferroelectric materials, are perovskite ceramics [1, 3]. Additionally, some relaxor based ferroelectrics with perovskite structure demonstrate ultra-high piezoelectric behaviour, e.g. $Pb(Zn_{1/3}Nb_{2/3}(O)_3$–$PbTiO_3$ [132].

The perovskite structure is named after the mineral calcium titanate, $CaTiO_3$. Its general formula is ABO_3 where both A and B represent cations, cationic mixtures or vacancies. As represented in Figure 2.7, the ideal perovskite structure has a cubic lattice and belongs to the space group *Pm*3*m*. The B cation is at the centre of an octahedron formed by 6 oxygen atoms. The first neighbours of the A cation are 12 oxygen atoms. The oxygen octahedra are linked at their corners, forming a cubic network within which the A cations are positioned. This particular atomic arrangement gives rise to interpenetrating B-O chains running parallel to the three crystallographic axes of the cubic unit cell. Oxygen atoms are contiguous to 4 A cations and 2 B cations, giving them a coordination of lower symmetry [106, 133].

In part due to the cationic A and B sites ability to accommodate a large number of elements, perovskites can form solid solutions, often displaying complete miscibility between two endpoint compounds. This leads to a wide range of properties including metallic or insulating behaviour, ferroelectricity, ferromagnetism and multiferroicity. The second cause for perovskites various properties is the possibility of cationic ordering through energy-lowering structural distortions. For example, ferroelectric perovskites arise from an off-centring of the B site cation with the ideal perovskite structure corresponding to the high-symmetry paraelectric phase [106, 134, 135].

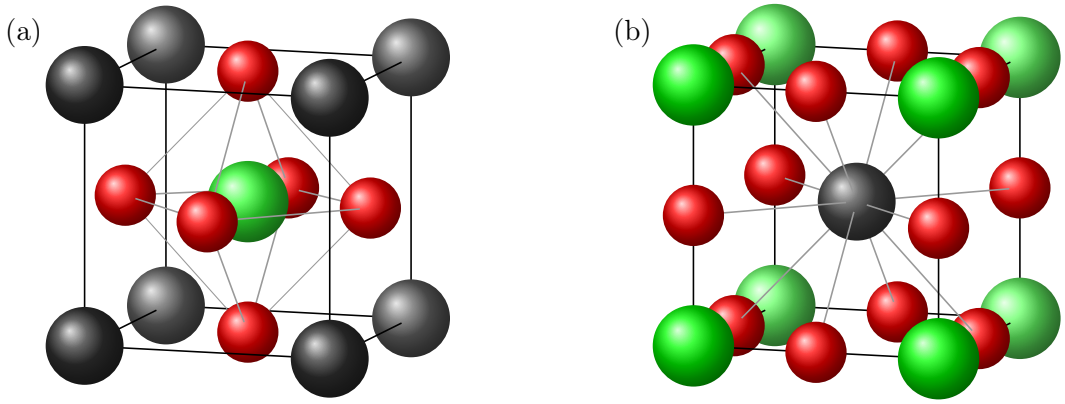

Figure 2.7.: Equivalent representations of the ABO_3 ideal cubic perovskite structure with the unit cell centred around (a) the B site cation or (b) the A site cation. The A site atoms are represented in black, the B site atoms are in green and the oxygen atoms are in red.

Perovskites are ionic solids and their proneness to distortions is due to structural frustration, encapsulated empirically by the Goldschmidt tolerance factor, t_G [136]:

$$t_G = \frac{r_A + r_O}{\sqrt{2}\,(r_B + r_O)}, \tag{2.23}$$

where r_A, r_B and r_O are the ionic radii of the A cation, B cation and oxygen atom, respectively. The tolerance factor describes the size requirements for the A and B cations to fit in the holes between and within the oxygen octahedra, respectively. For an ideal cubic perovskite, $t_G \simeq 1$. Otherwise, if t_G is strongly different from 1, the perovskite structure is not stable. However, small deviations around $t_G = 1$ can be tolerated by perovskites. If the A cation radius is smaller than the hole between the oxygen octahedra, then $t_G < 1$ and the A site is underbonded with the octahedra being prone to tilting and rotations, e.g. in $CaTiO_3$. Contrarily, if the B cation radius is too small to fill the oxygen octahedron, then $t_G > 1$ and a small polar distortion occurs, e.g. in $BaTiO_3$ [106, 134].

The vast majority of perovskites are subject to octahedral rotations, incompatible with the polar displacement required by ferroelectricity which is generally due to second-order Jahn-Teller effect [134, 135]. Out of the few ferroelectric perovskites, $BaTiO_3$ has been intensively studied due to its technological importance and as the first known ferroelectric perovskite [3]. As temperature decreases, $BaTiO_3$ transitions from its higher symmetry cubic paraelectric phase (space group *Pm*3*m*) to a tetragonal ferroelectric phase (space group *P*4*mm*) at 393 K. A second and third transition to ferroelectric phases, which are expected to be first order transitions, occur at 278 K to an orthorhombic phase (space group *Amm*2) and at 183 K to a rhombohedral phase (space group *R*3*m*), respectively. The structures of several perovskites sharing with $BaTiO_3$ a formal valence states of +2 for the A cation and +4 for the B cation are closely related. For example, $PbTiO_3$ displays the same rhombohedral-orthorhombic-tetragonal-cubic phase sequence with increasing temperatures. However, as phase transitions in ferroelectric perovskites are highly sensitive to the strain states, the orthorhombic phase can disappear from the rhombohedral-orthorhombic-tetragonal-cubic sequence under certain strain state [106, 133].

The ferroelectric perovskite lead zirconate titanate, including its phase diagram, is discussed in more details in the following section.

2.2. Materials relevant to this work

Through the course of this work, various materials have been considered, especially regarding the choice of buffer layers between the ferroelectric layer and the metallic substrate. For the sake of brevity, this work will only discuss the materials pertinent to the results hereby presented. Therefore, the following subsections introduce lead zirconate titanate as the ferroelectric material along with lanthanum nickelate, aluminium (III) oxide and platinum as buffer layers. AISI 304 stainless steel is also introduced as substrate material. It should be noted that lanthanum nickelate and platinum are also used as electrode materials.

2.2.1. Ferroelectric layer: lead zirconate titanate

Lead zirconate titanate, the most widely used ceramic for industrial piezoelectric applications, is a ferroelectric solid solution first investigated by Shirane, Suzuki and Tadeka in 1952 [2, 17, 23]. One of its end point compounds, $PbZrO_3$, is antiferroelectric. However, the substitution of less than 10 mol.% of Zr atoms by Ti atoms through the incorporation of ferroelectric $PbTiO_3$ is sufficient for $PbZrO_3$ antiferroelectricity to yield to a ferroelectric perovskite of formula $Pb(Zr_\gamma Ti_{1-\gamma})O_3$ (PZT, also noted PZT $(\gamma \times 100)/(1-\gamma) \times 100$) [137].

PZT, whose phase diagram is represented in Figure 2.8, exhibits a paraelectric phase, two antiferroelectric ones and three ferroelectric phases. The cubic paraelectric phase, with a lattice parameter of 4.085 Å, exists above the Curie temperature over the whole compositional range while the antiferroelectric phases, tetragonal and orthorhombic, are found at low $PbTiO_3$ content. At intermediate $PbTiO_3$ content, two rhombohedral ferroelectric phases occur, depending on the temperature. The third ferroelectric phase is tetragonal and prevails above 48 mol.% of $PbTiO_3$ content. Its lattice parameters are $a = 4.043$ Å and $c = 4.132$ Å [138–140].

Separating the rhombohedral and tetragonal phases in the PZT phase diagram is a morphotropic phase boundary. The interest of this almost vertical phase boundary resides in the possibility to transition, mostly insensitive to temperature, between the two phases by applying an electrical field on the system. This transition leads to a large strain response [17, 106].

To date, the phase diagram of PZT is still investigated [142, 143]. Recently, the long-range average rhombohedral phases have been found to coexist with two monoclinic structures over long- and short-range regions, respectively [141]. These structures, whose regions of existence are indicated in Figure 2.8, bridge the transition between rhombohedral and tetragonal phases [106].

Lead zirconate titanate is often employed with a composition of 48 mol.% of $PbTiO_3$ (PZT 52/48) in order to improve its piezoelectric response. Indeed, in bulk ceramics and often in thin films, the piezoelectric coefficients *d* and *e* (see section 2.1.2) are maximal at the morphotropic phase boundary. The transition temperature at the morphotropic phase boundary of bulk PZT, close to 360 °C, is among the highest ones for lead-based perovskites. This particularity limits the temperature dependence of its piezoelectric response, increases the coercive fields and reduces the risk of depoling, i.e. losing the effects of the poling process due to an electrical field applied in the opposite direction of the poling field. It should be noted that thin films sufficiently thick for MEMS applications have transition temperatures often within approximately 50 °C of those of single crystals and bulk ceramics [17].

Regarding the growth of PZT, understanding of the PbO–ZrO_2–TiO_2 system is crucial [24, 144]. PbO vapour pressure above PbO is of 1.1 Pa at 600 °C, which is two orders of magnitude larger than above PZT. Therefore, PbO molecules are highly volatile above 500 °C and diffuse easily [24, 145]. This phenomenon

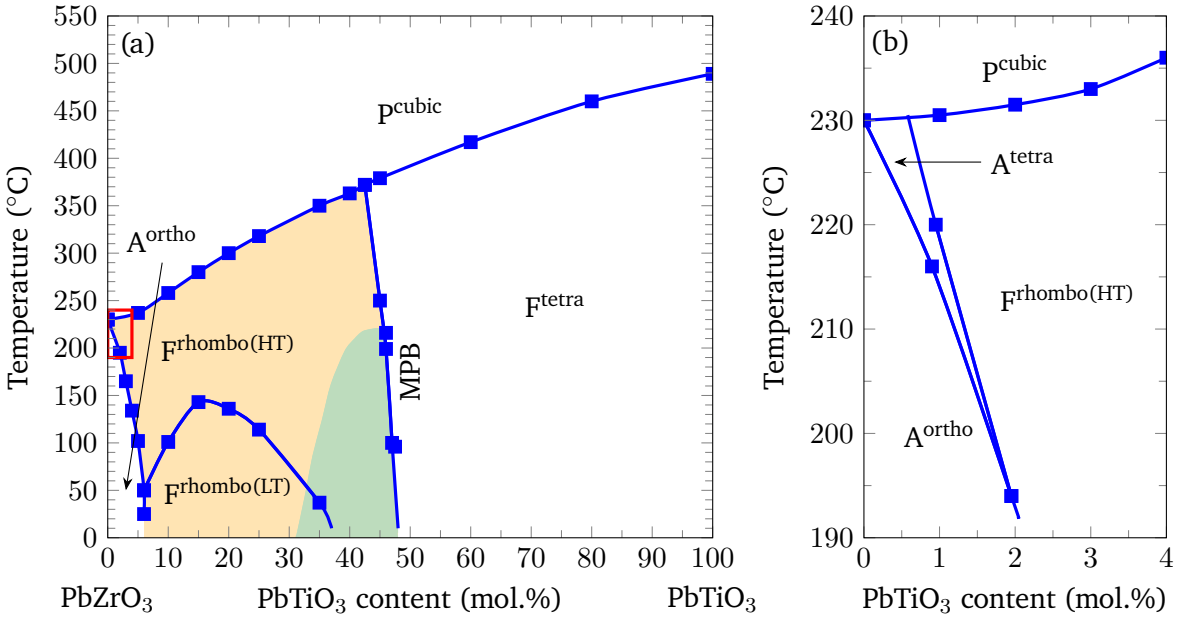

Figure 2.8.: $Pb(Zr_\gamma Ti_{1-\gamma})O_3$ phase diagram. (a) PZT phase diagram with $PbTiO_3$, γ, content ranging from 0 mol.% to 100 mol.%, (b) Detailed view of (a), indicated by the red box, with $PbTiO_3$ content ranging from 0 mol.% to 4 mol.%. Full lines and data points correspond to the widely used 1971 diagram from [138]. The paraelectric phase with a cubic lattice is indicated by P^{cubic}. Antiferroelectric phases with orthorhombic and tetragonal lattices are denoted by A^{ortho} and A^{tetra}, respectively. Ferroelectric phases with tetragonal and rhombohedral, at high and low temperature, are indicated by F^{tetra}, $F^{rhombo(HT)}$ and $F^{rhombo(LT)}$, respectively. The morphotropic phase boundary is indicated by MPB. The green coloured and orange coloured areas, data from [141], represent two monoclinic structures coexisting in long- and short-range regions, respectively, with the long-range average rhombohedral phases described by [138].

leads to important lead loss and the formation of a secondary phase with pyrochlore structure [24]. Yet, phases with pyrochlore as well as fluorite structures should be avoided as they are competing with the desired perovskite structure. In consequence, precise stoichiometric control is required for nucleation and growth [146].

Additionally, the activation energy of 441 $kJ{\cdot}mol^{-1}$ required to nucleate the perovskite structure of PZT is four times larger than the one of 112 $kJ{\cdot}mol^{-1}$ for its growth [147]. This indicates that PZT growth is nucleation controlled and allows the thin film texture to be selected by choosing appropriate electrodes as growth template [17, 24]. It should be noted that an increase in Zr content leads to higher activation energies for both nucleation and growth [147].

Due to smaller dimensions, a homogeneous composition can be obtained in thin films through diffusion on smaller distances than in bulk ceramics. Therefore, the growth temperatures for PZT thin films are lower than the sintering temperatures for bulk PZT. Consequently, deviations from stoichiometry may not be entirely redressed by local diffusion, leading to the formation of undesirable secondary phases. To compensate lead loss, which leads to pyrochlore formation, deposition methods generally provide excess lead. In cases where post-annealing is necessary for crystallisation, e.g. for chemical vapour deposition methods, rapid thermal annealing can be employed to limit lead loss [24].

The influence of the crystallographic orientation of PZT thin films on their piezoelectric properties can be difficult to assess. Indeed, the deposition residual stress state of thin films, either compressive or tensile, is dependent of their orientation and impacts the film ferroelectric domain state. In turn, the latter influences the remanent polarisation whose magnitude can be correlated to the piezoelectric response [17, 148]. As a result of the complexity of these mechanisms, some literature indicates a strong correlation with the texture [24] while some reviews point out that optimal piezoelectric properties have been reported for various orientations as well as for randomly oriented PZT thin films near the morphotropic phase boundary [17].

Nonetheless, texture engineering is important to optimise PZT thin film properties. Indeed, the anisotropy of the piezoelectric response , i.e. in-plane or out-of-plane, is linked to the orientation of the thin film. Therefore, texture engineering is of particular interest to improve piezoelectric response in thin films where domain wall motion is heavily clamped. Notably, {100}-oriented films display significantly larger piezoelectric responses than {111}-oriented films along with a high transition temperature of ~ 460 °C [17].

It should be noted that PZT ferroelectric properties are also dependent on composition, defects, grain size and mechanical boundary conditions. For example, the effect of composition on PZT permittivity and $e_{31,f}$ piezoelectric coefficient is shown in Figure 2.9 with the largest permittivity and $e_{31,f}$ coefficient being displayed by PZT 52/48. Furthermore, the $d_{33,f}$ coefficient of PZT thin films can be increased by increasing film thickness while it is not the case for the $e_{31,f}$ coefficient [17].

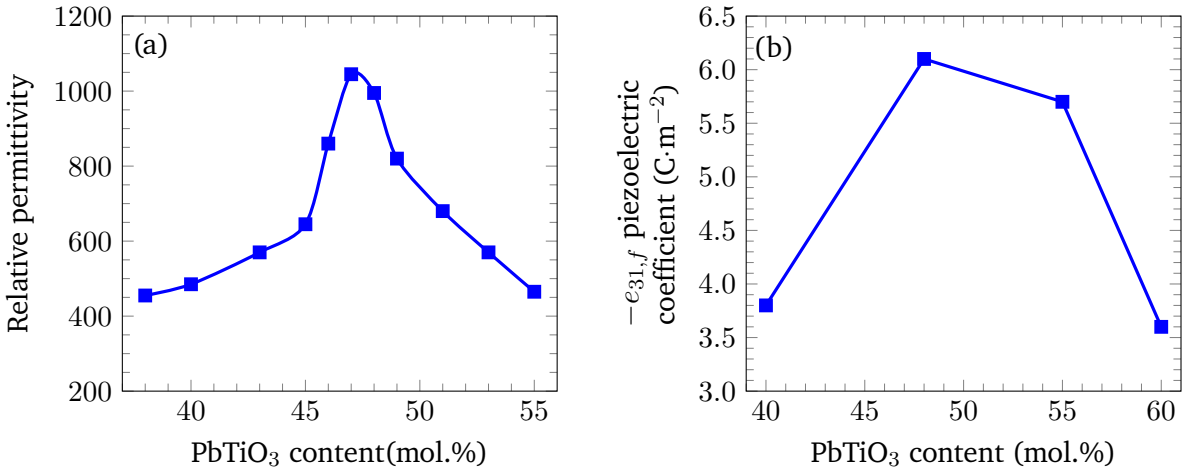

Figure 2.9.: Influence of PZT composition around the morphotropic phase boundary on (a) relative dielectric permittivity, ε_r, and (b) $e_{31,f}$ piezoelectric coefficient. The dielectric permittivity values shown in (a) correspond to bulk PZT ceramics sintered at $1,250$ °C for 16 hours, data from [149]. The $e_{31,f}$ coefficients presented in (b) are measured at room temperature on 2 µm PZT thin films, data from [150].

It is possible to tailor lead zirconate titanate for specific applications by altering its properties through doping. For MEMS applications, where a high dielectric constant and a large piezoelectric response are sought, donor-doped PZT, also known as *soft* PZT is often preferred over acceptor-doped or *hard* PZT. Since Nb-donor-doping of PZT is well established industrially, it is particularly interesting to assess its impact on the properties of PZT thin films on stainless steel substrates [53, 98, 146, 151–153].

Aliovalent Nb^{5+} doping substitutes for the *B* site cation in PZT perovskite structure. Compared to the 4+

valence of both Zr and Ti atoms, an additional positive charge is present in the lattice. To compensate for this charge created by donor-doping, one Pb^{2+} vacancy is created for every two Nb atoms introduced in the structure [98, 146, 151]. The general formula of Nb-doped PZT, noted PNZT, is $Pb_{1-\iota/2}\square_{\iota/2}(Zr_\gamma Ti_{1-\gamma})_{1-\iota}Nb_\iota O_3$ where $\square$ represents Pb vacancies [53, 146].

It has been established that the effects of Nb doping are extrinsic, due to the stabilisation of a pyrochlore phase and to structural changes, e.g. increased perovskite lateral grain size [146]. Notable properties modifications due to Nb doping in PZT thin films are an increase in electrical resistivity and dielectric constant [53, 98, 146, 151, 154]. The latter has notably been found to increase from 800 to 1,100 for undoped PZT and PZT doped with 2 mol.% Nb, respectively [155]. However, at larger concentrations, Nb-doping is detrimental to PZT properties, lowering the dielectric constant through the stabilisation of the pyrochlore phase [154].

Additional effects of Nb-doping are improved piezoelectric response and increased domain wall mobility though high dielectric loss has been reported [53, 98, 153–155]. Nb-doping up to 2 mol.% is reported to improve PZT thin films $e_{31,f}$ piezoelectric coefficient while larger amount of Nb leads to a decrease in the piezoelectric response [156]. The influence of Nb-doping on coercive field values for PZT thin films with compositions close to the morphotropic phase boundary remains ambiguous. While decreases of E_c values have been been reported with increasing Nb concentrations in PZT [98, 155, 157], there are literature reports of similar E_c values between undoped and 2 mol.% Nb-doped PZT [154]. Further studies on PZT 53/47 indicate an increase of E_c with 1 mol.% Nb-doping followed by a decrease of E_c at higher Nb concentrations [151].

2.2.2. Buffer layers and electrodes: lanthanum nickelate, aluminium oxide and platinum

Lanthanum nickelate

Lanthanum nickelate (LNO) is a rare earth nickelate of formula $LaNiO_3$ which crystallises with a rhombohedral structure in the space group $R\bar{3}c$. Its unit cell can be assimilated to a rhombohedrally distorted pseudocubic perovskite cell with a lattice parameter $a = 3.84$ Å. In this description, adjacent NiO_6 octahedra undergo an antiphase rotation around the [111] trigonal axis [158–160].

LNO is a metallic oxide with an isotropic resistivity at room temperature below 100 μΩ·cm. Hybridisation between Ni$3d$ and O$2p$ bands is responsible for its metallic behaviour [158, 159]. The metallicity of LNO and its origin is described in more details in [160].

Most of the time, when deposited on a perovskite single crystal substrate or electrode, PZT thin films grow with the same orientation as the growth template [17]. Therefore, LNO being a pseudocubic perovskite with a high chemical stability, it can be used as an efficient growth template for oriented PZT thin films [158]. Furthermore, its electrical conductivity also makes it a suitable bottom electrode in a parallel-plate capacitor structure [51, 159, 161, 162].

Aluminium (III) oxide

With the formula Al_2O_3, the only thermodynamically stable structure of aluminium (III) oxide is α-Al_2O_3. Its unit cell is hexagonal with lattice parameters $a = 4.754$ Å and $c = 12.99$ Å. Aluminium oxide is an insulating material and, therefore, cannot be employed as a bottom electrode. However, it is mostly insensitive to further oxidation and can act as a barrier layer for oxygen diffusion [163].

Platinum

Platinum, Pt, is a transition metal with a resistivity of 10.6 μΩ·cm, making it a good conductor [43]. As processes to deposit Pt by DC sputtering are well developed, Pt is a choice material for electrodes [18, 22, 46, 52, 54]. It is worthwhile to note that platinum might form intermetallic alloys, notably with chromium [164].

2.2.3. Substrate material: AISI 304 stainless steel

Stainless steels are a category of steels containing at least 11.5 wt.% of Cr which increases their oxidation resistance. Among these, austenitic steels contain between 17 wt.% and 25 wt.% of Cr and 8 wt.% to 20 wt.% of Ni. Austenitic steels have a face-centred cubic unit cell and may contain inclusions of magnetic ferritic steel, which is body-centred cubic, depending on their processing [165, 166]. AISI 304 austenitic stainless steel (SS304), also known as EN 1.4301 according to European norms, is the most commonly used stainless steel. Its standard composition is given in Table 2.1.

Table 2.1.: Standard composition of AISI 304 stainless steel, data from [165].

Elements	C	Mn	P	S	Si	Cr	Ni
Minimum chemical composition (wt.%)	-	-	-	-	-	18.00	8.00
Maximum chemical composition (wt.%)	0.08	2.00	0.045	0.030	1.00	20.00	10.50

Due to a low carbon content, austenitic steels are low-strength steels [165,166]. For the ferroelectric bending tongue applications envisioned in this work, this property of austenitic steels facilitate flexure. Indeed, strength is proportional to axial stiffness and a low axial stiffness is required to promote bending [167]. Furthermore, austenitic steels have a good high-temperature oxidation resistance in air which makes SS304 a substrate candidate likely to withstand the deposition conditions of the ferroelectric and buffer layers [165, 166].

Austenitic steels are easily shaped, notably into sheets through cold-rolling procedures [165]. This process leads to strain hardening of the steel due to the increase of the dislocation density [168]. However, it should be noted that stress relief occurs when the austenitic steel sheet is annealed above 500 °C [165].

Another side effect of annealing austenitic steel between 550 °C and 800 °C, is the formation of chromium carbide, $Cr_{23}C_6$, predominantly at grain boundaries, as chromium is rejected from the steel solid solution [166].

2.3. Thin film growth theory

While lacking a formal definition, the terminology *thin film*, by general agreement, encompasses layers whose thicknesses range from a few nanometres to one micrometre. It applies to films with one dimension sufficiently small relative to the other two to generate a high surface to volume ratio. As a result, some new properties, inexistent in the bulk, arise. The film can be considered as a *thin film* until the critical thickness where these surface properties are no longer predominant relative to the bulk properties [169].

Nowadays, the importance of thin films is increasing as large sectors of the economy are driven by technology: not only computers can be found in countless fields from industry, health care, transportation or even agriculture but numerous other technologies are also readily available ranging from coated glass to bio-compatible prostheses. For these applications, thin films are crucial as they can provide new optic or magnetic properties as well as exhibit conflicting properties. The reduced dimensions of thin films allow an increase in both dielectric breakdown voltages and device packing density in the semiconductors industry. Furthermore, different materials can be stacked in layers, creating *heterostructures*. For instance, the unique properties of transistors originate from the interfaces between the thin films composing them [169, 170].

The desired properties of thin films are achieved not only by controlling the composition but also the thermodynamic and kinetic conditions of the thin film growth [171]. Hence, the chosen growth method has a substantial impact on thin films. The atoms can be provided to the film from a solid, liquid or vapour phase; the latter being the most widely used approach. Indeed, solid-phase growth does not allow to transport atoms over long ranges while liquid-phase growth provides only limited control of the growth which must occur in conditions close to the thermodynamic equilibrium [172].

Within the growth methods providing the atoms from a vapour phase, two categories of processes can be distinguished: chemical vapour deposition and physical vapour deposition. The former processes rely on materials which are in a gaseous state under the reactor conditions. Conversely, the latter processes generate the vapour phase through physical means, for example, by impacting high energy particles with a target in a sputtering process or by heating a source in an evaporation process [172].

According to the kinetic theory of gases, the mean free path of a gas molecule between scattering events, λ_{gas}, is given by:

$$\lambda_{gas} = \frac{k_{\mathrm{B}} T}{\sqrt{2}\sigma_{cross-section} P_{gas}}, \tag{2.24}$$

where k_{B} is the Boltzmann constant, T is the absolute temperature, $\sigma_{cross-section}$ is the collision cross-section and P_{gas} is the pressure. Therefore, the pressure inside the deposition chamber must be sufficiently low to allow atoms to reach the substrate [172].

2.3.1. Thin film nucleation

The mechanisms described thereafter can apply to either atoms, ions or molecules. To facilitate understanding, the term *particle* will be employed in the current subsection.

Once particles reach the substrate, various processes might happen as schematically represented in Figure 2.10. The impinging particle might either *reflect* on, *penetrate* into or *adsorb* on the surface. In the two last cases, some energetic conditions must be met by the particle. If these conditions are not fulfilled, reflection occurs. For penetration to take place, the particle must impinge on the surface with a relatively high energy, though sufficiently low to avoid sputtering. Typically, particles reaching the surface with an energy of approximately 15 eV to 50 eV can penetrate into the surface [173]. The last possibility for an impinging particle is to adsorb on the surface. It is this process that leads to thin film *nucleation* and subsequent *growth*.

Based on the type of bonding between the impinging particle and the surface, two types of adsorption processes can be identified. If the particle is only bonded to the surface by weak van der Walls interactions, the mechanism is known as *physisorption*. Conversely, once ionic or covalent bonding are involved, the process is referred to as *chemisorption*. The physisorption energy, E_{phys}, is typically around 0.25 eV while

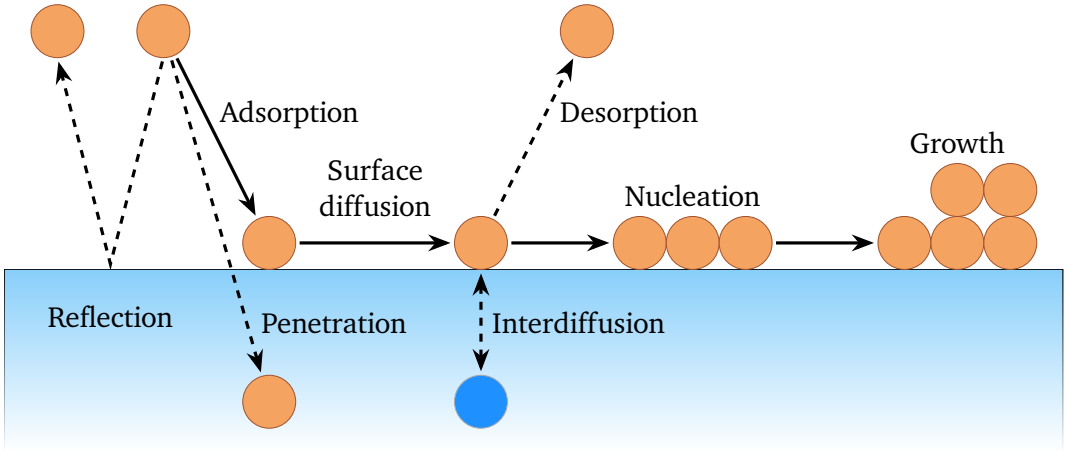

Figure 2.10.: Schematic representation of possible processes occurring in a thin film vapour-phase based growth process from surface adsorption of a particle to nucleation and growth. The full line arrows show the path towards growth, the dashed line arrows represent other possible paths. Adapted from [172].

the chemisorption energy, E_{chem}, larger, usually ranges between 1 eV and 10 eV [171]. A model, based on the Lennard-Jones potential, representing the potential energy and the distance to the surface of both a physisorbed and a chemisorbed particle is shown in Figure 2.11 [174].

Surface mobility is indispensable to obtain smooth films and is enhanced by providing heat to the substrate. This energy can be employed by the adsorbed particle to undergo *surface diffusion* by hopping from one bonding site to another. The surface diffusion coefficient, D_s, corresponding to the average distance an adsorbed particle will travel, is defined by:

$$D_s = a_h^2 k_s, \tag{2.25}$$

where a_h is the effective hopping distance between two bonding sites and k_s is the hopping rate from site to site, $k_s \propto exp\left(-V_s/\left(k_\mathrm{B}T\right)\right)$ with V_s the potential energy barrier between two bonding sites, k_B the Boltzmann constant and T the absolute temperature of the substrate. As nucleation proceeds, D_s decreases until it reaches a stable value [171, 175].

Surface diffusion allows adsorbed particles to nucleate when meeting another particle or to join an existing cluster of particles. It must be noted that surface diffusion is more likely to occur for a physisorbed particle than for a chemisorbed one as the bonds between particle and surface, dominated by van der Walls interactions, are weaker [172, 175]. *Interdiffusion*, represented in Figure 2.10, is less often present than surface diffusion as it presents higher energy barriers.

Whether a physisorbed particle has diffused or not, it needs to become chemisorbed for nucleation and growth to proceed. In this process, it is the heat provided to the substrate that allows the adsorbed particle to go over the potential energy activation barrier, E_a, as shown in Figure 2.11 [171, 172].

However, due to the heat provided to the substrate, *desorption* might arise corresponding to the re-evaporation of an adsorbed particle. It requires high energy to occur and can take place only if chemisorption is less favourable, i.e. if the potential energy activation barrier is larger than the desorption energy [172]. For a thorough description of adsorption and desorption processes, readers are referred to [171, 172, 174].

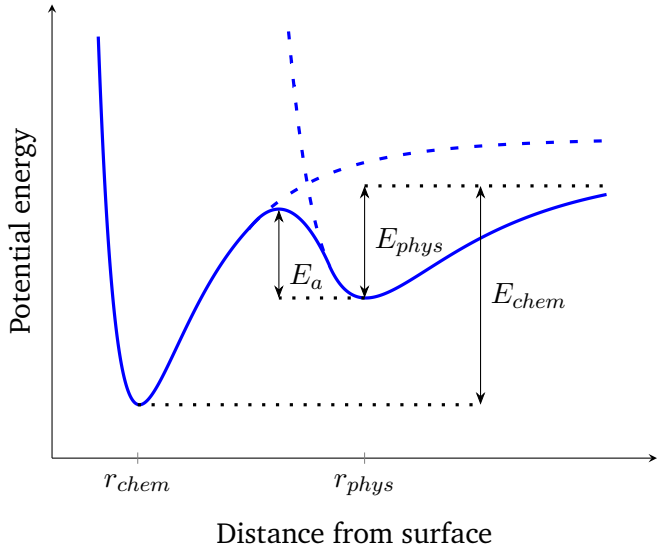

Figure 2.11.: Lennard-Jones potential based model of the interaction potential energy as a function of the distance between the impinging particle and the surface. The physisorption and chemisorption energies, E_{phys} and E_{chem}, respectively, are represented along with the energy barrier to transition from physisorption to chemisorption, E_a. Adapted from [171].

As a particle chemisorbs with the substrate or with other particles, it starts the nucleation process. Thermodynamics are the driving force of nucleation and determine the stability of clusters already formed. If the growth of a thin film island is solely driven by energetic considerations, its equilibrium shape is determined by the contact angle, $\theta_{contact}$, formed between the film and the substrate surface, as represented in Figure 2.12. The contact angle is linked to the change in free energy of the surface, ΔG_{surf}, and the change in the contact area between the film and the substrate, ΔA:

$$\Delta G_{surf} = \Delta A\left(\gamma_i - \gamma_s\right) + \Delta A \gamma_f cos\left(\theta_{contact} - \Delta\theta_{contact}\right), \tag{2.26}$$

where γ_s and γ_f are the surface energies per area of the substrate and film, respectively, γ_i is the interface energy per area and $\Delta\theta_{contact}$ is the change in the contact angle [172].

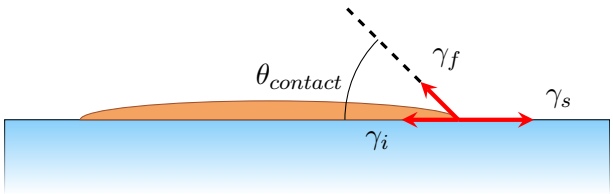

Figure 2.12.: Schematic representation of a film island growing on a substrate. The contact angle, $\theta_{contact}$, and the surface energies per area which are driving its growth are represented: for the substrate, γ_s, for the film, γ_f and for the interface between substrate and film, γ_i. Adapted from [171, 172].

If the change in the contact area is small, then the change in the contact angle is also small relative to

$\theta_{contact}$ and the equilibrium condition is [172]:

$$\frac{dG}{dA} = \gamma_i - \gamma_s + \gamma_f cos(\theta_{contact}) = 0. \tag{2.27}$$

The nucleation theory is described in more details in [171, 172, 174, 176].

2.3.2. Thin film growth

Depending on the surface and interface energies involved in Equation (2.27), thin films growth under equilibrium conditions can follow three basic growth modes represented in Figure 2.13.

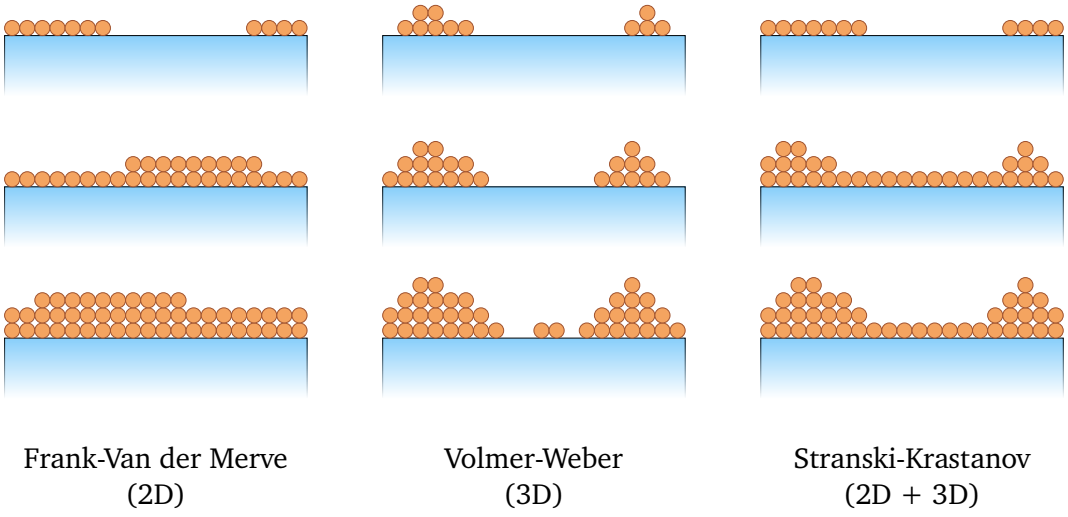

Figure 2.13.: Schematic representation of the three basic thin film growth modes. From left to right: Frank-Van der Merve or layer-by-layer growth, Volmer-Weber or island growth and Stranski-Krastanov growth. Adapted from [171].

In the first case, Frank-Van der Merve or *layer-by-layer growth* mode, it is energetically more favourable for the adsorbed particles to chemisorb onto the substrate rather than the film, leading to a two-dimensional (2D) growth mode with $\theta_{contact} \simeq 0°$. It corresponds to the growth of consecutive monolayers and fulfils the condition [171]:

$$\gamma_s \geq \gamma_i + \gamma_f. \tag{2.28}$$

In the second case, Volmer-Weber or *island growth* mode, the substrate surface energy is lower than the film surface energy, leading adsorbed particles to chemisorb onto the film, creating islands. It is therefore a three-dimensional (3D) growth mode with $\theta_{contact} > 0°$ fulfilling the condition [171]:

$$\gamma_f > \gamma_i + \gamma_s. \tag{2.29}$$

The third growth mode, called Stranski-Kratanov mode, is a combination of the two previous ones. Layer-by-layer growth occurs for the first few monolayers until a critical thickness where the film begins to follow

the island growth mode. This change from one growth mode to another may be due due to the misfit energy between the substrate and the film increasing with the growth [171, 176].

Several other growth modes can be described from the three basic growth modes mentioned above, e.g. *stepflow growth* or *columnar growth* [174, 176–179].

2.3.3. Crystallographic structure of thin film

Based on their atomic and microscopic order, thin films can be classified into four categories depending on their atomic and microscopic ordering. *Amorphous* thin films present only short range atomic order without any preferential orientation of grains. Long range atomic ordering in grains appears in *polycrystalline* thin films, though no preferential orientation of grains is noticeable. The preferential orientation is present in *textured* and *epitaxial* thin films. The orientation relation between grains and substrate, absent from textured films, is characteristic of epitaxial thin films.

From a technological viewpoint, epitaxial thin films are the most interesting ones as the continuity of their crystalline structure with the substrate makes them ideal candidates for planar devices and heterostructures [177]. Epitaxial thin films offer the possibility to stabilise compounds which would not be stable under other conditions. They can be classified into *homoepitaxial* or *heteroepitaxial* films depending on whether material of the film is the same as of the substrate or a different one [176].

In order to characterise the texture of a thin film in a preferred orientation, the relative intensities of X-Ray Diffraction (XRD) reflections from a 2θ-θ scan (see section 3.5.1.1) can be compared using the Lotgering factor. For a $\langle 00l \rangle$ orientation, as denoted with Miller indexes, the Lotgering factor, $f_{(00l)}$, is expressed as [180]:

$$f_{(00l)} = \frac{P_{(00l)} - P_{random}}{1 - P_{random}} \text{ with } P_{(00l)} = \frac{\sum I_{(00l)}}{\sum I_{(hkl)}} \text{ and } P_{random} = \frac{\sum I_{random(00l)}}{\sum I_{random(hkl)}}, \tag{2.30}$$

where $\sum I$ and $\sum I_{random}$ correspond to the summation of the XRD reflections intensities in the measured sample and in a randomly oriented XRD pattern, respectively. The reflections whose intensities are considered are indicated by the subscripts $(00l)$ and (hkl) for all the $00l$ reflections, i.e., 001, 002, etc., and for all the hkl reflections, respectively.

Despite not being directly correlated with the orientation distribution, the Lotgering factor represents the orientation degree in a simple manner. It ranges from 0 for a randomly oriented thin film to 1 for a perfectly textured film [181].

In this manuscript, heterostructures with multiple layers will be described using the notation *material of layer 2/material of layer 1/material of substrate*, listing the layers from the topmost one (left) to the substrate (right).

3. Experimental procedures

This chapter aims to describe the experimental procedures used in this work to prepare the samples and characterise thin films crystallographic structures. The different sample configurations developed in this thesis are introduced in section 3.1. Afterwards, the processes to prepare samples are detailed starting with substrate preparation in section 3.2. Sputtering and pulsed laser deposition, the thin film deposition methods employed in this work, are presented in section 3.3. The following step, consisting in electrodes patterning, is introduced in section 3.4 before the structure characterisation methods are described in section 3.5.

3.1. Sample configurations and custom-built sample holder

In the work presented in this thesis, two different arrangements of sample layers were developed. Both stackings are based on an AISI 304 stainless steel substrate and rely on ferroelectric PZT as the active layer. The first sort of stacking to be produced uses non-doped PZT, $PbZr_{0.52}Ti_{0.48}O_3$, and is referred to as *PZT stack*. The second sort of stacking, using Nb-doped PZT, $Pb_{0.99}\square_{0.01}(Zr_{0.52}Ti_{0.48})_{0.98}Nb_{0.02}O_3$, is referred to as *PNZT stack* through this thesis.

In both cases, to act as a bottom electrode and a growth template for PZT or PNZT (see section 2.2), a buffer layer of $LaNiO_3$ is deposited by PLD underneath the PZT or PNZT layer. While AISI 304 stainless steel has a good high-temperature corrosion resistance in air, the oxygen atmosphere necessary to the deposition of oxide thin films of lead zirconate titanate and lanthanum nickelate impedes SS304 oxidation resistance [165, 166]. Therefore, to prevent substrate oxidation during the deposition of the lanthanum nickelate and lead zirconate titanate layers, intermediate buffer layers are deposited between the SS304 substrate and the LNO growth template. This choice of buffer layers differs from one stacking to the other.

In the case of *PZT stacks*, this function is fulfilled by a sputtered platinum buffer layer. Furthermore, as indicated in section 2.2, under the deposition conditions of lanthanum nickelate thin films, described in section 3.3.2, SS304 rejects chromium from the steel solid solution. The rejected chromium forms intermetallic alloys with platinum [164, 166]. A consequence of this alloying process for *PZT stacks* is an instability of the Pt layer surface which hinders the {100}-oriented growth of the LNO layer [17, 51]. Therefore, to enable the oriented growth of LNO when a platinum buffer layer is present in the heterostructures, an amorphous layer of Al_2O_3 is sputtered on top of the Pt layer.

In the case of *PNZT stacks*, to avoid the formation of intermetallic compounds between the substrate and the platinum (see section 2.2), substrate oxidation is prevented by directly depositing a thicker amorphous Al_2O_3 buffer layer. Due to the relative deposition rates of Al_2O_3 by sputtering and by PLD, this thicker layer is deposited using the latter method.

In consequence, *PZT stacks* correspond to the arrangement $PbZr_{0.52}Ti_{0.48}O_3/LaNiO_3/Al_2O_3/Pt$/steel while *PNZT stacks* are made of $Pb_{0.99}\square_{0.01}(Zr_{0.52}Ti_{0.48})_{0.98}Nb_{0.02}O_3/LaNiO_3/Al_2O_3$/steel. Both sample configurations are represented in Figure 3.1 along with an optical microscope image of a *PNZT stack* with Pt electrodes and strain gauges on top. Another difference arising between these two sorts of stackings is due to the characterisation methods they are subjected to. Indeed, measurement of the $e_{31,f}$ piezoelectric

coefficient is performed only on *PNZT stacks*, requiring the back of the substrate to remain clean for $e_{31,f}$ piezoelectric coefficient measurements (see section 4.4). It is therefore not possible to employ silver paste to maintain thermal contact during *PNZT stacks* production.

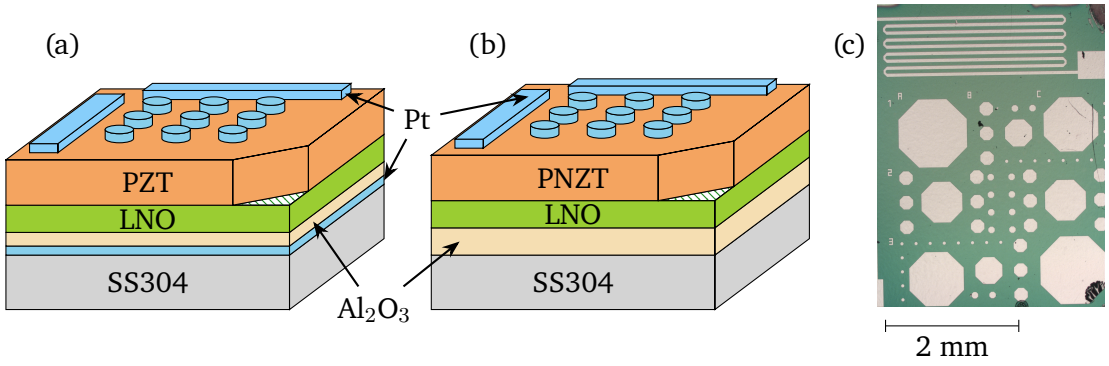

Figure 3.1.: Schematic representations of sample configurations for (a) *PZT stacks* and (b) *PNZT stacks* with Pt electrodes and strain gauges on top. The access to the LNO bottom electrode is indicated by the striped pattern. Dimensions of the schematics are not to scale. (c) Optical microscope image of a *PNZT stack* with Pt electrodes and strain gauges on top. The bottom electrode access is visible in the top right corner.

Due to the configurations of the thin film deposition systems described thereafter and the layers composing *PNZT stacks*, silver paste cannot be employed in two processes where it was previously utilised for *PZT stacks*. The first one is the deposition of the LNO layer and the second is the Ar ion milling of the PZT layer to access the bottom electrode. Both processes involve the same holder configuration known as *flag style holder*. Typically, a flag style holder presents a flat surface on which the substrate is glued using silver paste. To avoid relying on it, this holder design has been adapted during this thesis as represented schematically in Figure 3.2.

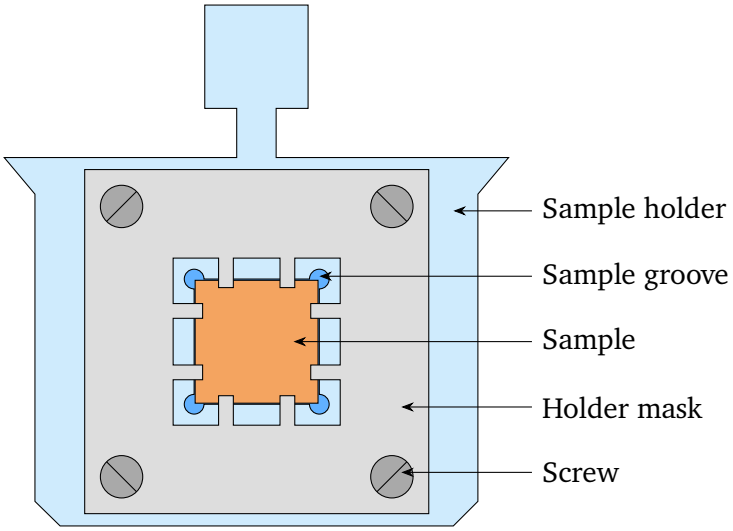

Figure 3.2.: Schematic representation of a modified flag style holder to be employed for metallic substrates without using silver paste for thermal contact. Dimensions are to scale.

The flag style holder is modified by manufacturing a groove to partially fit the sample within the holder. The substrate being metallic, it is considered that this configuration should provide sufficient thermal contact. The sample is maintained in contact with the modified holder by a mask reaching in front of the substrate and screwed in the sample holder. The mask design aims to cover a minimal surface of the sample to leave a sufficiently large area for the patterning of top electrodes. Furthermore, the mask design does not cover the sample corners where the bottom electrodes must be contacted, requiring the LNO layer to be deposited in the sample corners.

It should be noted that the absence of silver paste on the back of *PNZT stacks* lead to some oxidation of the SS304 substrates during the deposition processes. Therefore, to prevent oxidation, 30 nm of platinum are sputtered on the back of the substrates of *PNZT stacks*. This procedure has no impact on the polished side of the substrate were the thin films are deposited. The sputtering is performed according to the same process as described in section 3.3.1.

3.2. Substrate preparation

Substrates are produced from commercially available cold-rolled AISI 304 stainless steel sheets. A thickness of 0.2 mm was arbitrarily chosen for proof-of-concept of the growth of tetragonal {001}-textured PZT films on stainless steel while permitting some flexibility of the substrate for piezoelectric applications. As a preliminary step, the metal sheets are laser cut into 30×30 mm^2 pieces by the workshop of the Department of Electrical Engineering and Information Technology of the Technische Universität Darmstadt. To transform these metal pieces into substrates, they undergo dicing, lapping, polishing and cleaning, as described in the following sections.

3.2.1. Substrate dicing

The dicing of AISI 304 stainless steel is performed using a Microace 3 dicing saw by Loadpoint (Swindon, UK). The dicing saw is equipped with a resin bonded blade and operated at 10,000 rpm. The produced 5×5 mm^2 SS304 pieces are hereby referred to as *substrates*.

3.2.2. Substrate lapping and polishing

The average roughness of as-bought SS304 is measured by a Dektak XT profilometer by Bruker (Billerica, MA, USA) at 189 nm with a standard deviation of 236 nm. Such roughness, larger than or in the order of magnitude of thin films thickness, must be reduced to permit the growth of textured thin films. Therefore, diced substrates are lapped and subsequently mechanically polished using a PM5 Precision Lapping & Polishing Machine by Logitech (Glasgow, UK).

For these processes, the metallic substrates are glued by batches of 9 samples on a circular glass carrier plate using Crystalbond 509 by Aremco (Valley Cottage, NY, USA) adhesive. A minimal amount of adhesive is used in order to maintain the substrates parallel to the glass carrier. To ensure optimal adhesion during the lapping and polishing processes, the substrates are pressed onto the glass carrier before the adhesive cools down.

The substrates are lapped using a slurry of calcined Al_2O_3. The 3 µm particles are diluted into deionised water with a ratio of 200 mL of Al_2O_3 powder for 1.5 L of solvent. The lapping is carried out with an average jig load of 2 kg applied over a batch of 9 samples of 5×5 mm^2 at a speed of 5 rpm for about 100 minutes. The lapping time is adjusted by visual inspection of the sample through the process.

Once lapped, the substrates are polished using SF1 Polishing Fluid by Logitech (Glasgow, UK) containing amorphous SiO_2 particles with a size of 32 nm. The process is performed with an average jig load of 2 kg applied over a batch of 9 samples of 5×5 mm^2 at a speed of 30 rpm for 150 to 240 minutes. The polishing time is adjusted by visual inspection of the sample through the process to ensure the whole surface of each substrate is polished. In order to clean off the majority of the slurry, the substrates are rinsed with deionised water before being removed from the glass carrier. Further cleaning procedures are described in the following section.

After polishing, the substrate thicknesses are of 0.16 mm to 0.18 mm while their average roughnesses and standard deviations are reduced to 3 nm and 4 nm, respectively. This lowered roughness compared to as-bought SS304 is important to promote {100} texture of the LNO layer and, therefore, of the PZT layer [17, 51].

3.2.3. Substrate cleaning

The first step of the substrate cleaning process consists in removing from the substrates any slurry left over from the polishing. For this purpose, wearing latex gloves, the SS304 pieces are washed individually by rubbing them between fingers with detergent. Substrates are then rinsed thoroughly with deionised water and dried with nitrogen gas. The process is repeated until no traces of slurry remain on substrates.

Afterwards, in order to remove both polar and non-polar molecules from substrates, they are cleaned successively in aceton (99.8 %, Roth) and isopropyl alcohol (99.5 %, Roth) for 30 minutes each with an ultrasonic bath Transsonic Digital 3 by Elma (Singen, Germany). After each bath, substrates are dried with nitrogen gas. The use of an ultrasonic bath allows for a better impurity removal from substrate surfaces due to the cavitation phenomenon.

After storage, shortly before the thin film deposition process begins, substrate surfaces are cleaned again using an ultrasonic bath with successively aceton (99.8 %, Roth) and isopropyl alcohol (99.5 %, Roth) for 10 minutes each. After each bath, substrates are dried with nitrogen gas.

3.3. Thin film deposition methods

Through this thesis, several thin film deposition methods are utilised, depending on the nature of the layer to be grown. DC magnetron sputtering and RF magnetron sputtering are employed to deposit layers of platinum and aluminium oxide, respectively. It should be noted that Al_2O_3 was also grown by PLD along with lanthanum nickelate and lead zirconate titanate thin films.

3.3.1. DC and RF magnetron sputtering

Sputtering is a technique suitable for industrial scale, large-area deposition of both elemental and compound materials. Depending on the experimental setup, conducting or insulating materials can be deposited [182].

3.3.1.1. Sputtering principle

Sputtering is a non-equilibrium process where energetic particles impact on and remove particles from the surface of a target composed of the source material. Sputtering is performed inside a vacuum chamber filled with a process gas, generally argon, under a pressure of around 0.1 Pa to 10 Pa. Substrates are positioned at the anode, facing a target located at the cathode, a few centimetres in front of the substrates. The vacuum chamber is electrically connected to the anode. Therefore, upon application of a voltage between the cathode and the anode, the process gas is ionised and a plasma is ignited. The ionised ions are accelerated towards the target where, upon collision, they eject target particles [182, 183].

Depending on whether the target is conducting or insulating, the plasma is generated either with a constant current flowing through the cathode or with no net current flow. The experimental setup for the former technique, known as DC sputtering, is represented in Figure 3.3 (a). The latter method, RF sputtering, involves the excitation of the process gas at radiofrequency, usually 13.56 MHz, leading to negative charging of both cathode and anode with regard to the plasma [182, 183]. Figure 3.3 (b) offers a schematic of a RF sputtering setup.

In order to yield higher deposition rates, the process gas pressure is lowered and the number of collisions increased using a magnetron cathode in order to maintain the discharge. The magnetron cathode is fitted with permanent magnets to confine the electrons by magnetic field around the target, locally increasing collisions between electrons and ionised process gas [182].

3.3.1.2. Sputtering experimental procedure

In the case of *PZT stacks*, platinum is sputtered using DC magnetron sputtering to prevent substrate oxidation during the deposition of the subsequent layers. Additionally, sputtering is employed to deposit platinum top electrodes on the samples for both *PZT stacks* and *PNZT stacks*. The detailed procedure to pattern the Pt top electrodes is described in section 3.4.

Pt layers are sputtered from a target with 99.99 % purity (Umicore) at room temperature using a Q300T DC magnetron sputter coater by Quorum Technologies (Lewes, UK) with a current of 30 mA in Ar atmosphere under a pressure of 1 Pa. Both the Pt buffer layers and the Pt top electrodes are deposited with a thickness of 30 nm. The deposition rate for Pt sputtering is calibrated on a silicon substrate as 18 nm·min^{-1} using X-Ray Reflectivity (XRR). This technique is described in section 3.5.1.2.

To enable the oriented growth of LNO in *PZT stacks*, an amorphous layer of Al_2O_3 is sputtered on top of the Pt layer. Aluminium oxide being insulating, Al_2O_3 buffer layers are deposited by RF magnetron sputtering from a target with 99.5 % purity (Kurt J. Lesker). The sputter unit, a HEX Modular Deposition System by Mantis Deposition (Thame, UK), is equipped with a Fission Sputtering Source. The RF excitation is supplied by a RFX-600 generator and a ATX-600 matching network by Advanced Energy Industries (Fort Collins, CO, USA). The system is completed by a custom-made heating sample holder fitted with a ceramic heater FLE 100 679 by Bach Resistor Ceramics (Seefeld, Germany). The heating holder maximum temperature is $1,000$ °C and the actual temperature is measured on the sample holder by a K-type thermocouple. Amorphous Al_2O_3 layers with a thickness of 5 nm are deposited at 40 W in Ar atmosphere under a pressure of 0.64 Pa. Substrates are fixed to the holder using silver paste to ensure thermal contact and the deposition temperature is maintained at 100 °C. The deposition rate for Al_2O_3 sputtering is calibrated on a glass substrate as 0.13 nm·min^{-1} using XRR.

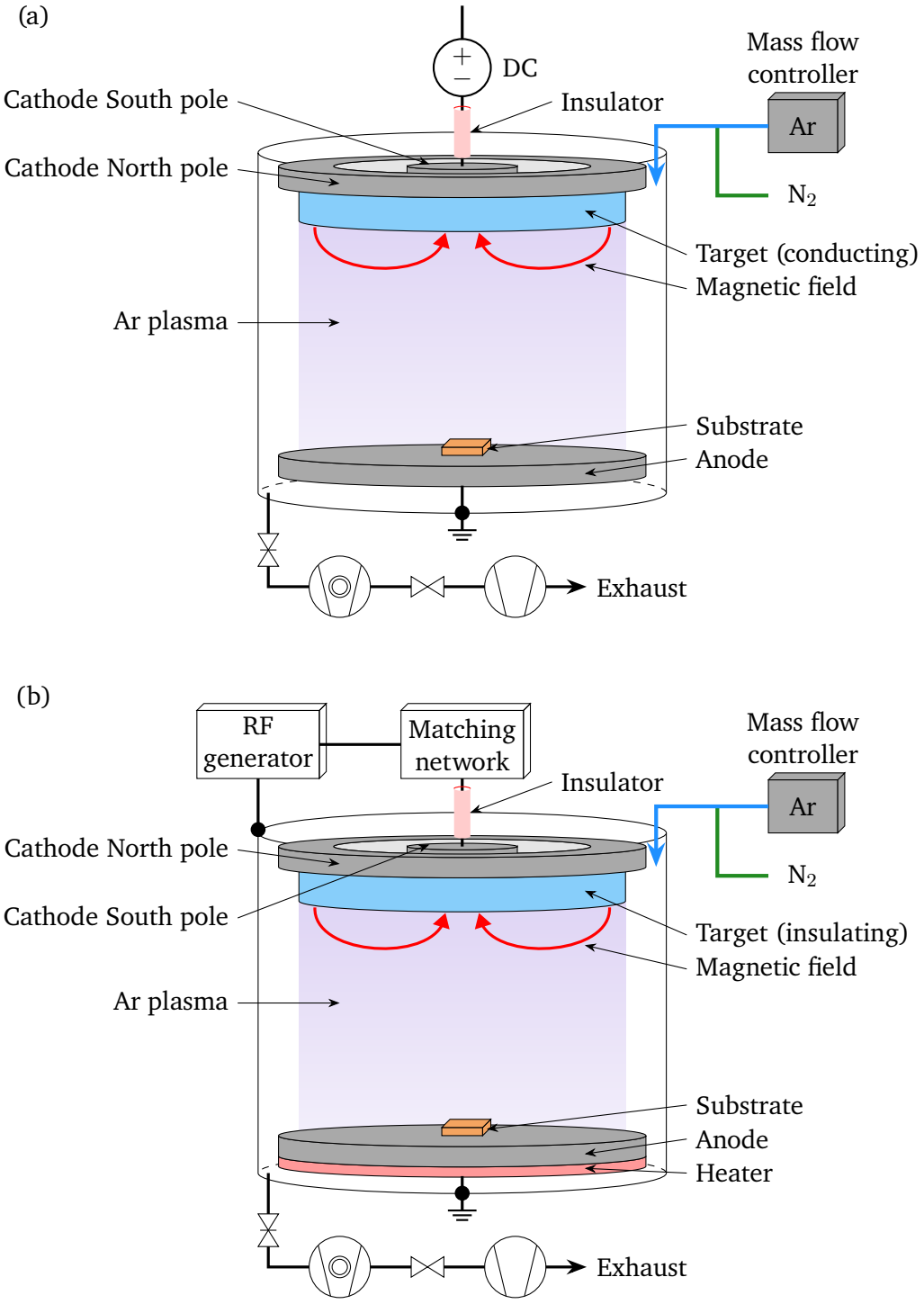

Figure 3.3.: Schematic representation of a sputtering chamber for (a) DC magnetron sputtering and (b) RF magnetron sputtering.

3.3.2. Pulsed laser deposition

Interest for pulsed laser deposition (PLD) as a physical vapour deposition technique started in earnest in the late 1980s after the successful deposition of epitaxial high temperature superconducting thin films. PLD allows the deposition of thin films with several cations in stoichiometric conditions, notably metals, semiconductors, polymers or biological materials [184, 185]. PLD offers the possibility to synthesise metastable materials and can be combined with reflective high energy electron diffraction to monitor thin film growth in situ, making it a widely used technique for research purposes, in particular to grow oxide thin films [186–188].

3.3.2.1. PLD principle

Performed between 10^{-7} Pa and 100 Pa, the PLD process relies upon a pulsed laser ablating material from a target and the material subsequent deposition on a substrate. Each laser pulse ablates a small amount of material, creating a forward-directed *plume*, providing a material flux for thin film growth, in mostly stoichiometric conditions with regard to the target [184, 185].

Upon incidence of a laser beam on a material, two concurrent processes might occur: thermal evaporation and non-thermal ablation. The former is an equilibrium process which occurs when the laser energy absorbed by the target is not sufficiently high. It leads to non-stoichiometric transfer of material to the plume and should be avoided during PLD. The latter is an out-of-equilibrium process accessible at energy above an *ablation threshold* when the optical penetration depth of the laser beam in the target material is longer than the heat diffusion length [186–190].

The pulse energy density is quantified by the laser *fluence*, ε_{laser} corresponding to the time integral of the laser energy intensity per surface unit over the pulse duration and expressed by [190]:

$$\varepsilon_{laser} = \frac{E_{laser}}{A_{spot}}, \tag{3.1}$$

where E_{laser} is the laser energy reaching the target and A_{spot} is the laser spot size. Both the target ablation rate and the film growth rate, usually of 0.001 Å to 1 Å per laser pulse, are dependent on the fluence [184].

In order to control the fluence through the laser energy and spot size, a series of optics must be employed between the laser and the deposition chamber. Typically, the setup is composed of an optical attenuator to adjust the laser pulse energy and a telescope to change the beam cross-section from rectangular to square. These devices are followed by a field lens to focus the laser beam towards the objective lens, an aperture, several mirrors to guide the beam towards the PLD chamber, an objective lens to focus the laser beam on the target, and an entrance window [184, 190, 191].

To obtain a homogeneous deposition, the ablation plume must be symmetric. It is the case on a flat target surface where the plume follows a $cos^{n_{laser}}(\theta_{target})$ distribution where n_{laser} depends on the laser spot size and θ_{target} is the angle to the target normal. However, repetitive ablation creates a trench on the target surface and plume inhomogeneity, modifying its stoichiometry. Trenching can be avoided by scanning the laser on the target surface or by sweeping and rotating the target, which is often preferred [184, 185, 192].

Targets for PLD processes must have a high optical absorption coefficient at the chosen laser wavelength for the ablation process to be efficient. The cations stoichiometry provided by one or several targets must be identical to that of the film due to the mainly stoichiometric transfer of cations from the target to the

plume through the ablation process [184, 185]. However, recent literature indicates the possibility of off-stoichiometry cations transfer from target to thin film, notably in perovskite structures, which could require to adjust target stoichiometry [193, 194]. To limit the amount of particles or droplets ejected from the target during the ablation process and deposited on the substrate, target density must be high. In the case of polycrystalline targets, made from bulk polycrystalline oxides, their density must be superior to at least 80 % of the single crystal density [184, 185].

To promote nucleation and growth of homogeneous layers, surface diffusion of atomic species must be enhanced through heating of the substrate. This is done from the substrate back side, notably by means of resistive-type heaters or infrared (IR) laser diodes. Inexpensive, robust and reliable, resistive-type heaters can be used for temperatures up to $950\ ^{\circ}\mathrm{C}$ but require the utilisation of silver or platinum paste to fix the substrate to the heating block, limiting uniform heating of large substrates. Fast and reliable, IR laser diodes are limited to small area substrates due to the laser beam size but can be scanned on the substrate back to make heating uniform. Deposition temperature can be monitored via a thermocouple or a pyrometer. The former is less reliable than the latter, however, it can be used with substrates transparent to IR [191].

As mentioned above, PLD can be performed at 10^{-7} Pa, in ultra-high vacuum. However, most of the time, a background gas is required both as a reactive specie and to decrease the kinetic energy of the ablated species which may damage the deposited film upon impingement with its surface. The most commonly used background gases are oxygen, argon or nitrogen. When employed as reactive species, the required quantity of gases depends on thermodynamics. Furthermore, it should be noted that post-deposition desorption from the film at high temperatures can be limited by high pressures [184, 185, 195].

3.3.2.2. PLD experimental systems

In the course of this work, four different thin film materials have been deposited by PLD: Al_2O_3, $LaNiO_3$, $PbZr_{0.52}Ti_{0.48}O_3$ and $Pb_{0.99}\square_{0.01}(Zr_{0.52}Ti_{0.48})_{0.98}Nb_{0.02}O_3$. At the exception of LNO, these materials are deposited in a custom-built PLD system known as *small PLD*. Equipped with a quartz deposition chamber that can be exchanged between different materials, it allows to deposit materials with volatile compounds, e.g. PbO, without risking cross-contamination of other samples. However, due to the geometry of the laser beam optical path, the accessible fluence is limited and hinders the deposition of LNO. To remedy to this aspect, the $LaNiO_3$ layer is deposited in another custom-made PLD system, part of the DAISY-BAT system (DArmstadt Integrated SYstem for BATtery research) known as *Daisy-Bat PLD*.

A schematic representation of the *small PLD* system can be found in Figure 3.4. Due to the many similarities between the two systems and the utilisation of the second one being limited to the deposition of LNO layers, a schematic of the *Daisy-Bat PLD* is not provided. Instead, differences between the two PLD systems are described thereafter.

The *small PLD* and the *Daisy-Bat PLD* are equipped, respectively, with COMPex 205 and LPXpro 210 F KrF excimer lasers with a wavelength $\lambda = 248$ nm by Coherent (Santa Clara, CA, USA). The laser pulses duration are shorter than 30 ns to minimise heat diffusion in the target. For both PLD systems, the laser energy is measured using a FieldMaxII energy meter coupled to an Excimer Laser EnergyMax Sensor, both by Coherent.

The *small PLD* deposition chamber is made of quartz and can be pumped down to approximately 10^{-3} Pa. Its pressure is monitored by a hot ion vacuum gauge BPG400 by Inficon (Bad Ragaz, Switzerland). In comparison, the *Daisy-Bat PLD* stainless steel spherical deposition chamber can be pumped down to

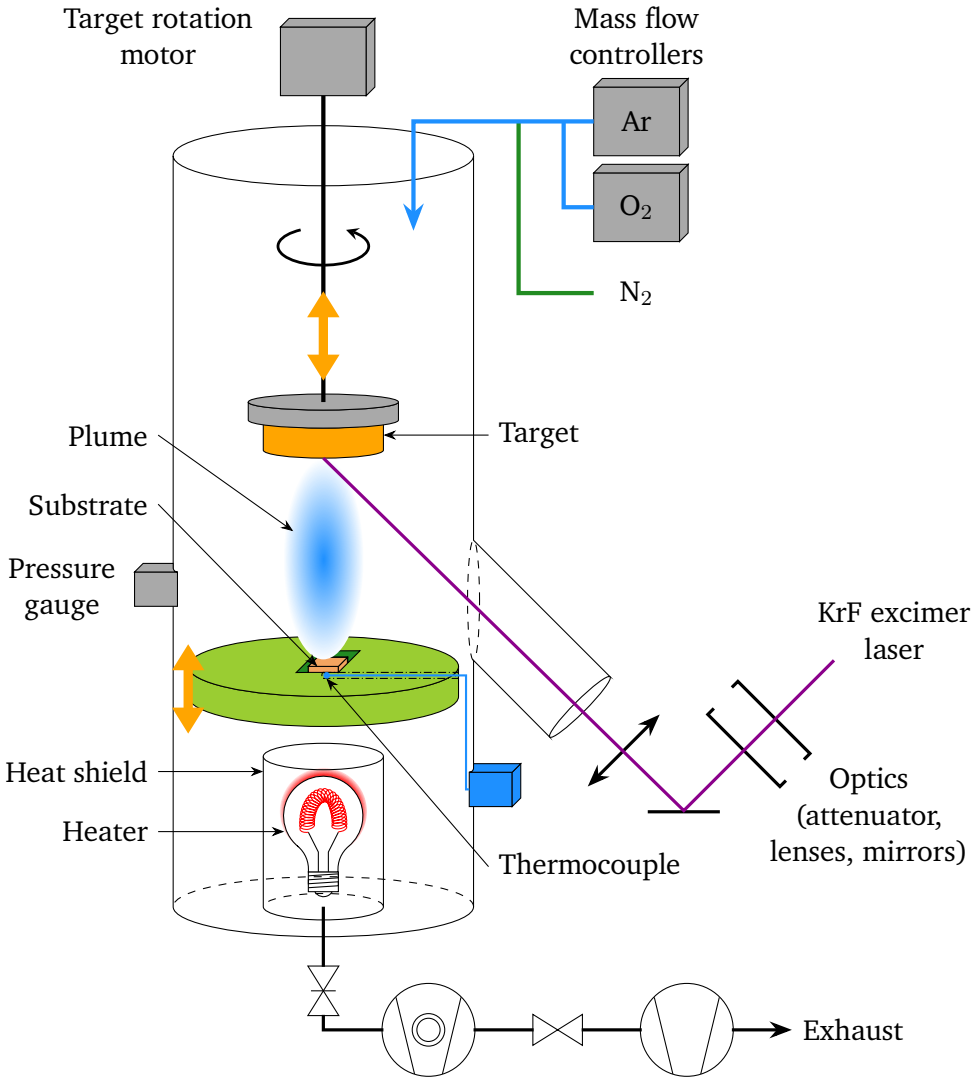

Figure 3.4.: Schematic representation of the *small PLD* system.

ultra-high vacuum at approximately 10^{-6} Pa. It is equipped with a load-lock from which samples can be transferred using a magnetic transfer arm. The pressure inside the deposition chamber is monitored by several pressure sensors, including capacitance manometers and ion gauges.

The atmosphere in both deposition chambers can be adjusted through the supply of O_2, N_2 and Ar gases. At the time where the *PZT stacks* were grown, O_2 was introduced in the *small PLD* chamber by a 100 sccm full scale mass flow controller by MKS Instruments (Andover, MA, USA). By the time the *PNZT stacks* were deposited, the O_2 mass flow controller had been replaced with a 5 sccm full scale mass flow controller by MKS Instruments to provide a more accurate control of limited gas flow. The *Daisy-Bat PLD* is equipped with a 10 sccm full scale mass flow controller by MKS Instruments.

In the *small PLD*, the substrate and target positions can be manually adjusted in the vertical direction only. The target is rotated during the deposition to limit trenching due to ablation on the target surface. In the case of the *Daisy-Bat PLD*, substrate and target positions can be adjusted both vertically and in the

horizontal plan by means of substrate and target manipulators. To ensure uniform ablation of the target surface, the target manipulator is equipped with a carousel allowing target rotation and sweeping.

The *small PLD* system provides substrate heating up to 700 °C by means of a 64664 HLX heating bulb by Osram (Munich, Germany) located at the back of the substrate holder and surrounded by directional heat shields. Additionally, to further limit heat diffusion in the *small PLD* chamber at higher temperatures and O_2 pressures, a heat shield can be installed on top of the substrate holder. Deposition temperature is measured by a thermocouple fixed on the substrate holder. On the other hand, in the *Daisy-Bat PLD*, the substrate is heated locally with an JOLD-x-CPXF-2PW infrared diode laser by Jenoptik (Jena, Germany) with a wavelength of 938 nm and a maximum power of 140 W. The IR laser is focused on the back of the substrate, providing localised heating above $1,000$ °C. Substrate temperature is monitored by a METIS MP25 IR pyrometer by SensorTherm (Sulzbach, Germany) focused on the back of the substrate.

3.3.2.3. PLD experimental procedure

As previously mentioned, Al_2O_3, LNO, PZT and PNZT thin films are grown by pulsed laser deposition. The Al_2O_3 PLD target is a commercially bought cylindrical α-Al_2O_3 ceramic with a 15 mm diameter and a purity superior to 99.5 % (Degussit AL23, Aliaxis). The $PbZr_{0.52}Ti_{0.48}O_3$ target with 15 mm of diameter was also commercially acquired (99.9 %, Testbourne). The target PZT 52/48 phase was confirmed by XRD and the stoichiometry was verified to be within the measurement error margin by Energy-Dispersive X-ray Spectroscopy (EDS). Both techniques are described in section 3.5. Its geometrical density corresponds to 88.0 % of the theoretical PZT 52/48 density [140].

Contrarily, the $Pb_{0.99}\square_{0.01}(Zr_{0.52}Ti_{0.48})_{0.98}Nb_{0.02}O_3$ target was prepared by Silvo Drnovšek in collaboration with Barbara Malič, both from the Electronic Ceramics Department of the Jožef Stefan Institute (Ljubljana, Slovenia). The PNZT target with a diameter of 18.5 mm was produced through a solid state synthesis route with 10 mol.% excess PbO. After two calcination steps at 850 °C for 1 h each, the target was sintered in the presence of inherent packing powder at $1,200$ °C for 2 h with a heating rate of 5 K·min^{-1}. The target phase was verified by XRD at the Jožef Stefan Institute. It shows a PZT 52/48 phase as well as a PbO phase by XRD which is consistent with the PbO excess introduced in the target. Its stoichiometry was verified to be within the measurement error margin by EDS. The PNZT target reaches a geometrical density of 7.55 g·cm^{-3} corresponding to 94.3 % of the theoretical PZT 52/48 density [140].

The $LaNiO_3$ PLD target is produced from a stoichiometric mixture of La_2O_3 (99.99 %, Alfa Aesar) and NiO (99.995 %, Chempur). The individual powders are first dried at $1,000$ °C for 12 h and at 400 °C for 1.5 h, respectively, to remove absorbed moisture. Afterwards, the powders are mixed in stoichiometric ratio, and made into a slurry with isopropyl alcohol (99.99 %). The slurry is ball-milled at 500 rpm for 30 min using ZrO_2 milling media. The powder is dried in air before being calcinated at $1,100$ °C for 20 h with a heating rate of 5 K·min^{-1}. Subsequently, the obtained powder is ball-milled in the same conditions as stated previously and then pressed uniaxially at ~ 28 MPa and isostatically at ~ 360 MPa into a pellet with a diameter of 12.2 mm. In the last step, the green body is sintered at $1,300$ °C for 24 h with a heating rate of 5 K·min^{-1} to obtain a LNO target with a geometrical density of 95.9 % of the theoretical LNO density [196]. The XRD analysis of the target does not indicate phase purity, however the stoichiometry was verified to be within the measurement error margin by EDS which makes it suitable for a PLD process.

The 50 nm thick Al_2O_3 films are deposited with the *small PLD* system with a substrate-target distance of 29 mm. The fluence is set at 1 J·cm^{-1} with a spot size of 2.26 mm^2 and the KrF laser is operated with a repetition rate of 2 Hz. The deposition of Al_2O_3 is performed at 150 °C, reached with a heating rate of

50 K·min^{-1}, under 3 Pa of O_2 and a flow of 1.6 sccm of O_2. The oxygen pressure is maintained during the sample cooling down at 30 K·min^{-1}. The deposition rate for Al_2O_3 by PLD is calibrated on a glass substrate as 10 nm per 1,000 pulses using XRR (see section 3.5.1.2).

The LNO thin films are grown using the *Daisy-Bat PLD* with a substrate-target distance of 40 mm. As mentioned in section 3.1, the samples for *PZT stacks* are fixed onto a flag style holder with silver paste while the samples for *PNZT stacks* are held by a modified flag style holder. A fluence of 2 J·cm^{-1} is employed with a spot size of 2.29 mm^2, the excimer laser repetition rate being set at 2 Hz. $LaNiO_3$ is deposited at 500 °C, reached with a heating rate of 50 K·min^{-1}, under 1.3 Pa of O_2 and a flow of ~ 3 sccm of O_2. The oxygen pressure is maintained during the sample cooling down at 30 K·min^{-1}. The thickness of the LNO layer in *PZT stacks* and in *PNZT stacks* is approximately 57 nm and 110 nm, respectively. The increased thickness in *PNZT stacks* is justified in section 3.4.2. Using the Laue oscillations (see section 3.5.1.1) to calculate the film thickness, the deposition rate for LNO by PLD is estimated on a $NdGaO_3$ substrate as 47 nm per 1,000 pulses.

Both PZT and PNZT thin films are deposited using the *small PLD* setup with a substrate-target distance of 32 mm. For the two materials, the fluence is set at 1 J·cm^{-1} with a spot size of 2.26 mm^2. The O_2 flow is of 3.0 sccm for both materials with a heating rate fixed at 50 K·min^{-1}. To limit the evaporation of PbO during the sample cooling down for PZT and PNZT thin films, the heater is turned off immediately at the end of the deposition and the O_2 pressure is increased to $1 \cdot 10^3$ Pa during the cooling down process [145].

Additionally, the repetition rate of the excimer laser is set at 10 Hz to deposit PZT thin films. The deposition temperature is of 650 °C under 6.5 Pa of O_2. The PZT films were grown with a thickness of either 200 nm or 400 nm. The 400 nm thick film was grown to see the influence of potential leakage currents. The deposition rate for PZT by PLD is estimated on a $NdGaO_3$ substrate as 12 nm per 1,000 pulses using XRR.

Regarding the growth of PNZT, the impact of several parameters on the material ferroelectric properties is studied during this work. The excimer laser repetition rate is set at 4 Hz and the deposition temperature ranges between 600 °C and 700 °C. During this thesis, the O_2 pressure during PNZT deposition is varied between 5 Pa and 10 Pa. The PNZT film thicknesses range from 187 nm to 400 nm. The deposition rate for PNZT by PLD is estimated using XRR on a $NdGaO_3$ substrate as 12.5 nm to 15.6 nm per 1,000 pulses, depending on the deposition conditions.

3.4. Electrodes preparation

To characterise the ferroelectric properties of PZT and PNZT thin films, it is necessary to complete the parallel plate capacitor structure. This is performed by patterning sputtered platinum top electrodes by photolithography before accessing the LNO bottom electrode for electrical contacting using Ar ion milling.

To avoid contributions from the Pt top electrodes, the samples are characterised by X-ray diffraction methods prior to the processes described in this section. When required, surface characterisation methods, e.g. Scanning Electron Microscopy (SEM), are also performed before top electrodes patterning.

3.4.1. Photolithography: lift-off process

Photolithography is a process which requires precise environmental conditions and for which exterior contaminants must be avoided. Therefore, the photolithography process is performed inside a cleanroom. The steps of the lift-off process are represented in Figure 3.5 and are described thereafter.

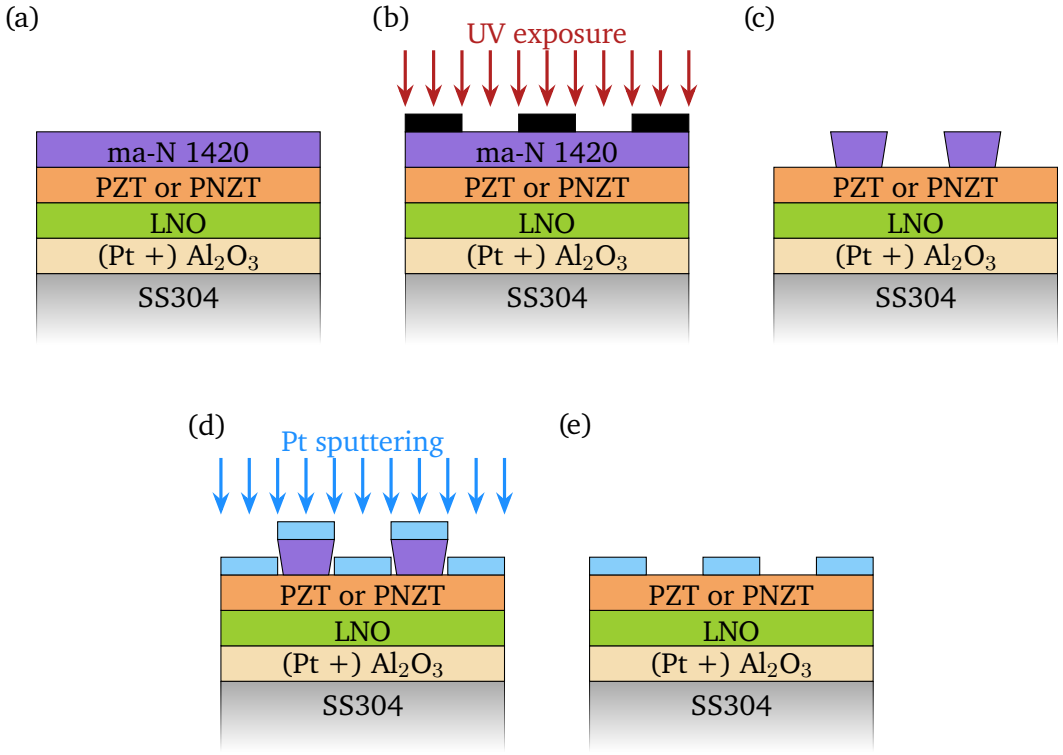

Figure 3.5.: Schematic representation of the photolithography lift-off process to pattern Pt top electrodes: (a) photoresist coating, (b) ultraviolet (UV) light exposure, (c) pattern development, (d) Pt sputtering and (e) photoresist lift-off. Dimensions are not to scale.

It should be noted that, while flat after substrates preparation steps, SS304 substrates bend in an U-shape concavely around the PZT or PNZT-deposited sample side during the deposition of buffer and ferroelectric layers. The sample curvature, with a bending radius of a few millimetres, is sufficiently pronounced to be observable by eye. While the cause of this phenomenon will be discussed in section 5.1.1, it has consequences on the photolithography process.

Initially, negative photoresist ma-N 1420 (Microresist) is spin coated onto the sample surface, i.e. the PZT or PNZT layer for *PZT stacks* or *PNZT stacks*, respectively (see Figure 3.5 (a)). The spin coating is performed at 6,000 rpm for 34 s, creating a 1.4 µm thick photoresist layer. To allow complete sample surface coverage by the photoresist despite the concave surface, the rotation speed is larger than required with a flat surface. Afterwards, the negative photoresist is soft baked for two minutes at 105 °C on a heating plate to evaporate the photoresist solvent. The spinning process generates a centripetal force applied on the photoresist which creates heaps at the sample edges. The pile-up is removed after baking with a razor blade to allow accurate mask alignment.

The photoresist is hardened according to a given pattern using ultraviolet (UV) light and a mask. The mask,

made of soda-lime glass and with chromium printed patterning, has been designed during this thesis to allow both electrical and electromechanical characterisation of the samples. It is represented in Figure 3.6.

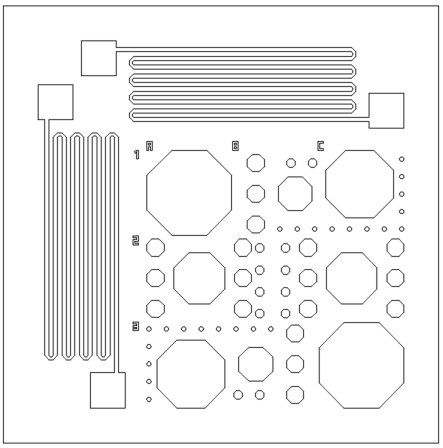

Figure 3.6.: Layout of the photolithography mask to pattern top electrodes and strain gauges onto 5×5 mm^2 samples. The electrode areas range from 0.0019 mm^2 to 0.7842 mm^2. The strain gauges are orthogonal and their straight sections are wide of 50 µm and have a total length of 229 mm. The length of curved sections is negligible. The strain gauges contact pads are 400×400 µm^2. Dimensions are to scale.

The designed photolithography mask is composed of electrodes and strain gauges. The electrodes are octagonal and their sizes vary from 0.0019 mm^2 to 0.7842 mm^2. The smaller electrodes are meant to facilitate samples electrical characterisation as it reduces the probability of inhomogeneities and defects in the thin film region located under the electrode. The larger electrodes are intended for measurement of the $e_{31,f}$ piezoelectric coefficient, as described in section 4.4 along with usage of the strain gauges.

The mask is precisely positioned onto the sample using a mask aligner MJB4 by Süss MicroTec (Garching, Germany). Once the alignment accuracy is ensured using an integrated microscope, the mask is brought in contact with the sample surface. It should be noted that the substrate curvature previously mentioned prevents uniform contact over the entire sample surface which might lead to inaccurate electrodes patterning. However, the resulting pattern does not display defects when checked with an Axio Lab.A1 optical microscope by Carl Zeiss (Oberkochen, Germany).

The UV light to harden the photoresist is generated by a mercury lamp emitting at Hg g-line (λ = 436 nm), h-line (λ = 405 nm) and i-line (λ = 365 nm). The exposure time is adjusted depending on the UV light intensity to obtain a dose of 0.81 mW·cm^{-2}·s. The regions where the negative photoresist was not protected by the mask during exposure to UV light harden (see Figure 3.5 (b)). Afterwards, the regions which are not hardened are removed by immersing the sample in ma-D-533s developer (Microresist) for 80 s (see Figure 3.5 (c)). To rinse the developer and stop the development process, the sample is then immersed in deionised water and dried with nitrogen gas. The quality of the pattern is verified with an optical microscope.

The next step in the process to pattern top electrodes is to clean the sample surface using a Femto O_2 plasma cleaner by Diener electronic (Ebhausen, Germany) for 1 min at 70 W. This cleaning procedure improves adhesion of the Pt top electrodes which are then sputtered according to the process described in section 3.3.1 (see Figure 3.5 (d)). Once the electrodes are deposited, the hardened photoresist is removed

from the sample by immersing it into aceton (99.8 %, Roth). After the photoresist has been entirely striped from the sample, the latter is dried with nitrogen gas and the electrodes and strain gauges quality is verified with an optical microscope (see Figure 3.5 (e)).

In the case of *PNZT stacks*, the Pt electrodes are annealed post-deposition to improve adhesion with the PNZT layer. Rapid thermal annealing would be the optimal technique for this process as it is sufficiently fast to limit lead loss in the sample [24]. However, in the absence of a rapid thermal annealing furnace, the electrodes and strain gauges are post-annealed at 400 °C for 1 min on a hot plate. To enhance temperature homogeneity at the sample surface during the annealing process, the sample is placed under a $30 \times 30 \times 30$ mm^3 heat shield made of 0.5 mm thick stainless steel.

3.4.2. Argon ion milling

Argon ion milling, also known as Ion Beam Etching (IBE), is a dry plasma etching technique relying on an ion bombardment from a plasma to anisotropically remove atoms from a material [197]. The IBE system used during this work was built by Mantis Deposition (Thame, UK) and operates with a background pressure of $1 \cdot 10^{-2}$ Pa. Due to this low pressure, the Ar ions, excited by a RF generator and accelerated with an energy of 500 eV, have a mean free path longer than the chamber dimensions. Equipped with a quadrupole mass spectrometer by Hiden Analytical (Warrington, UK), the IBE system allows in situ monitoring of the elements being etched. The mass spectrometer permits etch rate calibration and interface detection during the etching of successive layers with different chemical compositions.

Samples are introduced in the IBE system using a flag style holder or, in the case of *PNZT stacks*, a modified flag style holder, as mentioned in section 3.1. The Ar ion beam provides homogeneous etching of the 5×5 mm^2 samples with its diameter of 40 mm. To protect the areas that shall not be etched, photoresist is patterned on the sample surface. During the process, the sample heats up under the ion bombardment, leading, notably, to a hardening of the photoresist. The sample stage is cooled down with liquid nitrogen which limits the hardening of the photoresist and facilitates its lift-off at the end of the etching process.

The Ar ion milling process of the samples is represented schematically in Figure 3.7. In a similar manner to the photolithography process, described in section 3.4.1, it starts with the spin coating of negative photoresist ma-N 1420 (Microresist) onto the sample surface (see Figure 3.7 (a)). However, to facilitate the removal of the photoresist at the end of the etching process, its hardening must be limited as much as possible. For this purpose, the photoresist is not soft baked after spin coating, facilitating the removal of the photoresist after Ar ion milling and limiting damage to the Pt top electrodes and strain gauges previously deposited.

Due to the relatively large size of the combined top electrodes and strain gauges as compared to the sample size, the positioning and size of the bottom electrodes must be decided individually for each sample. The substrate bending described in section 3.4.1 and impeding sample alignment with the mask aligner also contributes to the difficulty to position the bottom electrodes. Additionally, in the case of *PNZT stacks*, there are areas of the sample lacking the LNO bottom electrode due to the modified flag style holder acting as a shadow mask during its deposition (see section 3.1). For these combined reasons, the photoresist patterning for the bottom electrodes must be done manually. The photoresist is removed in the sample corners using an aceton (99.8 %, Roth) soaked cleanroom wipe (see Figure 3.7 (b)). To allow precise photoresist removal, the wipe is wrapped around a razor blade.

Once the photoresist has been patterned, the sample is etched with Ar ion milling until the LNO layer is reached in the areas not covered by photoresist (see Figure 3.7 (c)). The etching end point is determined by

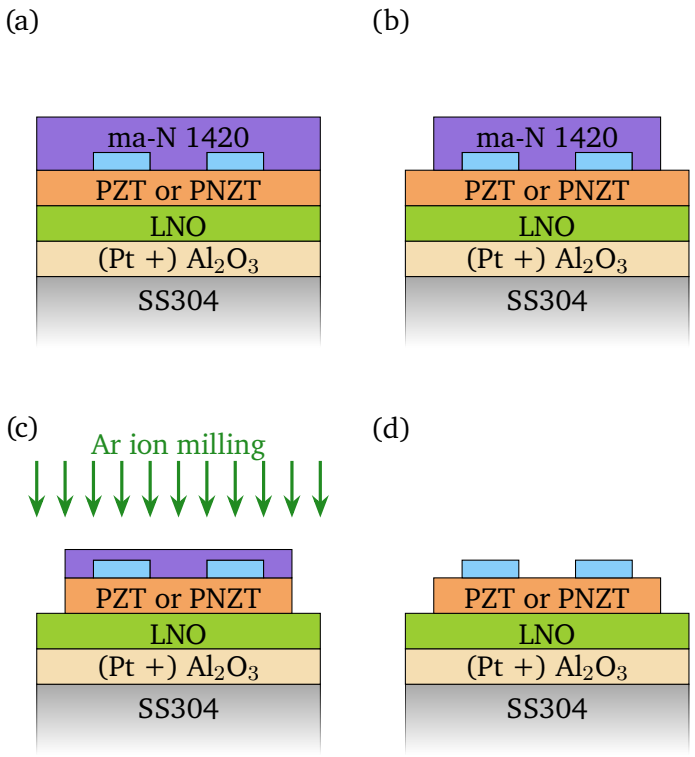

Figure 3.7.: Schematic representation of the Ar ion milling process to access $LaNiO_3$ bottom electrodes: (a) photoresist coating, (b) patterned photoresist lift-off, (c) Ar ion milling, (d) complete photoresist lift-off. Dimensions are not to scale.

monitoring the quantity of Ti, Zr and La etched from the sample surface using the IBE system quadrupole mass spectrometer. Due to the imprecision of manual patterning of the photoresist, the transition from ferroelectric to LNO layer during etching is not necessarily sharp. To allow optimal etching of the ferroelectric layer without risking milling the entire $LaNiO_3$ layer, the latter thickness has been increased in *PNZT stacks* compared to *PZT stacks*.

Afterwards, the photoresist is removed from the sample by immersing it into aceton (99.8 %, Roth). In some instances, the photoresist might be removed only partially due to hardening during the Ar ion milling process (see black spots on bottom right corner of Figure 3.1 (c)). Once the photoresist has been striped from the sample, the latter is dried with nitrogen gas and the bottom electrodes quality is verified with an optical microscope. The integrity of the electrodes and strain gauges quality is also checked in the process (see Figure 3.7 (d)). If, during the sample electrical characterisation described in chapter 4, electrical contact with the bottom electrodes is only partial or difficult to establish, a drop of silver paste can be applied on top of the bottom electrodes.

3.5. Structure characterisation methods

Before preparing the electrodes for electrical and electromechanical characterisation, sample structures are characterised with non-destructive methods. The phase and crystallographic orientation of the films are

analysed by X-ray diffraction. The latter is further investigated by electron backscatter diffraction while the microstructure is assessed by scanning electron microscopy. These techniques are also employed to characterise PLD targets.

3.5.1. X-ray diffraction

X-rays are electromagnetic radiations with an energy of 100 eV to 10 MeV and a wavelength of 10 nm to 1 pm. These wavelengths, in the same order of magnitude as crystallographic interatomic distances, allow X-rays to diffract on atoms, providing information on crystal structure [198]. X-Ray Diffraction (XRD) is a versatile characterisation technique for thin films from which several crystal properties can be accessed depending on the measurement method [199].

The thin films and targets produced in this work are characterised using a SmartLab diffractometer by Rigaku (Tokyo, Japan). The diffractometer is equipped with a tungsten filament and a rotating 9 kW Cu anode to generate a divergent X-ray beam. The measurements are performed in the parallel beam geometry were the X-ray beam is monochromatised around the Cu Kα line (λ = 1.5406 Å) and collimated on a paraboloidal synthetic multilayer mirror. The multilayer mirror reduces the divergence angle down to approximately $0.04°$. The irradiated sample area is restricted by a combination of vertical and horizontal slits placed in the incident beam path which define the width and height of the X-ray beam. Additionally, horizontal Soller slits consisting of evenly spaced metal foils are used to suppress the incident beam in-plane divergence.

The sample stage can be translated vertically or in the horizontal plane, as represented in Figure 3.8. The stage is incorporated in the Eulerian cradle of a four-circle goniometer, allowing the sample to be rotated around the axes perpendicular and parallel to the sample surface, respectively. The X-ray source, sample and detector are located in the measurement plane which they define. In this measurement plane, the X-ray source angle with respect to the sample surface is defined as ω. The diffraction angle, corresponding to the sum of the source angle and the angle between the detector and the sample surface, is known as 2θ.

On the receiving side of the diffractometer, slits can be employed to determine the 2θ resolution of the measurement or to shield the X-rays scattered by the sample. The optics are completed by a Soller slit to set the resolution and an attenuator to protect the scintillation counter measuring the diffracted X-ray intensity. Due to the crystallinity of the samples produced in this work, the use of an incident channel-cut crystal monochromator is not possible as the X-ray intensity would be too limited for accurate measurements. Therefore, a flat graphite monochromator is employed before the detector. This configuration leads to a collimation of 150 arcseconds.

The different measurement methods used in this work are described in the following sections.

3.5.1.1. X-ray diffraction: 2θ-ω scan

The 2θ-ω scan is an out-of-plane diffraction method giving notably access to the film phase, orientation and thickness [200]. In the case of a symmetrical-reflection measurement, as performed in this thesis, the angle between the detector and the sample surface is equal to the X-ray source angle ω and the diffraction angle is set as $2\theta = 2 \times \omega$. The source and detector are varied simultaneously while the sample position is fixed. In a symmetrical-reflection measurement, the collected X-rays are diffracted by crystal lattice planes

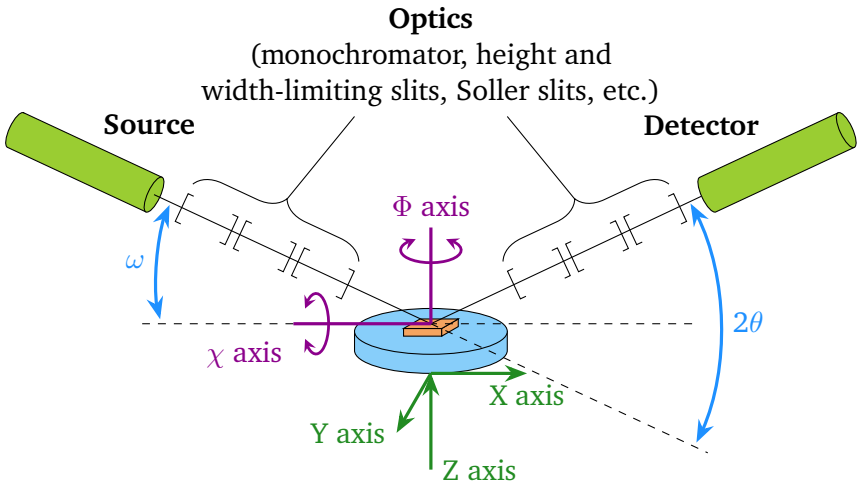

Figure 3.8.: Schematic representation of the SmartLab X-ray diffractometer by Rigaku with its degrees of freedom. The sample stage can be translated vertically (along the Z axis) or in the horizontal plane (along the X and Y axes). The sample can be rotated around the Φ and χ axes, perpendicular and parallel to the sample surface, respectively. The X-ray source angle, ω, and the diffraction angle, 2θ, are represented.

parallel to the sample surface [200]. The source angle is equal to the X-ray beam incidence angle with respect to the crystal planes within the substrate, θ, and the measurement is known as a 2θ-θ scan.

X-rays are diffracted by lattice planes and constructive interferences between the scattered X-rays occur when Bragg's condition is fulfilled [201]:

$$2d_{hkl}sin(\theta) = n\lambda, \tag{3.2}$$

where d_{hkl} is the interplanar distance in a crystal, θ is the incidence angle, n is a positive integer corresponding to the order of the reflection and λ is the wavelength of the incident wave. When Bragg's condition is met, a reflection appears in the detected spectrum at the corresponding diffraction angle, creating a pattern characteristic of the sample. This reflection is named hkl based on the Miller indexes of the diffracting crystallographic plane.

Prior to performing a measurement, it is necessary to align the sample with respect to the incident beam. Due to the polycrystalline nature of the stainless steel substrates used in this work, it is not possible to define a scattering angle to perform a surface normal alignment. Therefore, only a direct beam half-cut alignment is performed to align the sample vertically into the incident beam. To perform the measurement, 2θ is varied in the selected range and ω is varied accordingly.

In the case of thin films, additional oscillations, named *Laue oscillations*, can be developed around the reflections in the XRD pattern. These oscillations originate from the interference of the coherently diffracted X-ray beam on the finite crystal lattice. The layer thickness, t_{Laue}, can be estimated from the distance between Laue oscillations according to the equation [202]:

$$t_{Laue} = \frac{\lambda}{2\left(sin\theta_i - sin\theta_{i-1}\right)}, \tag{3.3}$$

where θ_i and θ_{i-1} are the diffraction angles of the i^{th} and the $(i-1)^{\text{th}}$ oscillations, respectively.

Furthermore, based on the Scherrer equation, it is possible to estimate the crystallite size, s_c, from the broadening of the breadth of the XRD reflections, β [203]. Various evaluation methods have been developed, including the Hall method following the equation [204]:

$$\frac{\beta cos\theta}{\lambda} = 4s_c\frac{sin\theta}{\lambda} + \frac{1}{\kappa_{lattice}}, \tag{3.4}$$

where $\kappa_{lattice}$ is the lattice strain. The Hall method can be applied by the software PDXL 2 v.2.8.4.0 by Rigaku Corporation (Tokyo, Japan), yielding the crystallite size from the XRD pattern.

3.5.1.2. X-ray reflectivity

X-Ray Reflectivity (XRR) is a technique based on both specular reflection and X-rays refraction at an interface between two media with different refractive indexes. From the analysis of the intensity of grazing incidence X-rays refracted by a sample, information on the thicknesses and densities of the sample layer as well as on interface roughnesses can be obtained [205]. The film thickness can be calculated more accurately from XRR than from Laue oscillations. However, the maximum thickness of the films that can be analysed by XRR is dependent on both the film properties and the diffractometer optics.

A XRR measurement corresponds to a 2θ-ω scan at low diffraction angles, typically with $0° < 2\theta < 6°$. When reaching the sample under this grazing angle, inferior to the critical angle for total reflection θ_c, all the incident X-rays are reflected. As ω the X-ray source angle increases and equals θ_c, the X-rays are only partially reflected and propagate along the sample surface. When ω becomes larger than θ_c, the X-rays are both reflected and penetrating inside the sample by refraction. Above θ_c, the ratio of reflected to refracted X-rays decreases proportionally to θ^4 [205].

Similar to a 2θ-ω scan, it is necessary to align the sample with respect to the incident beam before performing a measurement. After a direct beam half-cut alignment, a surface normal alignment is executed for a grazing incidence measurement at a scattering angle of $2\theta = 0.5°$. In these conditions, the polycrystalline nature of the stainless steel substrates used in this work does not prevent the surface normal alignment. To extract film characteristics from the reflectivity measurements, data are modelled using the software Rocking Curve & Reflectivity Curve Simulation & Fitting (RCRefSiW) v.1.09 by IHP Solutions (Frankfurt an der Oder, Germany).

The X-rays can be reflected on several interfaces in a sample including the atmosphere-film and the film-substrate interfaces. If the sample is composed of several layers, reflection can also occur on internal film-film interfaces. The alternation of constructive and destructive interferences from the X-rays reflected at these various interfaces creates oscillations in the intensity of the reflectivity profile named *Kiessig fringes*. The oscillation curve extracted from Kiessig fringes is a function of the refracted index of the layer and of its thickness which can be obtained by Fourier transformation. The period of these oscillations decreases as the film thickness increases [205]. The impact of several parameters on the oscillations, including thickness, is simulated using the software RCRefSiW for PZT 52/48 films deposited $NdGaO_3$ substrates and represented in Figure 3.9.

Additionally, the layer density can be extrapolated from the total reflection critical angle as indicated in Figure 3.9. The Kiessig fringes amplitude is dependent on the difference between film and substrate densities. Figure 3.9 also shows the effects of film surface and interface roughnesses. An increasing film surface roughness leads to a decrease of the reflectivity curve slope while the Kiessig fringes amplitude decreases when the interface roughness increases.

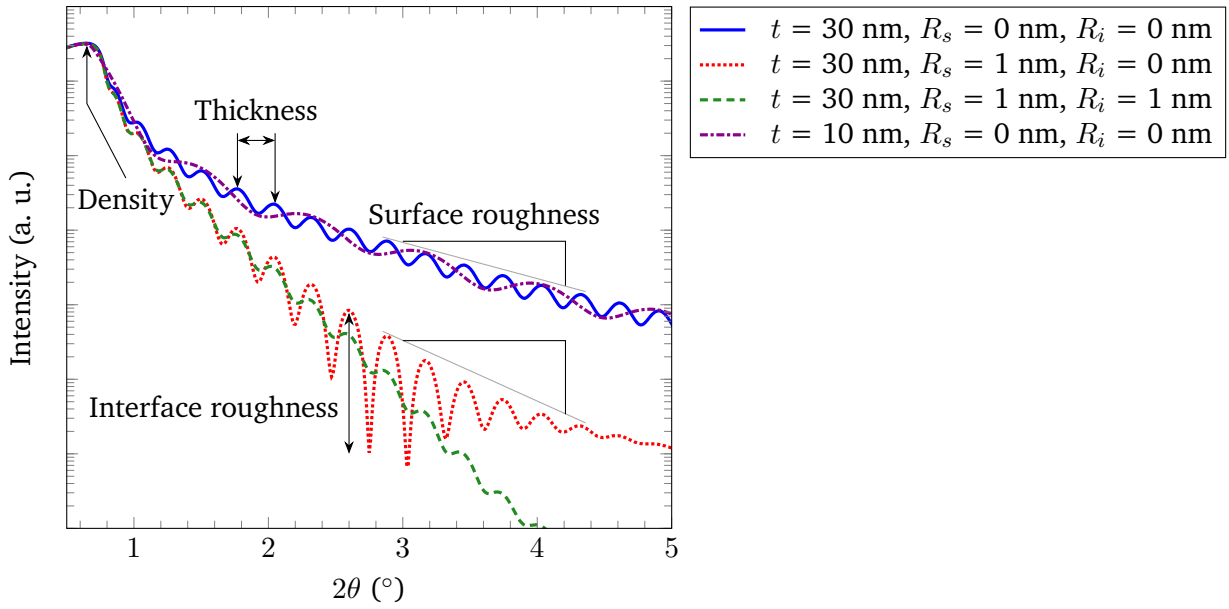

Figure 3.9.: Simulation of reflectivity curves of PZT 52/48 thin films on $NdGaO_3$ substrates with different thicknesses, t, surface roughnesses, R_s and interface roughnesses, R_i, using the software RCRefSiW.

3.5.2. Scanning electron microscopy and energy-dispersive X-ray spectroscopy

Scanning Electron Microscopy (SEM) is used to analyse the microstructure of PLD targets and of PZT thin films deposited in *PZT stacks*. Coupled with Energy-Dispersive X-ray Spectroscopy (EDS), SEM is also employed to assess the cations stoichiometry of the PLD targets. These non-destructive, ex situ techniques are based on the interactions between the sample material and an electron beam scanned point by point across the sample surface.

A scanning electron microscope relies on an ultra-high vacuum chamber in which an electron beam is generated by applying a high voltage of 1 keV to 30 keV between a cathode and an anode. The electron beam is focused on the sample using electromagnetic lenses. At each point where the beam is scanned over the sample, the impacting or primary electrons are scattered both elastically and inelastically by the material. Due to this electron bombardment, the sample emits characteristic X-rays and electrons which are measured and quantified by several detectors located inside the ultra-high vacuum chamber. Both SEM and EDS techniques are described in more details in [206].

During this work, unless otherwise mentioned, an SEM XL30 FEG from Phillips (Amsterdam, Netherlands) is employed, coupled with an EDS-CDU LEAP detector with a silicon crystal drifted with lithium, *Si(Li)*, cooled with liquid N_2 and with an energy resolution of 135 eV to perform EDS. Imaging of the surface topography is performed with a secondary electrons detector to measure the low-energy secondary electrons at approximately 50 eV interacting only with the first few nanometres of the sample material. To avoid surface charging of the electrically insulating targets due to the electron beam, thin metallic layers are sputtered on the target surface before measurement.

For cross-section images, the cross-section is accessed by cutting a trench in the sample with a focused ion

beam after depositing a thick Pt capping layer. This process is performed by Ulrike Kunz from the Institute of Materials Science of the Technische Universität Darmstadt (Darmstadt, Germany).

3.5.3. Electron Backscatter Diffraction

Electron Backscatter Diffraction (EBSD) is performed by Enrico Bruder from the Institute of Materials Science of the Technische Universität Darmstadt (Darmstadt, Germany) to analyse the texture of PZT thin films deposited in *PZT stacks*. The EBSD data are acquired using a Mira3-XMH high resolution SEM by TESCAN (Brno, Czech Republic), equipped with a DigiView 5 EBSD Camera by EDAX (Mahwah, NJ, USA). An acceleration voltage of 15 keV and a beam current of 500 pA are chosen to operate the system and achieve a high spatial resolution.

The EBSD analysis, also performed by Enrico Bruder, is done with a 10 nm step size, which is below the physical resolution of conventional EBSD, owing to the coarsening effect induced by the NPAR® (Neighbor Pattern Averaging and Reindexing) post-processing routine that is used to improve the data quality without further clean-up procedures. To calculate the crystallographic texture, the harmonic series expansion method is used on an EBSD dataset with more than 7,000 indexed grains with a series rank of 24, a Gaussian half width of $5°$, and no enforced symmetry. The measured sample does not have Pt top electrodes and, to avoid electrical charging, a thin layer of carbon is sputter-coated on the surface.

4. Ferroelectrics characterisation methods

This chapter describes the experimental setups and procedures employed in this thesis to characterise the dielectric, piezoelectric and ferroelectric properties of the samples. In section 4.1, the methods to characterise thin films dielectric permittivity and loss are introduced. The technique to measure *P-E* loops and access thin films ferroelectric properties are presented in section 4.2. Afterwards, sections 4.3 and 4.4 introduce the hot poling process and the wafer flexure $e_{31,f}$ coefficient measurement to assess piezoelectric properties of thin films. This chapter concludes on leakage measurements principles in section 4.5.

Contrarily to the experimental procedures previously introduced in chapter 3, the techniques and experimental setups here described were not implemented in the research group prior to this work. The selection of experimental methods and necessary hardware as well as the implementation of the experiments are an integral part of this thesis. Advice from the Susan Trolier-McKinstry group at the Materials Research Institute of The Pennsylvania State University (State College, PA, USA) is gratefully acknowledged.

4.1. Dielectric characterisation

As described in section 2.1, ferroelectric materials are dielectrics. Therefore, the first step to characterise ferroelectric thin films is to demonstrate that they are dielectric and to assess their quality by measuring their dielectric constant and loss. Section 2.1.1 introduced the former as the relative permittivity of a material, ε_r, thereafter referred to as *permittivity*, and the latter as $tan\ \delta$. Usually, these frequency dependent parameters are measured between 1 kHz and 10 kHz [17, 98].

The ferroelectric thin films deposited in this work are set in a parallel plate capacitor structure with top and bottom electrodes, as described in section 3.4. Permittivity depends on the electrode area, A_{elec}, and on the thickness of the dielectric layer, t_{dielec}. It is related to the capacitance of the dielectric, C, by the equation:

$$\varepsilon_r = \frac{C t_{dielec}}{A_{elec} \varepsilon_0}, \tag{4.1}$$

where ε_0 is the permittivity of free space.

Since dielectrics are imperfect capacitors with parasitic components, it is necessary to measure their complex impedances to access their capacitance and dielectric loss [207, 208]. Impedance, Z, is defined as the opposition, through resistance and reactance, brought up by a device to the flow of alternating current at a given frequency, f [209].

It should be noted that the samples studied in this work have relatively small capacitance values, in the order of magnitude of $\sim$ 100 pF to 10 nF. These low capacitances, when measured between 1 kHz and 10 kHz, lead to an impedance between $\sim$ 1 kΩ and 1 MΩ. Therefore, to measure the dielectric layer capacitance accurately, it is necessary to consider an equivalent circuit with a resistance, R_p, in parallel to the capacitor, C_p, as shown in Figure 4.1. In this configuration, complex impedance is expressed by [208]:

$$Z = \frac{1}{1/R_p + \mathrm{j}2\pi f C_p}. \tag{4.2}$$

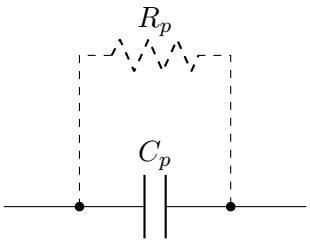

Figure 4.1.: Equivalent circuit model of a capacitor, C_p, with a parallel resistance, R_p, to measure the capacitance of dielectric thin films.

Furthermore, the dissipation factor, equivalent to the dielectric loss tangent, $tan\ \delta$, corresponds to the ratio of the real to the imaginary part of the impedance. In a parallel equivalent circuit, it is defined as [208]:

$$tan\ \delta = \frac{1}{2\pi f R_p C_p}. \tag{4.3}$$

Complex impedance measurements are performed with an Alternating Current (AC) impedance capacitance meter, also known as *LCR meter*, measuring both the impedance amplitude and phase angle. For this purpose, a LCR meter is equipped with four terminals called *Hcurr*, *Hpot*, *Lcurr* and *Lpot* corresponding to the high current, high potential, low current and low potential terminals, respectively. An AC voltage is supplied from the *Hcurr* terminal and the current through the dielectric layer is measured by the *Lcurr* terminal. Simultaneously, the voltage across the dielectric is measured by the *Hpot* and *Lpot* terminals while being phase-locked with the current. This allows to measure the phase angle between current and voltage [207].

When measuring low capacitance values, stray capacitances are a large source of measurement error. They can appear between the sample and a nearby conductor, e.g. a metallic sample stage. During the measurement, a difference of voltage is created between sample and conductor, leading to the measurement signal leaking towards the conductor. The leakage signal is then measured along with the sample signal, generating measurement errors due to stray capacitances. To suppress the voltage difference, a shielding plate, e.g. made of ceramic or quartz, is inserted between the sample and the sample stage [208].

In order to reduce the effects of lead impedances and contact resistances, the signal current path and the voltage sensing leads must be independent. This is achieved with a *four-terminal configuration* by connecting together the outer shields of the *Hcurr* and *Hpot*, *Lcurr* and *Lpot* terminals, respectively. The connection must be made as close as possible to the sample. To further compensate stray admittance and residual impedance due to the experimental setup, *open and short compensations* must be performed [208].

Since the dielectric layers characterised in this work are also ferroelectric, ferroelectric switching and poling must be avoided. Therefore, the amplitude of the AC voltage applied to the sample is chosen to produce a *subswitching field*, below the ferroelectric coercive field [98].

4.1.1. Parameters sweeps

Permittivity and dielectric loss depend on several parameters including the AC subswitching field frequency and amplitude. If a DC bias voltage is applied, these properties are also dependent on the resulting applied field. It is necessary to quantify these dependences through parameters sweeps.

At subswitching fields, field frequency and amplitude dependence of the permittivity are mainly due to extrinsic effects, e.g. domain wall motion and defect displacement. Besides the necessity for applications to account for their impact on devices, analysis of these dependences can provide information on the extrinsic mechanisms nature [98].

While the effect of subswitching field amplitude and frequency are measured at zero DC bias field, measuring a permittivity versus electrical field curve, also known as ε_r-E curve, requires a DC bias field to be applied simultaneously to the AC subswitching field. In this method, sometimes referred to as capacitance versus voltage or C-V curve, the DC bias is varied as a step-like function while the AC field is employed to measure the capacitance as described in the previous section [98]. As ε_r-E curves lead to ferroelectric switching and, therefore, remanent polarisation, they must be performed after *P-E* loops are measured.

In the absence of a DC field, domain walls can be *pinned* by defects, e.g. oxygen vacancies, limiting their mobility [6, 98]. Upon increase of the DC bias, domain walls are released from the defects which lead to an increase in permittivity. Furthermore, some ferroelectric domains with relatively low coercive fields can be switched by the combined AC and DC applied fields. The proportion of switching domains increases with the applied DC bias until the sample coercive field is reached. For DC bias fields larger than the coercive field, the permittivity decreases. This phenomenon is due both to the reduction of the number of domains as they aligned themselves with the applied field and to the domain wall motion inhibition by the DC bias field [98].

4.1.2. Dielectric characterisation experimental systems and parameters

At the exception of DC bias sweeps, permittivity and dielectric loss measurements are performed with a custom-built probe station. The probe station is contained in a lidded enclosure made of film faced plywood to dampen outside mechanical noise [210]. Its exterior is covered by metallic plates and electrically grounded to ensure electrical insulation of the measurement setup. This electrical ground is common to the probe tips positioners and, when required, sample. The probe station is equipped with S-725 micropositioners by Signatone (Gilroy, CA, USA) on which tungsten tips of 25 µm in diameter are mounted.

Permittivity and dielectric loss measurements are performed using an E4980A LCR meter by Agilent (Santa Clara, CA, USA). In order to perform accurate permittivity calculations from the measured capacitance value (see Equation (4.1)) the electrode area must be known. Therefore, the sample is driven by the bottom electrode, i.e. the top electrode, patterned by photolithography, is grounded so measurements are performed on an electrode whose exact area is known. The experimental setup is schematically represented in Figure 4.2 without the plywood enclosure.

As the E4980A LCR meter does not permit DC bias sweeping, DC bias sweeps are performed using a 4200-SCS Semiconductor Characterization System by Keithley Instruments (Solon, OH, USA) equipped with a 4210-CVU Multi-Frequency Capacitance Voltage Measure Unit card. This measurement system is connected to a commercial TTPX probe station by Lake Shore Cryotronics (Westerville, OH, USA), equipped with beryllium-copper tips of 25 µm in diameter. This particular experimental setup was already implemented in the research group prior to this work.

In the absence of parameters sweeps, permittivity and dielectric loss are measured at zero DC bias with an AC driving signal of $V_{AC} = 30$ mV at 1 kHz or 10 kHz. This amplitude of the driving signal is lower than half of the coercive field of the thin films. Sweeps of subswitching field frequency and amplitude are performed between 100 Hz and 10 kHz and between 0 kV·cm^{-1} and 20 kV·cm^{-1}, respectively. ε_r-E curves are measured between -200 kV·cm^{-1} and 200 kV·cm^{-1}.

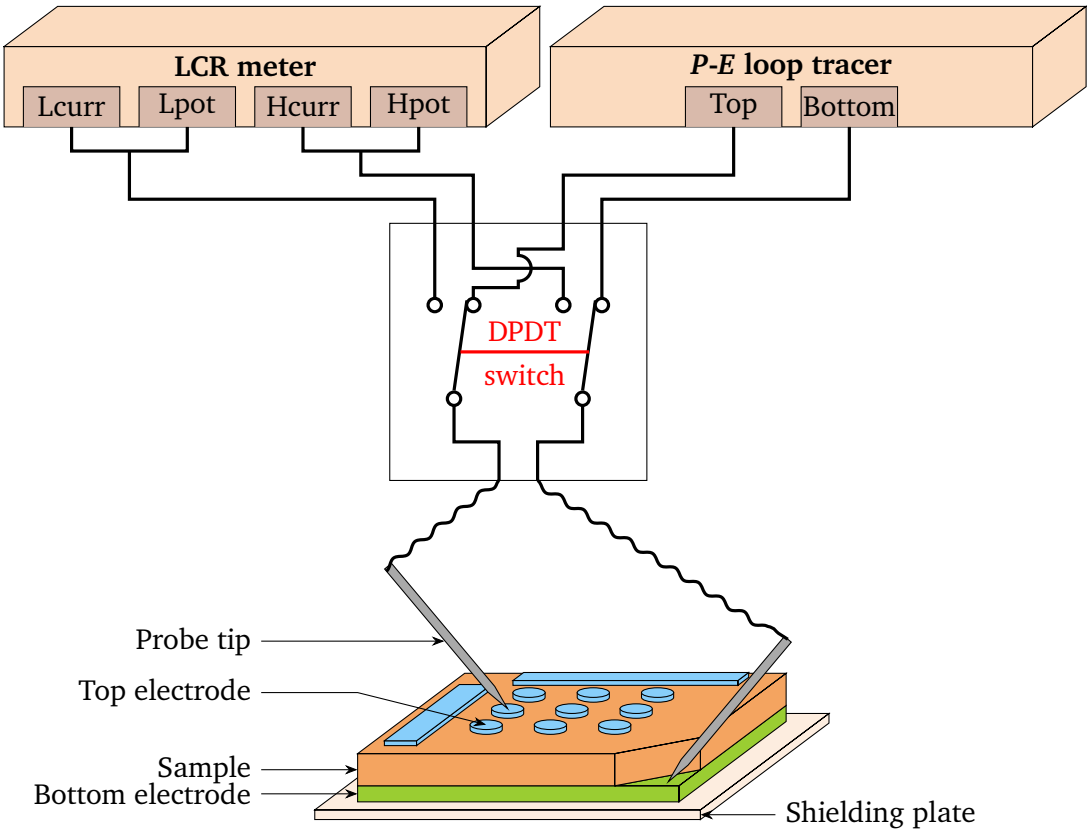

Figure 4.2.: Schematic representation of the combined experimental setups for dielectric and ferroelectric characterisation of a parallel plate capacitor structure (buffer layers and substrate are not represented). Permittivity and dielectric loss measurements are performed with the LCR meter in the four-terminal configuration while *P-E* loops are measured with the *P-E* loop tracer. A Double Pole Double Throw (DPDT) switch allows to switch between the two measurement systems. Dimensions are not to scale.

4.2. Ferroelectric characterisation

The second step to characterise ferroelectric thin films is to demonstrate their ability to reverse their polarisation and to measure their coercive field, saturation and remanent polarisation values. For this purpose, ferroelectric hysteresis loops, i.e. *P-E* loops, must be acquired. As developed in section 2.1.4, the absolute value of the polarisation cannot be accessed, therefore, it is the change in polarisation which is quantified [118].

Several methods exist to measure the change in polarisation which is dependent on the ferroelectric switching current density, as defined by Equation (2.20). The majority of these techniques relies on an excitation voltage, applied across the sample to measure the switching current or the polarisation charge response [211].

The first method to measure *P-E* loops was proposed by Sawyer and Tower in 1930 [212]. This method necessitates a reference capacitor mounted in series with the ferroelectric sample. As an excitation voltage is applied to the electrical circuit, a voltage drop occurs across the reference capacitor, proportionally to

the polarisation charge. While this method is suitable for high speed measurements, its main drawbacks are parasitic effects and the difficulty to find sufficiently precise reference capacitors [105, 106, 211, 212].

The second technique, known as the *shunt method*, is similar to the *Sawyer Tower method* while replacing the reference capacitor of the latter by a reference resistance. In this configuration, the charge is obtained by numerically integrating the measured switching current. This method can be accurate for large electrode sizes but parasitic capacitances make it unreliable for small area electrodes. Furthermore, the value of the reference resistance must be adapted to both the sample capacitance and the excitation voltage frequency [211].

The *virtual ground method*, is the third technique based on an excitation voltage. More complex, its electrical circuit comprises an operational amplifier and a feedback resistor, converting the measured switching current to voltage. This technique is efficient for samples with small capacitances. Despite the necessity to take into account several parameters linked to the operational amplifier, this method is the most precise for ferroelectric measurements [211].

The fourth method to measure ferroelectric hysteresis loop is the *current step method*. In that case, an excitation current is applied directly across the ferroelectric sample, creating a voltage drop over it. Since it does not necessitate a reference component, this method has the advantage of avoiding approximations [211].

Each of the methods described above presents advantages and drawbacks. The choice of a specific method depends not only on the sample but also on several technical considerations, e.g. range of signal magnitude, bandwidth or parasitic effects [211]. In consequence, ferroelectric hysteresis loops are often measured with commercial setups [106].

4.2.1. Accessing ferroelectric characteristic values

Before measuring a ferroelectric hysteresis loop, the sample must be pre-polarised by measuring a hysteresis loop with the same parameters and called *pre-polarisation pulse*. This creates a defined polarisation state, usually set as the negative state of the remanent polarisation. It is important to note that *P-E* loops are dependent on the sample electrical and mechanical history and also on the measurement method [211].

As described in section 2.1.4, *P-E* loops are obtained by measuring the sample polarisation versus the applied electrical field. Commonly, the excitation voltage applied to the sample is a triangular symmetric waveform. The shape of the ferroelectric hysteresis loop depends on the frequency of the excitation signal. Indeed, it defines the time constant for the sample to undergo a full *P-E* loop and, therefore, impacts the relaxation time between each data point [211, 213]. This measurement is known as a *dynamic hysteresis curve* in opposition to a *static hysteresis curve*. The latter aims to remove the influence of the excitation signal frequency on the *P-E* loop shape by measuring a quasi-static hysteresis loop. For this purpose, a defined relaxation time is set between each measured point of the hysteresis curve. Static hysteresis measurements allow the investigation of irreversible and reversible contributions to the sample polarisation [211, 214].

Saturation and remanent polarisation values can be obtained from the ferroelectric hysteresis loop, as mentioned in section 2.1.4 (see Figure 2.4) [120]. However, as the polarisation reversal is progressive for non-ideal single crystals and polycrystalline samples, measuring the coercive field from the *P-E* loop yields inaccurate values. To circumvent this problem, coercive fields are determined from the switching current versus voltage curve corresponding to the *P-E* loop and where the switching peaks are clearly identifiable [106, 120].

Another sample characteristic which can be obtained from ferroelectric hysteresis loops is the *imprint*, corresponding to an *internal bias field* in the ferroelectric sample. Generally present in virgin ferroelectric capacitors, imprint is manifested as a shift of the hysteresis loop along the electrical field axis. It corresponds to a preferred polarisation state over the other and can be due to defect dipoles [120, 211].

Depending on the respective directions of the internal bias field and applied field, imprint can either hinder or enhance the piezoelectric response for MEMS applications. Its consequences are a diminution or an increase of the remanent polarisation value and an asymmetry of the *P-E* loop along the electrical field axis. The internal bias field, $E_{c,shift}$ can be calculated by [211]:

$$E_{c,shift} = \frac{E_c - |E_{c,-}|}{2}, \tag{4.4}$$

where $E_{c,-}$ is the negative coercive field.

Additionally, qualitative information on the ferroelectric sample can be obtained from the shape of *P-E* loops. More "square" ferroelectric hysteresis loops indicate an abrupt reversal of the polarisation direction and the loop area is linked with the energy dissipated as heat within the sample. Avoiding heat generation is the reason for which *P-E* loops are measured at low frequency, typically at 100 Hz or below [213].

4.2.2. Ferroelectric characterisation experimental system and parameters

Ferroelectric hysteresis loops are measured using a TF Analyzer 2000 *P-E* loop tracer by aixACCT Systems (Aachen, Germany) equipped with a FE module. Electrical contacting of the samples is performed with the custom-built probe station described in section 4.1.2. To avoid field spreading, the sample is driven by the bottom electrode, as is done for permittivity and dielectric loss measurements. Connections between the *P-E* loop tracer and the ferroelectric sample are schematically represented in Figure 4.2.

To measure the *P-E* loops, dynamic hysteresis measurements are performed using a single triangular waveform with a frequency of 100 Hz. A pre-polarisation pulse loop is applied.

4.3. Hot poling process

As described in section 2.1.4, a poling process is necessary to generate a net polarisation by align the polarisations of ferroelectric domains in the direction of an applied electrical field, larger than the sample coercive field. As heating up a ferroelectric reduces its coercive field, poling is generally performed at elevated temperatures. Afterwards, the sample is cooled down before the poling field is removed [120].

It has been demonstrated in literature that poling at elevated temperatures creates imprint in ferroelectrics, leading to more stable polarisation states [215, 216]. This can notably be explain by the limited mobility of non-$180°$ domain walls in ferroelectric thin films, hindering modification of the ferroelastic domain orientation at room temperature once it has been set [17].

4.3.1. Key parameters of hot poling process

The efficiency of hot poling is dependent on the applied poling field, the poling temperature and the duration for which the poling field is applied before the cooling down process.

Literature reports that, for $Pb(Yb_{1/2}Nb_{1/2})O_3$-$PbTiO_3$ perovskite thin films, the optimal applied poling field is at least twice higher than the sample coercive field. Above this value, the $e_{31,f}$ coefficient absolute value saturates, indicating the maximum piezoelectric response. It has also been shown for these films that a poling duration longer than 10 minutes does not further improve the value of the $e_{31,f}$ coefficient [217].

An increase in the poling temperature of PNZT thin films from 25 °C to 150 °C leads to a sharper distribution of switching fields and an increased degree of imprint which improves the films $d_{33,f}$ coefficient. It should be noted that the internal bias field is further increased when poling is done at 200 °C [216].

The parameters described above can be applied to PZT thin films and several authors report the poling of PZT thin films at 150 °C under an applied field 2 to 3 times higher than the coercive field during 10 min to 15 min [53, 218].

4.3.2. Hot poling experimental system and parameters

During hot poling, the sample electrodes are electrically contacted with the custom-built probe station described in section 4.1.2. To avoid unnecessary heating of the film faced plywood, the interior of the probe station enclosure is protected with 5 mm thick plates of high-temperature glass wool type 1300-IN-LD-02 by Kager Industrieprodukte (Dietzenbach, Germany).

The sample is heated at 150 °C on a Fisherbrand™Isotemp™Hot Plate by fisher scientific (Pittsburgh, PA, USA) with an electrically insulating top surface. A DC electrical field is applied from the top to the bottom electrode with a Voltcraft Programmable Power Supply Unit DIGI 35 CPU by Conrad Electronic (Hirschau, Germany). The applied field is chosen equal to 2.5 times the sample coercive field and is maintained during 15 min before the sample is cooled down. Once the sample reaches room temperature the electrical field is removed.

4.4. Piezoelectric characterisation

Some key parameters for piezoelectric applications are the material piezoelectric coefficients introduced in section 2.1.2. In the case of thin films clamped to rigid substrates, the effective $e_{31,f}$ coefficient (see Equation (2.17)) is particularly relevant as it links the d_{31} piezoelectric coefficient and the thin film elastic compliances at constant electrical field [17, 24].

Several methods allow to measure the $e_{31,f}$ coefficient, either by measuring the substrate deflection when applying an electrical field (converse piezoelectric effect) or by collecting the charges related to in-plane strain developed when bending the substrate (direct piezoelectric effect) [17, 24]. The former possibility is generally implemented with laser interferometry where sample dielectric displacement can be measured by various interferometry techniques, including single-beam Michelson interferometer [219]. A comparison between single and double beam methods can be found in [220]. Another technique to measure $e_{31,f}$ coefficients when applying an electrical field on the sample is the *impulse method* [221, 222]. However,

these methods require complicated sample preparation and, for interferometry, careful alignment, making them difficult to implement.

The first attempts to measure the $e_{31,f}$ coefficient by collecting the developed charges when bending the substrate can be traced back to Deschanvres et al. who implemented cantilever flexure by statically straining and then releasing piezoelectric cantilever beams [223–225]. Further methods were developed over the years, including a pneumatic loading technique using a pressure probe [226] and point-loading methods [227]. Especially, the point-loading technique developed by Southin et al. makes use of a modified conventional point-loading *Berlincourt piezometer*. While simpler than other existing methodologies, this technique cannot be employed to characterise the samples produced in this work as it requires the piezoelectric thin film to cover an entire wafer [228].

A noteworthy *cantilever flexure method*, elaborated by Dubois and Muralt, is based on the bending of cantilevers using piezoelectric actuators and in-plane strain calculation from the applied force [229]. A variant of this technique, measuring the in-plane strain with strain gauges perpendicular to each other and glued on the sample, was developed by Garten and Trolier-McKinstry [53, 230]. However, this technique necessitates samples with a significantly larger area than the samples produced in this thesis.

Developed by Shepard et al., the *wafer flexure technique* to measure the $e_{31,f}$ coefficient, is suitable for small area samples and inexpensive [231–234]. It is introduced in the following section.

4.4.1. Wafer flexure technique principle

The wafer flexure technique aims to measure the $e_{31,f}$ coefficient of a thin film based on the direct piezoelectric effect. For this purpose, in-plane mechanical stress is applied dynamically to the sample by means of pneumatic excitation [231, 232].

The system is composed of four discrete components: a loudspeaker, a *uniform pressure rig*, a charge integrator and peripheral electronics. The loudspeaker, fitted on a cavity, is operated with a sinusoidal waveform, generating a pressure oscillation on the air contained in the cavity. This pressure oscillation propagates through a pipe towards the uniform pressure rig on which a silicon carrier wafer is fitted [231, 232].

The sample to characterise is glued on top of the carrier wafer. Both components are flexed by the pressure oscillation in the uniform pressure rig, generating controlled in-plane stress on the piezoelectric thin film. The strain in the sample is monitored with two strain gauges, oriented perpendicularly to each other. The sample being piezoelectric, it also develops a surface charge which is measured on an electrode by means of the charge integrator which converts the charge to voltage. A lock-in technique is employed to measure the converted charge value and the voltage variation in the strain gauges [231, 232].

From the measured charge and strains values, the $e_{31,f}$ coefficient of the piezoelectric thin film is given by the equation [24, 230]:

$$e_{31,f} = \frac{D_3}{\kappa_1 + \kappa_2} = \frac{Q_{surf}}{A_{elec}\,(\kappa_1 + \kappa_2)}, \tag{4.5}$$

where D_3 is the dielectric displacement perpendicular to the thin film surface, κ_1 and κ_2 are the thin film in-plane strains, Q_{surf} is the surface electrical charge developed by the sample and A_{elec} is the electrode area.

The components of the wafer flexure $e_{31,f}$ measurement system and the experimental process are described in further details in the next section.

4.4.2. Piezoelectric characterisation experimental system and parameters

The wafer flexure $e_{31,f}$ measurement system peripheral electronics comprise a computer, a SR830 DSP Lock-In Amplifier by Stanford Research Systems (Sunnyvale, CA, USA) and a custom-built *electronics box*. The computer hosts a LabVIEW^{TM} program to control the experiment whose code was written by Alexey Arzumanov from the Institute of Materials Science of the Technische Universität Darmstadt (Darmstadt, Germany) according to given specifications. Communication with the lock-in amplifier is performed through a RS232 connection while the electronics box is operated via a NI USB-6008 card by National Instruments (Austin, TX, USA). The LabVIEW^{TM} program takes the measurement parameters, controls the electronics to drive the wafer flexure system, acquires the measurement data, calculates the $e_{31,f}$ coefficient and generates an output file with the measurement results. A flowchart of the program is shown in Figure 4.3.

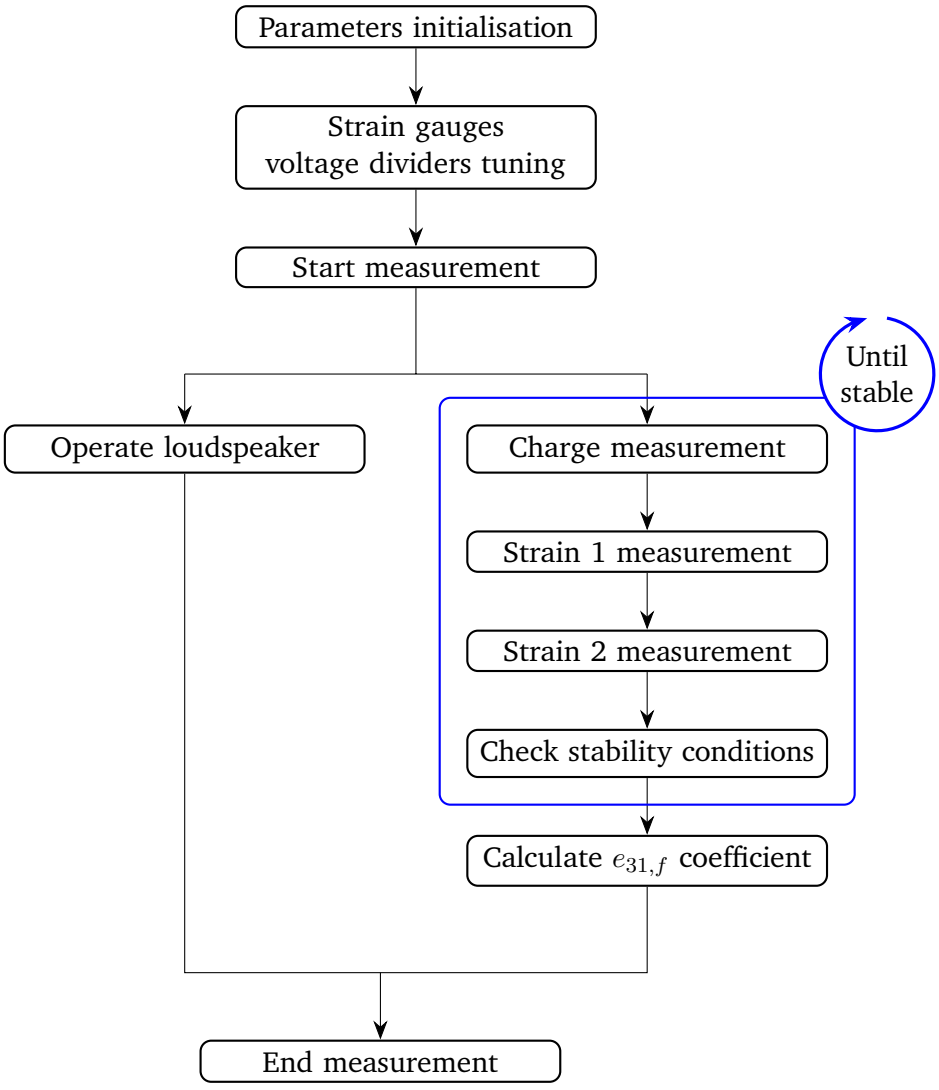

Figure 4.3.: Flowchart of the $e_{31,f}$ measurement LabVIEW^{TM} program.

The LabVIEW^{TM} program includes two initialisation steps before the measurement is started. At first, parameters set in the program are transmitted to the peripheral electronics. Afterwards, voltage dividers

used to monitor the sample in-plane strain via strain gauges are tuned with regard to the latter. This point will be developed below when strain measurements will be described. As the $e_{31,f}$ coefficient measurement is started, two processes are run in parallel.

In the first process, a sinusoidal signal of amplitude $0.5\ V_{RMS}$ and frequency 4 Hz is generated by the lock-in amplifier. This signal is taken as an internal reference for the charge and strain measurements. It also drives continuously a Legend BP102-8 loudspeaker by Eminence Speaker (Eminence, KY, USA) via the electronics box where it is amplified, as shown in Figure 4.4. The electrical schematic of the amplifier is given in Appendix A.

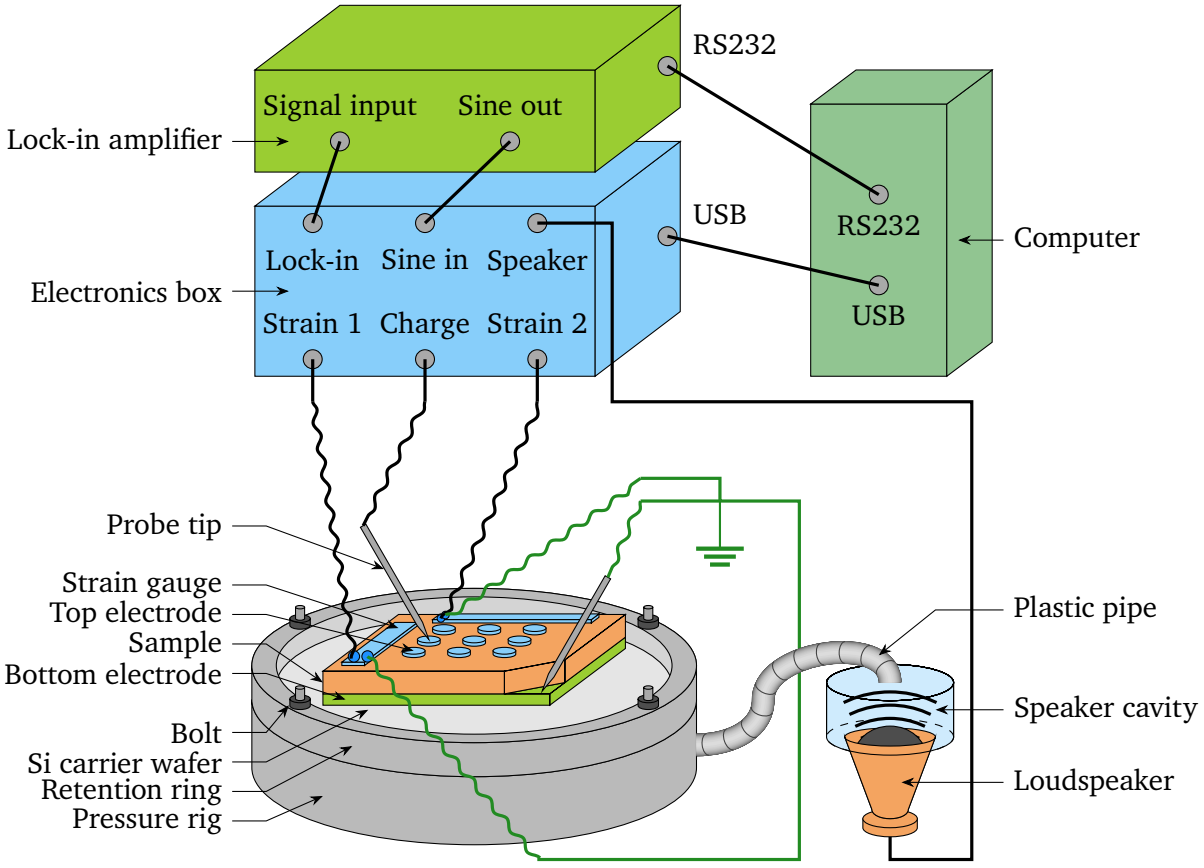

Figure 4.4.: Schematic representation of the wafer flexure $e_{31,f}$ measurement system, based on Shepard's work [231, 232], for a sample with a parallel plate capacitance structure (buffer layers and substrate are not represented). Green lines indicate grounded electrical connections. Dimensions are not to scale.

A representation and the technical drawings of the aluminium cavity on which the loudspeaker is fitted are given in Appendix B. To ensure that the cavity is airtight, the loudspeaker is glued on the cavity edge. The pressure oscillation is transmitted through a plastic pipe towards the aluminium uniform pressure rig. The rig, whose concept was developed by Shepard, is composed of several components: the rig housing, a base plate, two bushings and a retention ring [232]. A representation of the assembled uniform pressure rig and the technical drawings of its components are given in Appendix C. The uniform pressure rig is dimensioned to accommodate a 3" carrier wafer (76.2 mm in diameter) between its two bushings. Optimal positioning of the bushings is ensured by recesses on both the base plate and the retention ring. The latter

is held by four screws and bolts, sufficiently tightened to prevent horizontal motion of the carrier wafer. To improve the uniform pressure rig air tightness, paper rings at the bushings dimensions are inserted between each bushing and the carrier wafer [232].

Piezoelectric samples are glued at the centre of the silicon carrier wafer with Loctite Super Glue Ultra Liquid Control by Henkel (Düsseldorf, Germany). Once dry, this glue allows proper strain transmission between carrier wafer and sample. As mentioned in section 3.1, to ensure homogeneous gluing the substrate back must remain clean [232]. For more details on the mechanical equations describing strain in a sample fixed on the uniform pressure rig, the reader is referred to [232].

In the second process running as the measurement starts, the sample developed surface charge and applied in-plane strains in perpendicular directions are measured in succession until stability criteria are met simultaneously for each physical quantity. Switching between the different measurements is performed within the electronics box. The electrical schematic of the electronics box and the purpose of its components are given in Appendix D.

To monitor its surface charge, the sample is electrically contacted using the custom-built probe station described in section 4.1.2. Contrary to measurements previously introduced in this manuscript (see sections 4.1 and 4.2), the charge is measured by the top electrode while the bottom electrode is grounded. Indeed, in this mechanically oscillating configuration, the large area bottom electrode would generate a high noise to signal ratio if it was not electrically grounded. To ensure constant electrical contact despite the sample oscillation, a sufficiently large top electrode is chosen for contacting.

The surface charge developed by the sample as a function of mechanical stress is monitored by a charge integrator which converts the AC current to voltage and amplifies it, leading to more stable and reliable measurements [231, 232]. The electrical schematic of the charge integrator and the purpose of its components are given in Appendix E. The charge input into the integrator, Q_{in}, can be expressed as a function of the output voltage, V_{out}, by:

$$Q_{in} = -V_{out}C_{ref}, \tag{4.6}$$

where $C_{ref} = 10$ nF is the reference capacitance on which the charge is developed.

Once the surface charge value is acquired, in-plane strains in perpendicular directions, κ_1 and κ_2 referred to as *strain 1* and *strain 2* in Figures 4.3 and 4.4, are measured using strain gauges. Each in-plane strain is measured using a voltage divider in which the strain gauge constitutes a resistor. The in-plane strain as a function of the measured voltage crossing the voltage divider is given by:

$$x = \frac{1}{GF}\left[\frac{R_{ref}}{R_g}\left(\frac{V_{app}}{V_{no\_strain} + V_{meas,RMS}/0.707} - 1\right)^{-1} - 1\right], \tag{4.7}$$

where GF is the gauge factor, $R_{ref} = 1.2$ kΩ is the reference resistance in the voltage divider and R_g is the strain gauge nominal resistance. $V_{app} = 1.1$ V corresponds to the voltage applied on the voltage divider by the NI USB-6008 card, $V_{no\_strain} = 0.1$ V is the output voltage when no strain is applied and $V_{meas,RMS}$ is the output voltage as function of the strain measured by the lock-in amplifier. The 0.707 coefficient converts the RMS voltage value into voltage.

The strain measurements can be performed with two sort of strain gauges [232]. Platinum sputtered strain gauges give a more accurate value of strain as they are placed directly on the piezoelectric sample surface during the photolithography process, as described in section 3.4.1. However, due to the non-standardised resistance value of the sputtered strain gauges, the reference resistances in the voltage dividers are tuned

with 5 kΩ potentiometers before the $e_{31,f}$ measurement starts to ensure that $V_{no\_strain} = 0.1$ V (see Appendix D). To be within the tunable range of the reference resistances in the voltage dividers, sputtered strain gauges must have a nominal resistance of approximately $200\ \Omega$. With their length of 229 mm and their width of 50 µm, as indicated in Figure 3.6, it corresponds to an approximate thickness of 240 nm.

However, due to the large aspect ratio of the sputtered strain gauges, with a very high thickness as compared to their width, the platinum adhesion to the sample surface is not sufficient and the strain gauges present defects. These defects are missing areas where the sputtered platinum lifted-off from the sample and the strain gauge pattern is incomplete. To remediate to this problem, 2 mm long $120\ \Omega$ commercial strain gauges by RS PRO (Frankfurt am Main, Germany) are utilised. In aluminium, these strain gauges total dimensions are 6×2.5 mm^2. They have a gauge factor of 2.0 and are equipped with lead wires on which extension copper wires can be soldered. The commercial strain gauges are glued on the carrier wafer next to the sample with Loctite Super Glue Ultra Liquid Control by Henkel (Düsseldorf, Germany). To measure in-plane strain accurately, the strain gauges are glued as close as possible to the sample edges and perpendicular to each other. When commercial strain gauges are utilised, the potentiometers allowing tuning of the reference resistances in the voltage dividers are by-passed by switches in the electronics box (see Appendix D).

The charge and strains measurements are iterated until two stability conditions are met. The first condition, arising from the surface charge being developed in response to the in-plane strain, is for the charge signal to be in-phase or exactly out-of-phase with the strain signals with a $\pm 20°$ tolerance. The second condition is for the standard deviation of each strain signal over the last 20 data points to be inferior to a termination condition multiplied by the strain mean value. The termination condition is set at 0.05. If both stability conditions are met over 20 sets of data points, the $e_{31,f}$ coefficient is calculated using Equation (4.5).

4.5. Leakage measurements

Leakage measurements aim to quantify leakage currents through a dielectric and to identify the mechanisms involved in the process. Often complex, these mechanisms depend notably on the dielectric material itself and the interfaces with its electrodes. Several leakage mechanisms can take place under different values of applied field in a sample [235].

4.5.1. Key aspects of leakage measurements

Leakage measurements are performed on dielectric thin films by applying a constant voltage to the sample and measuring the resulting current after a given period, the *soak* time. Indeed, under an applied DC field, a transient current is present which decays exponentially with time. Therefore, it is necessary for the leakage current to stabilise before being measured [236]. For ferroelectrics, the transient current originates from dielectric relaxation and from polarisation [237, 238].

It should be noted that leakage measurements differ from switching current versus voltage measurements (see section 4.2.1) by the applied voltage being DC instead of AC. Furthermore, switching current versus voltage measurements do not involve soak time.

The source measure unit is a method to measure leakage in which the ammeter is connected to the voltage source internally. Generally, leakage currents have very small amplitude, in the order of magnitude of

the nanoampere. To protect the measurement devices in case of dielectric breakdown of the sample, a compliance value is set to limit the measured current [236].

4.5.2. Leakage measurements experimental system and parameters

Leakage measurements are performed using the 4200-SCS Semiconductor Characterization System by Keithley Instruments (Solon, OH, USA) employed for DC bias sweeps during dielectric characterisation. However, in this case, it is equipped with two 4200-SMU source measure unit cards and a 4200-PA preamplifier. The sample is contacted, using the TTPX probe station by Lake Shore Cryotronics (Westerville, OH, USA), equipped with beryllium-copper tips of 25 µm in diameter. This particular experimental setup was already implemented in the research group prior to this work. The bottom electrode is grounded, while the DC bias is applied to the top electrode.

Before measuring each data point, a soak time of 75 s is observed. The selected soak time is sufficient for the transient current to decrease to the order of magnitude of nanoamperes [237]. It is therefore negligible with regard to the measured leakage currents. The compliance value is set at 0.1 A.

5. Experimental results and discussion

In this chapter the experimental results of the characterisation of the *PZT stacks* and the *PNZT stacks* are given and discussed. Sections 5.1 and 5.2 endeavour to characterise the *PZT stacks* and the *PNZT stacks*, respectively, before the conclusions of the chapter are given in section 5.3.

In further details, a discussion on substrate curvature is included in section 5.1.1 and an analysis of the PZT thin films texture and morphology is given in section 5.1.2. The ferroelectric properties and leakage current through these samples are also examined in sections 5.1.3 and 5.1.4, respectively. Afterwards, properties of the *PNZT stacks* are presented in section 5.2 with a study of the influence of the O_2 deposition pressure and the deposition temperature in sections 5.2.1 and 5.2.2, respectively. Furthermore, the effect of the PNZT layer thickness and of measurement parameter sweeps on the *PNZT stacks* properties are investigated in sections 5.2.3 and 5.2.4, respectively. Leakage current and piezoelectric $e_{31,f}$ coefficient measurements are presented in sections 5.2.5 and 5.2.6, respectively.

5.1. {001}-textured PZT thin films: getting the orientation

Figures of this section have been adapted from:

J. Cardoletti, P. Komissinskiy, E. Bruder, C. Morandi, and L. Alff,
"{001}-textured Pb(Zr, Ti)O_3 thin films on stainless steel by pulsed laser deposition",
Journal of Applied Physics*, vol. 128, no. 10, p. 104103, 2020. DOI: 10.1063/5.0019967*

In literature, there are several reports of lead zirconate titanate thin films deposited on metallic substrates, including on stainless steel substrates, as mentioned in section 1.1.1. However, there are no compelling reports demonstrating direct growth on stainless steel of tetragonal {001}-textured lead zirconate titanate thin films grown by pulsed laser deposition.

Yet, as crystallographic orientation is crucial to MEMS applications, engineering of {001} texture is required to improve the piezoelectric response of PZT thin films [17, 53]. Therefore, **this section investigates the texture and ferroelectric properties of PZT thin films deposited by PLD in the *PZT stack* configuration** described in section 3.1.

5.1.1. Substrate curvature during thin films deposition

After the dicing and polishing steps of the experimental procedure described in section 3.2, it is observed that the SS304 substrates are flat. However, during the deposition of buffer and PZT layers, substrates bend in an U-shape concavely around the PZT-deposited side. The sample curvature, which is sufficiently pronounced to be observable by eye, appears in the steel rolling direction with a bending radius of a few millimetres. The bending here described also occurs when an uncoated substrate undergoes thermal treatment equivalent to the successive depositions of buffer and PZT layers. This substrate curvature phenomenon can be attributed to steel elongation during heating at deposition temperatures.

The industrial processing of commercially available stainless steel into thin sheets includes cold rolling and coiling/uncoiling procedures. These processes generate residual stresses in the material. The successive depositions of LNO at 500 °C and PZT at 650 °C represent a stress relief annealing for the SS304 substrate, which, in the presence of an asymmetric residual stress distribution, can lead to warpage [165].

It is important to note that the observed substrate curvature cannot be explained by thermal strain. Indeed, AISI 304 stainless steel thermal expansion coefficient at 20 °C is of $16.5 \cdot 10^{-6}$ K^{-1} [239]. This is larger than PZT thermal expansion coefficient, which ranges from $8 \cdot 10^{-6}$ K^{-1} in the paraelectric phase to $28 \cdot 10^{-6}$ K^{-1} in the ferroelectric phase with a discontinuity at the Curie temperature [53]. Therefore, if thermal strain was acting as the driving force leading to substrate curvature, the samples should be convex on the PZT-deposited side, the opposite of what is observed in this work.

5.1.2. PZT thin films texture and morphology analysis

The pattern obtained by XRD analysis of a *PZT stack* is shown in Figure 5.1, detailing the different layers. It should be emphasised that before the deposition of PZT, only the LNO reflections and the ones from SS304 and Pt are observed.

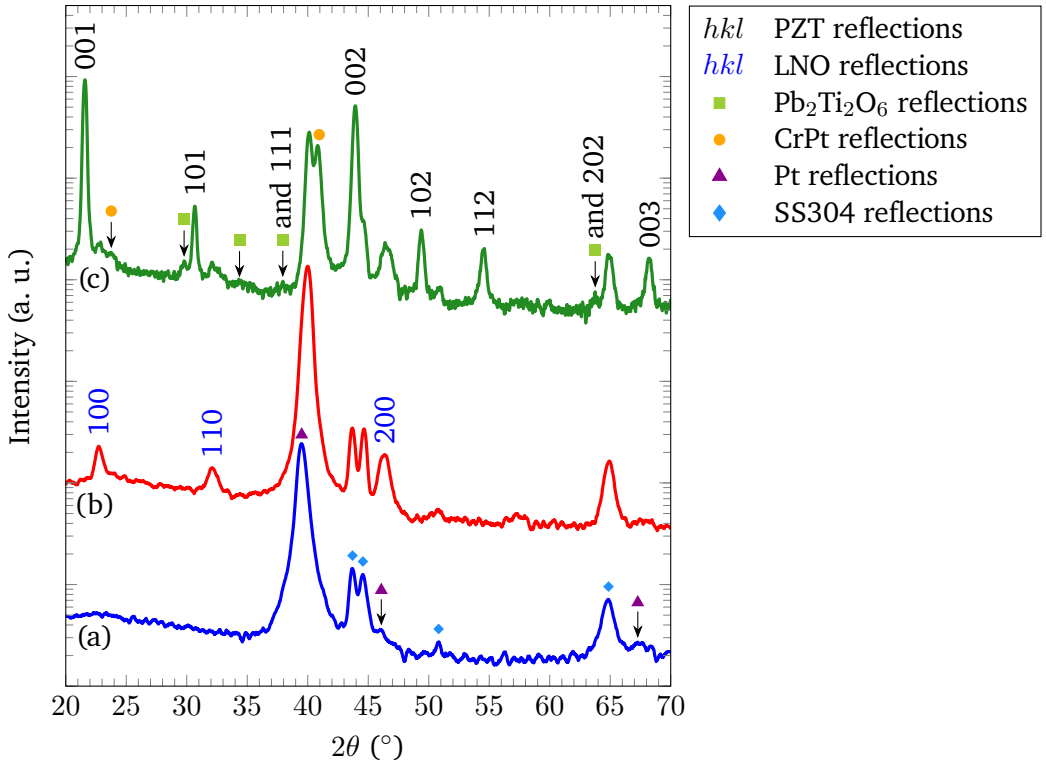

Figure 5.1.: 2θ-θ XRD patterns of (a) an Al_2O_3/Pt/steel sample covered with (b) LNO and (c) PZT layers. The reflections are denoted for the PZT [140] (tetragonal black hkl indexes), LNO [196] (cubic blue hkl indexes) and Pt [240] (purple triangles) layers of the heterostructure, as well as for $Pb_2Ti_2O_6$ [241] (red squares) and CrPt [242] (orange circles) additional phases. The SS304 substrate [243, 244] reflections (green diamonds) are also indicated. The Al_2O_3 layer is amorphous. Adapted from [245].

The PZT thin film presents a perovskite structure with visible reflections from multiple orientations in the XRD pattern, e.g., 011, 101, 111, 102, and 112. The film orientation is predominantly {001} which is confirmed by the calculated Lotgering factor for the PZT thin films [180], ${f_{(00l)}}^{\mathrm{PZT}} = 0.91$. It is noteworthy that, during the deposition of the PZT layer at 650 °C, the chromium present in the SS304 substrate is rejected from the stainless steel solid solution [166]. A consequence of this phenomenon is the formation of an intermetallic compound, CrPt, as can be seen in Figure 5.1 (c). Additionally, low intensity $Pb_2Ti_2O_6$ pyrochlore reflections are also visible in the XRD pattern.

The formation of these additional phases does not prevent the growth of {001}-textured PZT with ${f_{(00l)}}^{\mathrm{PZT}}$ being larger than the Lotgering factor for the LNO layer, ${f_{(00l)}}^{\mathrm{LNO}}$. The latter acts as a growth template [51,55] which is itself {100}-textured, with ${f_{(00l)}}^{\mathrm{LNO}} = 0.68$. In literature, a similar value of ${f_{(00l)}}^{\mathrm{LNO}} = 0.70$ is reported for LNO films grown using a sol-gel method on stainless steel substrates [57].

To dispel any ambiguity regarding the texture of the PZT thin films in spite of the substrate curvature, Electron Backscatter Diffraction (EBSD) and its analysis were performed by Enrico Bruder from the Institute of Materials Science of the Technische Universität Darmstadt (Darmstadt, Germany) on a small area of the sample. On this 3.8 µm by 10 µm area, substrate bending is small and can be neglected. Indeed, the dimensions of the primary electron beam used for the EBSD measurements are much smaller than the X-ray beam used to record the XRD pattern in Figure 5.1.

The resulting pole figure of the PZT thin film is given in Figure 5.2. The reflection with the highest intensity is plotted in red, while the lower intensities are indicated in green and blue hues. Along the {001}-axis, a single reflection can be seen which indicates a strong {001} texture of the PZT thin film, consistent with the high ${f_{(00l)}}^{\mathrm{PZT}} = 0.91$ calculated from the XRD data. As this crystallographic orientation induces a large piezoelectric response in PZT thin films, it is an interesting characteristic for MEMS applications [246].

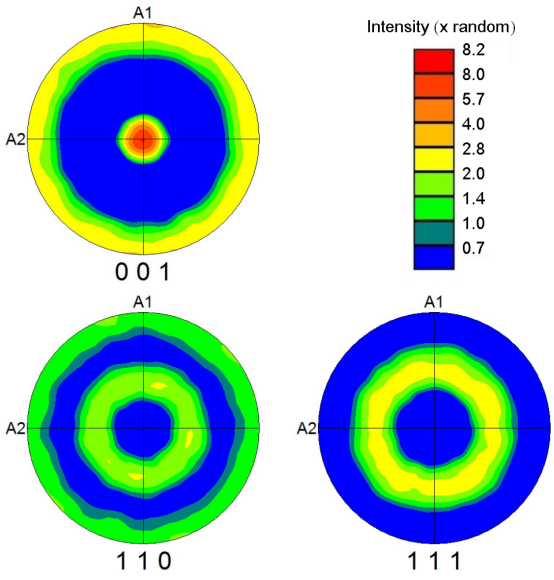

Figure 5.2.: Pole figure of the PZT layer of a PZT/LNO/Al_2O_3/Pt/steel sample by EBSD. A dataset with more than 7,000 indexed grains covering a 3.8 µm by 10 µm area is used to calculate the crystallographic texture using the harmonic series expansion method with a series rank of 24, a Gaussian half width of $5°$, and no enforced symmetry. The colour scale is logarithmic. Data acquisition and analysis by Enrico Bruder. Adapted from [245].

Within the resolution limit of the EBSD, other reflections along the {111}- and {110}-axes cannot be observed, which indicates the absence of other orientations in the PZT thin films. However, it remains possible for a limited number of grains with orientations other than {001} to occur in the investigated samples. Nonetheless, a strong texture is achieved which is a key parameter to improve piezoelectric response, as will be demonstrated in chapter 6.

The surface and cross-section of the sample analysed by EBSD were imaged by Enrico Bruder using the Mira3-XMH high resolution SEM (see section 3.5.3). The SEM images of the PZT film surface and cross-section are depicted in Figure 5.3. Both images are taken in secondary electrons mode, using the in-beam detector for the cross-section.

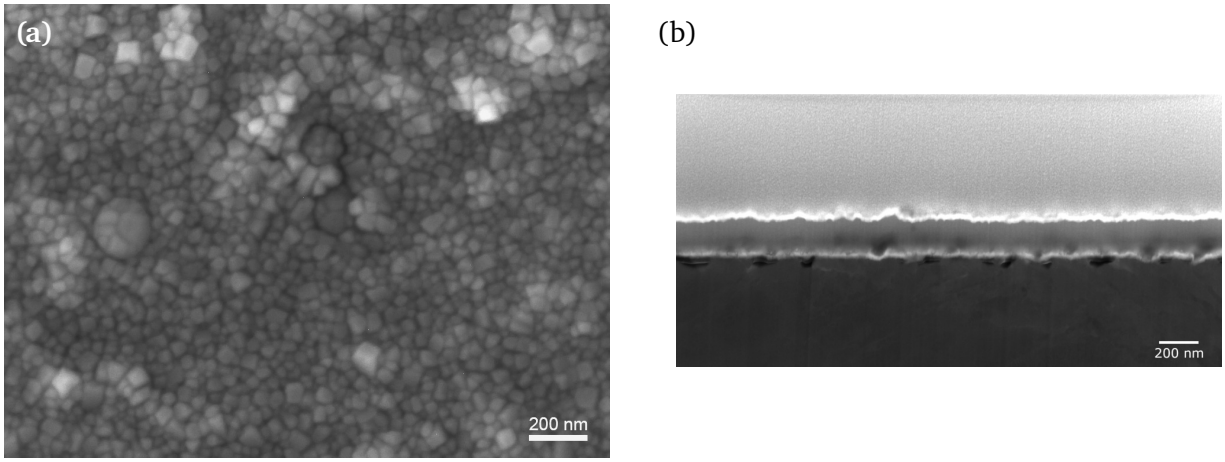

Figure 5.3.: SEM image of (a) the surface and (b) the cross-section of a PZT/LNO/Al_2O_3/Pt/steel sample. The heterostructure layers are ordered from top to bottom in the SEM image. The images are taken using secondary electrons mode and the in-beam detector for the cross-section. Images by Enrico Bruder. Adapted from [245].

The PZT grain size is estimated to be ~ 45.3 nm by the intercept method averaged over 30 measurements from the surface image presented in Figure 5.3 (a). The grain size is mainly homogeneous over the area covered by the SEM image. The grain size calculated from the SEM image is larger than the out-of-plane crystallite size of 30 ± 5 nm. The latter is calculated using the Hall method with the software PDXL 2 v.2.8.4.0 by Rigaku Corporation (Tokyo, Japan) on the $00l$ reflections of the XRD pattern shown in Figure 5.1 [204]. The difference between these dimensions can be attributed to both the film strain and the XRD instrumental error.

Surface pyrochlore phase generally forms small grains of few nanometres in size and located at the grain boundaries [51]. Grains presenting these characteristics are not visible in the SEM image, indicating that the pyrochlore phase observed in the XRD pattern in Figure 5.1 is located in the film depth.

In the cross-section SEM image shown in Figure 5.3 (b), a “veil” effect is visible on the surface which is created by the focused ion beam cutting. Both this effect and the physical resolution limitations of the SEM impede a clear view of the microstructure. Nonetheless, porosities can be observed at the Pt/steel interface. This interface is sensitive to the diffusion of Cr, rejected from the stainless steel during the deposition at 650 °C of the PZT thin film, into the Pt layer, leading to the formation of a CrPt phase, observed in Figure 5.1. It is not possible to observe porosities at the other interfaces.

5.1.3. PZT thin films dielectric and ferroelectric properties

Before *P–E* loop measurements, the 200 nm and 400 nm thick PZT films exhibit a permittivity at 1 kHz of 350 and 349 and a dielectric loss of 4.1 % and 2.6 %, respectively. The instrumental error is of 0.15 %.

The predominantly {001} texture of the PZT films leads to the occurrence of ferroelectric domains with an out-of-plane polarisation, referred to as *c*-domains, which can partially explain the low permittivity values. It has indeed been demonstrated in literature that the permittivity of *c*-domains is lower than the one of *a*-domains with an in-plane polarisation [51, 53].

The dielectric permittivity values of the PZT films, measured at 1 kHz before *P–E* loop measurements, are lower than that reported in literature of ~ 600 for 0.6 µm thick {001}-oriented Nb-doped PZT films on Ni foils [53]. The higher values reported in literature, as compared to the non-doped PZT thin films from *PZT stacks*, are consistent with the effects of Nb-doping. Indeed, domain wall mobility in PZT is enhanced by Nb-doping, leading to increased permittivity [53]. The values reported in this thesis are also significantly lower than these of ~ 780 for 1 µm thick PZT films on Ni foils [51] and ~ 790 for 500 nm thick rhombohedral PZT films on ferritic steel deposited by the sol-gel method [57] which are reported in literature. The difference can be attributed to the presence, even in limited quantities, of pyrochlore phase in the thin films deposited in this work which would also contribute to lower their permittivity.

Nevertheless, the values of permittivity for the {001}-textured PZT thin films deposited in this work are higher than the value of 192 reported in the literature for non-textured films on austenitic stainless steel [64]. Furthermore, the dielectric losses of 4.1 % and 2.6 % for the PZT films in *PZT stacks* is lower than that of 10.2 % reported for those films.

Moreover, it should be noted that the grain size calculated here is relatively small as compared to the values of 63 nm to 192 nm reported in literature for PZT films grown by PLD on various substrates [247]. The density of both grain boundaries and domain walls is increased by small grain sizes which might lower domain wall mobility, hence limiting ferroelectric properties [248]. The reduced thicknesses of the produced PZT films as compared to that of about 1 µm, which is usually reported in the literature [51, 53], might also be the cause of their lower permittivity [249].

For both the 200 nm and 400 nm thick samples, the *P–E* loops are measured at 100 kHz and with a maximum applied field of 200 kV·cm^{-1}. They are presented in Figure 5.4 along with the corresponding switching current versus electrical field hysteresis loops. For each sample, both curves, represented in Figure 5.4 (a) and (b), originate from the same dataset. The 200 nm thick film displays a larger and more rounded hysteresis than the 400 nm thick film for which the polarisation is nearly saturated. The difference can be attributed to the 200 nm thick film reduced thickness, leading to larger leakage.

The positive and negative branches of the 200 nm thick sample *P–E* loop are shaped differently along the polarisation axis; there is higher conduction on the upper branch. In the 400 nm thick PZT film, due to the lower leakage, this phenomenon is less pronounced. Leakage current measurements on a *PZT stack* with a 400 nm thick PZT layer will be presented in the next section.

To improve accuracy, the values of the coercive fields for the 200 nm and 400 nm thick samples are determined from the switching current versus field hysteresis loops in Figure 5.4 (b). The positive and negative coercive fields are the fields corresponding to the switching current peaks. In the case of the 200 nm thick sample, the positive coercive field at 100 Hz is $E_c = 135.9$ kV·cm^{-1} and the displayed internal bias field is $E_{c,shift} = 21.0$ kV·cm^{-1}. The coercive field for the 400 nm thick sample is $E_c = 93.9$ kV·cm^{-1} and its internal bias field is $E_{c,shift} = 12.0$ kV·cm^{-1}.

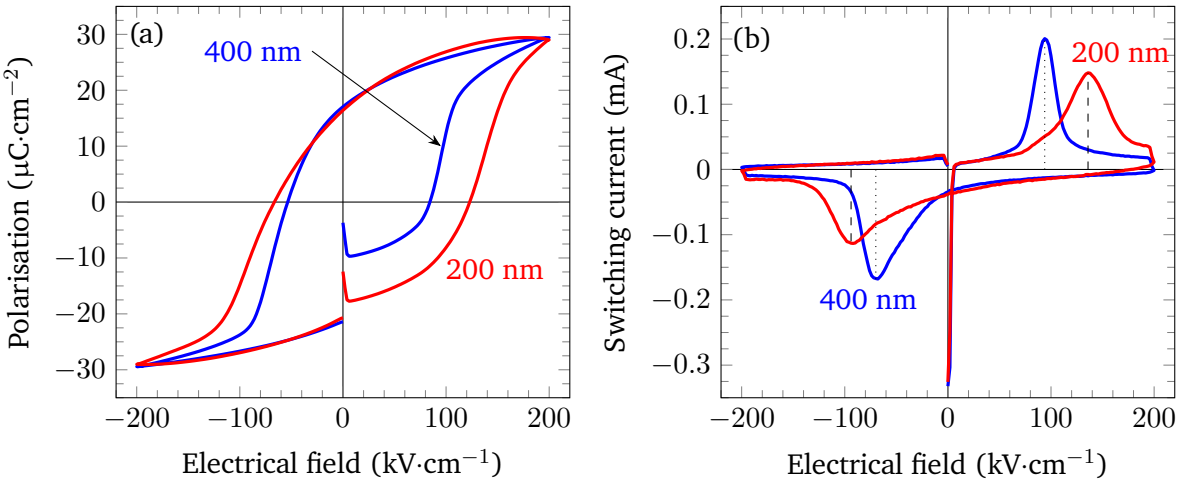

Figure 5.4.: (a) Polarisation, P, versus electrical field, E, hysteresis loops and (b) corresponding switching current versus electrical field hysteresis loops at 100 Hz of 200 nm (red curves) and 400 nm (blue curves) thick PZT layers of PZT/LNO/Al_2O_3/Pt/steel samples, respectively. The dashed and dotted lines indicate the position of the positive and negative coercive fields of 200 nm and 400 nm thick PZT films, respectively. Adapted from [245].

The coercive fields reported in this work for PZT thin films are larger than those of ~ 73 kV·cm^{-1} for 1 μm thick PZT films deposited on Ni foils reported in literature [51]. The presence of an internal bias field causes the asymmetry of the *P-E* loop along the electrical field axis and indicates a preferred polarisation direction [120,211]. Therefore, an external field applied in the opposite direction would result in significant changes in the polarisation [233].

The remanent polarisation, P_r, of the 200 nm and 400 nm thick PZT films after the applied electrical field of 200 kV·cm^{-1} was released is obtained from the *P–E* loops in Figure 5.4 (a). It is of $P_r = 16.7$ μC·cm^{-2} and $P_r = 16.4$ μC·cm^{-2}, respectively.

In *PZT stacks*, both 200 nm and 400 nm thick PZT films show similar remanent polarisation and permittivity values. The major difference between the behaviour of these thin films is the higher leakage in the thinner film, leading to a less saturated *P–E* loop.

5.1.4. Leakage current measurements on *PZT stacks*

In order to identify the leakage current mechanism in the 400 nm thick PZT layer of *PZT stacks* from a virgin top electrode with an area of 0.0327 mm^2, several representations of the DC leakage current density, J, are plotted Figure 5.5. The first representation in Figure 5.5 (a), known as a *J–E* curve, plots the DC leakage current density as a function of the positive and negative applied electrical field.

The *J–E* curve can be fitted with polynomial functions of the electrical field for the positive and negative polarities, $J \propto E^{3.15}$ and $J \propto E^{3.12}$, respectively. These functions are attributed to a Space-Charge Limited Current (SCLC) mechanism with trap filling which is described by $J \propto E^N$ with $N > 2$ [235, 250].

For both polarities, the leakage current density is similar. With regard to the rounded shape of the *P–E* loops in Figure 5.4 (a), the presence of leakage in the PZT thin films is coherent, particularly for the thinner

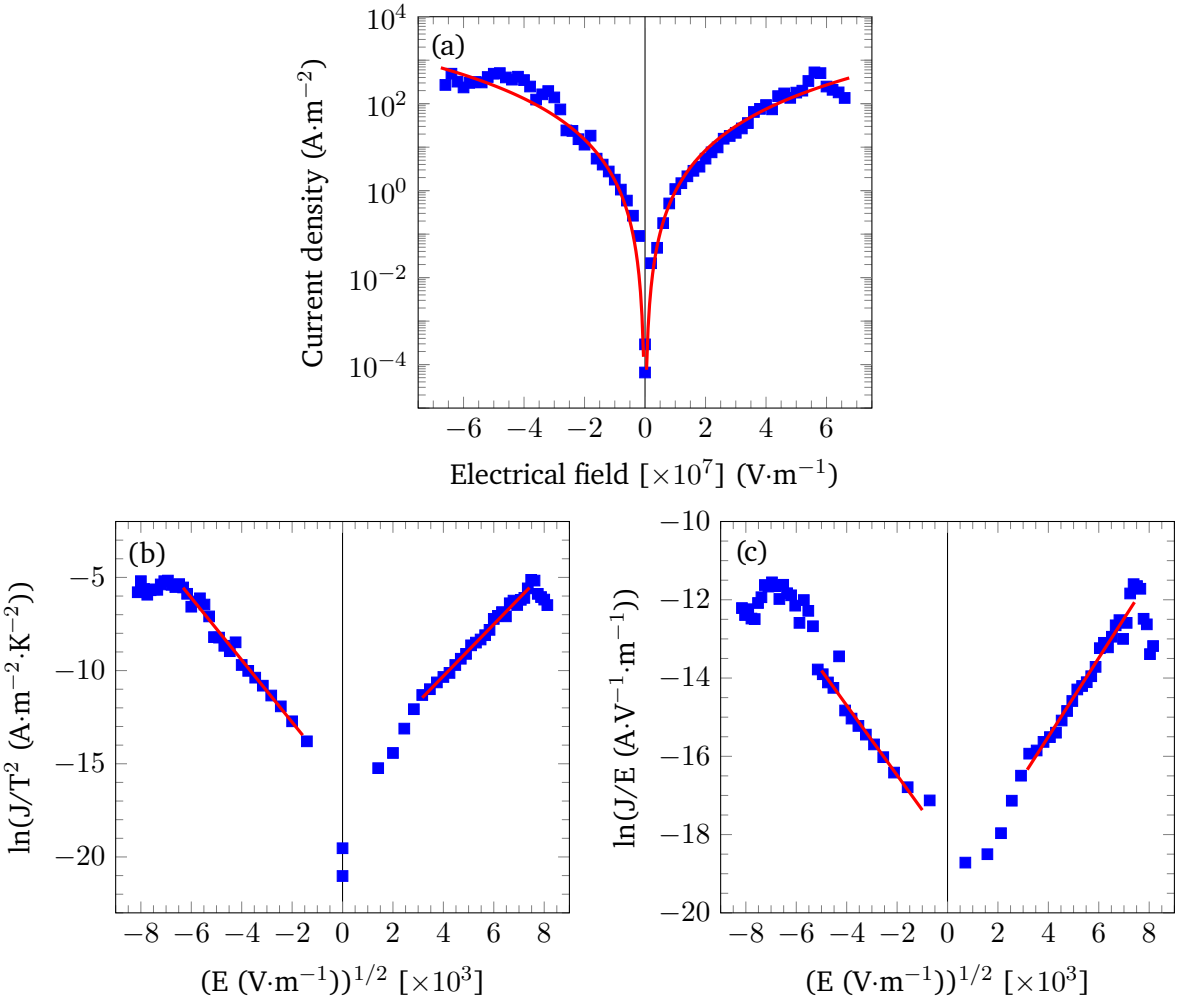

Figure 5.5.: Leakage current density, J, as a function of the applied electrical field, E, for the 400 nm thick PZT layer of a PZT/LNO/Al_2O_3/Pt/steel sample (blue squares) (a) fitted within the space-charge limited current scenario with the polynomial functions $J \propto E^{3.15}$ for the positive polarity and $J \propto E^{3.12}$ for the negative polarity (red curves), (b) plotted for the Schottky emission scenario with a linear fit (red lines) between 100 kV·cm^{-1} and 550 kV·cm^{-1} for the positive polarity and between -400 kV·cm^{-1} and -25 kV·cm^{-1} for the negative polarity, (c) plotted for the Poole-Frenkel emission scenario with a linear fit (red lines) between 100 kV·cm^{-1} and 550 kV·cm^{-1} for the positive polarity and between -250 kV·cm^{-1} and -10 kV·cm^{-1} for the negative polarity. Adapted from [245].

200 nm thick film. However, as the SCLC fit of the *J*–*E* curve in Figure 5.5 (a) is not perfect, it indicates the potential contributions of other physical mechanisms in the leakage transfer through the PZT film. Therefore, in addition to the SCLC mechanism, the DC leakage current density is fitted according to Schottky emission and to Poole-Frenkel emission in Figure 5.5 (b) and (c), respectively.

Under the hypothesis of Schottky emission, the current density can be expressed as [235]:

$$J = A^{*}T^{2}exp\left[\frac{-q\left(\phi_B - \sqrt{qE/4\pi\varepsilon_{r,optical}\varepsilon_0}\right)}{k_{\mathrm{B}}T}\right], \tag{5.1}$$

where A^{*} is the effective Richardson constant, T is the absolute temperature, q is the electronic charge, $q\phi_B$ is the Schottky barrier height, $\varepsilon_{r,optical}$ is the optical dielectric constant, and k_{B} is the Boltzmann constant.

In consequence, by plotting the *J-E* measurements as $ln\left(J/T^2\right)$ versus $E^{1/2}$, the optical dielectric constant under the hypothesis of Schottky emission can be calculated from the slope of the linear region. It is expressed as:

$$\varepsilon_{r,optical} = \frac{q^3}{4\pi\varepsilon_0(slope \cdot k_{\mathrm{B}}T)^2}, \tag{5.2}$$

and the optical refractive index, $n_{optical} = \sqrt{\varepsilon_{r,optical}}$, can be estimated from this slope.

On the plot of $ln\left(J/T^2\right)$ versus $E^{1/2}$ presented in Figure 5.5 (b), linear fits are represented. Under the hypothesis of Schottky emission, at room temperature ($T = 298$ K), for the positive polarity, the fitting between 100 kV·cm^{-1} and 550 kV·cm^{-1} has a slope absolute value of $1.4 \cdot 10^{-3}$ with a linear fit coefficient $R^2 = 0.987$. The corresponding refractive index is $n_{optical,Schottky} = 1.06$. For the negative polarity, the linear fit between -250 kV·cm^{-1} and -10 kV·cm^{-1} presents a slope absolute value of $1.7 \cdot 10^{-3}$ with $R^2 = 0.977$. The corresponding refractive index is $n_{optical,Schottky} = 0.88$.

The theoretical refractive index of PZT 52/48 is $n_{optical,th} = 2.2 - 2.7$ [251]. Therefore, the Schottky emission hypothesis cannot be validated for the PZT layer of *PZT stacks* as the refractive indexes obtained in this work by applying this hypothesis are less than half the value of $n_{optical,th}$.

Under the hypothesis of Poole-Frenkel emission, the current density is expressed by [235]:

$$J = q\mu_{elec}N_C Eexp\left[\frac{-q\left(\phi_T - \sqrt{qE/\pi\varepsilon_{r,optical}\varepsilon_0}\right)}{k_{\mathrm{B}}T}\right], \tag{5.3}$$

with μ_{elec} the electronic drift mobility, N_C the density of states in the conduction band and $q\phi_T$ the trap energy level.

Therefore, the optical dielectric constant under the hypothesis of Poole-Frenkel emission can be calculated from the slope of the linear region when plotting $ln\left(J/E\right)$ versus $E^{1/2}$ with:

$$\varepsilon_{r,optical} = \frac{q^3}{\pi\varepsilon_0(slope \cdot k_{\mathrm{B}}T)^2}, \tag{5.4}$$

and the refractive index can be estimated.

On the plot of $ln\left(J/E\right)$ versus $E^{1/2}$ given in Figure 5.5 (c), linear fits are indicated. Under the hypothesis of Poole-Frenkel emission, for the positive polarity, the linear fit between 100 kV·cm^{-1} and 550 kV·cm^{-1} presents a slope absolute value of $1.0 \cdot 10^{-3}$ with a linear fit coefficient $R^2 = 0.973$. The corresponding refractive index is $n_{optical,Poole-Frenkel} = 2.92$. For the negative polarity, the fitting between 10 kV·cm^{-1} and 250 kV·cm^{-1} has a slope absolute value of $8.9 \cdot 10^{-4}$ with $R^2 = 0.945$. The corresponding refractive index is $n_{optical,Poole-Frenkel} = 3.31$.

The optical dielectric constants for the PZT layer under the hypothesis of Poole-Frenkel emission are slightly larger than $n_{optical,th}$ and, therefore, the hypothesis can be neither validated nor dismissed.

While the conduction mechanism in the PZT thin films deposited in this work is not predominantly interface driven, the interfaces between the PZT layer and the electrodes, influenced by the electrode materials, impact on leakage current. This is particularly pronounced on the thinner 200 nm thick film. If the Schottky emission hypothesis gives a refractive index incoherent with literature values for $PbZr_{0.52}Ti_{0.48}O_3$, the Poole-Frenkel emission hypothesis, contrarily, remains a possibility. Nevertheless, the hypothesis of a SCLC mechanism with trap filling is the most likely to occur of the conduction mechanisms studied in this work.

5.2. {001}-textured PNZT thin films: improving the properties

In the previous section, **predominantly {001}-textured $PbZr_{0.52}Ti_{0.48}O_3$ thin films have been deposited on stainless steel substrates by PLD**. The films low dielectric constant and high coercive fields indicate their potential as transducer applications. **In order to improve the ferroelectric properties achieved with the *PZT stacks*, series of *PNZT stacks* are deposited to study the impact of several deposition parameters, as well as film thickness influence**. Increased dielectric constants and lower coercive fields are expected from the 2 mol.% Nb-doping of PZT 52/48 (see section 2.2.1). As key parameters to control the evaporation of PbO during the growth of PNZT by PLD, substrate temperature and O_2 pressure are varied between 600 °C and 700 °C and from 5.0 Pa to 10.0 Pa, respectively.

Preliminaries studies have shown that the laser repetition rate of 10 Hz previously employed for the *PZT stacks* leads to the presence of a Pb phase in the films. Originating from the 10 mol.% excess PbO included in the PNZT target to hinder the formation of a pyrochlore phase during deposition (see section 2.2.1), the formation of the Pb phase can be avoided by lowering the laser repetition rate. However, this introduces a strong reflection of the pyrochlore phase in the XRD patterns of the films. Additional preliminaries studies established that the presence of pyrochlore phase in PZT thin films can be avoided if the deposition temperature is superior or equal to 650 °C. Below this temperature, PZT and pyrochlore phases coexist in the films. It should be noted that Nb-doping of the PZT thin films, while improving the piezoelectric response, might tends to stabilise the formation of a pyrochlore phase [146, 154].

Therefore, to both avoid the formation of a Pb phase and limit the presence of a pyrochlore phase, the initial deposition parameters for *PNZT stacks* have been chosen at 700 °C for the deposition temperature and of 4 Hz for the laser repetition rate, respectively higher and lower than for *PZT stacks*.

As for the *PZT stacks*, dielectric and ferroelectric characterisations have been performed on *PNZT stacks*. Additionally, $e_{31,f}$ piezoelectric coefficients, which could not be measured on the *PZT stacks* due to the presence of silver paste on the back of the samples (see section 3.1), have been measured on the *PNZT stacks*. The possibility to perform these measurements is enabled by the utilisation of a modified flag style holder, designed specifically to hold samples during LNO deposition and argon ion milling processes (see section 3.1).

5.2.1. Influence of O_2 deposition pressure on ferroelectric properties

The patterns obtained by XRD analysis of PNZT/LNO/Al_2O_3/steel heterostructures with PNZT layers deposited under 5.0 Pa, 6.5 Pa, 8.0 Pa and 10.0 Pa of O_2 are shown in Figure 5.6 (a). The PNZT reflections, assimilated to those of PZT, and the $Pb_2Ti_2O_6$ reflections both appear during the deposition of the PNZT layer.

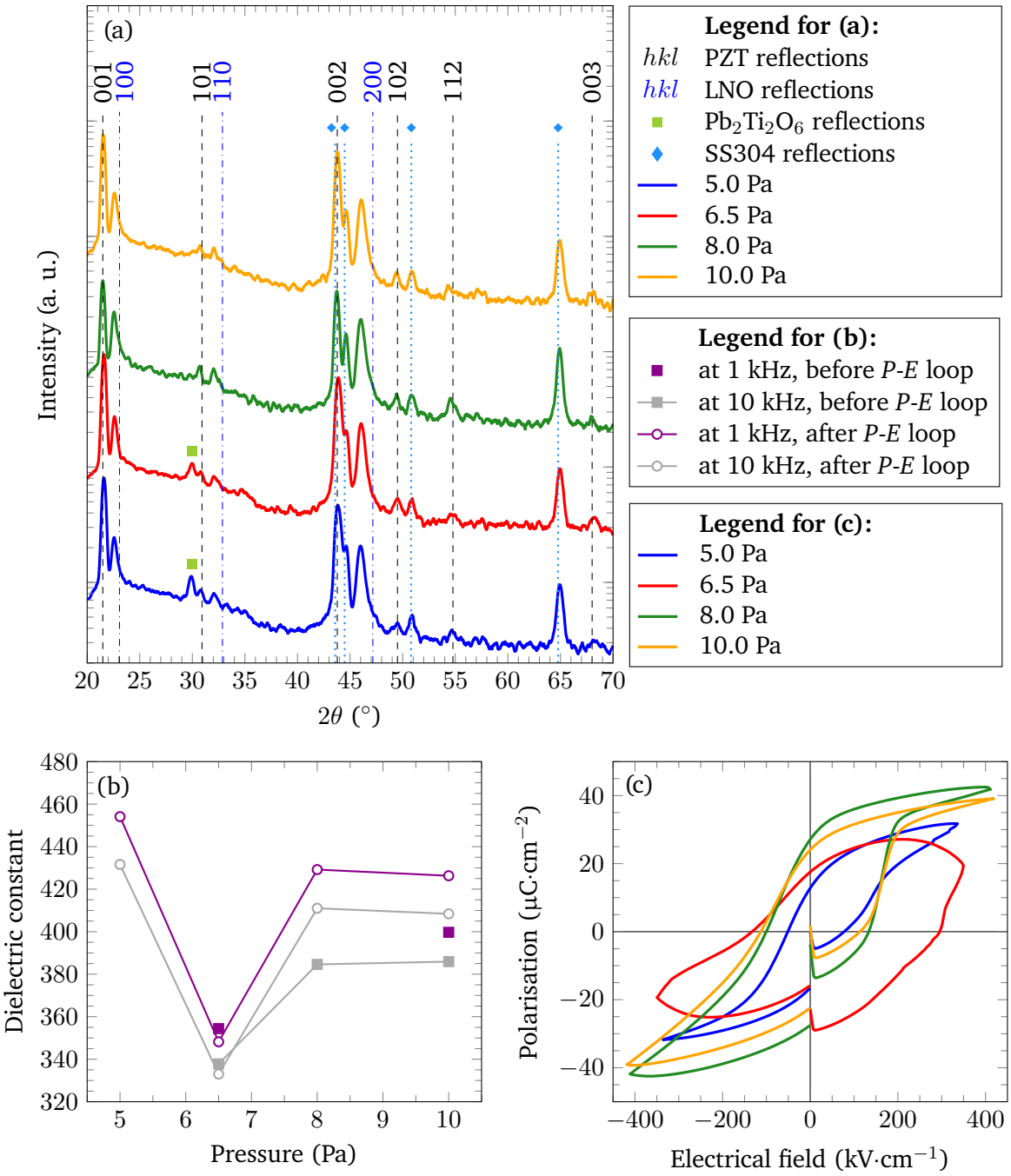

Figure 5.6.: Effect of PNZT O_2 deposition pressure on *PNZT stacks* with $\sim 170 - 208$ nm thick PNZT layers on (a) 2θ-θ XRD patterns with reflections denoted for PZT [140] (tetragonal black hkl indexes), LNO [196] (cubic blue hkl indexes) and SS304 [243, 244] (light blue diamonds) as well as for $Pb_2Ti_2O_6$ [241] (light green squares) additional phase, the Al_2O_3 layer being amorphous, (b) values of PNZT dielectric constant, ε_r, at 1 kHz (purple marks) and at 10 kHz (grey marks) with $V_{AC} = 30$ mV before (closed squares) and after (open circles) measuring *P-E* loops, (c) PNZT polarisation, P, versus electrical field, E, hysteresis loops at 100 Hz. In (a) and (c), PNZT O_2 deposition pressures of 5.0 Pa, 6.5 Pa, 8.0 Pa and 10.0 Pa are represented by the blue, red, green and orange curves, respectively.

As for the PZT thin films discussed in section 5.1.2, the PNZT films present a perovskite structure and are predominantly {001}-oriented despite visible reflections from multiple orientations in the XRD pattern. Contrary to the PZT thin films, the 111 reflection is absent from the XRD pattern. The predominantly {001} orientation is indicated by the Lotgering factors of the PNZT layers which, while slightly lower than ${f_{(00l)}}^{\text{PZT}} = 0.91$ from section 5.1.2, remain high, ranging between ${f_{(00l)}}^{\text{PNZT}} = 0.82$ and ${f_{(00l)}}^{\text{PNZT}} = 0.89$.

It is suggested that the lower PNZT Lotgering factors originate not from a lower quality of the LNO seed layer but from the PNZT layer itself, either due to the Nb doping or to non-optimised deposition parameters. Indeed, the LNO Lotgering factor for *PNZT stacks* ranges from ${f_{(00l)}}^{\text{LNO}} = 0.72$ to ${f_{(00l)}}^{\text{LNO}} = 0.84$ which is higher than the value of ${f_{(00l)}}^{\text{LNO}} = 0.68$ reported in this work for *PZT stacks*. The improvement is attributed to the absence of the Pt buffer layer in *PNZT stacks* which was forming an intermetallic phase with Cr from the stainless steel substrate in *PZT stacks*. It is considered that this CrPt phase was hindering the oriented growth of the LNO layer. It should be noted that the LNO Lotgering factor achieved for *PNZT stacks* is larger than the value of ${f_{(00l)}}^{\text{LNO}} = 0.70$ reported in literature on stainless steel substrates using a sol-gel method [57].

Additionally, $Pb_2Ti_2O_6$ reflections are visible in the XRD patterns of the PNZT films deposited under an O_2 pressure of 5.0 Pa and 6.5 Pa. This is not the case for the thin films deposited under 8.0 Pa and 10.0 Pa of O_2, indicating that the last two O_2 deposition pressures could be suitable parameters for the growth of PNZT by PLD, producing a limited amount of pyrochlore phase which cannot be detected by XRD.

To determine the appropriate O_2 deposition pressure, further measurements are conducted on the PNZT thin films. Figure 5.6 (b) gives the values of PNZT dielectric constant at 1 kHz and at 10 kHz with $V_{AC} = 30$ mV before and after measuring *P-E* loops at 100 Hz which are represented in Figure 5.6 (c). For each sample, the permittivity and *P-E* loop measurements shown in Figure 5.6 are performed on the same electrode. To facilitate comparison of the results, all electrodes are chosen with an area of 0.0327 mm^2, at the exception of the sample deposited under 5.0 Pa of O_2 for which this size of electrode is not available for measurement and, therefore, a 0.1252 mm^2 electrode is selected.

Concerning PNZT dielectric constant, no clear trends emerge as a function of the O_2 deposition pressure, neither before or after measuring *P-E* loops. This phenomenon can partly be explained by the absence of data for samples deposited under 5.0 Pa and 8.0 Pa of O_2 before measuring *P-E* loops due to important dielectric losses, larger than 10 %. It is further illustrated in Table 5.1 which summarises the average values and standard deviations of both dielectric constant and loss depending on the O_2 deposition pressure at 1 kHz and at 10 kHz with $V_{AC} = 30$ mV before measuring *P-E* loops. Data are collected from a selection of four electrodes which comprises two 0.0327 mm^2, one 0.1252 mm^2 and one 0.2828 mm^2 electrodes. Should there be electrodes with a dielectric loss superior to 10 % on the sample, they are not taken into account. Due to the limited number of electrodes analysed in this work, Table 5.1 also indicates minimal and maximal values to give a more accurate representation of the samples.

Compared with the permittivity of 350 for the 200 nm thick PZT thin films at 1 kHz before measuring *P-E* loops discussed in section 5.1.3, the average dielectric constant of the PNZT films under the same conditions is higher at 354.4, 391.6 and 424.3 for O_2 deposition pressures of 6.5 Pa, 8.0 Pa and 10.0 Pa, respectively. It is noteworthy that the minimal values of permittivity for PNZT films deposited under 8.0 Pa and 10.0 Pa of O_2 are higher than the values reported in this work for PZT. This permittivity increase can be attributed to the Nb-doping of PZT [53, 146, 151] and, at higher O_2 deposition pressures, to the absence or limited amount of pyrochlore phase in the PNZT thin films.

Under these conditions, the PNZT thin films deposited under 6.5 Pa, 8.0 Pa and 10.0 Pa of O_2 have average dielectric losses of 8.6 %, 5.9 % and 4.1 %, respectively. This is globally higher than the 4.1 % reported in

Table 5.1.: Effect of PNZT O_2 deposition pressure on *PNZT stacks* with $\sim 170 - 208$ nm thick PNZT layers on their dielectric constant, ε_r, and loss values at 1 kHz and at 10 kHz with $V_{AC} = 30$ mV before *P-E* loop measurements. Minimum, average, maximum and standard deviation values are indicated. When only one electrode could be measured, the single value is given as the average.

O_2 pressure (Pa)		**5.0**		**6.5**		**8.0**		**10.0**	
Measured at		1 kHz	10 kHz	1 kHz	10 kHz	1 kHz	10 kHz	1 kHz	10 kHz
Dielectric constant	Minimum	-	-	-	-	-	376.4	399.7	385.9
	Average	-	-	354.4	337.8	391.6	388.6	424.3	408.7
	Maximum	-	-	-	-	-	404.9	448.9	432.4
	Standard deviation	-	-	-	-	-	12.0	24.6	17.1
Dielectric loss (%)	Minimum	-	-	-	-	-	3.1	2.8	2.6
	Average	-	-	8.6	3.6	5.9	5.7	4.1	4.8
	Maximum	-	-	-	-	-	7.2	5.3	8.1
	Standard deviation	-	-	-	-	-	0.4	1.3	2.0

this thesis for the 200 nm thick PZT sample and can be an effect of Nb-doped on PZT [98]. It is suggested that the increased dielectric losses are linked to the presence of more defects in the crystalline structure. This hypothesis is consistent with the less pronounced {001} orientation of the PNZT layers compared to that of the PZT thin films, as indicated by their respective Lotgering factors.

Moreover, an important feature of Figure 5.6 (b) is the increase of the dielectric constant after *P-E* loops are measured for the samples deposited under 8.0 Pa and 10.0 Pa of O_2, reaching 429.2 and 426.3 at 1 kHz, respectively. This aspect will be discussed in section 5.2.4.

The analysis of PNZT thin films dielectric constants as a function of their O_2 deposition pressures being insufficient to indicate an optimal choice of deposition parameter, their ferroelectric characteristic values provide additional insight. From Figure 5.6 (c), it appears that the PNZT layer deposited under 6.5 Pa of O_2 presents a rounded *P-E* loop without clear saturation, characteristic of a thin film with significant leakage. This is sensible with the presence of a pyrochlore phase in this thin film as well as with the reduced dielectric constant of 354 at 1 kHz coupled with a dielectric loss of 8.6 %.

On the other hand, PNZT thin films deposited under 5.0 Pa, 8.0 Pa and 10.0 Pa of O_2 exhibit well defined *P-E* loops with marked saturation, characteristic of ferroelectrics. Similar to the behaviour of the *PZT stacks*, the positive and negative branches of the *P-E* loops are asymmetrical along the polarisation and the electrical field axes. The values of remanent polarisation, saturation polarisation, coercive field and internal bias field are given in Table 5.2. The coercive fields values are determined from the switching current versus field hysteresis loops, with the same methodology as in section 5.1.3 where the positive and negative coercive fields are the fields corresponding to the switching current peaks. To determine the ferroelectric characteristic values *P-E* loops with the same maximum applied voltage are selected for all

samples in the series. This allows for comparable data between samples.

Table 5.2.: Effect of PNZT O_2 deposition pressure on *PNZT stacks* with $\sim 170 - 208$ nm thick PNZT layers on their ferroelectric characteristic values obtained from a *P-E* loop measured at 100 Hz with a maximum applied voltage of 7 V ($337 - 412$ kV·cm^{-1}). Remanent polarisation, P_r, saturation polarisation, P_{sat}, coercive field, E_c, and internal bias field, $E_{c,shift}$, values are indicated with their respective minimum, average, maximum and standard deviation values. The electrodes measured are the same as in Table 5.1. When only one electrode could be measured, the single value is given as the average.

O_2 pressure (Pa)		**5.0**	**6.5**	**8.0**	**10.0**
P_r (μC·cm^{-2})	Minimum	12.8	-	27.1	19.5
	Average	23.6	17.5	28.4	23.5
	Maximum	34.3	-	29.7	27.1
	Standard deviation	10.8	-	1.3	2.9
P_{sat} (μC·cm^{-2})	Minimum	27.7	-	36.8	28.4
	Average	46.0	24.6	38.9	31.4
	Maximum	64.2	-	41.0	33.7
	Standard deviation	18.3	-	2.1	1.9
E_c (kV·cm^{-1})	Minimum	141.2	-	160.3	163.2
	Average	141.2	-	162.4	164.2
	Maximum	141.2	-	164.4	167.3
	Standard deviation	0.0	-	2.1	1.8
$E_{c,shift}$ (kV·cm^{-1})	Minimum	42.0	-	43.1	41.8
	Average	42.0	-	44.2	48.2
	Maximum	42.0	-	45.3	52.4
	Standard deviation	0.0	-	1.1	4.0

The PNZT thin film deposited under 5.0 Pa of O_2 shows large standard deviations relative to its P_r and P_{sat} values, 8 to 9 times larger than for the film deposited under 8.0 Pa of O_2. It is consistent with the presence of a pyrochlore phase in the former sample which generates inhomogeneities in the PNZT thin film during its nucleation [146]. Contrarily, the films grown under 8.0 Pa and 10.0 Pa of O_2 present low standard deviation values, which is expected in homogeneous samples from material properties independent of electrode area.

The highest average values of remanent and saturation polarisation are both associated with the PNZT thin film deposited under 8.0 Pa of O_2 with $P_r = 28.4$ μC·cm^{-2} and $P_{sat} = 38.9$ μC·cm^{-2}. The remanent polarisation is 1.7 times larger than for the 200 nm thick film discussed in section 5.1.3 which is both promising for MEMS applications and consistent with the effect of 2 mol.% of Nb-doping reported in

literature [154]. However, it should be noted that the remanent polarisation of PNZT thin films was obtained after the release of an applied electrical field of 412 kV·cm^{-1}, about twice larger than the applied field of 200 kV·cm^{-1} employed for the PZT films in section 5.1.3, which might lead to a larger ferroelectric response by switching a larger number of ferroelectric domains.

A better assessment of the remanent polarisation can be obtained by comparison with the value of ~ 39.5 μC·cm^{-2} reported in literature for 600 nm thick PNZT films on Ni foils after the release of a 900 kV·cm^{-1} applied field, i.e. a value 1.4 times higher than for the PNZT thin films deposited in this work for an applied field more than twice larger [53]. Furthermore, 500 nm thick rhombohedral PZT films on ferritic steel and 1 μm thick PZT films on Ni foils display remanent polarisations of 41.5 μC·cm^{-2} and ~ 36 μC·cm^{-2}, i.e. only 1.5 and 1.3 times higher than the value reported in this thesis for applied fields at least 2.4 times larger, respectively [51, 57]. Therefore, the PNZT thin films deposited in this work on stainless steel substrates by PLD present encouraging values of remanent polarisation, indicating both a good ferroelectric response and a limited amount of back switching from the saturation polarisation.

The average positive coercive field, E_c, and internal bias field, $E_{c,shift}$, obtained from a *P-E* loop measured at 100 Hz range from $E_c = 141.2$ kV·cm^{-1} to $E_c = 167.3$ kV·cm^{-1} and between $E_{c,shift} = 42.0$ kV·cm^{-1} and $E_{c,shift} = 48.2$ kV·cm^{-1}, respectively, for the PNZT thin films deposited under 5.0 Pa, 8.0 Pa and 10.0 Pa of O_2. The coercive field of the sample deposited under 6.5 Pa of O_2 cannot be determined since its switching current versus field hysteresis loop does not show a marked switching current peak. The coercive field of the PNZT layer is slightly larger than the one of the 200 nm thick PZT thin film discussed in section 5.1.3 while its internal bias field is approximately twice larger. This increase is consistent with literature reports of similar E_c values between 2 mol.% Nb-doped and undoped PZT thin films [154]. It is also suggested that the comparatively high dielectric losses reported in this work for the PNZT thin films hinder efficient ferroelectric switching, leading to higher coercive fields.

The O_2 deposition pressure of $Pb_{0.99}\square_{0.01}(Zr_{0.52}Ti_{0.48})_{0.98}Nb_{0.02}O_3$ thin films in *PNZT stacks* impacts their composition and ferroelectric properties. Higher O_2 pressures of 8.0 Pa and above are necessary to limit the amount of pyrochlore phase below levels detectable in XRD patterns. The thin film deposited under 8.0 Pa of O_2 shows a good permittivity and tolerable dielectric loss while exhibiting the largest remanent and saturation polarisation of the series. Therefore, an O_2 deposition pressure of 8.0 Pa is selected for further experiments.

5.2.2. Influence of deposition temperature on ferroelectric properties

Figure 5.7 (a) presents the XRD patterns for 170 nm thick PNZT thin film deposited at temperatures of 600 °C, 650 °C, 675 °C and 700 °C within *PNZT stacks*.

The PNZT reflections, assimilated to those of PZT, appear during the deposition of the PNZT thin films, along with the $Pb_2Ti_2O_6$ and Pb reflections. The perovskite structure and the predominant {001} texture of the PNZT thin films reported in section 5.2.1 are confirmed by the XRD patterns. The 111 reflection remains absent from the XRD pattern of the PNZT layers.

At a deposition temperature of 600 °C, additional reflections of both $Pb_2Ti_2O_6$ and Pb phases are visible on the XRD pattern. The presence of these additional phases hinders the {001} texture of the thin film and is accompanied by a small Lotgering factor of ${f_{(00l)}}^{\text{PNZT}} = 0.72$. More elevated temperatures of 650 °C and 675 °C prevent the formation of a Pb phase but not of a pyrochlore phase. The associated Lotgering factors are ${f_{(00l)}}^{\text{PNZT}} = 0.79$ and ${f_{(00l)}}^{\text{PNZT}} = 0.88$, respectively. The thin film grown at 700 °C is the same sample

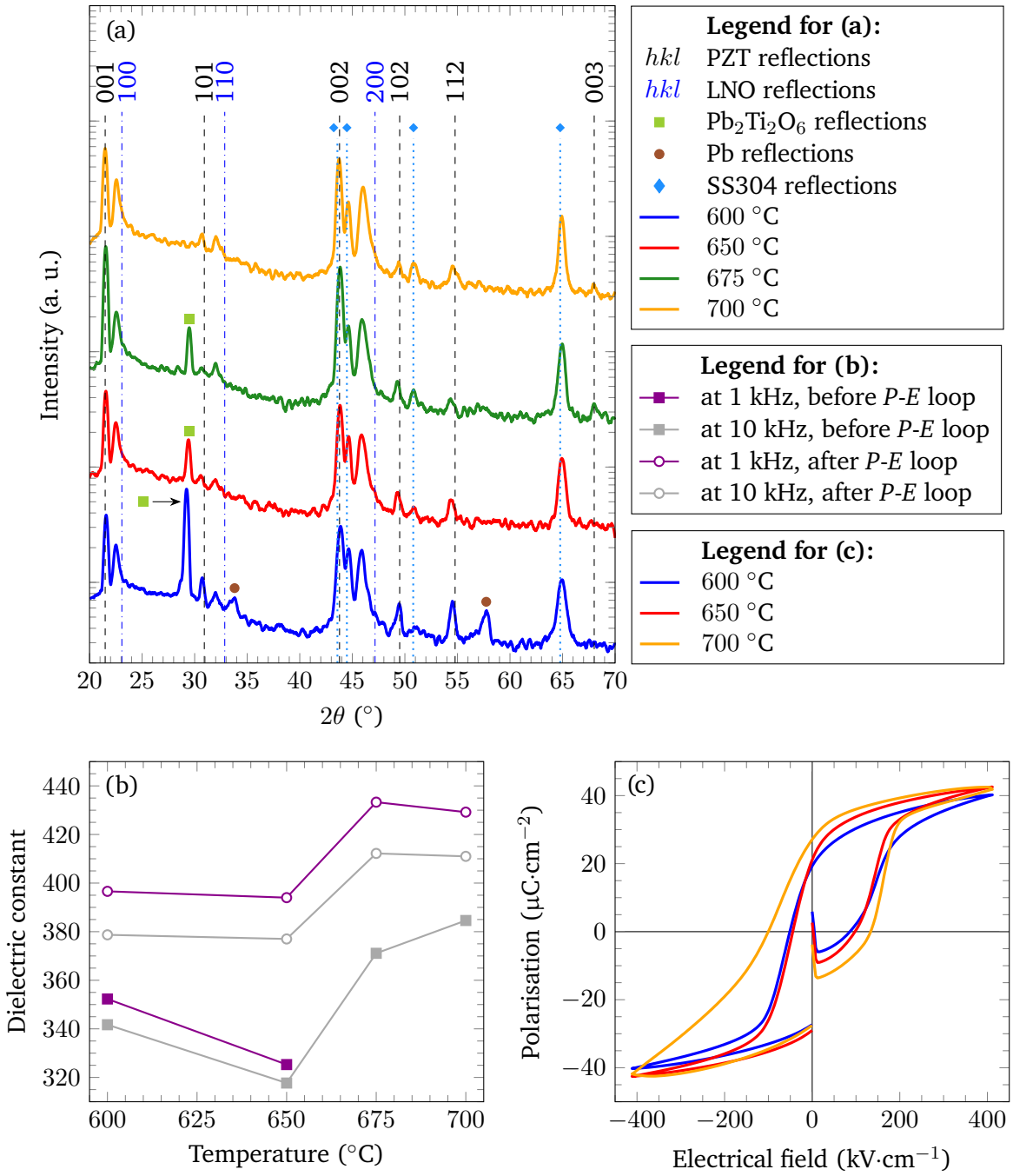

Figure 5.7.: Effect of PNZT deposition temperature on *PNZT stacks* with 170 nm thick PNZT layers on (a) 2θ-θ XRD patterns with reflections denoted for PZT [140] (tetragonal black hkl indexes), LNO [196] (cubic blue hkl indexes) and SS304 [243, 244] (light blue diamonds) as well as for $Pb_2Ti_2O_6$ [241] (light green squares) and Pb [252] (brown circles) additional phases, the Al_2O_3 layer being amorphous, (b) values of PNZT dielectric constant, ε_r, at 1 kHz (purple marks) and at 10 kHz (grey marks) with $V_{AC} = 30$ mV before (closed squares) and after (open circles) measuring *P-E* loops, (c) PNZT polarisation, P, versus electrical field, E, hysteresis loops at 100 Hz. In (a) and (c), PNZT deposition temperatures of 600 °C, 650 °C, 675 °C and 700 °C are represented by the blue, red, green and orange curves, respectively.

as the one previously included in the deposition pressure series and standing for deposition under 8.0 Pa of O_2. Its Lotgering factor is ${f_{(00l)}}^{\text{PNZT}} = 0.82$ and no additional phases can be observed in its XRD pattern.

The presence of a pyrochlore phase competing with the PNZT phase at lower deposition temperatures is consistent with preliminaries studies performed on PZT thin films (see introduction of section 5.2). The 222 $Pb_2Ti_2O_6$ reflection being more intense than the 001 reflection of PZT in the XRD pattern of the film deposited at 600 °C, contrary to the XRD patterns of the films deposited at 650 °C and 675 °C, confirms this trend. The concomitant formation of a pyrochlore phase, characteristic of lead loss [24], and of a Pb phase, indicating an excess of lead, hints towards kinetics at the film surface with a substrate temperature of 600 °C being inadequate to the growth of PNZT.

Similar to the results reported in section 5.2.1, LNO Lotgering factor ranges from ${f_{(00l)}}^{\text{LNO}} = 0.73$ to ${f_{(00l)}}^{\text{LNO}} = 0.84$, larger than literature values [57].

Dielectric permittivity measurements at 1 kHz and at 10 kHz with $V_{AC} = 30$ mV are conducted on the deposition temperature series of PNZT thin films before and after measuring *P-E* loops and results are given in Figure 5.7 (b). The polarisation versus electrical field hysteresis loops acquired at 100 Hz are represented in Figure 5.7 (c). For each sample, the dielectric constant and *P-E* loop measurements in Figure 5.7 are performed on the same electrode. To facilitate comparison of the results, all electrodes are selected with an area of 0.0327 mm^2.

Regarding PNZT permittivity values, there is a slight trend indicating that dielectric constant at 10 kHz before *P-E* loops increases from ~ 330 to ~ 370 with deposition temperature. This effect is most likely linked with the presence of additional phases in the thin films, notably $Pb_2Ti_2O_6$ pyrochlore at lower deposition temperatures. A similar trend is observed at 1 kHz and 10 kHz after *P-E* loop measurements and is also noticeable in Table 5.3 compiling the average values and standard deviations of dielectric constant and loss as a function of the deposition temperature at 1 kHz and 10 kHz with $V_{AC} = 30$ mV before measuring *P-E* loops. In the same manner as for the O_2 deposition pressure series, data are collected from a set of four electrodes which comprises two 0.0327 mm^2, one 0.1252 mm^2 and one 0.2828 mm^2 electrodes. Should there be electrodes with a dielectric loss superior to 10 % on the sample, they are not taken into account. Due to the limited number of electrodes analysed in this work, Table 5.3 also gives minimal and maximal values to allow a more accurate representation of the samples.

The dielectric constant average values at 1 kHz and 10 kHz before measuring *P-E* loops are largest for the sample deposited at 700 °C and previously discussed in section 5.2.1. It should be noted that both the minimal and maximal values of permittivity follow the same trend. The standard deviation values are moderate except for the sample deposited at 600 °C which contains pyrochlore and Pb additional phases, creating inhomogeneities during the PNZT film nucleation [146]. The absence of data for the sample deposited at 675 °C is due to important dielectric losses, larger than 10 %.

The average dielectric losses at 1 kHz of the PNZT thin films deposited at 600 °C, 650 °C and 700 °C are of 2.8 %, 1.7 % and 5.9 %, respectively. These values are on par with the 4.1 % reported in section 5.1.3 for the 200 nm thick PZT sample and with literature values being below 5 % [24, 51, 53].

Similar to the phenomenon observed in Figure 5.6 (b), there is an increase of the dielectric constant after *P-E* loop measurements for all samples which will be discussed in section 5.2.4.

To complete the study of PNZT thin films deposition temperature impact on their properties, their ferroelectric characteristic values are analysed. In Figure 5.7 (c), the polarisation versus electrical field hysteresis loops display clear saturation accompanied by the convex and concave shapes characteristic of ferroelectric

Table 5.3.: Effect of PNZT deposition temperature on *PNZT stacks* with 170 nm thick PNZT layers on their dielectric constant, ε_r, and loss values at 1 kHz and at 10 kHz with $V_{AC} = 30$ mV before *P-E* loop measurements. Minimum, average, maximum and standard deviation values are indicated. When only one electrode could be measured, the single value is given as the average.

Temperature (°C)		**600**		**650**		**675**		**700**	
Measured at		1 kHz	10 kHz	1 kHz	10 kHz	1 kHz	10 kHz	1 kHz	10 kHz
Dielectric constant	Minimum	202.0	194.4	-	303.6	-	371.1	-	376.4
	Average	314.7	303.4	325.3	320.3	-	380.8	391.6	388.6
	Maximum	354.6	341.7	-	342.9	-	389.3	-	404.9
	Standard deviation	65.1	63.0	-	14.2	-	7.5	-	12.0
Dielectric loss (%)	Minimum	2.3	2.2	-	1.9	-	4.5	-	3.1
	Average	2.8	3.3	1.7	4.8	-	5.5	5.9	5.7
	Maximum	3.6	4.9	-	8.3	-	6.5	-	7.2
	Standard deviation	0.5	1.0	-	2.3	-	0.8	-	1.9

hysteresis. The *P-E* loop of the sample deposited at 675 °C is not plotted due to important leakage, leading to inaccurate polarisation measurement and bringing the plot out of the scale of this figure.

The asymmetry along the polarisation axis previously reported between the positive and negative branches of the *P-E* loops (see sections 5.1.3 and 5.2.1) is also visible in the hysteresis loop of the sample deposited at 700 °C. It can be attributed to the different nature of the top and bottom electrodes [154]. Indeed, the different heights of the Schottky barriers at the interfaces of the PZT film with the top Pt and bottom $LaNiO_3$ electrodes impact charge injection and ferroelectric switching [253]. In turn, the shape of *P-E* loops is modified as it is dependent on the reversal of the polarisation within the ferroelectric material [213].

In the case of the samples deposited at 600 °C and 650 °C, the *P-E* loops are mostly symmetric. It can indicate that the contribution of charge injection at the electrodes to the current measured by the *P-E* loop tracer is either more limited than for previous samples in this work or less predominant than bulk contribution. The difference is attributed to the additional pyrochlore and Pb phases present in the film which modify the conduction mechanisms in PNZT thin films by changing their nature.

Table 5.4 presents the values of remanent polarisation, saturation polarisation, coercive field and internal bias field. The methodology previously used in this work is employed to determine the coercive field values as the fields corresponding to the switching current peaks from the switching current versus field hysteresis loops. To determine the ferroelectric characteristic values, *P-E* loops with the same maximum applied field are selected for all samples in the series. This provides comparable data between samples.

Since the *P-E* loop of the sample deposited at 675 °C was not plotted due to important leakage, characteristic ferroelectric values could not be accessed. All other samples in this series display low standard deviation values of their ferroelectric properties, hinting to a homogeneity in the films despite the presence of a pyro-

Table 5.4.: Effect of PNZT deposition temperature on *PNZT stacks* with 170 nm thick PNZT layers on their ferroelectric characteristic values obtained from a *P-E* loop measured at 100 Hz with a maximum applied field of 412 kV·cm^{-1}. Remanent polarisation, P_r, saturation polarisation, P_{sat}, coercive field, E_c, and internal bias field, $E_{c,shift}$, values are indicated with their respective minimum, average, maximum and standard deviation values. The electrodes measured are the same as in Table 5.3 except for the PNZT film deposited at 675 °C for which no reasonable *P-E* loop could be measured due to large leakage.

Temperature (°C)		**600**	**650**	**675**	**700**
P_r (μC·cm^{-2})	Minimum	19.3	21.1	-	27.1
	Average	24.0	22.3	-	28.4
	Maximum	29.7	24.2	-	29.7
	Standard deviation	4.1	1.1	-	1.3
P_{sat} (μC·cm^{-2})	Minimum	31.9	34.0	-	36.8
	Average	36.8	36.1	-	38.9
	Maximum	40.4	38.8	-	41.0
	Standard deviation	3.2	1.8	-	2.1
E_c (kV·cm^{-1})	Minimum	144.0	144.0	-	160.3
	Average	146.0	144.0	-	162.4
	Maximum	148.0	144.0	-	164.4
	Standard deviation	2.0	0.0	-	2.1
$E_{c,shift}$ (kV·cm^{-1})	Minimum	41.2	47.4	-	43.1
	Average	43.8	48.9	-	44.2
	Maximum	47.4	51.4	-	45.3
	Standard deviation	2.3	1.7	-	1.1

chlore phase in those deposited at lower temperatures. The smaller standard deviations presented by the deposition temperature series as compared to the O_2 deposition pressure series could also be associated with an improvement of the film-electrode interface homogeneity between different top electrodes.

The highest average values of both remanent and saturation polarisation are displayed by the PNZT thin film deposited at 700 °C and previously discussed in section 5.2.1. It should be noted that this sample also presents the highest values of both minimal and maximal values of remanent and saturation polarisation.

The average positive coercive fields and internal bias fields at 100 Hz remain similar to those of the O_2 deposition pressure series. For the PNZT thin films deposited at 600 °C, 650 °C and 700 °C they range from $E_c = 144.0$ kV·cm^{-1} to $E_c = 160.3$ kV·cm^{-1} and between $E_{c,shift} = 41.2$ kV·cm^{-1} and $E_{c,shift} = 47.4$ kV·cm^{-1}, respectively.

According to the data acquired with this series of PNZT thin films, PNZT deposition temperature mainly influences the co-existence of the PNZT phase with additional phases. The presence of $Pb_2Ti_2O_6$ pyrochlore and Pb phases is noticeable in the XRD patterns of the samples deposited at lower temperatures and indicates that 700 °C is the optimal deposition temperature for PNZT thin films. This conclusion is bolstered by this sample displaying the largest dielectric constant, remanent polarisation and saturation polarisation of the series. It should be noted that higher deposition temperatures could be more suitable but cannot be implemented on the *small PLD* system used in this thesis for the deposition of PNZT thin films.

5.2.3. Influence of PNZT layer thickness in *PNZT stacks*

A series of PNZT/LNO/Al_2O_3/steel heterostructures are deposited with PNZT layer thicknesses of 200 nm, 300 nm and 400 nm. The O_2 deposition pressure and the deposition temperature of the PNZT layer are chosen as 8.0 Pa and 700 °C, as previously optimised. The patterns obtained by XRD analysis of the *PNZT stacks* are shown in Figure 5.8 (a). The PNZT reflections, assimilated to those of PZT, and the $Pb_2Ti_2O_6$ reflections both appear during the deposition of the PNZT layer and are not visible after the deposition of the LNO layer.

The perovskite structure and the predominance of the {001} texture of the PNZT thin films is confirmed by the XRD patterns for each of the thicknesses of the PNZT layer. However, the 111 PZT reflection becomes distinctly visible in the XRD patterns of the 300 nm and 400 nm thick PNZT thin films. The ratio of its intensity compared to the intensity of the 001 PZT reflection is of 0.060 and 0.045 for the 300 nm and 400 nm thick layers, respectively, indicating that the relative quantity does not increase with the film thickness. A small amount of grains with this orientation is most likely present in every film deposited in this work. However, the reduced thickness of the previously deposited thin films led to smaller amounts of grains in the {111} orientation with a lower intensity of the associated reflection, preventing its detection by XRD analysis.

For the 200 nm and 300 nm thick PNZT films, additional reflections of $Pb_2Ti_2O_6$ pyrochlore phase are visible on the XRD patterns. The lack of visible pyrochlore reflection in the XRD pattern of the thicker PNZT thin film is consistent with the observation made in section 5.1.2 that the pyrochlore phase is located in the depth of the films deposited in this work. It is an indication that while the pyrochlore phase nucleates along with the PNZT phase, the latter becomes predominant as the film grows.

The Lotgering factors of the PNZT thin films are on par with values previously reported in this work with ${f_{(00l)}}^{\text{PNZT}} = 0.87$, ${f_{(00l)}}^{\text{PNZT}} = 0.85$ and ${f_{(00l)}}^{\text{PNZT}} = 0.85$ for 200 nm, 300 nm and 400 nm thick films, respectively. This is also the case for the LNO Lotgering factor which ranges from ${f_{(00l)}}^{\text{LNO}} = 0.75$ to ${f_{(00l)}}^{\text{LNO}} = 0.79$, remaining larger than literature values on stainless steel [57].

The results of dielectric permittivity measurements at 1 kHz and at 10 kHz with $V_{AC} = 30$ mV before and after measuring *P-E* loops for *PNZT stacks* with varying PNZT layer thicknesses are introduced in Figure 5.8 (b) while the *P-E* loops at 100 Hz are given in Figure 5.8 (c). The dielectric constant and *P-E* loop measurements for each sample in Figure 5.8 are performed on the same electrode. To facilitate comparison of the results, all electrodes are selected with an area of 0.0327 mm^2.

Due to the different thicknesses of the PNZT layers and the AC driving signal to measure the permittivity being constant, the subswitching field amplitude is specific to each sample. Therefore, since dielectric constant is dependent on the subswitching field amplitude, comparison between the samples of this series is meaningless [98]. The only features of interest are the trends common to all samples that permittivity

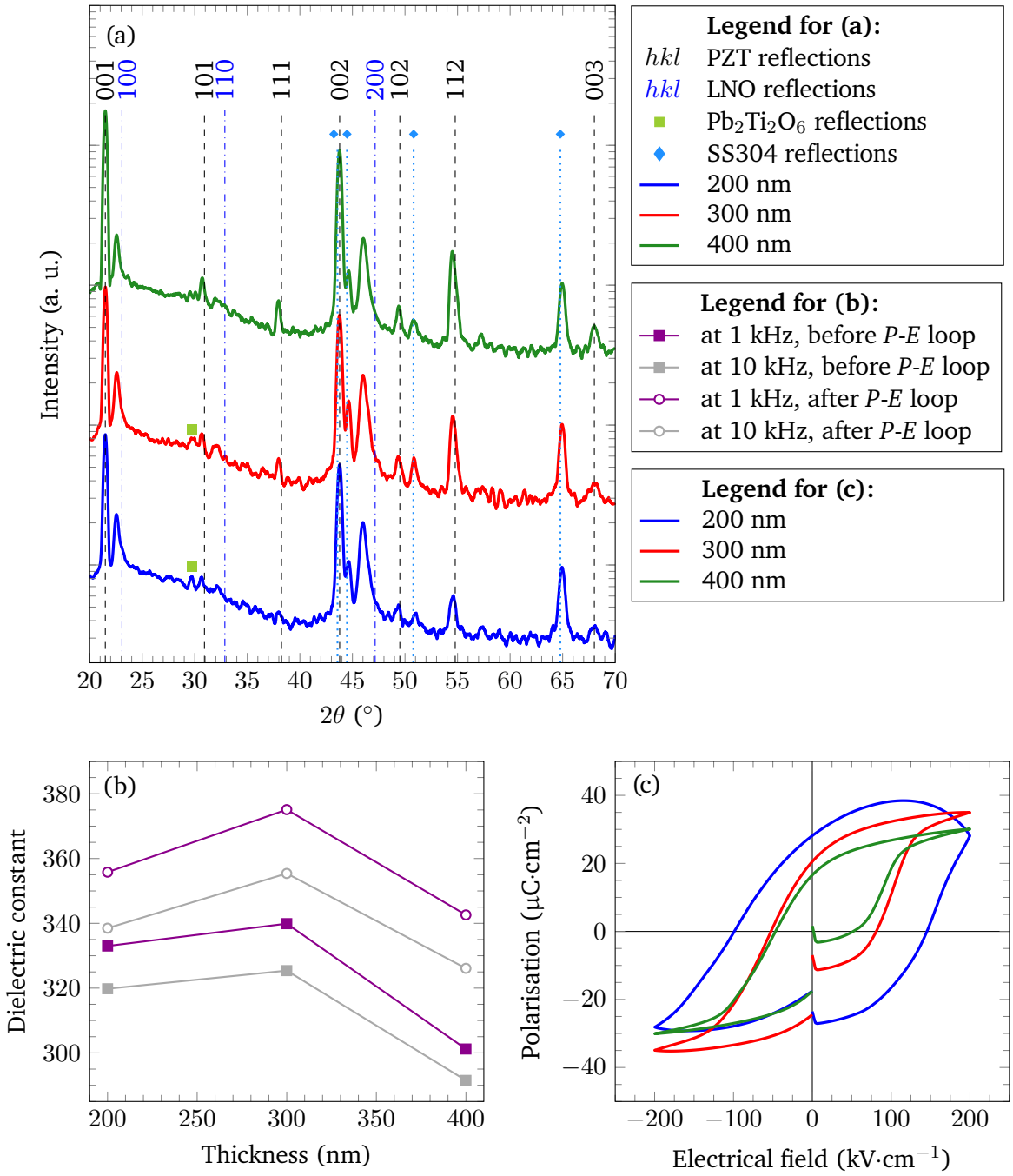

Figure 5.8.: Effect of PNZT layer thickness in *PNZT stacks* on (a) 2θ-θ XRD patterns with reflections denoted for PZT [140] (tetragonal black hkl indexes), LNO [196] (cubic blue hkl indexes) and SS304 [243, 244] (light blue diamonds) as well as for $Pb_2Ti_2O_6$ [241] (light green squares) additional phase, the Al_2O_3 layer being amorphous, (b) values of PNZT dielectric constant, ε_r, at 1 kHz (purple marks) and at 10 kHz (grey marks) with $V_{AC} = 30$ mV before (closed squares) and after (open circles) measuring *P-E* loops, (c) PNZT polarisation, P, versus electrical field, E, hysteresis loops at 100 Hz. In (a) and (c), PNZT layer thicknesses of 200 nm, 300 nm and 400 nm are represented by the blue, red and green curves, respectively.

is larger at 1 kHz than at 10 kHz and lower before *P-E* loops are measured than after. Both of these phenomena will be discussed in section 5.2.4 which discusses parameters sweeps during dielectric constant and loss measurements.

Table 5.5 also displays permittivity values larger at 1 kHz than at 10 kHz before measuring *P-E* loops, whether for the average, minimal or maximal values, respectively. Relying on the methodology previously used in this work, data are collected from a set of four electrodes which comprises two 0.0327 mm^2, one 0.1252 mm^2 and one 0.2828 mm^2 electrodes. If there are electrodes with a dielectric loss superior to 10 % on the sample, they are not taken into account. Due to the limited number of electrodes analysed in this work and to give a more accurate representation of the samples, Table 5.5 also gives minimal and maximal values.

Table 5.5.: Effect of PNZT layer thickness in *PNZT stacks* on the dielectric constant, ε_r, and loss values at 1 kHz and at 10 kHz with $V_{AC} = 30$ mV before *P-E* loop measurements. Minimum, average, maximum and standard deviation values are indicated.

Thickness (nm)		**200**		**300**		**400**	
Measured at		1 kHz	10 kHz	1 kHz	10 kHz	1 kHz	10 kHz
Dielectric constant	Minimum	333.0	319.8	338.3	307.7	295.7	286.0
	Average	350.2	331.8	346.7	326.7	303.9	293.8
	Maximum	367.4	348.3	361.8	346.3	310.3	300.6
	Standard deviation	17.2	12.0	10.7	13.7	5.8	5.6
Dielectric loss (%)	Minimum	3.7	2.9	2.8	2.8	2.3	2.3
	Average	5.2	3.7	4.2	3.7	4.1	2.7
	Maximum	6.6	4.7	6.7	5.3	8.1	3.6
	Standard deviation	1.5	0.7	1.8	1.0	2.4	0.5

When *PNZT stacks* of this series are subjected to an identical $V_{AC} = 30$ mV, their dielectric loss values, ranging between 5.2 % and 4.1 % at 1 kHz and between 3.7 % and 2.7 % at 10 kHz, are also dependent on the subswitching field amplitude. Moreover, standard deviation values remain moderate for both dielectric constant and loss, indicating that the samples are mostly homogeneous. Compared to PNZT thin films deposited under various O_2 pressures and at several temperatures, samples grown with the optimised parameters of 8.0 Pa and 700 °C display smaller dielectric loss values.

The impact of PNZT layer thickness in *PNZT stacks* is further investigated, particularly on the films ferroelectric properties. For comparison purposes, in Figure 5.8 (c), polarisation versus electrical field hysteresis loops are plotted with the same maximum applied field value of 200 kV·cm^{-1} for the 200 nm, 300 nm and 400 nm thick PNZT films.

The *P-E* loops of both the 300 nm and 400 nm thick films show the convex and concave shapes characteristic of ferroelectric hysteresis with distinct saturation. However, the 200 nm thick PNZT film presents a more rounded hysteresis for which saturation is not pronounced and ferroelectricity is debatable. This behaviour does not occur for the *P-E* loop with a maximum applied field value of 400 kV·cm^{-1} which has sharp convex

and concave features along with a marked saturation. It is suggested that this phenomenon is due to larger leakage currents in the PNZT films before *P-E* loop at higher maximum applied fields are measured. Further discussion on this topic will be introduced in section 5.2.5.

The positive and negative branches of the *P-E* loops for the 300 nm and 400 nm thick PNZT films are largely symmetric. A similar behaviour is observed in the 400 nm thick PZT thin film described in section 5.1.3 and for the PNZT films deposited at 600 °C and 650 °C in section 5.2.2. In the former case, it is suggested that the thicker film lead to less leakage and, along the polarisation axis, to a less asymmetric loop than the 200 nm thick PZT film deposited under the same conditions. In the later instance, it is hypothesised that charge injection at the electrodes is more limited than for the sample deposited at 700 °C or that the bulk contribution to the current measured by the *P-E* loop tracer is predominant. This hypothesis is based on the presence in the PNZT thin film of additional pyrochlore and Pb phases which modify its conduction mechanisms.

To unify the hypotheses concerning the symmetry along the polarisation axis of the *P-E* loop shapes, it is suggested that the asymmetry of the positive and negative branches is indeed linked to charge injection and to the different nature of the top and bottom electrodes [154, 253]. This effect can become secondary in regard to bulk conduction mechanisms, leading to more symmetric *P-E* loops. Bulk conduction mechanisms can become prevalent over interface mechanisms if the nature of the film is modified by additional phases (see section 5.2.2) or if the film thickness is increased, as is the case for the 400 nm thick PZT film in section 5.1.3 and for the 300 nm and 400 nm thick PNZT thin films introduced in this section.

The remanent polarisation, saturation polarisation, coercive field and internal bias field values for the 200 nm, 300 nm and 400 nm thick PNZT films in *PNZT stacks* are given in Table 5.6. To accurately determine these values, data for each sample are obtained from *P-E* loops measured with a maximum applied field of 8 V to avoid the more rounded *P-E* loop shape of the 200 nm thick sample at lower maximum fields (see Figure 5.8 (c)). The coercive field values are determined as the fields corresponding to the switching current peaks from the switching current versus field hysteresis loops according to the methodology previously used in this work.

All ferroelectric properties given in Table 5.6 present very low standard deviation values for each analysed thickness of the PNZT layer. It is indicative of homogeneous samples and of good film-electrode interface homogeneity between different top electrodes. It is consistent with the fact that only a limited amount of pyrochlore phase is found in *PNZT stacks* by XRD analysis.

Since the maximum applied voltage for *P-E* loop from which characteristic values are obtained is constant, thinner films are subjected to a higher electrical field. It induces switching of a larger number of ferroelectric domains and leads to a larger ferroelectric response. This phenomenon is evidenced by the 200 nm, 300 nm and 400 nm thick PNZT thin films exhibiting average remanent polarisation values of $P_r = 34.0$ μC·cm^{-2}, $P_r = 22.0$ μC·cm^{-2} and $P_r = 16.5$ μC·cm^{-2} after the release of maximal applied fields of 400 kV·cm^{-1}, 300 kV·cm^{-1} and 200 kV·cm^{-1}, respectively. The remanent polarisation exhibited by samples of this PNZT layer thickness series increases proportionally to the maximal applied field applied during the *P-E* loop with a remanent polarisation approximately doubled between a 200 kV·cm^{-1} and a 400 kV·cm^{-1} applied field. Similar trends can be observed with the average saturation polarisation and with minimum and maximum values of both remanent and saturation polarisation.

It is interesting to compare the properties of the *PNZT stacks* with those of the *PZT stacks* described in section 5.1.3. The remanent polarisation of both 200 nm and 400 nm thick PZT thin films are measured after a 200 kV·cm^{-1} field was released and with values of $P_r = 16.7$ μC·cm^{-2} and $P_r = 16.4$ μC·cm^{-2}, respectively. Therefore, the 400 nm thick films of PZT and PNZT are measured under the same conditions

Table 5.6.: Effect of PNZT layer thickness in *PNZT stacks* on the ferroelectric characteristic values obtained from a *P-E* loop measured at 100 Hz with a maximum applied voltage of 8 V ($200-400$ kV·cm^{-1}). Remanent polarisation, P_r, saturation polarisation, P_{sat}, coercive field, E_c, and internal bias field, $E_{c,shift}$, values are indicated with their respective minimum, average, maximum and standard deviation values. The electrodes measured are the same as in Table 5.5.

Thickness (nm)		**200**	**300**	**400**
P_r (μC·cm^{-2})	Minimum	31.6	20.6	16.1
	Average	34.0	22.0	16.5
	Maximum	37.4	22.9	17.0
	Standard deviation	2.5	0.9	0.3
P_{sat} (μC·cm^{-2})	Minimum	42.0	29.7	24.2
	Average	42.9	31.7	24.8
	Maximum	44.0	33.1	25.7
	Standard deviation	0.8	1.3	0.5
E_c (kV·cm^{-1})	Minimum	163.9	106.5	89.9
	Average	165.2	107.9	91.5
	Maximum	167.8	109.3	92.0
	Standard deviation	1.8	1.4	0.9
$E_{c,shift}$ (kV·cm^{-1})	Minimum	28.0	23.9	19.0
	Average	29.3	25.3	20.5
	Maximum	30.0	26.6	23.0
	Standard deviation	0.9	1.0	1.5

and exhibit equivalent remanent polarisations. The 200 nm thick PZT film remanent polarisation is approximately half of that of the 200 nm thick PNZT film for a maximum applied field half as large. This behaviour is consistent with the previous observation that remanent polarisation increases proportionally with the maximum applied field of the *P-E* loop. Nb-doping has no noticeable impact on the remanent polarisation of the PZT thin films analysed in this study, contrary to the literature report by Sun et al. of P_r values twice larger for 2 mol.% Nb-doped than for undoped PZT [154]. It should be noted that the possibility to apply an electrical field twice larger on the 200 nm thick PNZT thin film than on the 200 nm thick PZT film without reaching dielectric breakdown opens new possibilities for MEMS applications.

Nonetheless, the remanent polarisation of the PNZT thin films deposited in this work should be compared with further literature values. These PNZT thin films have the same chemical composition as those developed by Coleman et al. on Ni foils. The 200 nm thick PNZT film displays a remanent polarisation equivalent to that of ~ 39.5 μC·cm^{-2} reported in literature for thicker 600 nm thick PNZT films on Ni foils after the release of a 900 kV·cm^{-1} applied field, i.e. more than twice larger than in this work [53]. The 200 nm thick PNZT thin film remanent polarisation is also equivalent to that of ~ 36 μC·cm^{-2} reported in literature

for 1 µm thick PZT films on Ni foils with a maximum applied field of 1,000 kV·cm^{-1} [51]. Therefore, the PNZT thin films deposited by PLD on stainless steel substrates exhibit a remanent polarisation on par with literature values and potentially larger should comparable fields be applied to measure the *P-E* loops.

For the *P-E* loop measured at 100 Hz with a maximum applied field of 200 kV·cm^{-1}, the average value of the 200 nm thick PNZT thin film positive coercive field is $E_c = 165.2$ kV·cm^{-1}, slightly larger than the value of 135.9 kV·cm^{-1} for the 200 nm thick PZT thin film discussed in section 5.1.3. On the other hand, the 400 nm thick PNZT thin film displays a positive coercive field average value of $E_c = 91.5$ kV·cm^{-1}, slightly lower than the coercive field of the 400 nm thick PZT sample at 93.9 kV·cm^{-1}. The influence of 2 mol.% Nb-doping on PZT thin films coercive field is therefore, negligible. Despite diverging from the majority of literature which states that E_c values decrease with increasing Nb concentrations in PZT [98, 155, 157], the stability of the coercive field between PZT and PNZT thin films deposited in this work is consistent with literature reports of equivalent E_c values between undoped and 2 mol.% Nb-doped PZT [154]. The results of this work are also in agreement with literature reports indicating limited effect of low concentrations of Nb-doping on the coercive field of PZT thin films [151, 153].

It is noteworthy that both coercive field and internal bias field also present a dependency on the PNZT layer thickness. While it can be attributed to a lower maximum field applied on thicker samples during *P-E* loop measurement, leading to a more moderate ferroelectric response, this observation is coherent with literature reports of E_c decreasing with increasing thickness [157, 254].

This series of *PNZT stacks* shows {001}-textured PNZT layers for thicknesses of 200 nm, 300 nm and 400 nm. Nb-doping does not appear to influence remanent polarisation and coercive field values. However, PNZT thin films deposited in this work can withstand larger applied electrical fields without reaching dielectric breakdown than the PZT thin films. While this phenomenon is not formally linked to Nb-doping, an increased electrical resistivity as compared to non-doped PZT is reported in literature [98, 146]. Indeed, Nb-doping reduces the hole conductivity in PZT by bringing additional electrons as compared to the B site cation for which it substitutes [255]. It is thought that these intrinsic changes are also responsible for the higher dielectric breakdown field which is a significant improvement for MEMS applications. Nonetheless, further investigations are needed to draw thorough conclusions on the influence of 2 mol.% Nb-doping on PZT thin films ferroelectric properties.

Indeed, as Nb-doping effect is extrinsic, notably leading to structural changes, e.g. increased grain size [146], it is difficult to establish whether these changes are due only to Nb-doping or also to other factors. For example, bulk Nb-doped PZT 52/48 is known to display a decrease in E_c values and an increase in P_r values for increasing grain sizes, the later being due to a change in sintering temperature [256]. The PZT and PNZT thin films produced in this work are deposited under different conditions which can impact their structural characteristics, independently of Nb-doping effect.

5.2.4. Effect of parameters sweeps on *PNZT stacks* dielectric constant and loss

The influence of measurement parameters on the dielectric constant and loss values of a 300 nm thick PNZT layer within a *PNZT stack* are shown in Figure 5.9. The impact of subswitching field amplitude and frequency are both quantified before and after high electrical field measurements while the effect of DC bias field amplitude is analysed only after high electrical field measurements. Dielectric constant and loss are measured on an electrode with an area of 0.2828 mm^2 and the high electrical field measurements correspond to the *P-E* loops described in section 5.2.3 with a maximum applied field of 300 kV·cm^{-1}.

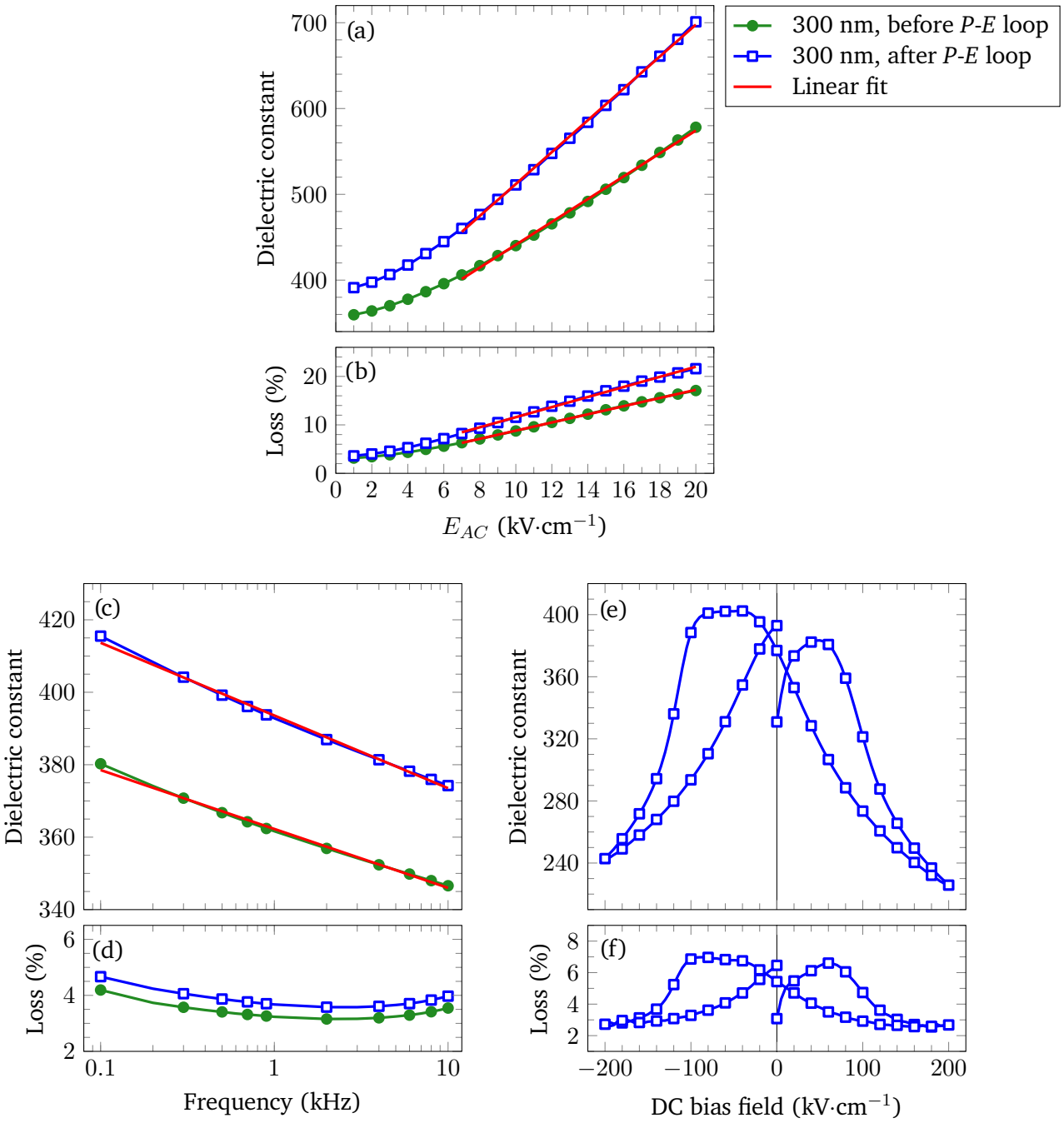

Figure 5.9.: Dielectric constant, ε_r, and loss of a 300 nm thick PNZT thin film in *PNZT stacks* as a function of (a), (b) E_{AC}, the subswitching field amplitude at 1 kHz and zero bias field, (c), (d) subswitching field frequency with an AC driving signal amplitude of 30 mV and zero bias field, and (e), (f) DC bias field at 10 kHz with an AC driving signal amplitude of 30 mV, respectively. Measurements taken before (green circles) and after (blue open squares) high electrical field ferroelectric measurements, i.e. *P-E* loops. Linear fits (red lines) are indicated in (a), (b) and (c).

The dependence between dielectric constant and both amplitude and frequency of the subswitching field is usually considered within the framework of the Rayleigh analysis of domain walls dynamics. Rayleigh analysis aims to quantify the contribution of irreversible domain wall motion to the piezoelectric response under low applied electrical fields [127].

The dielectric constant of a ferroelectric, ε_r, has both intrinsic and extrinsic components. The former corresponds to the average dielectric response of single domains with a given orientation distribution and is due to reversible interface motion. The later originates from motion of phase boundaries and ferroelectric domain wall motion. Within the framework of Rayleigh analysis, the dielectric permittivity can be expressed as [51, 248]:

$$\varepsilon_r = \varepsilon_{init} + \alpha_{irr} E_{AC}, \tag{5.5}$$

where ε_{init} and α_{irr} are the reversible and irreversible Rayleigh constants, respectively, and E_{AC} is the subswitching field amplitude. In this context, the linear dependence of dielectric permittivity on subswitching field amplitude is due to ferroelectric domain walls pinning on a random distribution of defects, hindering their mobility [98].

As shown in Figure 5.9 (a), the PNZT thin film dielectric constant increases from 360 and 391 at 1 kV·cm^{-1} to 578 and 701 at 20 kV·cm^{-1} before and after *P-E* loop measurements, respectively. It should be noted that the amplitude of the driving field E_{AC}, is largely inferior to half of the coercive field value of $\sim$108 kV·cm^{-1} reported in section 5.2.3 for 300 nm thick PNZT thin films. In both cases, this increase is linear between 7 kV·cm^{-1} and 20 kV·cm^{-1}, above the low field region, as is characteristic of a Rayleigh regime. Before *P-E* loop measurements, extrapolation at $E_{AC} = 0$ kV·cm^{-1} yields $\varepsilon_{init} = 308$ and the linear fit slope gives $\alpha_{irr} = 13.3$ cm·kV^{-1} with a linear fit coefficient $R^2 = 0.9978$. After *P-E* loop measurements, permittivity can be expressed with $\varepsilon_{init} = 326$ and $\alpha_{irr} = 18.6$ cm·kV^{-1} with $R^2 = 0.9992$.

The increase of both reversible and irreversible Rayleigh constants after high electrical field measurements as compared to before indicates larger contributions from both reversible domain wall motion and irreversible motions, e.g. phase boundaries and ferroelectric domain wall motion [51, 53]. While further studies are necessary to understand which phenomena lead to increased ε_{init} and α_{irr}, it is suggested that the ferroelectric underwent significant intrinsic changes, either in its ferroelectric domain state or in its defect distribution during *P-E* loop measurements. The improvement of PNZT thin films dielectric performance might be linked to leakage mechanisms which will be discussed in section 5.2.5.

Following a trend similar to that of the permittivity, 300 nm thick PNZT thin film dielectric loss increases from 3.1 % and 3.6 % at 1 kV·cm^{-1} to 17.1 % and 21.6 % at 20 kV·cm^{-1} before and after *P-E* loop measurements, respectively, as shown in Figure 5.9 (b). This increase is linear between 7 kV·cm^{-1} and 20 kV·cm^{-1} with linear fits displaying coefficients $R^2 = 0.9996$ and $R^2 = 0.9989$, respectively.

Increasing the subswitching field frequency from 100 Hz to 10 kHz, as represented in Figure 5.9 (c), leads to a decrease of the PNZT thin film dielectric constant from 380 and 416 to 347 and 374 before and after *P-E* loop measurements, respectively. Due to the pinning of domain walls controlling the extrinsic piezoelectric response, this decrease is linear with the logarithm of the subswitching field frequency [98]. This applies to the 300 nm thick PNZT thin film for which linear fits can be established between 100 Hz and 10 kHz with $R^2 = 0.9963$ and $R^2 = 0.9968$ before and after *P-E* loop measurements, respectively.

The larger values of permittivity after *P-E* loops as compared to before their measurements which is observed here is consistent with the results presented in Figure 5.9 (a). It also conforms with previous observations made in sections 5.2.1 to 5.2.3.

The dielectric loss as a function of the subswitching field frequency, shown in Figure 5.9 (d), is maximal at 100 Hz, reaching 4.2 % and 4.7 % before and after *P-E* loop measurements, respectively. In both cases, between 2 kHz and 3 kHz, the loss decreases to minimum values of 3.2 % and 3.6 %, respectively, before progressively increasing until 10 kHz.

To complete this analysis, dielectric constant and loss after *P-E* loop measurements are plotted in Figure 5.9 (e) and (f) as a function of the DC bias field which was maintained to 0 kV·cm^{-1} in previous measurements. As the DC bias field is swept from 0 kV·cm^{-1} to 200 kV·cm^{-1} then to -200 kV·cm^{-1} and back to 0 kV·cm^{-1}, both curves adopt a *butterfly* shape, characteristic of ferroelectrics [51]. This behaviour is expected since the applied field maximum amplitude for both polarities is approximately twice larger than the coercive field value of $\sim$108 kV·cm^{-1} reported in section 5.2.3 for 300 nm thick PNZT thin films. As the DC bias is increased, domain walls previously pinned by the defects in the PNZT thin film are released and ferroelectric switching occurs [6, 98].

Both the dielectric constant and loss versus DC bias field curves are asymmetric, as reported for *P-E* loops in sections 5.1.3 and 5.2.1 to 5.2.3. As previously suggested, the asymmetry of these curves can be attributed to the different nature of the top and bottom electrodes [253]. The dielectric permittivity reaches local minima of 226 at 200 kV·cm^{-1} and 243 at -200 kV·cm^{-1} as well as local maxima of 383 at 50 kV·cm^{-1} and 402 at -45 kV·cm^{-1}. The dielectric loss follows a similar trend with local minima of 2.7 % at 200 kV·cm^{-1} and 2.7 % at -200 kV·cm^{-1} while its local maxima are of 6.6 % at 60 kV·cm^{-1} and 7.0 % at -85 kV·cm^{-1}. For both quantities, a gap can be observed at 0 kV·cm^{-1} between the starting and ending points of the curves. This gap, whose origin is thought to be related to the gap present in *P-E* loops, goes from 331 to 393 for the dielectric constant and between 3.1 % and 6.5 % for the dielectric loss.

5.2.5. Leakage current measurements on *PNZT stacks*

The DC leakage current density of a 400 nm thick PNZT layer within a *PNZT stack* is plotted in Figure 5.10 with several representations to identify the leakage current mechanism. Measurements are performed on a 0.0327 mm^2 virgin top electrode.

The *J-E* curve presented in Figure 5.10 (a) shows a strong asymmetry between the positive and negative polarities. For the positive polarity, the current density increases up to 500 A·m^{-2} at $3.5 \cdot 10^7$ V·m^{-1} before decreasing slightly down to approximately 200 A·m^{-2}. Contrarily, the negative polarity displays a lower current density, increasing up to approximately 15 A·m^{-2} around $-2 \cdot 10^7$ V·m^{-1} before oscillating between 5 A·m^{-2} and 500 A·m^1.

The leakage through the 400 nm thick PNZT thin film is less important than through the 400 nm thick PZT thin film discussed in section 5.1.4 and for which the current density reaches up to ~ 500 A·m^{-2} for both polarities. The observed shape of the *J-E* curve of the 2 mol.% Nb-doped PZT thin film deposited in this work resembles those reported in literature for PZT thin films with 1 mol.% and 3 mol.% Nb-doping with a marked decrease of the current density at higher electrical fields for the positive polarity. Regarding the negative polarity, the oscillating values of the current density at higher electrical fields corresponds to the behaviour of the 3 mol.% Nb-doped PZT film described in literature [151]. It is suggested this behaviour is linked to Nb-doping which reduces hole mobility [255]. Indeed, electrons mobility is increased at higher applied field, facilitating electron-hole recombination and ultimately decreasing current density.

At lower electrical fields, the *J-E* curves in Figure 5.10 (a) can be partially fitted with polynomial functions of the electrical field, between 0 kV·cm^{-1} and 200 kV·cm^{-1} with $J \propto E^{5.28}$ for the positive polarity and

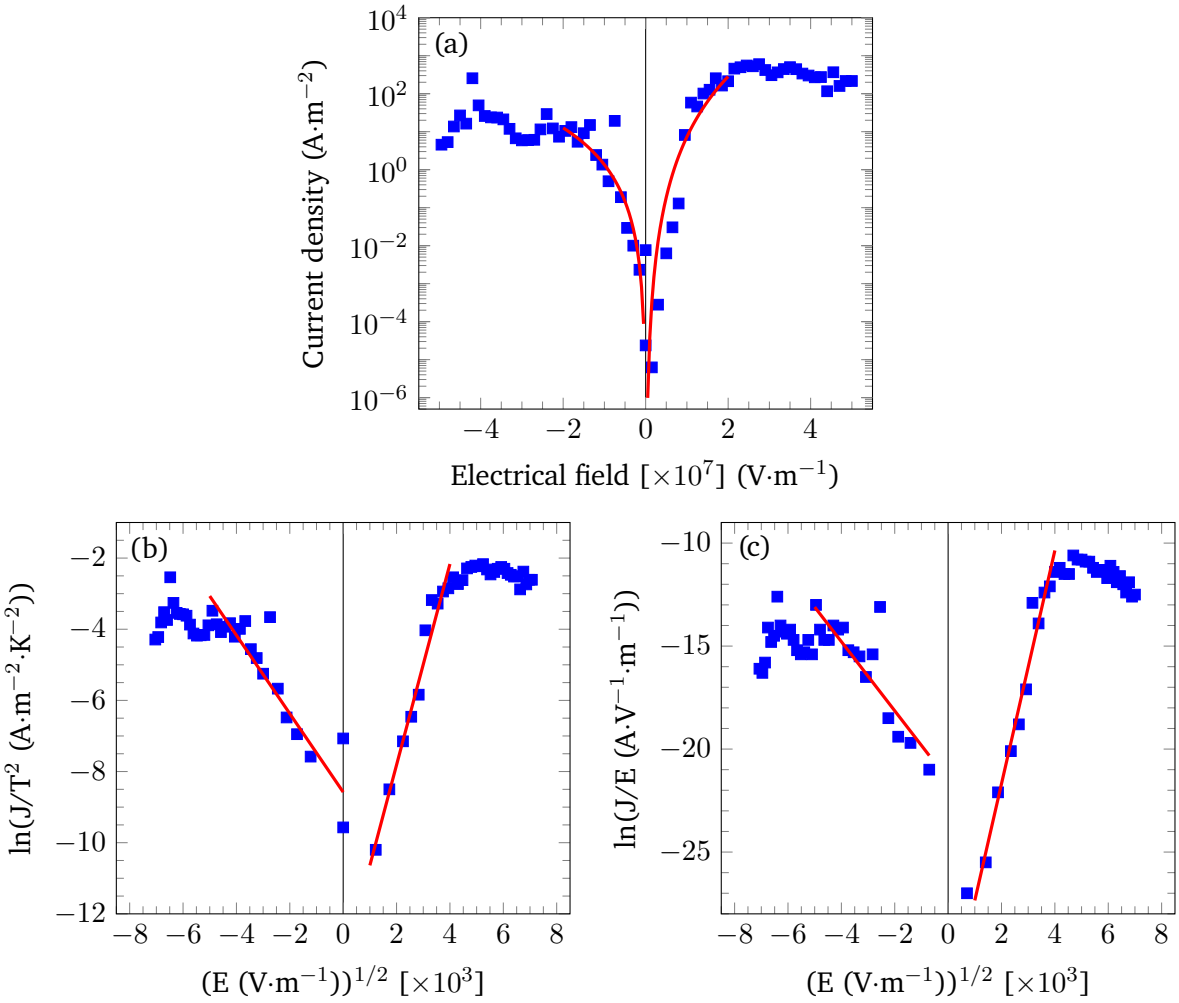

Figure 5.10.: Leakage current density, J, as a function of the applied electrical field, E, for the 400 nm thick PNZT layer of a PNZT/LNO/Al_2O_3/steel sample (blue squares) (a) fitted within the space-charge limited current scenario between 0 kV·cm^{-1} and 200 kV·cm^{-1} with the polynomial functions $J \propto E^{5.28}$ for the positive polarity and between -200 kV·cm^{-1} and 0 kV·cm^{-1} with $J \propto E^{3.22}$ for the negative polarity (red curves), (b) plotted for the Schottky emission scenario with linear fits (red lines) between 100 kV·cm^{-1} and 400 kV·cm^{-1} for the positive polarity and between -500 kV·cm^{-1} and 0 kV·cm^{-1} for the negative polarity, (c) plotted for the Poole-Frenkel emission scenario with linear fits (red lines) between 100 kV·cm^{-1} and 400 kV·cm^{-1} for the positive polarity and between -500 kV·cm^{-1} and -70 kV·cm^{-1} for the negative polarity.

between -200 kV·cm^{-1} and 0 kV·cm^{-1} with $J \propto E^{3.22}$ for the negative polarity. These polynomial functions described $J \propto E^N$ with $N > 2$ are characteristic of a SCLC mechanism with trap filling [235, 250].

However, as the *J-E* curves cannot be fitted over the whole range of analysed electrical fields, at least another mechanism must be involved in the leakage process besides the SCLC mechanism with trap filling. The DC leakage current is therefore also fitted according to Schottky emission and Poole-Frenkel emission to verify the validity of these hypotheses.

Following the hypothesis of Schottky emission, at room temperature ($T = 298$ K), linear fits are represented on the plot of $ln\left(J/T^2\right)$ versus $E^{1/2}$ presented in Figure 5.10 (b). For the positive polarity, the linear fit between 100 kV·cm^{-1} and 400 kV·cm^{-1} has a slope absolute value of $2.8 \cdot 10^{-3}$ with a linear fit coefficient $R^2 = 0.972$. With the optical dielectric constant calculated according to Equation (5.2), the corresponding refractive index defined as $n_{optical} = \sqrt{\varepsilon_{r,optical}}$ is $n_{optical,Schottky} = 0.53$. For the negative polarity, the fitting between -500 kV·cm^{-1} and 0 kV·cm^{-1} displays a slope absolute value of $1.1 \cdot 10^{-3}$ with $R^2 = 0.846$. The corresponding refractive index is $n_{optical,Schottky} = 1.34$.

The theoretical refractive index of PZT 52/48 is $n_{optical,th} = 2.2 - 2.7$ [251] and is assumed to be similar to that of PNZT. The Schottky emission hypothesis cannot be validated for the PNZT layer of *PNZT stacks* as the refractive indexes obtained under this hypothesis are approximately half of the value of $n_{optical,th}$ and less than half the value of $n_{optical,th}$ for the positive and negative polarities, respectively.

Figure 5.10 (c) presents the plot of $ln\left(J/E\right)$ versus $E^{1/2}$ according to the Poole-Frenkel emission hypothesis and indicates linear fits. For the positive polarity, the linear fit between 100 kV·cm^{-1} and 400 kV·cm^{-1} has a slope absolute value of $5.7 \cdot 10^{-3}$ with a linear fit coefficient $R^2 = 0.963$. Calculating the optical dielectric constant from Equation (5.4), the corresponding refractive index is $n_{optical,Poole-Frenkel} = 0.52$. The curve is linearly fitted between -500 kV·cm^{-1} and -70 kV·cm^{-1} for the negative polarity, with a slope absolute value of $1.7 \cdot 10^{-3}$ with $R^2 = 0.721$. The corresponding refractive index is $n_{optical,Poole-Frenkel} = 1.74$.

The PNZT layer optical dielectric constants under the Poole-Frenkel emission hypothesis are approximately two thirds of the value of $n_{optical,th}$ and less than half the value of $n_{optical,th}$ for the positive and negative polarities, respectively. Therefore, the hypothesis of Poole-Frenkel emission cannot be validated either for the PNZT layer of *PNZT stacks*.

While both the Schottky and Poole-Frenkel emission hypotheses give refractive indexes inconsistent with literature values for $PbZr_{0.52}Ti_{0.48}O_3$, the hypothesis of space-charge limited current mechanism with trap filling is a sensible possibility in PNZT thin films for applied fields with an absolute amplitude inferior to 200 kV·cm^{-1}. At higher fields, it is thought that electron-hole recombination due to Nb-doping is responsible for the decreased current density. However, other leakage mechanisms, unidentified in this work, could also be involved in leakage in PNZT thin films [255].

To supplement the analysis of leakage currents, the evolution of polarisation through series of *P-E* loops measured with increasing maximum applied voltage is investigated. Indeed, it was remarked in section 5.2.3 that the 200 nm thick PNZT thin film displays a rounded hysteresis loop when measured with lower maximum applied field while its *P-E* loop is well defined for larger fields, which is probably due to leakage. This phenomenon, which can be observed in most *PNZT stacks*, is shown in Figure 5.11 where two series of *P-E* loops at 100 Hz are plotted with increasing maximum applied voltages from 1 V to 10 V for a 300 nm thick PNZT thin film. The second series is measured consecutively to the first one with identical parameters and on the same electrode with an area of 0.2828 mm^2.

The first series of *P-E* loops, shown in Figure 5.11 (a), displays a small rounded hysteresis for the 1 V loop which is not yet saturated. The following hystereses at 2 V and 3 V show misleadingly large values of polarisation, resulting from large leakage currents measured alongside the switching currents and inaccurately accounted for in the polarisation calculations by the *P-E* loop tracer. This is demonstrated by the subsequent 4 V *P-E* loop being only slightly rounded and reaching towards saturation. This trend is continued with the 5 V and 6 V loops, almost superimposed. Ultimately, well-shaped *P-E* loops, characteristic of a ferroelectric material, and with a clear saturation are achieved for the hysteresis loops with maximum applied voltage of 7 V to 10 V. The temporary behaviour observed for the 2 V and 3 V *P-E* loops is attributed to the ferroelectric thin film undergoing significant intrinsic changes, as indicated by the increase of

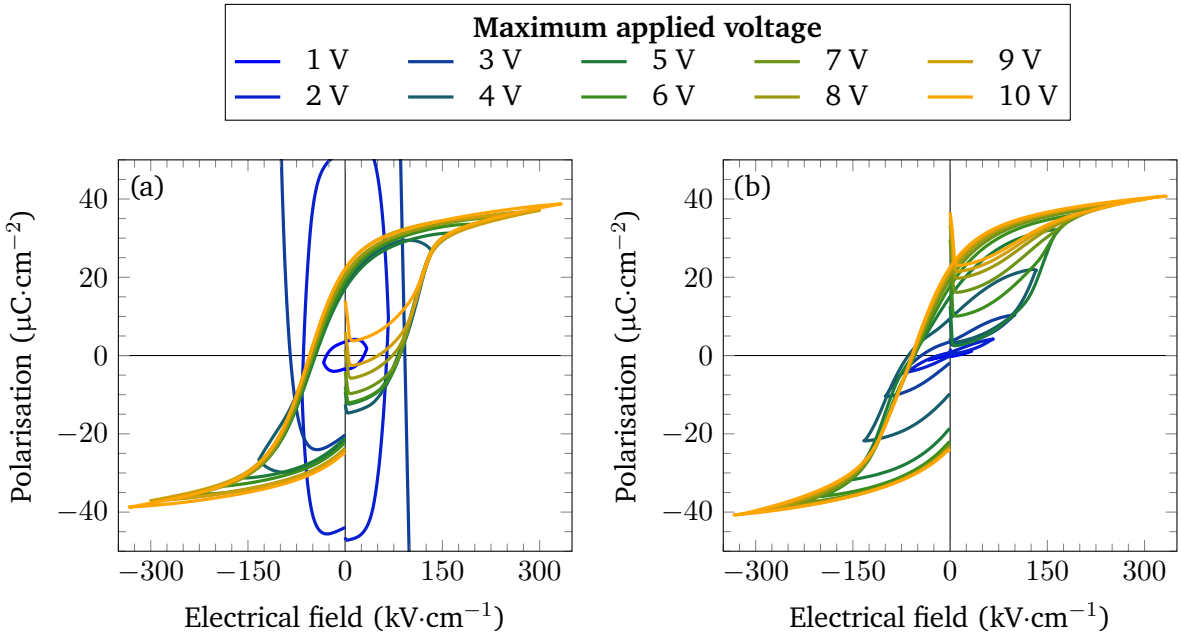

Figure 5.11.: Series of polarisation, P, versus electrical field, E, hysteresis loops at 100 Hz for a 300 nm thick PNZT thin film within a *PNZT stack* for increasing maximum applied voltage. (a) First series, (b) second series measured consecutively to the first one with the same parameters.

reversible and irreversible Rayleigh constants reported in section 5.2.4. The exact nature of these intrinsic changes is not determined in this work and could originate either in the defect distribution or in the ferroelectric domain state of the PNZT thin films.

It should be noted that the hystereses at 2 V and 3 V in Figure 5.11 (a) are represented out of scale on purpose, both to highlight the inordinately large polarisation values and to facilitate comparison with the second series of *P-E* loops plotted at the same scale in Figure 5.11 (b).

Marked differences can be observed between the shapes of the first and second series of *P-E* loops. The 1 V loop of the second series is barely opening. Afterwards, the hystereses from 2 V to 4 V open progressively and are clearly *pinched* at zero field. The corresponding switching current versus field hysteresis loops present no switching current peak, indicating that this behaviour is not associated with an antiferroelectric phase. The *P-E* loops with higher maximum applied voltage do not display this pinched shape and, while the 5 V loop does not yet reach saturation, the 6 V to 10 V hysteresis loops are well-shaped with a clear saturation. It is noteworthy that the saturation and remanent polarisation values of the higher maximum applied voltage loops are similar for the first and second series of *P-E* loops.

Pinched *P-E* loops, also referred to as *constricted* hysteresis loops, are shaped as a *double hysteresis* with a reduced remanent polarisation at zero field. This phenomenon is due to ferroelectric domain walls pinning on a random distribution of defects and internal bias fields. In lead zirconate titanate thin films, domain walls are generally pinned by charged point defects, likely lead vacancy–oxygen vacancy defect complexes, V_{Pb}"$-V_O^{\bullet\bullet}$ in the Kröger–Vink notation. These defects pin domain walls either electrically or elastically, hindering their reversible motion [98, 257–259]. It should be noted that the Nb-doping of the PNZT thin film should limit the extent of *P-E* loop pinching by reducing the concentration of oxygen vacancies, Nb^{5+} being a donor dopant [257].

P-E loop pinching normally occurs as a result of an ageing process. De-ageing can be achieved either by cycling at higher fields or by thermal treatment, leading to a *depinched P-E* loop [98, 260]. It is suggested that, during the first series of *P-E* loops performed in this work on the 300 nm thick PNZT sample, an ageing process takes place, generating large leakage currents as it occurs (see Figure 5.11 (a)) and inducing intrinsic changes in the sample, transforming the defect distribution or the domain state. It is hypothesised that the same phenomenon is responsible for the increase of both reversible and irreversible Rayleigh constants after *P-E* loops which was described in section 5.2.4. The cycling through the second series of *P-E* loops appears to have a de-ageing effect on the PNZT thin film as the maximum applied field increases.

A gap is present at 0 kV·cm^{-1} between the starting and ending points of the 4 V to 10 V *P-E* loops of the first series and for the 3 V to 10 V loops of the second series. In both series, the gap amplitude increases with the maximum applied voltage. It should also be noted that the asymmetry along the polarisation axis increases with the maximum applied voltage. As the nature of the top and bottom electrodes to which the asymmetry was previously attributed remain unchanged [253], it suggests that changes occur at the ferroelectric-electrode interfaces. These modifications are associated to the migration of oxygen vacancies, involved in domain wall pinning and reported to accumulate at the film-electrode interface under field cycling [98, 261, 262].

5.2.6. $e_{31,f}$ measurements on *PNZT stacks*

To measure the piezoelectric response of the *PNZT stacks*, $e_{31,f}$ coefficient measurements are performed on a sample with a 200 nm thick PNZT layer using the wafer flexure method described in section 4.4. An electrode with an area of 0.5006 mm^2 yields $e_{31,f} = -1.2$ C·m^{-2} while a value of $e_{31,f} = -4.4$ C·m^{-2} is obtained for an electrode of 0.7842 mm^2. Further measurements on a 400 nm thick PNZT thin film give a piezoelectric coefficient $e_{31,f} = -1.1$ C·m^{-2} for a 0.1252 mm^2 electrode.

The values obtained in this work for the $e_{31,f}$ coefficient of the *PNZT stacks* are in the same order of magnitude as literature values for 2.5 µm thick PZT thin films deposited on austenitic and ferritic stainless steel foils of -1.5 C·m^{-2} and -2.4 C·m^{-2}, respectively [64]. However, the $e_{31,f}$ values reported in this work are up to 9 times lower that those of $|e_{31,f}| = 10.6$ C·m^{-2} reported in literature for 1 µm thick PZT 52/48 on Ni foils [51].

It is estimated that the discrepancies between the different *PNZT stacks* and their respective electrodes might be due to inhomogeneous gluing of the substrates on the carrier wafer while using the wafer flexure method. A direct consequence of non-optimal gluing would be a reduced efficiency in the transmission of in-plane mechanical strain from the carrier wafer to the sample, leading to reduced $e_{31,f}$ coefficients. Furthermore, the utilisation of commercial strain gauges, glued on the carrier wafer next to the sample, instead of Pt strain gauges, sputtered directly on the sample surface (see section 4.2), might lead to measurement of in-plane strains larger than effectively experienced by the sample. This experimental setup configuration can also lead to reduced $e_{31,f}$ coefficients values for the PNZT thin films.

Nonetheless, the value of $e_{31,f} = -4.4$ C·m^{-2} measured for the 200 nm thick PNZT thin film, being larger than literature values for PZT thin films on stainless steel foils, is promising for future MEMS applications [64].

5.3. Conclusions relative to the experimental results

The growth of nearly single oriented {001}-textured ferroelectric $PbZr_{0.52}Ti_{0.48}O_3$ thin films by pulsed laser deposition onto AISI 304 stainless steel substrates is achieved. Their orientation is assessed by XRD and EBSD and the thin films have a Lotgering factor $f_{(00l)}{}^{\mathrm{PZT}} = 0.91$. To prevent substrate oxidation, Pt and Al_2O_3 buffer layers are used. **A $LaNiO_3$ layer promotes the {001} orientation of the PZT thin film** in which additional CrPt and $Pb_2Ti_2O_6$ pyrochlore phases are present. **The PZT thin films display a permittivity of approximately 350 at 1 kHz with dielectric loss below 5 %. Polarisation versus electrical field hysteresis loops indicate that the films are ferroelectric with a remanent polarisation $P_r \sim$16.5 µC·cm^{-2}**. Analysis of leakage currents infers that leakage is most likely due to a space-charge limited current with trap filling mechanism.

In order to improve the properties of the PZT thin films, the effect of 2 mol.% Nb-doping is studied under several deposition conditions. **$Pb_{0.99}\square_{0.01}(Zr_{0.52}Ti_{0.48})_{0.98}Nb_{0.02}O_3$ thin films are also predominantly {001}-oriented**, as verified by XRD. Compared to the *PZT stacks*, the Pt buffer layer was omitted, efficiently preventing the formation of an additional CrPt intermetallic phase while **protecting the stainless steel substrates against oxidation with a thicker Al_2O_3 layer**. The Lotgering factors up to 0.84 reported in this work for the LNO buffer layers are larger than literature values on steel substrates [57]. For the PNZT thin films, Lotgering factors are similar to those of PZT layers with $f_{(00l)}{}^{\mathrm{PNZT}} = 0.89$.

It is showed that higher O_2 deposition pressures and deposition temperatures are necessary to hinder the formation of additional pyrochlore and Pb phases. **Optimised PNZT thin films are deposited under 8.0 Pa of O_2 and with a substrate temperature of 700 °C.** The **PNZT thin films are ferroelectric** and a 200 nm thick layer displays a **dielectric permittivity up to 370 at 1 kHz, increasing up to 430 after *P-E* loop measurements, with a dielectric loss inferior to 5 %**. Measured under the same conditions as the PZT thin films, 400 nm thick PNZT layers have a remanent polarisation $P_r = 16.5$ µC·cm^{-2} and exhibit a coercive field $E_c = 91.5$ kV·cm^{-1}. **The 2 mol.% Nb-doping has no noticeable impact on the properties of the PNZT thin films as compared to those of the PZT layers.** The effect of doping is extrinsic and might be damped by other phenomena as the *PNZT stacks* and the *PZT stacks* are deposited under different conditions. However, **PNZT thin films ability to withstand higher applied electrical fields than PZT thin films without breaking down electrically** could be due to Nb-doping. This improvement of the thin films properties is **promising for MEMS applications**.

The PNZT thin films undergo intrinsic changes in the sample during *P-E* loop measurements with increasing maximum applied field. This leads to **increased reversible and irreversible Rayleigh constants along with larger permittivity and dielectric loss values after *P-E* loop measurements**. Analysis of leakage current measurements suggests the existence of a space-charge limited current with trap filling mechanism combined with at least another mechanism at higher applied fields. Furthermore, a de-ageing process appears to take place while measuring a second series of *P-E* loops, indicating that the intrinsic changes occurring during the first series of *P-E* loop measurements could act as an ageing process. **The piezoelectric $e_{31,f}$ coefficient of the PNZT thin films reaches up to $-$4.4 C·m^{-2} for the 200 nm thick thin** film which is within range of literature reports for PZT thin films on metallic substrates.

Globally, **the {001} orientation and ferroelectric properties of the PZT and PNZT thin films deposited by PLD on stainless steel substrates make them suitable candidates for future MEMS applications**.

6. Modelling of ferroelectric bending tongues

Portions of this chapter have been reproduced from:

J. Cardoletti, A. Radetinac, D. Thiem, J. Walker, P. Komissinskiy, B.-X. Xu, H. Schlaak, S. Trolier-McKinstry, and L. Alff,
"Modelling of the vertical deflection of ferroelectric bending tongues loaded at their free end",
AIP Advances*, vol. 9, no. 2, p. 025017, 2019. DOI: 10.1063/1.5082392*

This chapter aims to understand the influence of some parameters, e.g. applied electrical field or geometry, on MEMS efficiency. For this purpose, a model to describe the vertical deflection of a fundamental MEMS system composed of a ferroelectric bending tongue loaded at its free end is developed. The approach to the modelling chosen in this work is presented in section 6.1. Section 6.2 indicates the extents and limits of the proposed model. The fundamentals of the model will be introduced in section 6.3. Afterwards, the results of the modelling are discussed in section 6.4 before the conclusions of the chapter are given in section 6.5.

6.1. Approach to the modelling

As stated in section 1.1.2, **to model the behaviour of ferroelectric MEMS it is necessary to bridge the gap between the description of ferroelectric switching and the mechanical approach for linear piezoelectric structures**. Therefore, the model here described is **based on the ferroelectric switching criterion developed by Hwang et al. [77] and the Euler-Bernoulli beam theory**. It endeavours to give accurate estimates of the vertical deflection for MEMS applications based on ferroelectric bending tongues fixed at one end and loaded at their free end while taking into account ferroelectric switching at the grain scale.

The MEMS modelled in this work have been restricted to **ferroelectric bending tongues fixed at one end** as these are the most fundamental piezoelectric devices. This constraint is necessary to both limit the number of parameters and determine bases that could later be applied to more complex systems. The **bending tongues are modelled with a load at their free end** to emulate practical applications, e.g. an actuator applying strength against a mechanical element or a displacement sensor. The bending tongues considered here are **composed of a substrate, one or several buffer layers and a ferroelectric layer**.

The model studies the impact of the geometry of the bending tongue, the mechanical and piezoelectric material properties, the applied electrical field, the crystallographic state (polycrystalline, textured or epitaxial) of the ferroelectric thin film and its built-in strain on the vertical deflection. The accuracy of the model initially proposed by Hwang et al. is improved by incorporating macroscopic polarisation and strain saturation at high field, as expected for the *butterfly* loop. By analysing in details the different contributions to the vertical deflection, the proposed model also allows optimisation of the geometry of the bending tongue for various applications.

The model is implemented through a MATLAB® program. Named *FeBeTo – Ferroelectric Bending Tongues modelling program*, it is designed so internal functions could easily be replaced by more advanced ones

should the need arises. It presents a user-friendly interface, as shown in Figure 6.1. The program installer is available online (DOI: 10.25534/tudatalib-11.3) [263] under a Creative Commons Attribution-NonCommercial-NoDerivatives 4.0 International (CC BY-NC-ND 4.0) licence. The code of the program is included in Appendix F.

Figure 6.1.: Interface of the *FeBeTo – Ferroelectric Bending Tongues modelling program*. The modelling parameters can be set on the left panel and the results are displayed on the right panel.

The abbreviations and notations introduced earlier in this manuscript are still valid through this chapter. However, due to the large number of notations relevant to this chapter and its appendices (Appendices G and H) only, a specific list of notations is provided in *List of notations specific to the modelling chapter*.

6.2. Extent and limits of the modelling

6.2.1. Extent of the model

The described model applies to a composite bending tongue fixed at one end and with a width-to-depth ratio larger than 12 [264]. Therefore, while the Euler-Bernoulli beam theory can be used to describe its vertical deflection, it is necessary to apply corrections for both the inhomogeneity and the width of the bending tongue.

The composite bending tongue, represented in Figure 6.2, is composed of three distinct layers: a ferroelectric layer, one or more buffer layers referred to as *buffer layer* in this chapter and a polycrystalline substrate.

The bending tongue is subjected to the gravity force of its own weight and to a load applied at its free end. The former is applied over its whole length while the latter is distributed over a certain length referred to

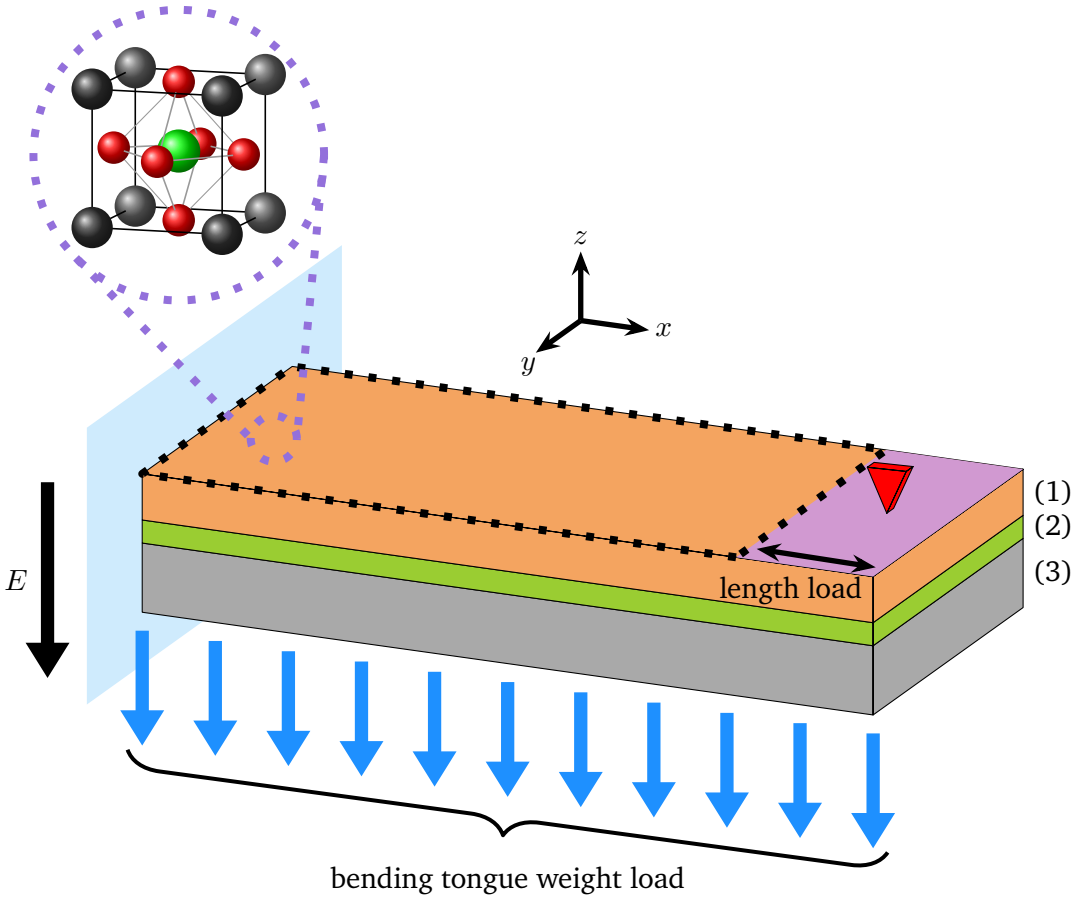

Figure 6.2.: Schematic representation of the modelled bending tongue in the *global reference frame* (xyz). The electrical field E is applied over the area delimited by dashes through all layers: (1) ferroelectric layer (orange colour), (2) buffer layer(s) (light green colour), (3) substrate (grey colour). The load at the free end (red arrow) is applied over *length load* (purple colour) and the bending tongue weight load (blue arrows) is applied over the whole bending tongue length. Adapted from [265].

as *length load*. Additionally, the bending tongue is subjected to both built-in strain, due to eventual misfit strain and to thermal strain, and to ferroelectric strain. The former is applied over its whole length and the latter is applied over the region where the electrodes used to activate the ferroelectric layer are located, i.e. the length of the bending tongue minus the *length load*.

The bending tongue is described in a Cartesian coordinate frame, (xyz), known as the *global reference frame*, where it is fixed at $x = 0$ and $z = 0$ with the x-direction along the length of the bending tongue. Upon application of an electrical field, the bending tongue is deflected vertically in the z-direction.

As the model is aimed at functional applications, it considers four distinct states of the bending tongue: *as deposited*, i.e. before any electrical field is applied; *poled*, i.e. corresponding to the final step of the poling process, before the poling electrical field is released; *inactive*, i.e. after poling, while no electrical field is applied; and *active*, i.e. after poling, while an electrical field is applied.

6.2.2. Assumptions of the model

The model presumes several general assumptions: each individual layer composing the bending tongue is homogeneous and its properties are either isotropic or transversely isotropic in the xy-plane. The bonding between the individual layers is assumed to be perfect.

Mechanical hypotheses are also assumed in order to apply the Euler-Bernoulli beam theory [167]: the composite beam has the same modulus of elasticity for both tension and compression and is presumed to be straight or slightly curved in the plane of bending, i.e. with a radius of curvature at least 10 times as long as the thickness of the bending tongue. The cross-section of the beam is assumed to be uniform along the x-axis and the bending tongue has at least one longitudinal plane of symmetry, i.e. the xz-plane. All loads and reactions are presumed to be perpendicular to the axis of the bending tongue, i.e. along the z-direction, as well as to lie in the same plane as the bending tongue which is a longitudinal plane of symmetry, i.e. in the xz-plane. Deformations are assumed to be small and within the range of linear elastic deformation. The bending tongue is also presumed to be long with respect to its thickness: considering it as a metal beam of compact section, its span-to-thickness ratio is at least equal to 8.

The model also supposes the following crystallographic assumptions: the ferroelectric layer contains only tetragonal unit cells and the substrate is polycrystalline. It is presumed that there is no phase transition in any of the materials, neither during the thin film deposition processes nor during the bending tongue operation.

Since this model is based on Hwang et al.'s model for ferroelectric switching [77], it takes into account neither the correlation between ferroelectric domains nor domain wall motion. For such purpose, the phase field models can be utilised [73–75]. The model also considers that $180°$ and $90°$ switching requires the same amount of energy.

Due to the large number of parameters required for the modelling, the results might be strongly impacted by the selected values.

6.3. Equations of the model

As mentioned in section 6.2.1, the bending tongue, being a composite, requires a correction for its inhomogeneity by means of an equivalent cross-section [167]. The substrate is taken as the reference layer, implying:

$$w_{eff}{}^{subs} = w^{subs}, \tag{6.1}$$

$$w_{eff}{}^{film} = w^{film} \frac{E_{\mathrm{Y}}{}^{film}}{E_{\mathrm{Y}}{}^{subs}}, \tag{6.2}$$

where w^{subs} and $w_{eff}{}^{subs}$ refer to the width and the effective width of the substrate, respectively. The width and the effective width of any subsequent layer are noted w^{film} and $w_{eff}{}^{film}$, respectively, and $E_{\mathrm{Y}}{}^{subs}$ and $E_{\mathrm{Y}}{}^{film}$ refer to the Young moduli of the substrate and of any subsequent layer, respectively.

The neutral axis of the equivalent cross-section of the bending tongue and its second moment of area are impacted by taking the effective width of each layer into account. It is therefore necessary to consider the effective neutral axis, n_{eff} and the effective second moment of area I_{eff} calculated using w_{eff}.

Therefore, n_{eff}, which is also dependent on the mid-plane of each individual layer, n^i, can be expressed as:

$$n_{eff} = \frac{\sum_i {w_{eff}}^i t^i n^i}{\sum_i {w_{eff}}^i t^i}, \tag{6.3}$$

where t^i corresponds to the thickness of every individual layer of the bending tongue, and with n^i defined as:

$$n^i = \frac{t^i}{2} + \sum_{j=0}^{i-1} t^j. \tag{6.4}$$

Using Equation (6.3), I_{eff} can be calculated as:

$$I_{eff} = \sum_i \frac{{w_{eff}}^i t^i}{12} + {w_{eff}}^i t^i \left(n^i - n_{eff}\right)^2. \tag{6.5}$$

As the bending tongue is incorporated in a wide beam, i.e. width-to-depth ratio larger than 12 [264], it is also necessary to apply a correction in order to use the Euler-Bernoulli beam theory [167]. The Young modulus of the composite beam, $E_{\mathrm{Y},eff}$ should be substituted by:

$$E_{\mathrm{Y},eff} \rightarrow \frac{E_{\mathrm{Y},eff}}{1 - {\nu_{eff}}^2}, \tag{6.6}$$

where ν_{eff} corresponds to the Poisson ratio of the substrate as per the equivalent cross-section obtained from Equation (6.2).

Due to both loads, i.e. the own weight of the bending tongue and load applied at its free end, and strains, i.e. built-in and ferroelectric strains, acting simultaneously on the bending tongue, the equation describing its vertical deflection, $z(x)$, along the z-axis, is complex. However, the method of superposition [167] allows the total vertical deflection to be defined as the sum of the deflections due to both loads and strains. Therefore, each component of the deflection can be calculated independently.

6.3.1. Deflection due to loads

$Q(x)$, the load distribution of the own weight of the bending tongue, q^W, over its whole length and the load applied at its free end, q^L, over the *length load* can be described by the following equation using the Macaulay brackets:

$$Q(x) = q^W + q^L < x - x_m >^0, \tag{6.7}$$

where x_m corresponds to the position on the x-axis at which *length load* begins, ranging from $x = x_m$ to $x = x_l$, the position at the free end of the bending tongue. The Macaulay brackets describe a discontinuous function expressed by the following equation [266]:

$$< x - x_m >^p = \begin{cases} 0 & x \leq x_m \\ (x - x_m)^p & x > x_m \end{cases}, \tag{6.8}$$

where p is an integer.

According to the Euler-Bernoulli beam theory, the equation describing the vertical deflection of the bending tongue can be obtained through four consecutive integrations of the load distribution over the length of the bending tongue. As the bending tongue is fixed at one end in $x = 0$ and $z = 0$, it is subjected to neither any shear force nor bending moment at its free end at which $x = x_l$. It also does not have a slope or a deflection at its fixed end. Therefore, the following boundary conditions can be applied:

$$z^{III}(x = x_l) = 0, \tag{6.9}$$

$$z^{II}(x = x_l) = 0, \tag{6.10}$$

$$z^{I}(x = 0) = 0, \tag{6.11}$$

$$z(x = 0) = 0, \tag{6.12}$$

where z^I, z^{II} and z^{III} are the first, second and third derivatives of $z(x)$, the vertical deflection.

From Equations (6.7) and (6.9) to (6.12), the equation of vertical deflection due to the own weight of the bending tongue and the load applied at its free end can be obtained:

$$z(x) = \frac{1 - {\nu_{eff}}^2}{24 E_{\mathrm{Y},eff} I_{eff}} \Bigg[q^W x^4 + q^L < x - x_m >^4 + 4\left(-q^W x_l - q^L (x_l - x_m)\right) x^3 + 12 \left[q^W \frac{{x_l}^2}{2} + q^L (x_l - x_m) \left(x_l - \frac{x_l - x_m}{2} \right) \right] x^2 \Bigg]. \tag{6.13}$$

The detailed calculations from Equation (6.7) to Equation (6.13) are given in Appendix G.

6.3.2. Deflection due to strains

Both terms of the built-in strain in the ferroelectric layer, i.e thermal strain and eventual misfit strain, as well as ferroelectric strain have components in the xy-plane and in the z-direction. However, their components in the z-direction can be neglected as the top surface of the bending tongue is free and, therefore, unconstrained.

To maintain the force equilibrium in the bending tongue, the in-plane built-in strain, κ_b, and the in-plane ferroelectric strain, κ_f, generate longitudinal strains in both the x-direction and the y-direction [267]. These created strains, ${\kappa_b}^{long}$ and ${\kappa_f}^{long}$, respectively, are defined as:

$${\kappa_b}^{long} = -\frac{{E_\mathrm{Y}}^{ferro} t^{ferro} \kappa_b}{\sum_i {E_\mathrm{Y}}^i t^i}, \tag{6.14}$$

$${\kappa_f}^{long} = -\frac{{E_\mathrm{Y}}^{ferro} t^{ferro} \kappa_f}{\sum_i {E_\mathrm{Y}}^i t^i}, \tag{6.15}$$

where ${E_\mathrm{Y}}^{ferro}$ and ${E_\mathrm{Y}}^i$ correspond to the Young moduli of the ferroelectric layer and of every individual layer of the bending tongue, respectively. t^{ferro} corresponds to the thickness of the ferroelectric layer of the bending tongue.

The in-plane built-in and ferroelectric strains also generate a bending moment due to a net force created in each individual layer and acting through a moment arm spanning from the mid-plane of the layer, n^i (see Equation (6.4)), to the neutral axis of the bending tongue with the equivalent cross-section, n_{eff}

(see Equation (6.3)) [267]. The bending moment due to the built-in strain, M_b, and the one due to the ferroelectric strain M_f, arising from the forces acting in each layer due to ${\kappa_b}^{long}$ and to ${\kappa_f}^{long}$, respectively, as well as to the forces acting in the ferroelectric layer due to κ_b and to κ_f, respectively, are expressed as:

$$\begin{aligned} M_b = &\sum_i {E_Y}^i t^i {w_{eff}}^i \left(n^i - n_{eff}\right) {\kappa_b}^{long} \sin(\theta_{strain}) \\ &+ {E_Y}^{ferro} t^{ferro} {w_{eff}}^{ferro} \left(n^{ferro} - n_{eff}\right) \kappa_b \sin(\theta_{strain}), \end{aligned} \tag{6.16}$$

$$\begin{aligned} M_f = &\sum_i {E_Y}^i t^i {w_{eff}}^i \left(n^i - n_{eff}\right) {\kappa_f}^{long} \sin(\theta_{strain}) \\ &+ {E_Y}^{ferro} t^{ferro} {w_{eff}}^{ferro} \left(n^{ferro} - n_{eff}\right) \kappa_f \sin(\theta_{strain}), \end{aligned} \tag{6.17}$$

where ${w_{eff}}^{ferro}$ and n^{ferro} are the effective width and the mid-plane of the ferroelectric layer, respectively. The angle between the in-plane force due to the strain and the moment arm is noted θ_{strain}. If the mid-plane of a layer, n^i, is located above the effective neutral axis of the bending tongue, n_{eff}, then $\theta_{strain} = -90°$ and if n^i is smaller than n_{eff} then $\theta_{strain} = 90°$.

The bending moment M_b, due to the built-in strain, is acting over the whole length of the bending tongue while M_f, due to the ferroelectric strain, is acting over the length of the bending tongue minus the *length load*. The distribution of these bending moments, $M(x)$, is described by the following equation using the Macaulay brackets:

$$M(x) = M_b + M_f \left(1 - < x - x_m >^0\right). \tag{6.18}$$

According to the Euler-Bernoulli beam theory, integrating twice the equation for the distribution of the bending moments due to κ_b and κ_f gives the corresponding equation for the vertical deflection. It can be obtained from Equations (6.11), (6.12) and (6.18):

$$z(x) = \frac{1 - {\nu_{eff}}^2}{2{E_Y}^{eff} I_{eff}} \left[\left(M_b + M_f\right) x^2 - M_f < x - x_m >^2\right]. \tag{6.19}$$

The detailed calculations from Equation (6.18) to Equation (6.19) are given in Appendix H.

Both the built-in strain and the ferroelectric strain are dependent on the crystallographic state of the ferroelectric layer (polycrystalline, textured or epitaxial). Therefore, it is necessary to describe the crystallographic state mathematically.

6.3.2.1. Mathematical formulation of the crystallographic state

Following Hwang's model [77] for ferroelectric switching, the orientation of each crystallographic grain has an impact on the global ferroelectric strain and should therefore be taken into account. For this purpose, a series of systems of local coordinates defined relative to the *global reference frame* and referred to as *grain coordinates* is defined.

The orientation of each grain is set by a group of three Euler angles, φ_1, ϕ, φ_2, allowing conversion of coordinates from the *global reference frame* to the *grain coordinates* of each grain. As various conventions exist to define the Euler angles, the one chosen here is described below and represented in Figure 6.3.

The first rotation of angle φ_1 around the z-axis creates the u-axis and v-axis in the xy-plane. The second rotation is made around the v-axis with an angle of ϕ. It creates the w-axis as well as the z'-axis. The third

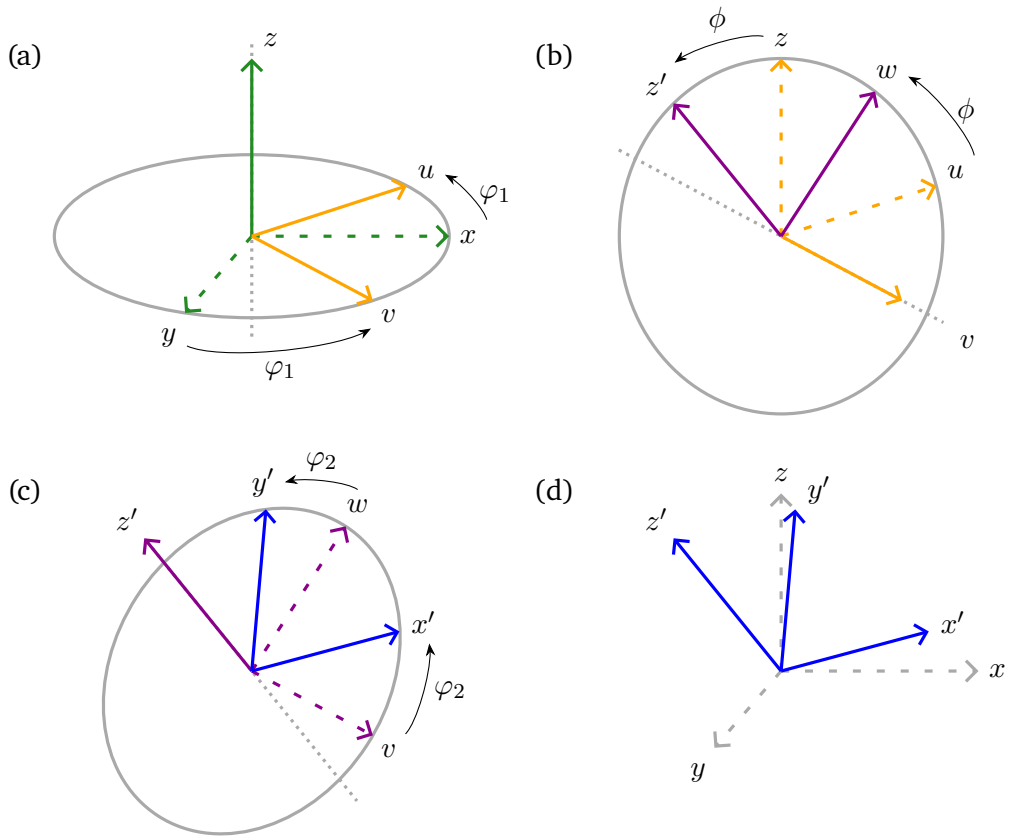

Figure 6.3.: Schematic representation of the three Euler angles to convert coordinates from the *global reference frame* (green vectors) to the *grain coordinates* (blue vectors) of each grain. (a) *global reference frame* defined by the vectors x, y and z with the first rotation of angle φ_1 around the z-axis, (b) second rotation of angle ϕ around the v-axis, (c) third rotation of angle φ_2 around the z'-axis and (d) representation of the *global reference frame* and the *grain coordinates* defined by the vectors x', y' and z'. Adapted from [265].

rotation occurs around the z'-axis with an angle of φ_2 and creates the x'-axis and the y'-axis. The *grain coordinates* of each grain are expressed in the reference frame made by the x'-axis, y'-axis and z'-axis.

These three successive rotations are described by the transformation matrix allowing to express the *grain coordinates* in the *global reference frame* as shown in the following equation:

$$\begin{pmatrix} x' \\ y' \\ z' \end{pmatrix} = \begin{pmatrix} k_{1,1} & k_{1,2} & k_{1,3} \\ k_{2,1} & k_{2,2} & k_{2,3} \\ k_{3,1} & k_{3,2} & k_{3,3} \end{pmatrix} \begin{pmatrix} x \\ y \\ z \end{pmatrix}, \tag{6.20}$$

where $k_{g,h}$ corresponds to the coefficients of the transformation matrix with $g, h = 1, 2, 3$.

The coefficients $k_{g,h}$ are given in the following equations:

$$k_{1,1} = cos(\varphi_1)cos(\varphi_2) - sin(\varphi_1)sin(\varphi_2)cos(\phi), \tag{6.21}$$
$$k_{1,2} = -sin(\varphi_2)cos(\varphi_1) - cos(\phi)sin(\varphi_1)cos(\varphi_2), \tag{6.22}$$
$$k_{1,3} = sin(\phi)sin(\varphi_1), \tag{6.23}$$
$$k_{2,1} = cos(\varphi_2)sin(\varphi_1) + cos(\phi)cos(\varphi_1)sin(\varphi_2), \tag{6.24}$$
$$k_{2,2} = -sin(\varphi_2)sin(\varphi_1) + cos(\phi)cos(\varphi_1)cos(\varphi_2), \tag{6.25}$$
$$k_{2,3} = -sin(\phi)cos(\varphi_1), \tag{6.26}$$
$$k_{3,1} = sin(\phi)sin(\varphi_2), \tag{6.27}$$
$$k_{3,2} = sin(\phi)cos(\varphi_2), \tag{6.28}$$
$$k_{3,3} = cos(\phi). \tag{6.29}$$

The Euler angles inherent to the grains are defined according to the three possible crystallographic states of the modelled ferroelectric layer. If the sample is polycrystalline, then all grains of the ferroelectric are randomly oriented and, therefore, the values of the three Euler angles are each randomly defined within their bounds, i.e. $0 < \varphi_1 < 2\ \pi$; $0 < \phi < \pi$ and $0 < \varphi_2 < 2\pi$.

In the case of a textured ferroelectric layer, a given percentage of grains are rotated by a few degrees around a given orientation, O_{ferro}, while the remaining grains are randomly oriented. The distribution of grains around the orientation O_{ferro} can be simulated by the following Gaussian function [268]:

$$S(\Psi) = \frac{8\sqrt{\pi}}{\zeta\Psi_0^3} \exp\left(\frac{-\Psi^2}{\Psi_0^3}\right), \tag{6.30}$$

where Ψ is the rotation angle around the orientation O_{ferro}, Ψ_0 is the full width at half-maximum of the Gaussian distribution and ζ is the multiplicity due to the symmetry of the crystallographic unit cell.

Once normalised, the Gaussian distribution given in Equation (6.30) contains 99.9 % of the grains oriented around the orientation O_{ferro} between -3Ψ and $+3\Psi$. The distance between these two angles is separated into 10 segments, each containing a number of grains as defined by the Gaussian distribution. The grains contained in each segment are rotated by the average angle of the given segment around the orientation O_{ferro}.

If the ferroelectric layer is textured in-plane, the angle of rotation is the first Euler angle, φ_1, while ϕ and φ_2 are set to $0°$. In the case of an out-of-plane texture, it is the second Euler angle, ϕ, which corresponds to the angle of rotation while φ_1 and φ_2 are set to $0°$. A combination of in-plane and out-of-plane texture can be described by simultaneous rotations of φ_1 and ϕ.

The remaining grains which do not display texture around the orientation O_{ferro} are modelled by applying random values to their three Euler angles, as it is the case for a polycrystalline ferroelectric.

In this model, epitaxy is defined as the perfect alignment of grains in a given orientation O_{ferro}. Therefore, if the ferroelectric layer is epitaxial, all the Euler angles are set to $0°$, independent of any possible long range order between ferroelectric layer and substrate.

6.3.2.2. Built-in strain

The built-in strain in the ferroelectric layer, κ_b, is the sum of the thermal strain and the misfit strain. The choice of equation to calculate the former is dependent on the thickness of the thin film. The equation for the latter is dependent on both the thin film thickness and its crystallographic state.

The thickness of the thin film mainly impacts the ability of the ferroelectric layer to relax. As the nature (strain, morphology, etc.) of the modelled thin film is unknown, its relaxation threshold should be determined and the corresponding equations should be used.

If the ferroelectric is not relaxed, its thermal strain, ${\kappa_b}^{thermal}$, due to cooling down from its deposition temperature, T_{depo}, to the operating temperature of the bending tongue, T_{oper}, is expressed by:

$$ {\kappa_b}^{thermal} = (T_{depo} - T_{oper}) \left(\alpha^{subs} - \alpha^{ferro} \right), \tag{6.31} $$

where α^{subs} and α^{ferro} correspond to the thermal expansion coefficients of the substrate and of the ferroelectric layer, respectively.

If the ferroelectric layer is relaxed, the bi-axial stress present at the Curie temperature, T_{C}, is partially released through the development of a domain structure [269]. The transformation stress concept implies that the thermal strain of a relaxed ferroelectric layer is described by [270]:

$$ {\kappa_b}^{thermal} = (T_{depo} - T_{\mathrm{C}}) \left(\alpha^{subs} - \alpha^{ferro} \right). \tag{6.32} $$

Regarding the misfit strain, polycrystalline films are relaxed. For non-relaxed epitaxial ferroelectric films the misfit strain, ${\kappa_b}^{misfit}$, calculated at the film deposition temperature is described by:

$$ {\kappa_b}^{misfit} = \left(\frac{a^{buffer} - a^{ferro}}{a^{ferro}} \right)_{T_{depo}}, \tag{6.33} $$

where a^{ferro} and a^{buffer} are the lattice parameters for misfit strain calculation for the ferroelectric layer and the adjacent buffer layer, respectively.

If the ferroelectric layer is textured and not relaxed, its misfit strain is calculated from Equation (6.33) and is multiplied by the ratio of textured grains.

In all of the above mentioned cases, the total strain can be reduced by a given degree of relaxation to model any further relaxation which could happen after the ferroelectric layer deposition.

6.3.2.3. Ferroelectric strain

The ferroelectric strain originates from both the ferroelectric switching strain component and the linear strain component. Hwang's model [77] processes each grain individually before averaging the ferroelectric strain and polarisation values over the number of grains modelled. This individual processing of the grains imposes the need to work in *grain coordinates*. Therefore, every value in the *global reference frame* should be converted into *grain coordinates* through the use of the Euler angles. Once the ferroelectric strain and matching polarisation values are known for each individual grain, they should be converted back into the *global reference frame* before averaging.

Each grain is treated as if it is composed of unit cells displaying the same behaviour, i.e. the same orientation relative to the *global reference frame*, simultaneous ferroelectric switching, etc., and therefore in this section *grain* can be replaced by *unit cell* for ease of comprehension.

Hwang et al. considered the sum of the electrical and mechanical work resulting from switching the polarisation from its current direction to another one. Ferroelectric switching occurs if the applied electrical field is larger than a switching criterion expressed by [77]:

$$E\Delta P + \sigma\Delta\kappa_{int} > 2P_s E_c, \tag{6.34}$$

where E and σ correspond to the electrical field and to the stress, respectively, applied to the ferroelectric during the switching process. ΔP and $\Delta\kappa_{int}$ refer to the difference between before and after ferroelectric switching for the polarisation and internal unit cell strain values, respectively. P_s refers to the spontaneous polarisation of the ferroelectric and E_c refers to its coercive field.

According to Hwang's model, the polarisation vector is parallel to the edge of the tetragonal unit cell. In the model presented in this thesis, the polarisation vector lies at the centre of the unit cell and can only take six different orientations which is in agreement with Hwang's model. The six possible orientations of the polarisation in a tetragonal perovskite ferroelectric (see Figure 2.5), labelled from 1 to 6, are expressed in *grain coordinates* as [100], [$\bar{1}$00], [010], [0$\bar{1}$0], [001] and [00$\bar{1}$], respectively.

The internal unit cell strain values correspond to the elongation or the contraction of the cubic unit cell into the tetragonal one. These values are expressed as a function of strain along the unit cell a-axis, κ_a, or along its c-axis, κ_c. These two quantities are defined by:

$$\kappa_a = \frac{a^{tetragonal} - a^{cubic}}{a^{cubic}}, \tag{6.35}$$

$$\kappa_c = \frac{c^{tetragonal} - a^{cubic}}{a^{cubic}}, \tag{6.36}$$

where a and c refer to the lattice parameters of the ferroelectric unit cell. The crystal system is indicated by the superscript, either $tetragonal$ or $cubic$.

The internal unit cell strains inherent to the polarisation orientations from 1 to 6 are $[\kappa_c, \kappa_a, \kappa_a]$, $[\kappa_c, \kappa_a, \kappa_a]$, $[\kappa_a, \kappa_c, \kappa_a]$, $[\kappa_a, \kappa_c, \kappa_a]$, $[\kappa_a, \kappa_a, \kappa_c]$ and $[\kappa_a, \kappa_a, \kappa_c]$, respectively.

From the values of the polarisation orientations and of the internal unit cell strains, it can be noted that $180°$ ferroelectric switching would give rise to electrical work only while $90°$ switching would give rise to both electrical and mechanical work if dynamic poling is ignored [122].

If several switching cases are possible for the same grain, i.e. the work associated with several switching events between the current polarisation direction and a resulting one are larger than Hwang's switching criterion (see Equation (6.34)), then switching occurs in the direction resulting in the largest possible work.

The stress σ applied on the ferroelectric layer which is used to calculate the mechanical work is the one inherent to the built-in strain κ_b described in section 6.3.2.2. According to the assumptions stated in section 6.2.2, the ferroelectric material is a linear, homogeneous and isotropic material. In this case:

$${\kappa_b}^x = \kappa_b, \tag{6.37}$$

$${\kappa_b}^y = {\kappa_b}^x, \tag{6.38}$$

$${\kappa_b}^z = -\frac{{\kappa_b}^x}{\nu^{ferro}}, \tag{6.39}$$

where the superscripts x, y and z correspond to the directions in which the built-in strain is expressed in the *global reference frame* and ν^{ferro} in the Poisson ratio of the ferroelectric layer.

By combining Equations (6.37) to (6.39) with Hooke's law for a linear, homogeneous and isotropic material, it yields:

$$\sigma^x = 0, \tag{6.40}$$

$$\sigma^y = 0, \tag{6.41}$$

$$\sigma^z = {E_Y}^{ferro} \frac{2\nu^{ferro} - \frac{1}{\nu^{ferro}} + 1}{(1+\nu^{ferro})(1-2\nu^{ferro})} {\kappa_b}^x. \tag{6.42}$$

The electrical field applied to the ferroelectric layer which is used to calculate the electrical work depends on which one of the four states of the bending tongue is being modelled (see section 6.2.1). While the states *as deposited* and *inactive* are not subjected to any electrical field, the states *poled* and *active* are subjected to the poling and applied electrical fields, respectively.

The ferroelectric switching strain corresponds to the average, in the *global reference frame*, of the strain resulting from Hwang's switching criterion method. The second component of the ferroelectric strain is the linear strain in the xy-plane, ${\kappa_f}^{linear}$, described by:

$${\kappa_f}^{linear} = E d_{31}, \tag{6.43}$$

where E is the applied electrical field along the z-axis and d_{31} is the piezoelectric coefficient linking E and the strain along the x-axis.

While Hwang's model allows the calculation of the ferroelectric strain, it has two severe limitations: the saturation of the linear ferroelectric strain is not taken into account and the remanent strain is calculated empirically. The model here described proposes a solution to these two points.

From Hwang's model the polarisation can be plotted versus the applied electrical field, E. It is possible to determine the applied field at which saturation is reached, E_{sat}, as the point where the *P-E* loop closes. This point is located on loops subsequent to the poling step, when the respective values of E and polarisation are equal on the branches of increasing and decreasing applied field.

Once the value of the applied electrical field at which saturation is reached is known, all further calculations can be adapted by replacing E with E_{sat} in Equation (6.43) once E becomes larger than E_{sat}. This approach generates underestimated strain values above saturation, which is more relevant for applications than neglecting saturation.

It is also possible, by plotting the ferroelectric strain κ_f versus the applied electrical field E, to obtain the remanent strain which corresponds to the value of κ_f at $E = 0$, after the poling step.

In summary, the bending tongue is subjected to the ferroelectric switching and linear strains in the *poled* state, to the remanent strain in the *inactive* state and to the remanent and linear strains in the *active* state. This is due to the fact that during operation the bending tongue is driven between the *inactive* and *active* states which does not cause any ferroelectric switching.

To recapitulate the calculation method of the vertical deflection of a ferroelectric bending tongue loaded at its free end with the model introduced in this thesis, a flowchart of the process is shown in Figure 6.4.

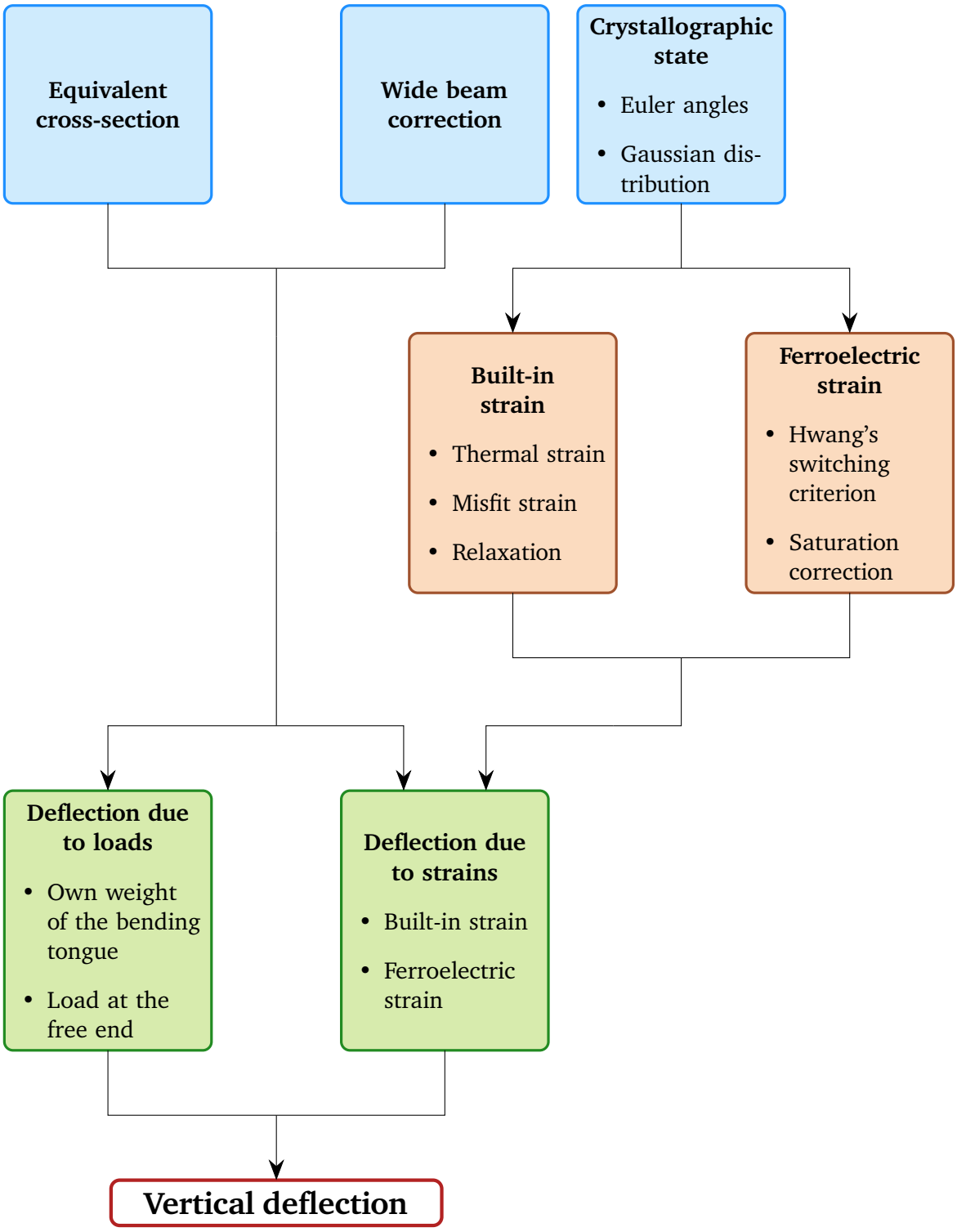

Figure 6.4.: Flowchart of the process to calculate the vertical deflection of a ferroelectric bending tongue loaded at its free end with the proposed model.

6.4. Results and discussion of the modelling

The modelling results presented in this section are not calculated based on the material properties of the samples deposited in this thesis (see chapter 5). Indeed, due to the large number of material properties necessary for the modelling, the measurement of a significant number of these properties is out of the scope of this thesis, e.g. Young modulus, Poisson ratio, thermal expansion coefficient, etc. Therefore, the material properties used thereafter are extracted from literature.

Unless otherwise mentioned, the results given hereafter correspond to the modelling with the developed *FeBeTo* program [263] of a bending tongue composed of AISI 304 stainless steel as a substrate, $LaNiO_3$ as a buffer layer and $PbZr_{0.52}Ti_{0.48}O_3$ for the ferroelectric layer. The layers have thicknesses of 100 µm, 0.004 µm and 1 µm, respectively. The modelled bending tongue has a length of 10 mm, a width of 3 mm and is subjected to a load of $5 \cdot 10^{-5}$ N applied over 1 mm at its free end. The $PbZr_{0.52}Ti_{0.48}O_3$ layer is epitaxial and has the density of tetragonal PZT, as assumed in the model. The applied electrical field is 500 $kV{\cdot}cm^{-1}$. The modelling parameters used for the physical and mechanical properties of the ferroelectric, buffer and substrate layers are given in Table 6.1.

A polarisation versus applied electrical field curve, or *P-E* loop, has been modelled in Figure 6.5 for an epitaxial and a polycrystalline $PbZr_{0.52}Ti_{0.48}O_3$ layer. It can be noted that the polycrystalline *P-E* loop is rounded and wider than the epitaxial one, which is more square-shaped. Indeed, due to the random orientation of grains in the polycrystalline layer, the alignment of each grain polarisation towards the applied field direction is progressive. Each grain perceives the applied electrical field differently due to its own orientation.

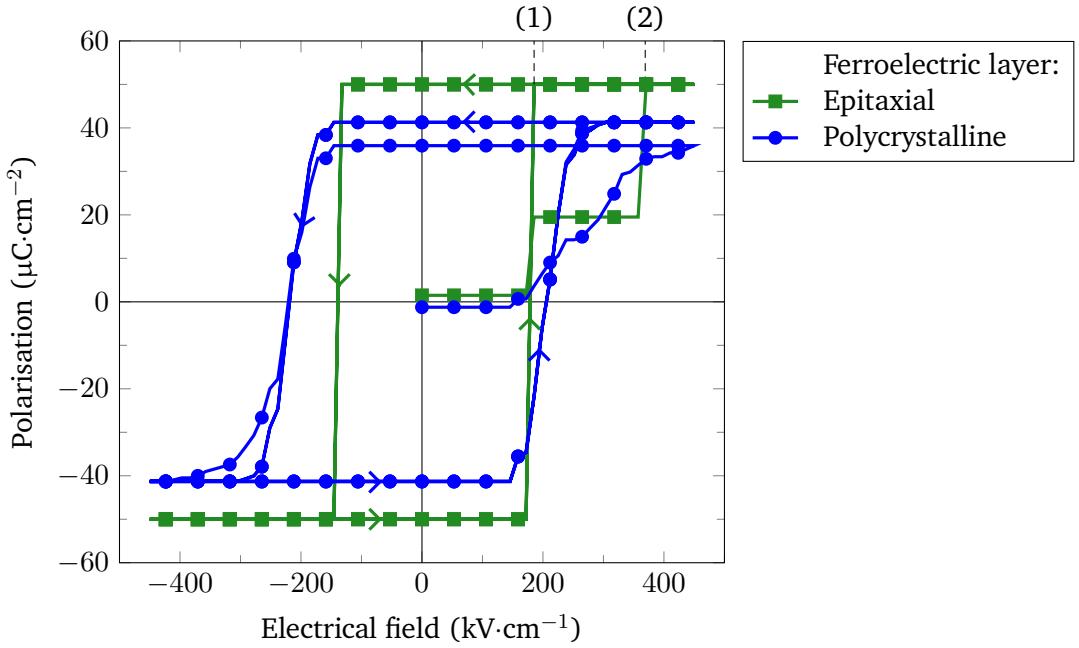

Figure 6.5.: Modelled polarisation, P, versus applied electrical field, E, curve in the case of an epitaxial (green squares) and a polycrystalline (blue circles) ferroelectric layer. (1) and (2) indicate $180°$ and $90°$ switching of the epitaxial film, respectively.

Table 6.1.: Physical and mechanical properties of materials used for modelling. Ferroelectric material: $PbZr_{0.52}Ti_{0.48}O_3$, buffer layer: $LaNiO_3$ and substrate: AISI 304 stainless steel (EN: 1.4301). Adapted from [265].

	Parameter	Value
Ferroelectric layer	Young modulus [271]	$9.9 \cdot 10^{10}$ Pa
	Poisson ratio [272]	0.31
	Coercive field [273]	$1.5 \cdot 10^{7}$ V·m^{-1}
	Spontaneaous polarisation [274]	0.5 C·m^{-2}
	Piezoelectric coefficient d_{31} [275]	$-97 \cdot 10^{-12}$ V·m^{-1}
	Lattice parameter tetragonal a [140]	$4.043 \cdot 10^{-10}$ m
	Lattice parameter tetragonal c [140]	$4.132 \cdot 10^{-10}$ m
	Lattice parameter cubic a (above the Curie temperature) [139]	$4.085 \cdot 10^{-10}$ m
	Thermal expansion coefficient [276]	$2 \cdot 10^{-6}$ K^{-1}
	Curie temperature [275]	573 K
	Density [275]	7,600 kg·m^{-3}
Buffer layer	Young modulus [277]	$5.63 \cdot 10^{7}$ Pa
	Lattice parameter for epitaxial strain calculation [196]	$3.851 \cdot 10^{-10}$ m
	Density [196]	7,141 kg·m^{-3}
Substrate	Young modulus [239]	$2.0 \cdot 10^{11}$ Pa
	Poisson ratio [278]	0.27
	Thermal expansion coefficient [239]	$16.5 \cdot 10^{-6}$ K^{-1}
	Density [239]	7,900 kg·m^{-3}

The sharp ferroelectric *P-E* loop for the epitaxial case, on the other hand, is due to the perfect alignment of all grains. As they perceive the applied electrical field in the same manner, they answer to it simultaneously.

Furthermore, in the epitaxial *P-E* loop the poling appears as a two steps process. $180°$ ferroelectric switching occurs at a lower applied field of 175 kV·cm^{-1} than $90°$ switching which occurs at 360 kV·cm^{-1}. This phenomenon is consistent with the modelling of the ferroelectric strain described in section 6.3.2.3: as $180°$ switching is only due to electrical work, it requires less energy than $90°$ switching, which is due to both electrical and mechanical work. Indeed, while both $180°$ and $90°$ switching involve a change in polarisation, $90°$ switching also implies a change in strain. The tetragonal unit cell is deformed, shortening along its c-axis and elongating along its a-axis, effectively inverting its a-axis and its c-axis.

Once the individual polarisation of each grain has been switched and aligned as closely as possible with the applied field direction, only $180°$ switching remains.

Both epitaxial and polycrystalline *P-E* loops are shifted towards the right-hand side of the graph by

26.5 kV·cm^{-1}. This shift is due to the built-in strain, i.e. thermal and eventual misfit strains, which generates stress on the ferroelectric layer, impacting the mechanical work required to switch the polarisation of a given grain (see Equations (6.34) and (6.42)).

Besides the poling step from 0 to 450 kV·cm^{-1}, the *P-E* loops have been plotted by decreasing the applied field to -450 kV·cm^{-1} and subsequently increasing it to 450 kV·cm^{-1} three consecutive times. In the case of the epitaxial *P-E* loop, only one trace can be seen from these three consecutive loops. Hence, the epitaxial ferroelectric displays reproducible behaviour.

In the case of the polycrystalline *P-E* loop, two traces can be seen while the applied electrical field is decreasing: one starting from the poling step and one from the first branch where the applied field increases. This originates from the random alignment of the grains in the polycrystalline sample: as they do not all perceive the applied field in the same manner due to their own orientation, the electrical work is different from one grain to the other. Some grains might not have had enough energy during the poling step to switch and align their polarisation with the applied field direction. In this case, the ferroelectric switching might be more favourable when the applied field is oriented in the opposite direction. It can be noticed, that once the field has been increased through the poling step and decreased once, the second and third *P-E* loops are identical indicating that all grains are switching when the applied field direction is reversed.

The grain orientation also impacts the vertical deflection of the bending tongue as can be seen in Figure 6.6. Based on the definition of the crystallographic state given in section 6.3.2.1, a polycrystalline ferroelectric should behave in the same way as a 0 % textured one while an epitaxial ferroelectric should behave identically to a 100 % textured one, which is confirmed by the simulation.

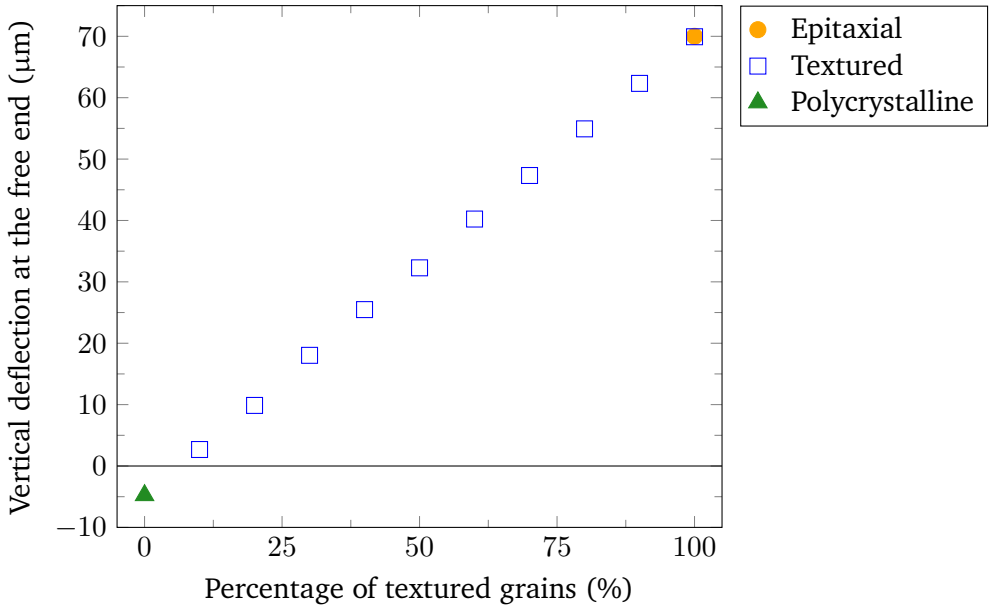

Figure 6.6.: Evolution of the vertical deflection at the free end of the bending tongue, z_l, as a function of the percentage of textured grains (blue open squares). The case of an epitaxial (orange circle) and a polycrystalline (green triangle) ferroelectric layer are shown for comparison.

It can be noted that the polycrystalline sample displays a slightly negative vertical deflection of -4.77 µm while every bending tongue modelled with either a textured or epitaxial ferroelectric layer bends upwards.

The ferroelectric strain being smaller than in the other cases, the deflection is determined by the other terms which are bending the bending tongue downwards, e.g. the own weight of the bending tongue or the load applied at its free end.

The strain versus applied electrical field curve, or *butterfly* loop, is represented in Figure 6.7. It displays the ferroelectric strain saturation and the remanent strain, characteristic of ferroelectric behaviour. Along with the hysteretic behaviour shown in the *P-E* loops, it proves that ferroelectrics are properly modelled.

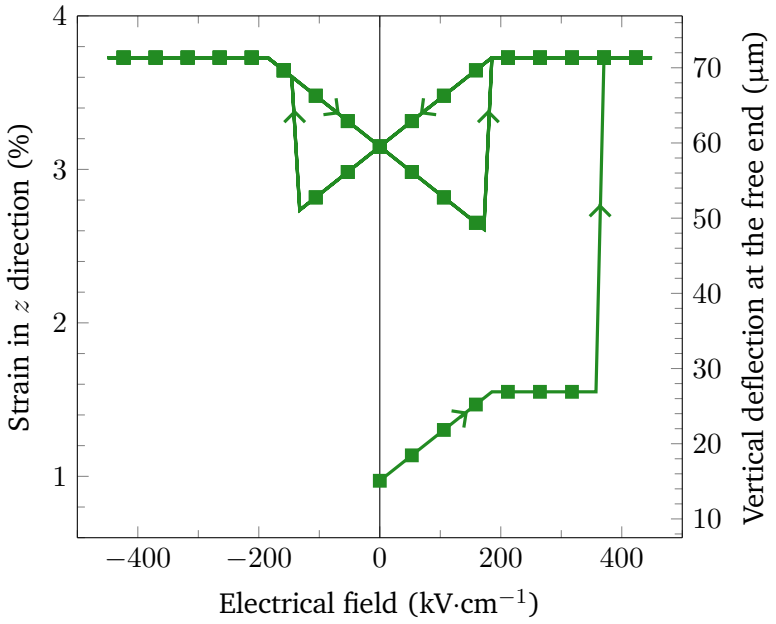

Figure 6.7.: Modelled strain in the z-direction, κ^z, and vertical deflection at the free end of the bending tongue, z_l, versus applied electrical field, E, curve in the case of an epitaxial ferroelectric layer.

It should be noted that the strain in the z direction, κ^z, is calculated through:

$$\kappa^z = -\frac{\kappa_f}{\nu^{ferro}}, \tag{6.44}$$

and corresponds to the ferroelectric strain in the bending tongue perpendicular to its surface. The vertical deflection is obtained through the equations of section 6.3 for the corresponding strain values of the *butterfly* loop.

The lack of symmetry in the *butterfly* loop is due to the built-in strain, generating stress on the ferroelectric layer, similar to the *P-E* loops.

Two key elements of the *butterfly* loop, which were not present in Hwang's model, are the saturation of the ferroelectric strain, clearly visible, and the remanent strain. The modelled ferroelectric saturates at 3.73 % strain, equivalent to 71.4 μm of vertical deflection. This last value is essential for applications as it defines the maximum vertical deflection of the bending tongue. The modelled remanent strain, 3.15 %, is 3.8 times larger than the empirical remanent strain calculated from Hwang et al. [77]. This is due to the built-in strain, constraining the ferroelectric layer, which has not been taken into account by Hwang's model.

The respective contributions of the own weight of the bending tongue, the load applied at its free end, the built-in and the ferroelectric strains to the vertical deflection, $z(x)$, are shown in Figure 6.8. In the given example, under an applied field of 500 kV·cm^{-1}, the main contribution comes from the ferroelectric strain. The built-in strain, load at the free end of the bending tongue and its weight account for 4.43 %, 1.19 % and 0.71 % of the vertical deflection due to the ferroelectric strain, respectively. However, as these three terms are deflecting the bending tongue downwards opposing the ferroelectric strain, the sum of all terms is smaller than the vertical deflection due to the ferroelectric strain.

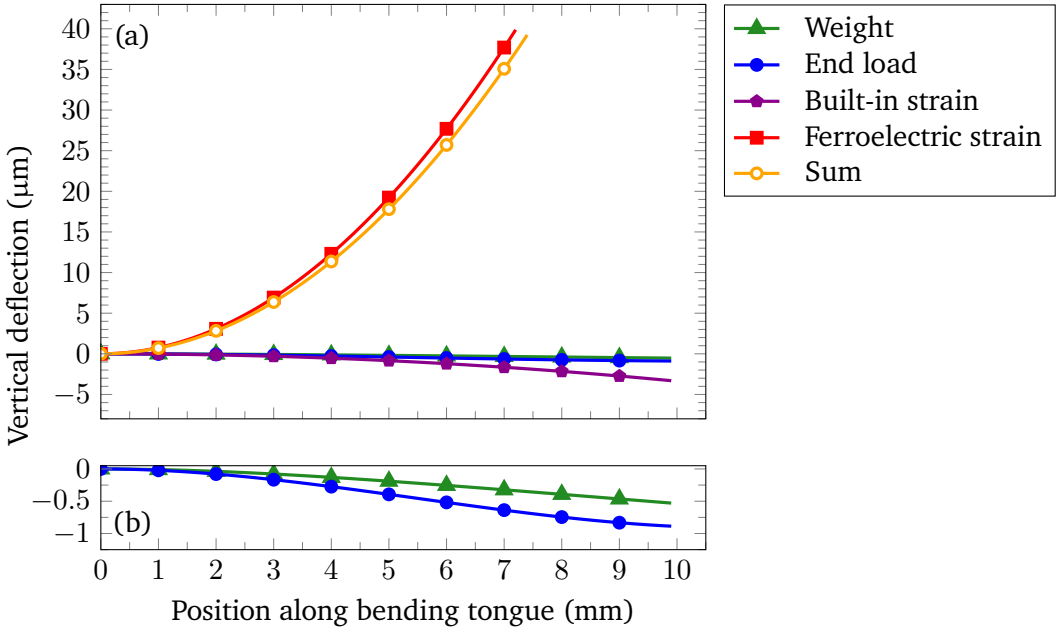

Figure 6.8.: Contributions to the vertical deflection, $z(x)$, of the bending tongue. (a) Individual contributions from weight (green triangles), end load (blue circles), built-in strain (purple pentagons) and ferroelectric strain (red squares) as well as sum of all contributions (orange open circles), (b) zoom on weight and end-load individual contributions.

The relative importance of each contribution is strongly dependent on the parameters chosen for the modelling. While all parameters, i.e. materials related or geometrical, can be varied in the proposed model, a set of relevant parameters is being varied in the following examples to discuss their impact. The applied electrical field is kept constant at 500 kV·cm^{-1} to model results at saturation.

A crucial component of the bending tongue is the ferroelectric layer, its thickness being decisive for the vertical deflection, as shown in Figure 6.9. In the given example, the vertical deflection at the free end of the bending tongue which can be reached, z_l, increases almost proportionally to the thickness of the ferroelectric layer. As the ferroelectric thickness increases from 0.2 µm to 2.0 µm, the vertical deflection at the free end of the bending tongue increases from $z_l = 50.2$ µm to $z_l = 552.9$ µm.

While the vertical deflection is important for applications, the variation in vertical deflection at the free end of the bending tongue between the *active* state, ${z_l}^E$, where an electrical field E is applied and the *inactive* state, ${z_l}^0$, where no electrical field is applied is the key to the accessible range of motion of the bending tongue. For the modelled example, it ranges from ${z_l}^E - {z_l}^0 = 9.5$ µm to ${z_l}^E - {z_l}^0 = 91.2$ µm when the ferroelectric thickness is increased from 0.2 µm to 2.0 µm.

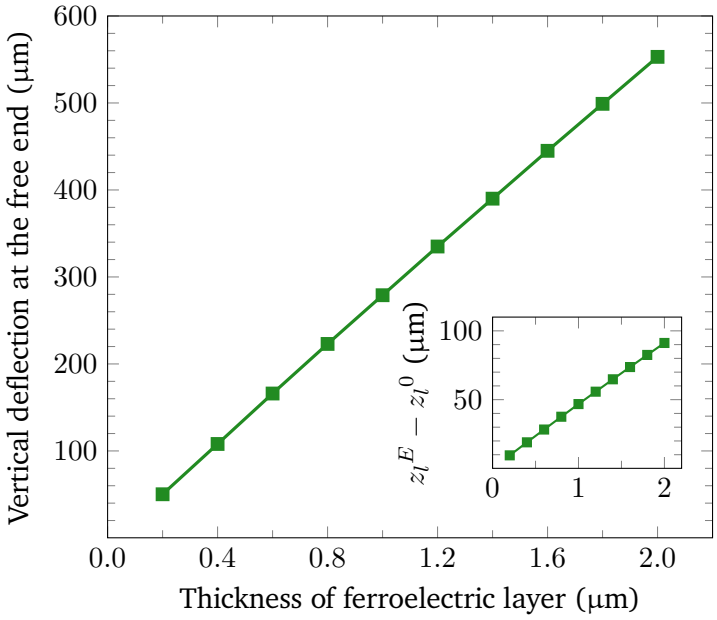

Figure 6.9.: Evolution of the vertical deflection at the free end of the bending tongue, z_l, as a function of the ferroelectric layer thickness with a length of 10 mm and a load at its free end of $5 \cdot 10^{-5}$ N. ${z_l}^E - {z_l}^0$ represents the variation in vertical deflection between the states where an electrical field E is applied and where no electrical field is applied. As E is kept constant at 500 kV·cm^{-1}, saturation is reached.

On the other hand, the vertical deflection at the free end of the bending tongue is not proportional to the length of the bending tongue, as can be seen in Figure 6.10. The vertical deflection increases from $z_l = 2.1$ µm to $z_l = 279.4$ µm as the length is extended from 2 mm to 20 mm. The most important result is once more the variation in vertical deflection between the *active* state and the *inactive* state, reaching ${z_l}^E - {z_l}^0 = 0.4$ µm at a length of 2 mm and ${z_l}^E - {z_l}^0 = 46.8$ µm at a length of 20 mm. The length of the bending tongue, if not restricted in a given application, is therefore an interesting parameter to increase the vertical deflection.

Other parameters also impact the vertical deflection, like the load applied at the free end as represented in Figure 6.11. As the end load increases from 0 mN to 10 mN, the deflection of the bending tongue is inverted from upwards to downwards. This corresponds to the increase of the end load component relative to the ferroelectric component up to the point where it becomes the dominant component of deflection. The critical point at which the direction of the deflection is inverted is reached at an end load of 3.9 mN.

Increasing the load applied at the free end of the bending tongue does not impact the variation in vertical deflection between the *active* state and the *inactive* state, which is mainly determined by the ferroelectric layer thickness and the length of the bending tongue.

It should be noted that some of the parameters impact the vertical deflection in various ways through Equations (6.13) and (6.19). This is the case for the geometrical dimensions of the bending tongue, i.e. length, width, thicknesses of the layers and *length load*, which are parameters of both the own weight of the bending tongue and its effective second moment or area, I_{eff}. This is particularly relevant for the

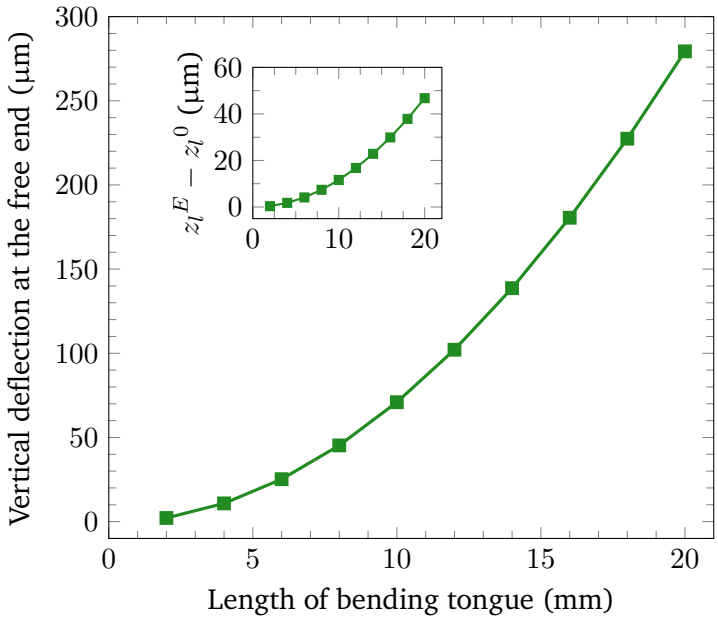

Figure 6.10.: Evolution of the vertical deflection at the free end of the bending tongue, z_l, as a function of the length of the bending tongue with a ferroelectric layer thickness of 1 µm and a load at its free end of $5 \cdot 10^{-5}$ N. ${z_l}^E - {z_l}^0$ represents the variation in vertical deflection between the states where an electrical field E is applied and where no electrical field is applied. As E is kept constant at 500 kV·cm^{-1}, saturation is reached.

length and *length load* as these two parameters are further involved into the equations of vertical deflection (Equations (6.13) and (6.19)).

Other parameters, while having a global impact on the vertical deflection of the bending tongue, impact all terms of the deflection, i.e. the own weight of the bending tongue, the load applied at its free end, the built-in and the ferroelectric strains, in an almost similar manner, maintaining the relative proportions between them. For example, the Young moduli of the materials are mostly taken into account at the forefront of Equations (6.13) and (6.19), effectively impacting all the terms of the deflection. However, these parameters will also have some minor impact on the built-in and ferroelectric strains (see Equations (6.14) to (6.17) and (6.42)). The same behaviour is visible with the respective Poisson ratios of the materials.

Finally, some parameters impact a single component of the vertical deflection. It is the case for the material densities, which affect only the weight component, as well as for the piezoelectric coefficient, d_{31}, and the applied electrical field, which influences only the ferroelectric strain component.

Any built-in strain parameter, like the operating and deposition temperatures, texture parameters, thermal expansion coefficients and lattice parameters of the materials, necessarily influence the ferroelectric strain. This occurs through the stress generated by the built-in strain on the ferroelectric layer, which influences the ferroelectric switching (see Equation (6.42)).

When working towards applications, the main advantage of this large array of parameters resides in the tunability of the bending tongue modelling. Indeed, it is possible to fix a set of parameters based on the constraints of the application and to adapt the other parameters to reach the chosen range of vertical deflection.

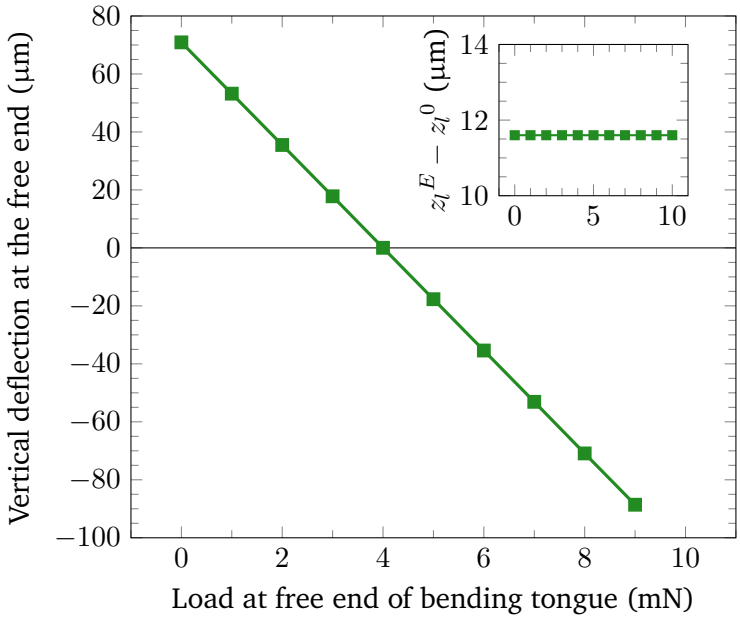

Figure 6.11.: Evolution of the vertical deflection at the free end of the bending tongue, z_l, as a function of the load at its free end with a length of 10 mm and a ferroelectric layer thickness of 1 µm. ${z_l}^E - {z_l}^0$ represents the variation in vertical deflection between the states where an electrical field E is applied and where no electrical field is applied. As E is kept constant at 500 kV·cm^{-1}, saturation is reached.

For example, it is possible to study the impact of the load applied at the free end of the bending tongue on the maximum vertical deflection at the free end. If this load, considered only in Equation (6.13), is the only parameter which can be varied, the deflection at the free end of the bending tongue, in $x = x_l$, can be expressed as:

$$\Delta z(x) = \Delta q^L \frac{1 - {\nu_{eff}}^2}{24 {E_Y}^{eff} I_{eff}} \left(3{x_l}^4 - 4{x_m}^3 x_l + {x_m}^4 \right), \tag{6.45}$$

where $\Delta z(x)$ and Δq^L are the variations in the vertical deflection and in the load applied at the free end of the bending tongue, respectively.

Therefore, if the materials and length of the bending tongue, the ferroelectric layer thickness and the *length load* at the free end are fixed, it is possible to calculate the maximum end load to reach a chosen vertical deflection.

This analysis can be performed for any parameter, giving insight into the respective impact of each parameter and allowing optimisation of the bending tongue when some parameters are constrained by the application.

6.5. Conclusions relative to the modelling

The proposed modelling of ferroelectric bending tongues gives **access to the vertical deflection while taking ferroelectric switching on the grain scale into account**. The proper modelling of ferroelectric

switching can be verified through the ***P-E* loop and the *butterfly* loop, both displaying hysteretic behaviour and saturation**.

The description of the saturation in the *butterfly* loop is an improvement of Hwang et al.'s model on which the description of ferroelectric switching is based. This addition is **crucial for applications were the maximum accessible deflection and the corresponding applied electrical field required to reach it are needed**.

Additional features have been added, notably the calculation of the remanent strain and the **impact of the crystallographic state of the ferroelectric** (polycrystalline, textured or epitaxial). The influence of built-in strain on the polarisation highlighted by this model has been demonstrated experimentally by Coleman, Walker, Beechem and Trolier-McKinstry [53] since its publication [265].

The large amount of parameters taken into account in this model allows the relative importance of the contributions to the vertical deflection, i.e. own weight of the bending tongue, load applied at its free end, built-in and ferroelectric strains, to be ascertained and the geometry of the bending tongue to be optimised. As the material properties cannot be changed easily, the geometry of the bending tongue optimisation is essential for specific applications, ensuring that ferroelectric strain is the main driving force of the bending tongue vertical deflection.

The model predicts, for a 10 mm long and 3 mm wide bending tongue with a load of $5 \cdot 10^{-5}$ N applied at its free end, a change in vertical deflection under an applied electrical field of 500 kV·cm^{-1} ranging from 9.5 µm to 91.5 µm as the epitaxial PZT layer thickness increases from 0.2 µm to 2.0 µm. These results indicate that **PZT thin films deposited on stainless steel substrates are good candidates as bending tongues in MEMS applications**.

7. Conclusions and outlooks

Numerous future technological developments, including the implementation of wearable sensors and the Internet of Things, are dependent on the integration of ferroelectrics into MEMS applications. However, fundamentals questions, stated in section 1.2, must be answered to enable the direct deposition of lead zirconate titanate thin films on stainless steel substrates by pulsed laser deposition and to establish the suitability of these films for piezoelectric MEMS applications.

This chapter formulate the answers that this work has endeavoured to provide to these questions. Section 7.1 treats each of the aforementioned questions individually to draw the conclusions of this work. The outlooks of this thesis and future work necessary to expand knowledge on the topic are discussed in section 7.2.

7.1. Conclusions and answers to the statement of purpose

The fundamental questions regarding the integration of ferroelectrics into MEMS applications that this thesis aims to address are recalled and answered below.

1. How to incite the growth of tetragonal {001}-oriented or textured lead zirconate titanate thin films on steel substrates by pulsed laser deposition to engineer a larger piezoelectric response?

This thesis establishes that **the crystallographic orientation of lead zirconate titanate thin films grown directly on stainless steel by pulsed laser deposition can be tailored with selected buffer layers and appropriate substrate preparation**.

As demonstrated in literature with sol-gel procedures, it is possible to obtain predominantly {001}-textured PZT thin films **using pseudo-cubic {100}-oriented $LaNiO_3$ as a growth template and bottom electrode**. Furthering the state of the art, this work shows that **LNO thin films can be deposited with a {001} orientation on stainless steel substrates by physical vapour deposition** and, therefore, that PZT thin films orientation can be engineered on stainless steel substrates.

The process necessitates **substrates with limited roughness** which can be obtained by mechanical polishing, reducing as-bought AISI 304 stainless steel substrates roughness from 189 nm down to 3 nm. To maintain surface quality through the subsequent depositions, **substrate oxidation must be prevented**. For this purpose, a Pt buffer layer was initially used, however, it interacts with the substrate at elevated temperatures, creating an intermetallic phase, CrPt. The formation of the CrPt phase generates surface instability during LNO deposition, preventing the latter from growing in a {001} orientation. This can be circumvented with an amorphous Al_2O_3 buffer layer between the Pt and LNO thin films. Thereby, **{001}-textured PZT thin films have been deposited in $PbZr_{0.52}Ti_{0.48}O_3/LaNiO_3/Al_2O_3$/Pt/steel heterostructures**. These *PZT stacks* display Lotgering factors for the LNO and PZT layers of ${f_{(00l)}}^{\text{LNO}} = 0.68$ and ${f_{(00l)}}^{\text{PZT}} = 0.91$, respectively.

Further series of samples have been deposited, confirming that **tetragonal {001} texture can also be achieved for 2 mol.% Nb-doped PZT thin films. To prevent the formation of an intermetallic phase, the Pt buffer layer is removed from these $Pb_{0.99}\square_{0.01}(Zr_{0.52}Ti_{0.48})_{0.98}Nb_{0.02}O_3/LaNiO_3/Al_2O_3$/steel**

heterostructures and the thickness of the Al_2O_3 layer is increased to 50 nm to avoid oxidation of the stainless steel substrates during the deposition of the LNO and PNZT layers. The Lotgering factor for the LNO layer of *PNZT stacks* reaches up to ${f_{(00l)}}^{\text{LNO}} = 0.84$, an improved value compared to those reported in literature on steel substrates. The PNZT thin films show Lotgering factors of ${f_{(00l)}}^{\text{PNZT}} = 0.89$, a value equivalent to those observed for the PZT thin films deposited in this work.

The keys elements enabling {001}-textured deposition of PZT and PNZT thin films on stainless steel substrates by pulsed laser deposition are a limited substrate roughness, the prevention of substrate oxidation with an Al_2O_3 buffer layer and the deposition of a pseudo-cubic {100}-oriented $LaNiO_3$ thin film as a growth template.

2. Are the ferroelectric properties of lead zirconate titanate thin films on steel substrates suitable for piezoelectric MEMS applications?

This work shows that **the ferroelectric properties of {001}-textured lead zirconate titanate thin films deposited on AISI 304 stainless steel substrates make them good candidates for future piezoelectric MEMS applications**.

The dielectric constant of both 200 nm thick PZT and PNZT thin films is approximately 350 at 1 kHz with dielectric loss lower than 5 %. In the case of the PNZT thin films, higher permittivity is reported for some electrodes, up to 370 at 1 kHz. Furthermore, PNZT dielectric constant can increase up to 430 after *P-E* loop measurements. While these permittivity values are lower than most reported in literature for PZT thin films on metallic substrates [51, 53, 57], they are larger than those of 192 reported for non-textured PZT on austenitic stainless steel [64]. The dielectric losses here described are equivalent to literature values.

Thin films of both undoped PZT and PZT doped with 2 mol.% Nb are ferroelectric, displaying **well defined polarisation versus electrical field hysteresis loops with a clear saturation**. Measured under the same conditions, **400 nm thick PZT and PNZT thin films both present a remanent polarisation P_r ~16.5 μC·cm^{-2} and a coercive field E_c ~92 kV·cm^{-1}**. The values of remanent polarisation and coercive field are **on par with and larger than those reported in literature for thicker PZT thin films**, respectively [51, 53].

While **2 mol.% Nb-doping has no noticeable impact on the properties of the PNZT thin films as compared to those of the PZT layers**, the effect of doping could be damped by other phenomena as the *PNZT stacks* and the *PZT stacks* are deposited under different conditions. Nonetheless, **the PNZT thin films deposited in this work can withstand higher applied electrical fields than PZT thin films without undergoing dielectric breakdown**.

Phenomena not yet fully understood occur in the PNZT thin films, leading to intrinsic changes within samples during *P-E* loop measurements with increasing maximum applied field. **The reversible and irreversible Rayleigh constants are increased after these measurements, along with larger dielectric constant and loss values.** It appears from leakage current measurements that the space-charge limited current with trap filling mechanism, which was identify for the PZT thin films, is combined with at least another mechanism at higher applied fields for the PNZT thin films.

The piezoelectric $e_{31,f}$ coefficient of the PNZT thin films is within range of literature reports for PZT thin films on metallic substrates. However, the $e_{31,f}$ coefficient reaching up only to −4.4 C·m^{-2} for the 200 nm thick PNZT thin film, **improvement would be advisable**.

The lead zirconate titanate thin films deposited in this work present **acceptable dielectric constants**. Nonetheless, future piezoelectric MEMS applications **would benefit from an increase of their permittivity**. Contrarily, **dielectric losses are satisfying**, being below 5 %. The **remanent polarisation values are on par with literature and could potentially be higher** if the *P-E* loops were measured with larger maximum applied field. This is possible with the PNZT thin films on which larger electrical field can be applied without reaching dielectric breakdown than on the PZT thin films. Therefore, the **remanent polarisation values are promising for MEMS applications and are combined with rather larger coercive fields as compared to literature**. The presence of an **internal bias field** should be noted in both the PZT and the PNZT thin films, **indicating a preferred polarisation direction which can be used efficiently for piezoelectric MEMS applications**. The current properties hint towards **sensor technology rather than actuation applications**.

The ferroelectric tetragonal {001}-textured lead zirconate titanate thin films, in particular with 2 mol.% Nb-doping, deposited by pulsed laser deposition on stainless steel substrates are noteworthy candidates for future piezoelectric MEMS applications requiring non-brittle substrates.

3. How to calculate the accessible vertical deflection of ferroelectric bending tongues, taking into account both their linear piezoelectric structure and ferroelectric switching?

This work demonstrates that **the gap between the description of ferroelectric switching and the mechanical approach for linear piezoelectric structures can be bridged**. A model is proposed to calculate the vertical deflection of ferroelectric bending tongues based on **the Euler-Bernoulli beam theory** while taking ferroelectric switching on the grain scale into consideration, relying on **the switching criterion developed by Hwang et al.** [77].

The proposed model gives rise to both ***P-E* loops and *butterfly* loops, displaying hysteretic behaviour and saturation**, indicating the proper modelling of ferroelectric switching. An improvement of Hwang et al's model is the description of the saturation in the *butterfly* loop which is critical **to calculate the maximum accessible deflection and corresponding applied electrical field required to reach it for MEMS applications**.

The combination of the ferroelectric switching criterion with the Euler-Bernoulli beam theory and the inclusion of a significant number of parameters to the model give access to additional features. With the loading at the bending tongue free end to represent practical MEMS applications, and parameters describing bending tongues physical characteristics, i.e. geometry, material properties, crystallographic state, etc., it becomes **possible to optimise the geometry of the bending tongue**. Since the material properties cannot be modified easily, this is essential **to tailor bending tongues for specific MEMS applications**.

This wide range of available parameters has notably permitted to **highlight the impact of the crystallographic state of the ferroelectric (polycrystalline, textured or epitaxial) onto vertical deflection**. Furthermore, the modelling confirms that **PZT thin films deposited on stainless steel substrates are suitable candidates as bending tongues in MEMS applications** with a change in vertical deflection up to 9.5 µm under an applied electrical field of 500 kV·cm^{-1} for a 10 mm long bending tongue with a $5 \cdot 10^{-5}$ N load applied at its free end.

Through the analysis of the impact of the different parameters onto the bending tongue vertical deflection, **the full potential of combining the modelling of the mechanical approach for linear piezoelectric structures and the description of ferroelectric switching to predict the behaviour of ferroelectric MEMS is unequivocal**.

7.2. Outlooks and future work

To fully exploit the potential of this work and create piezoelectric MEMS applications based on {001}-oriented lead zirconate titanate thin films deposited directly on stainless steel substrates, additional investigations are necessary. Future work towards this goal can be sundered into several segments.

7.2.1. Potential improvements to ferroelectric bending tongues modelling

The *FeBeTo - Ferroelectric Bending Tongues modelling program* introduced in chapter 6 was developed with the possibility to easily replace internal functions within the main program. Despite the significant improvements brought by the modelling proposed in this work, further enhancement could be achieved by relying on a new function to calculate ferroelectric strain in the program.

Indeed, in this work, the calculation of ferroelectric strain relies on Hwang et al.'s model for ferroelectric switching [77]. Domain wall motion and the correlation between ferroelectric domains are not accounted for in the proposed model despite the large impact they have on ferroelectric switching [248]. Therefore, it would be interesting to integrate in the *FeBeTo* program several models of ferroelectric behaviour developed in the recent years and described in literature. These models could bring additional information on the dynamics of the switching process [279] or on the impact of domain wall pinning [74] which would contribute to a more accurate prediction of the accessible vertical deflection of ferroelectric bending tongues.

Additionally, it would be interesting to fully characterise the lead zirconate titanate thin films deposited in this work to perform the modelling with the effective material properties. It would give more insight into the capabilities of lead zirconate titanate thin films on stainless steel in MEMS applications and would further enable the optimisation of device geometry for a specific application.

7.2.2. Potential improvements in materials selection and deposition methods

Several improvements can also be made in the materials selection for the *PZT stacks* and the *PNZT stacks*, ranging from the choice of stainless steel for the substrate to the doping of the lead zirconate titanate thin films.

As passive components in MEMS applications, substrates must not hinder the action of the active ferroelectric layer. Therefore, it would be interesting to reduce the current substrate thickness of 0.2 mm down to a few tens of microns as reported in literature for some experimental investigations [51, 53]. However, we note that thinner substrates would pose difficulties for the substrates mechanical polishing with the current experimental setup and would require to establish new polishing procedures.

Furthermore, as described in section 5.1.1, substrate bending occurs during the deposition of the buffer and lead zirconate titanate layers at elevated temperatures. This bending, due to a relief of processing stresses, could be avoided by utilising a thermally treated stainless steel in which stress is relieved prior to thin films deposition [165]. During this thermal treatment, cooling down should be performed sufficiently fast to avoid the precipitation of chromium carbide during the process, which would make the steel easily oxidisable [166]. Due to the technical difficulties to achieve such rapid cooling, the process should be performed industrially.

Besides improvements of the substrate characteristics, the current work could benefit from a tuning of the amount of Nb-doping into the PNZT thin films as only 2 mol.% Nb-doping has been investigated. The sometimes contradictory literature reports on Nb-doping effects on lead zirconate titanate properties, e.g. on coercive field, emphasise the importance of investigating the impact of doping in the specific deposition conditions encountered in the heterostructures developed in this work [98, 154]. Indeed, ferroelectrics coercive fields, determining their ease to be poled and depoled, are critical for some applications.

Additionally, it is conceivable to replace the pulsed laser deposition employed for the different layers by sol-gel methods. While out of the scope of this thesis, these procedures can be performed at lower temperatures, followed by post-deposition rapid thermal annealing, efficiently limiting the oxidation of stainless steel and reducing thermal strain on the heterostructures [24]. It should also be pointed out that the pulsed laser deposition system currently used to deposit lead zirconate titanate thin films has a relatively slow deposition rate compared to that of a sol-gel procedure. Furthermore, a PbO capping layer deposited on top of lead zirconate titanate thin films would compensate lead evaporation during the deposition and stabilise the perovskite phase [51]. However, the current pulsed laser deposition system does not permit to switch between two different targets while maintaining the deposition conditions, suppressing the possibility to deposit a capping layer from a secondary PbO target. For this reason, the heterostructures deposited in this work would also benefit from the implementation of a sol-gel procedure.

7.2.3. Towards future MEMS applications

As for any devices, MEMS applications require not only to optimise material properties but to meet a set of technical specifications. For this purpose, an accurate understanding of the phenomena within the lead zirconate titanate thin films under an applied electrical field is needed. Therefore, the nature of the intrinsic changes described in section 5.2.5 and, notably, their relation with the large leakage currents in the first measured series of *P-E* loops, must be determined.

Furthermore, the effective $e_{31,f}$ transverse piezoelectric coefficient could be asserted more accurately if the in-plane strain was measured by Pt strain gauges sputtered directly on the sample surface (see section 4.4) instead of commercial strain gauges glued next to the sample. Accessing this improved characterisation method necessitate to solve the adhesion problem between the lead zirconate titanate thin films and the sputtered strain gauges.

Moreover, the adhesion between the different layers of the heterostructures must be assessed to ensure their structural integrity when operated as MEMS devices. Studies under various conditions are yet to be carried out, in particular, the impact of temperature, crucial for ferroelectric properties [54], needs to be investigated. After selection of a specific application for MEMS devices based on this work's heterostructures, the corresponding figure of merit should be calculated.

Ultimately, the replacement of lead zirconate titanate thin films by lead-free ferroelectrics could be considered as the Restriction of Hazardous Substances (RoHS) in Electrical and Electronic Equipment set by the European Union in February 2003 [280] is getting increasingly stringent [281, 282]. This last point should be carefully examined in terms of advantages and drawbacks outside of the academic perspective as the industrial significance of lead-free materials is, to date, not clearly established and they might ultimately have a larger environmental impact [283].

Until lead-free ceramics can fully replace PZT and while further improvements and characterisation of the ferroelectric {001}-textured lead zirconate titanate thin films deposited on stainless steel

substrates are necessary, the results presented in this thesis position them as good candidates for piezoelectric MEMS applications.

List of appendices

A. Wafer flexure $e_{31,f}$ measurement system loudspeaker amplifier

In the wafer flexure $e_{31,f}$ measurement system described in section 4.4 whose concept was developed by Shepard, a Legend BP102-8 loudspeaker by Eminence Speaker (Eminence, KY, USA) used to generate a pressure oscillation inside the uniform pressure rig is driven by a sinusoidal signal generated by a SR830 DSP Lock-In Amplifier by Stanford Research Systems (Sunnyvale, CA, USA) [232]. Before being transmitted to the loudspeaker, the sinusoidal signal is amplified inside the *electronics box*. The electrical schematic of the amplifier which was designed by Michael Weber from the Institute of Materials Science of the Technische Universität Darmstadt (Darmstadt, Germany) is introduced in Figure A.1.

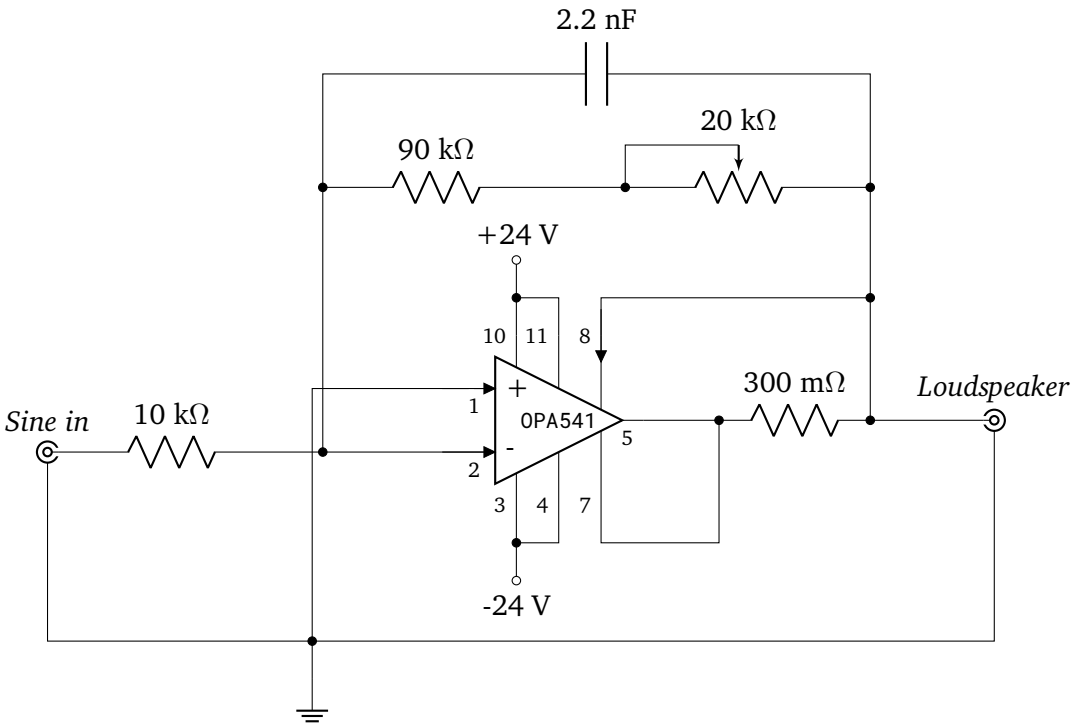

Figure A.1.: Electrical schematic of the amplifier to amplify the sinusoidal signal generated by the lock-in amplifier before its transmission to the loudspeaker. The *Sine in* terminal corresponds to the sinusoidal signal input into the amplifier and *Loudspeaker* is the output signal terminal. Design by Michael Weber.

B. Wafer flexure $e_{31,f}$ measurement system loudspeaker cavity

In the wafer flexure $e_{31,f}$ measurement system described in section 4.4 whose concept was developed by Shepard, a Legend BP102-8 loudspeaker by Eminence Speaker (Eminence, KY, USA) is fitted on an aluminium cavity to generate a pressure oscillation in the air inside the cavity [232]. A representation of the cavity is given in Figure B.1. The technical drawings of the cavity four supports and the cavity itself are given in Figures B.2 and B.3, respectively.

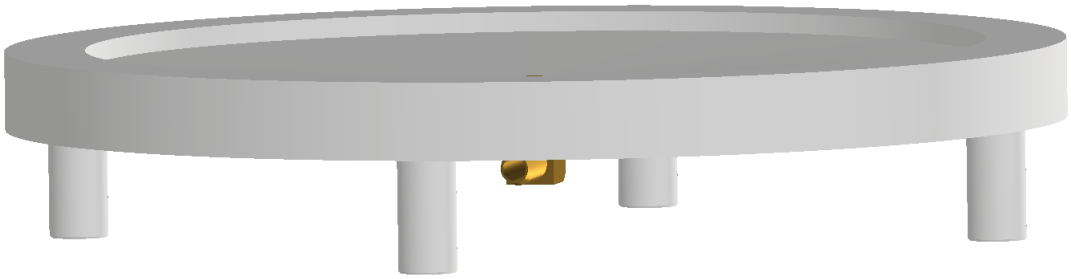

Figure B.1.: Representation of the cavity on which the loudspeaker is fitted to generate a pressure oscillation for the $e_{31,f}$ measurement with the wafer flexure system. Pipe connector is represented.

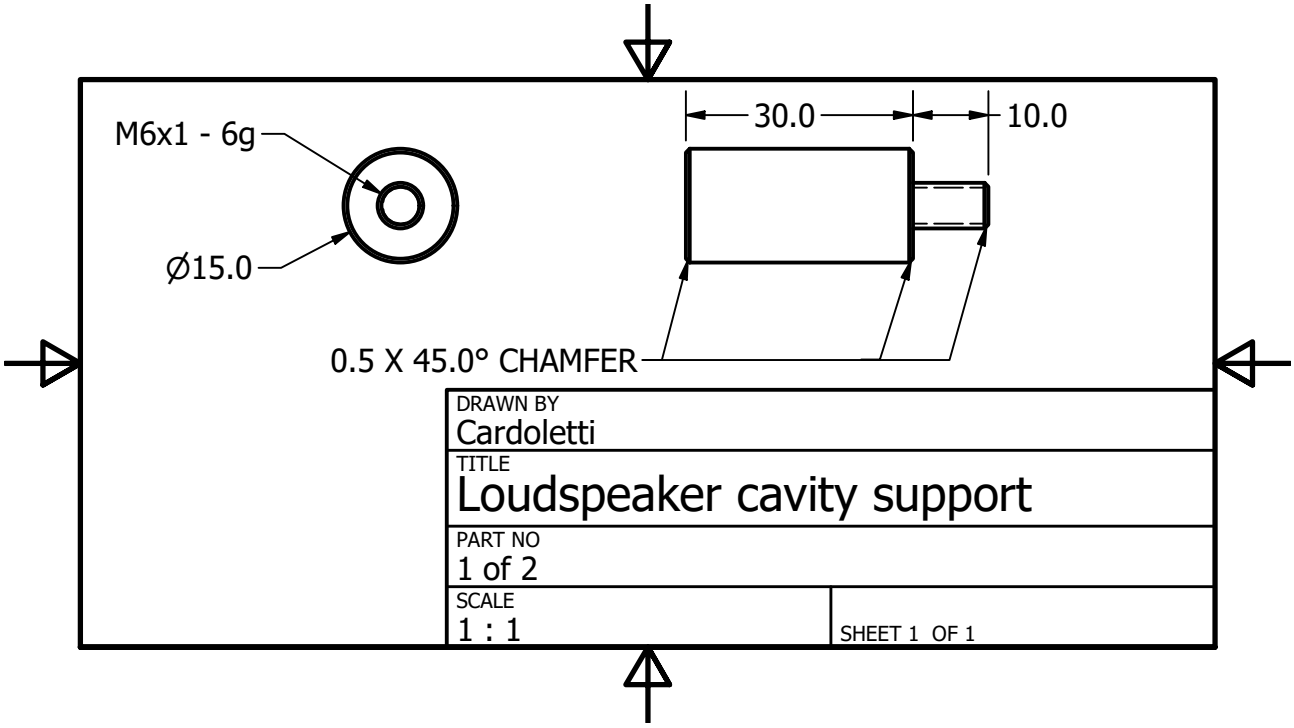

Figure B.2.: Technical drawing of the four supports of the cavity on which the loudspeaker is fitted to generate a pressure oscillation for the $e_{31,f}$ measurement with the wafer flexure system.

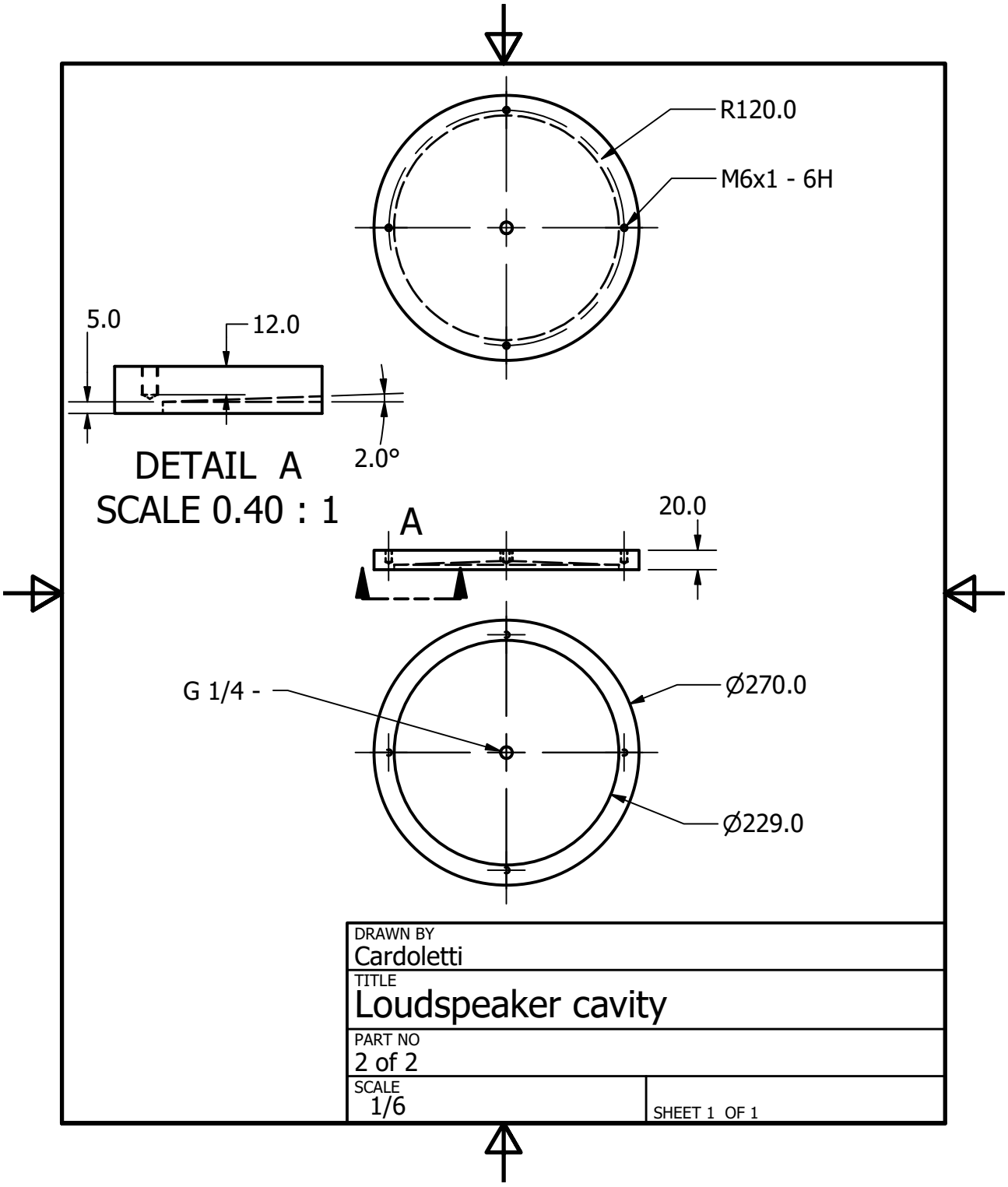

Figure B.3.: Technical drawing of the cavity on which the loudspeaker is fitted to generate a pressure oscillation for the $e_{31,f}$ measurement with the wafer flexure system.

C. Wafer flexure $e_{31,f}$ measurement system uniform pressure rig

In the wafer flexure $e_{31,f}$ measurement system described in section 4.4, the silicon carrier wafer supporting the piezoelectric sample to characterise is fixed on a uniform pressure rig. The uniform pressure rig whose concept was developed by Shepard, is composed of several components [232]. A representation of the assembled uniform pressure rig is given in Figure C.1. The technical drawings of the rig housing, the base plate, the two bushings and the retention ring are given in Figures C.2 to C.5, respectively.

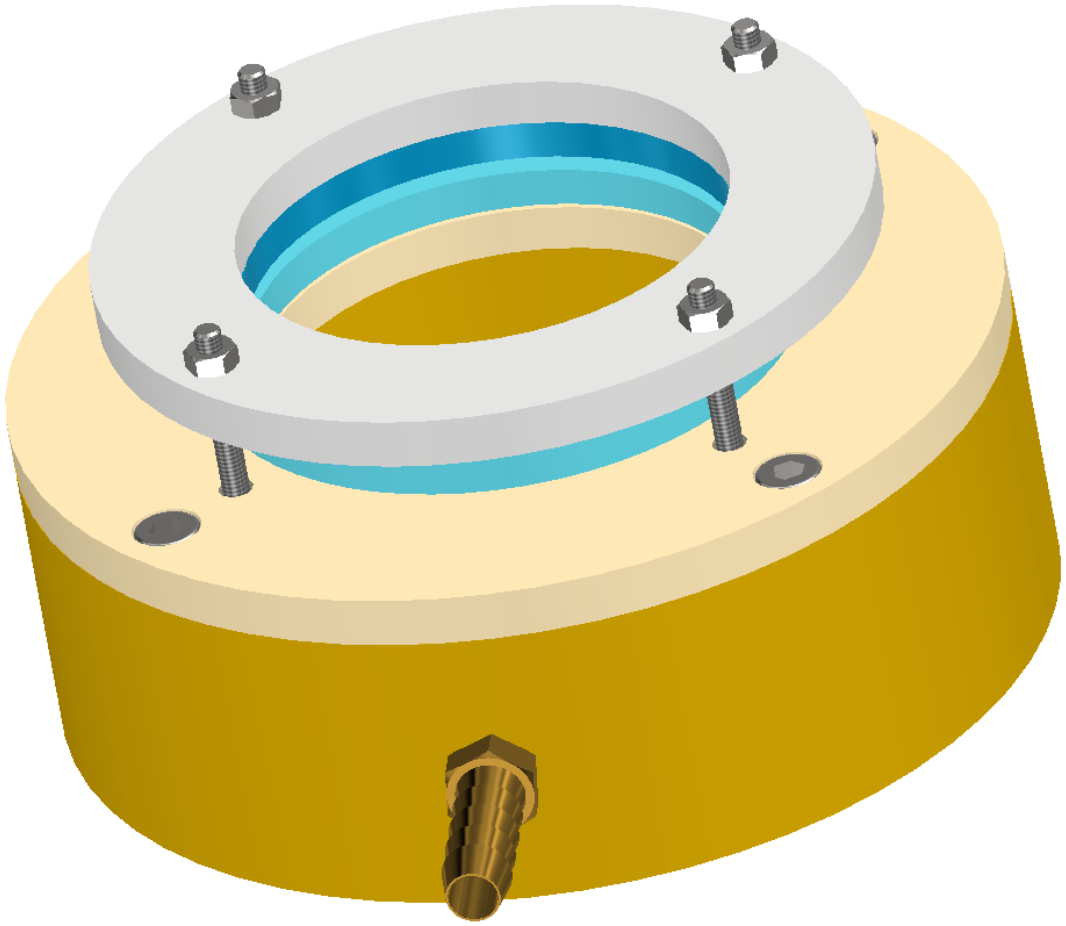

Figure C.1.: Representation of the assembled uniform pressure rig, whose concept was developed by Shepard, on which the silicon carrier wafer supporting the piezoelectric sample to characterise is fixed [232]. The rig housing is represented in light brown and the base plate in beige. Space to fit the silicon carrier wafer is visible between the two bushings, represented in light blue and darker blue. The retention ring is shown in light grey. Assembly screws, retention ring fixation screws and bolts and pipe connector are represented.

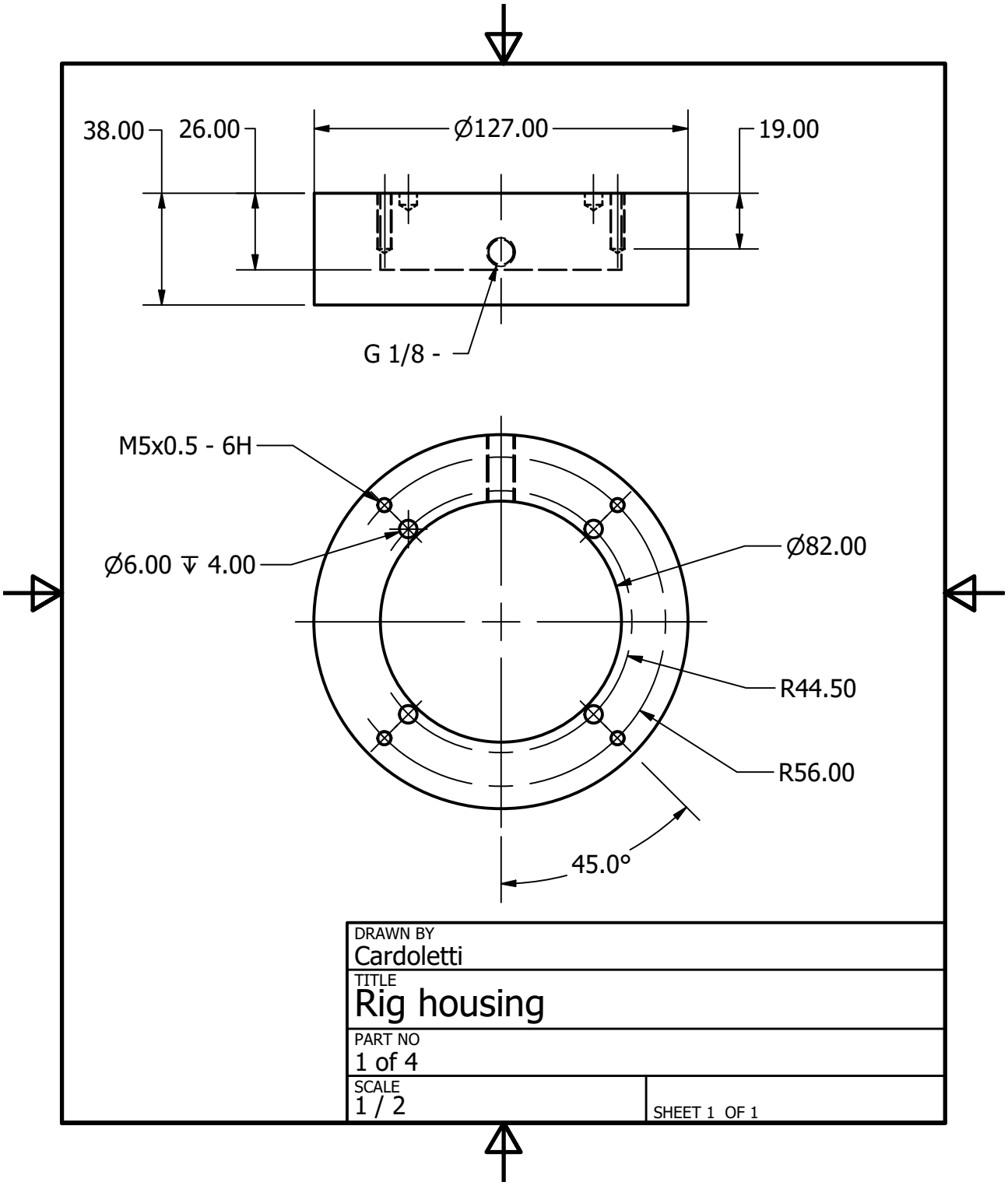

Figure C.2.: Technical drawing of the rig housing component of the uniform pressure rig for the $e_{31,f}$ measurement with the wafer flexure system.

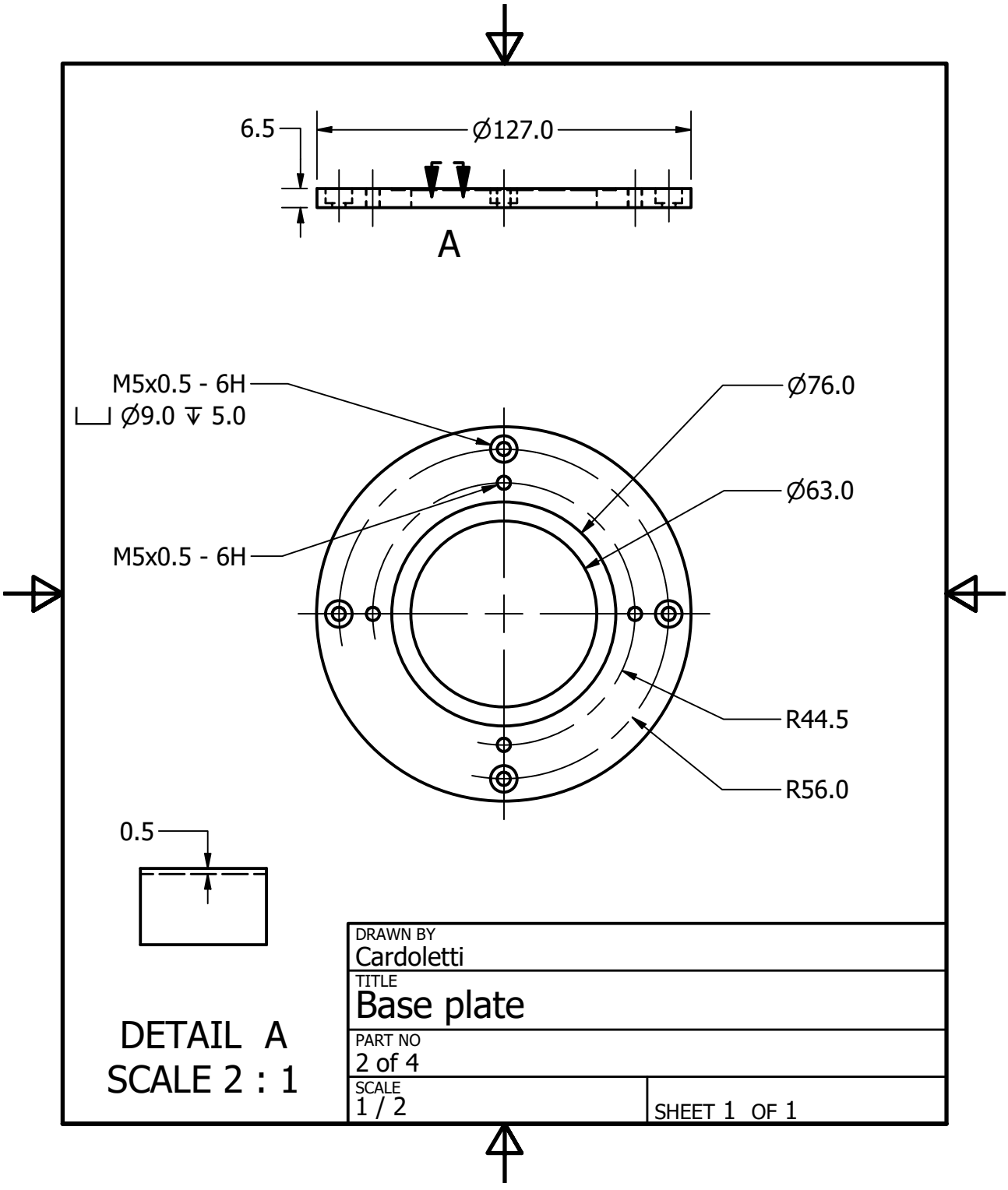

Figure C.3.: Technical drawing of the base plate component of the uniform pressure rig for the $e_{31,f}$ measurement with the wafer flexure system.

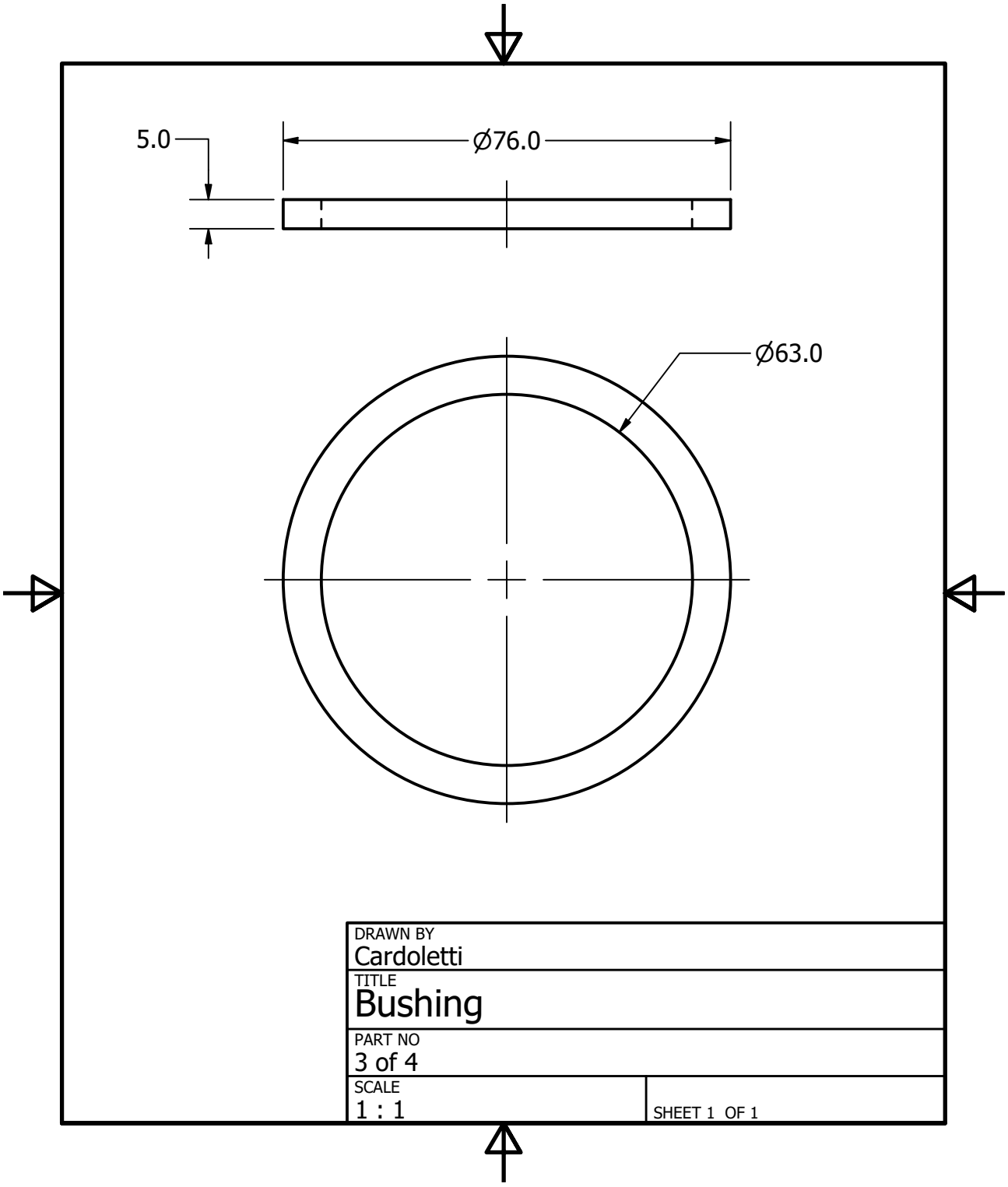

Figure C.4.: Technical drawing of the bushing component of the uniform pressure rig for the $e_{31,f}$ measurement with the wafer flexure system. Two units are needed for the uniform pressure rig.

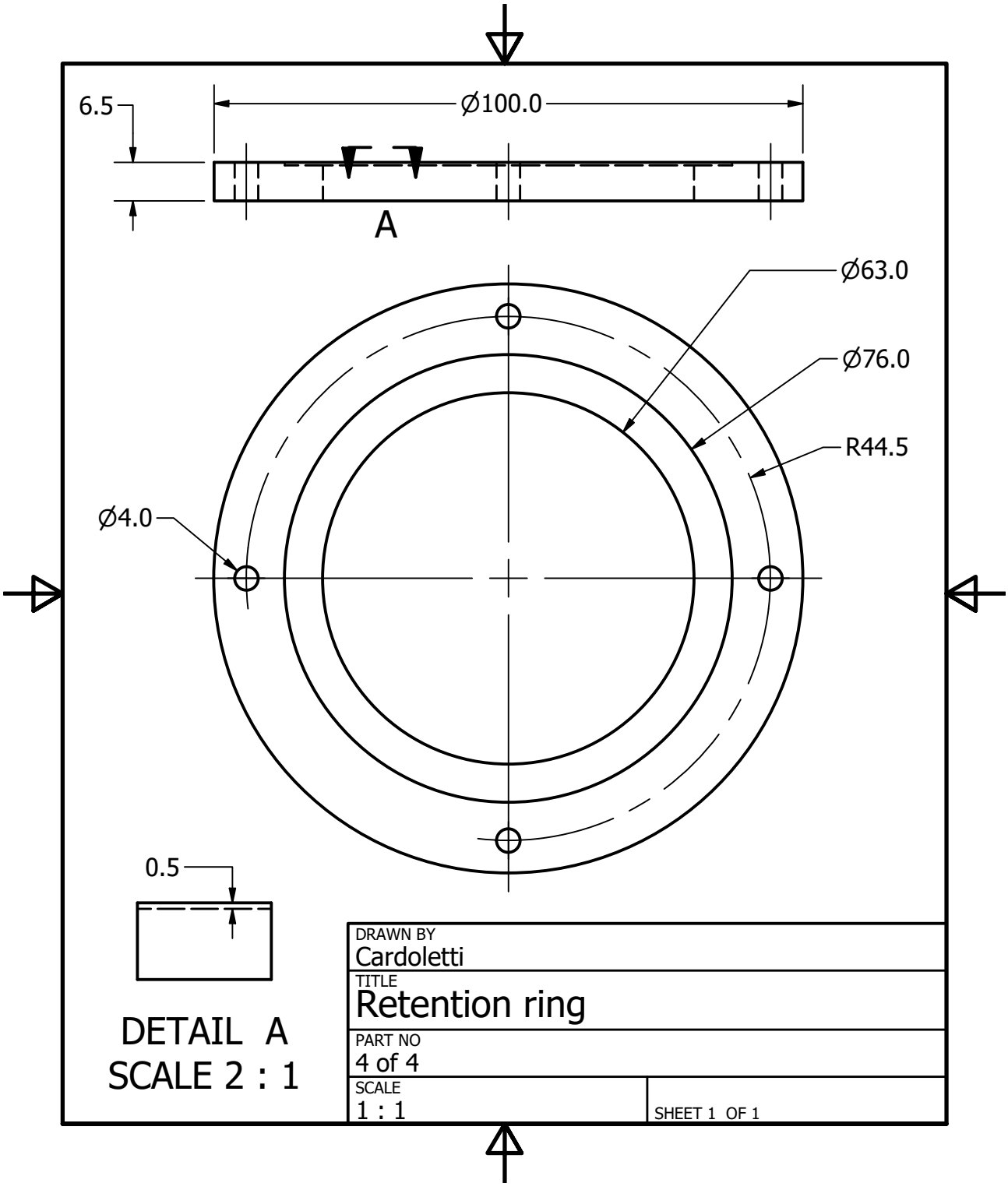

Figure C.5.: Technical drawing of the retention ring component of the uniform pressure rig for the $e_{31,f}$ measurement with the wafer flexure system.

D. Wafer flexure $e_{31,f}$ measurement system electronics box

In the wafer flexure $e_{31,f}$ measurement system described in section 4.4 whose concept was developed by Shepard, the *electronics box* performs several processes [232]. It was designed by Michael Weber from the Institute of Materials Science of the Technische Universität Darmstadt (Darmstadt, Germany) upon a concept by the Susan Trolier-McKinstry group at The Pennsylvania State University [232]. The electrical schematic of the electronics box is introduced in Figure D.1.

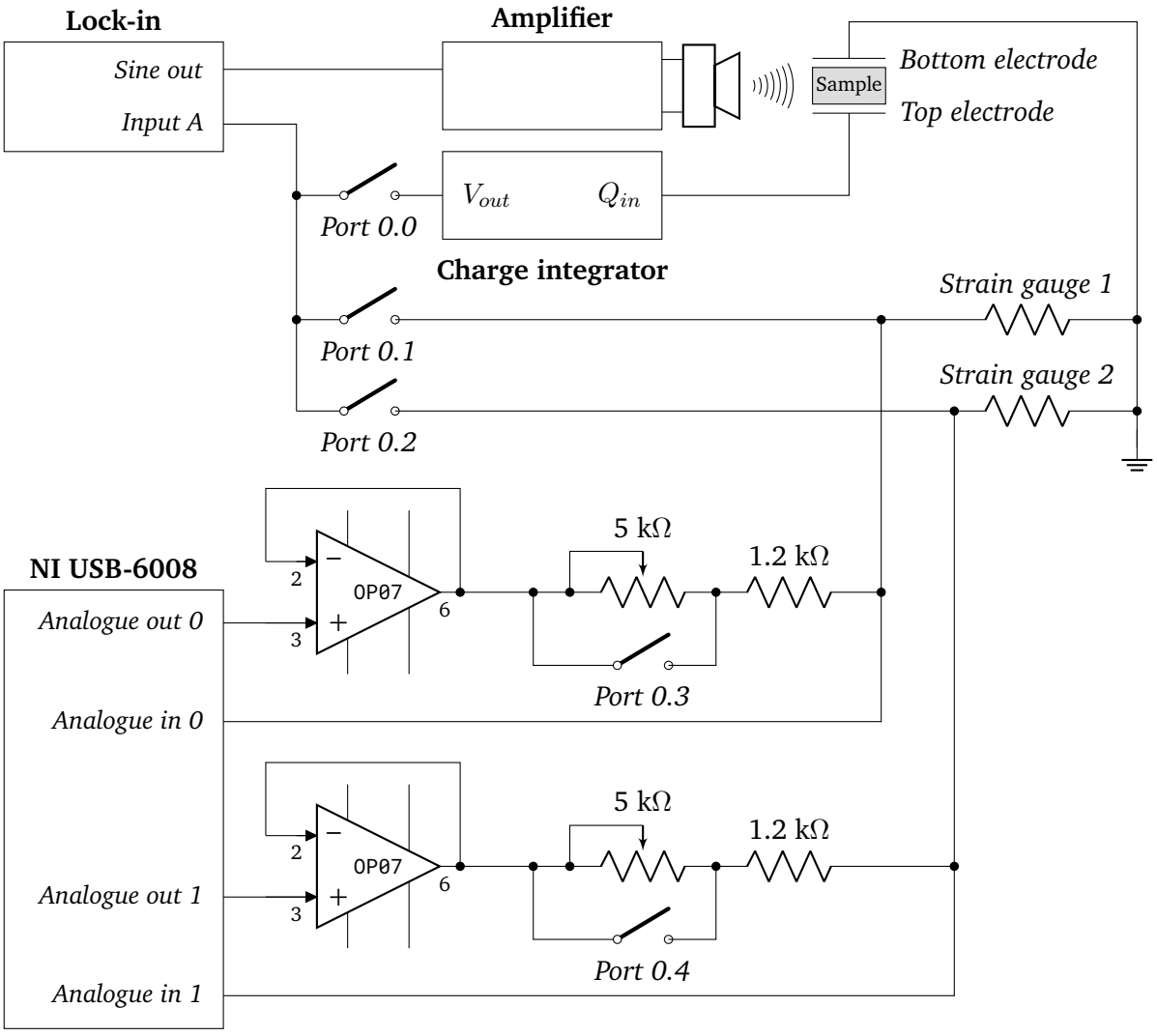

Figure D.1.: Electrical schematic of the electronics box of the wafer flexure $e_{31,f}$ measurement system containing the amplifier for the loudspeaker, the charge integrator and voltage dividers to measure strain from *Strain gauge 1* and *Strain gauge 2*. Devices connected to the electronics box are represented. Design by Michael Weber.

Starting from the top left corner of Figure D.1, the electronics box is connected to the *Sine out* terminal of a SR830 DSP Lock-In Amplifier by Stanford Research Systems (Sunnyvale, CA, USA). The signal is amplified inside the loudspeaker amplifier (see Appendix A) and transmitted to a Legend BP102-8 loudspeaker by

Eminence Speaker (Eminence, KY, USA).

The electronics box transfers the measured surface charge and in-plane strains to the *Input A* terminal of the lock-in amplifier. Switching between the different signals is performed by the relay contacts labelled *Port 0.0* to *Port 0.2* which are commanded by a NI USB-6008 card by National Instruments (Austin, TX, USA) inside the electronics box.

Port 0.0 controls the surface charge measurement via the charge integrator which converts the AC current to voltage and amplifies it (see Appendix E). *Port 0.1* and *Port 0.2* control the in-plane strain measurements via *Strain gauge 1* and *Strain gauge 2*, respectively. Both strain gauges are mounted into identical voltage dividers with 1.2 kΩ reference resistors.

The 5 kΩ potentiometers in parallel to *Port 0.3* and *Port 0.4* allow tuning of the reference resistance in the voltage dividers in case of sputtered strain gauges with non-standard resistances values. In case of commercial strain gauges, the potentiometers are by-passed by closing *Port 0.3* and *Port 0.4*.

The OP07 operational amplifiers ensure stability at 1.1 V of the analogue outputs of the NI USB-6008 card despite resistance variations in the voltage dividers. The connections with the analogue inputs of the NI USB-6008 card allow to measure the output of the voltage dividers to tune, if necessary, the potentiometers before the $e_{31,f}$ measurement starts.

E. Wafer flexure $e_{31,f}$ measurement system charge converter

In the wafer flexure $e_{31,f}$ measurement system described in section 4.4 whose concept was developed by Shepard, the surface charge developed by the sample as a function of mechanical stress is monitored by a charge integrator which was designed by Michael Weber from the Institute of Materials Science of the Technische Universität Darmstadt (Darmstadt, Germany) upon a concept by the Susan Trolier-McKinstry group at The Pennsylvania State University [232]. The charge integrator converts to voltage and amplifies the AC current, leading to more stable and reliable measurements. The electrical schematic of the integrator is introduced in Figure E.1.

The two $50\ \Omega$ resistors installed directly after the Q_{in} terminal and before the V_{out} terminal are present for impedance matching purposes. The 1 μH inductor aims to limit the voltage spike that would result from a sample failure, i.e. dielectric breakdown. Should this phenomenon happen, the additional energy would be dissipated through the two diodes towards the electrical ground.

The current entering the negative terminal of the operational amplifier (*Terminal 2*) is limited by the parallel resistor-capacitor combination placed before it. To prevent saturation of the output at the operational amplifier supply voltage, charge build-up on the C_{ref} capacitor is prevented by the 100 MΩ feedback resistor installed in parallel with C_{ref}.

The charge developed on C_{ref} and, therefore, on the sample, is given by Equation (4.6), assuming that the contributions to the complex impedance from both $50\ \Omega$ resistors and from the 1 μH inductor are negligible.

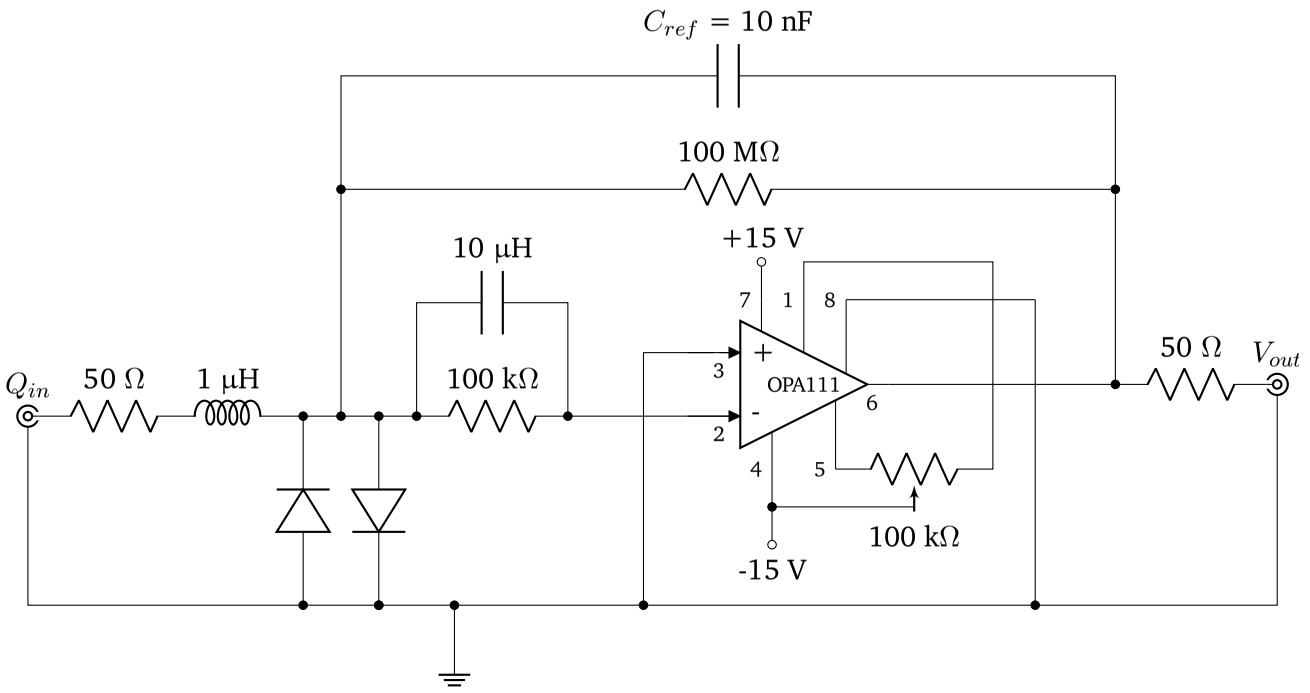

Figure E.1.: Electrical schematic of the charge integrator to convert and amplify the AC current from the piezoelectric sample surface charge into a voltage. Q_{in} corresponds to the charge input into the integrator terminal, V_{out} is the output voltage terminal and C_{ref} is the reference capacitance on which the charge is developed. Design by Michael Weber.

F. Modelling of ferroelectric bending tongues: Code of the *FeBeTo - Ferroelectric Bending Tongues modelling program*

The MATLAB® code of the *FeBeTo – Ferroelectric Bending Tongues modelling program* whose concept is developed in chapter 6 is stored on TUdatalib Repository, the institutional repository of the Technische Universität Darmstadt, under the DOI 10.25534/tudatalib-11.3.

Due to its length of more than 3,000 lines, the code could not be printed in this appendix. The program installer, the main code file and the files containing the various functions can be found in the online repository. All code files are extensively commented.

The *FeBeTo* program is distributed under a Creative Commons Attribution-NonCommercial-NoDerivatives 4.0 International (CC BY-NC-ND 4.0) licence.

G. Modelling of ferroelectric bending tongues: Development from the load distribution equation to the equation of vertical deflection due to loads

For the modelling of ferroelectric bending tongues, the load distribution on the bending tongues is described by Equation (6.7), using the Macaulay brackets. Its development until the equation of vertical deflection due to loads (Equation (6.13)) is given below. According to the Euler-Bernoulli beam theory, Equation (6.7) can be written:

$$E_{flex} I z^{IV} = q^W + q^L < x - x_m >^0 , \tag{G.1}$$

where E_{flex} is the flexural modulus, which is taken as equivalent to the Young modulus, E_{Y}, based on the assumptions of the model (see section 6.2.2). I is the second moment of area and z^{IV} is the fourth derivative of $z(x)$, the vertical deflection.

It is necessary to take into account the corrections of the beam inhomogeneity through $E_{\mathrm{Y},eff}$ and I_{eff} (Equation (6.5)) and of its disproportionate width (Equation (6.6)). Therefore, Equation (G.1) can be formulated as:

$$\frac{1-{\nu_{eff}}^2}{E_{\mathrm{Y},eff} I_{eff}} z^{IV} = q^W + q^L < x - x_m >^0 . \tag{G.2}$$

Following the Euler-Bernoulli beam theory, Equation (G.2) should be integrated four consecutive times over the length of the bending tongue. The first integration yields:

$$\frac{1-{\nu_{eff}}^2}{E_{\mathrm{Y},eff} I_{eff}} z^{III} = q^W x + q^L < x - x_m >^1 + cst_1, \tag{G.3}$$

where z^{III} is the third derivative of $z(x)$ and cst_1 is an integration constant. It can be calculated using the boundary conditions given in Equation (6.9):

$$z^{III}(x = x_l) = 0 \rightarrow cst_1 = -q^W x_l - q^L (x_l - x_m). \tag{G.4}$$

By combining Equations (G.3) and (G.4), it yields:

$$\frac{1-{\nu_{eff}}^2}{E_{\mathrm{Y},eff} I_{eff}} z^{II} = q^W \frac{x^2}{2} + \frac{q^L}{2} < x - x_m >^2 - \left[q^W x_l + q^L (x_l - x_m)\right] x + cst_2, \tag{G.5}$$

where z^{II} is the second derivative of $z(x)$ and cst_2 is an integration constant. It can be calculated using the boundary conditions given in Equation (6.10):

$$z^{II}(x = x_l) = 0 \rightarrow cst_2 = q^W \frac{{x_l}^2}{2} + q^L (x_l - x_m) \left(-\frac{x_l - x_m}{2} + x_l \right). \tag{G.6}$$

By combining Equations (G.5) and (G.6), it yields:

$$\frac{1-{\nu_{eff}}^2}{E_{\mathrm{Y},eff}I_{eff}}z^I = q^W\frac{x^3}{6} + \frac{q^L}{6} < x-x_m >^3 - \left[q^W x_l + q^L(x_l - x_m)\right]\frac{x^2}{2} + \left[q^W\frac{{x_l}^2}{2} + q^L(x_l-x_m)\left(x_l - \frac{x_l-x_m}{2}\right)\right]x + cst_3, \tag{G.7}$$

where z^I is the first derivative of $z(x)$ and cst_3 is an integration constant. It can be calculated using the boundary conditions given in Equation (6.11):

$$z^I(x=0) = 0 \rightarrow cst_3 = 0. \tag{G.8}$$

By combining Equations (G.7) and (G.8), it yields:

$$\frac{1-{\nu_{eff}}^2}{E_{\mathrm{Y},eff}I_{eff}}z = q^W\frac{x^4}{24} + \frac{q^L}{24} < x-x_m >^4 - \left[q^W x_l + q^L(x_l - x_m)\right]\frac{x^3}{6} + \left[q^W\frac{{x_l}^2}{2} + q^L(x_l-x_m)\left(x_l - \frac{x_l-x_m}{2}\right)\right]\frac{x^2}{2} + cst_4, \tag{G.9}$$

where cst_4 is an integration constant. It can be calculated using the boundary conditions given in Equation (6.12):

$$z(x=0) = 0 \rightarrow cst_4 = 0. \tag{G.10}$$

By combining Equations (G.9) and (G.10), it yields:

$$z(x) = \frac{1-{\nu_{eff}}^2}{24E_{\mathrm{Y},eff}I_{eff}}\left[q^W x^4 + q^L < x-x_m >^4 + 4\left(-q^W x_l - q^L(x_l-x_m)\right)x^3 + 12\left[q^W\frac{{x_l}^2}{2} + q^L(x_l-x_m)\left(x_l - \frac{x_l-x_m}{2}\right)\right]x^2\right], \tag{G.11}$$

corresponding to Equation (6.13).

H. Modelling of ferroelectric bending tongues: Development from the bending moments due to strain distribution equation to the equation of vertical deflection due to bending moments

For the modelling of ferroelectric bending tongues, the bending moments due to strain distribution on the bending tongue is described by Equation (6.18), using the Macaulay brackets. Its development until the equation of vertical deflection due to bending moments (Equation (6.19)) is given below. According to the Euler-Bernoulli beam theory, Equation (6.18) can be written:

$$E_{flex} I z^{II} = M_b + M_f \left(1 - < x - x_m >^0\right), \tag{H.1}$$

where E_{flex} is the flexural modulus, which is taken as equivalent to the Young modulus, E_{Y}, based on the assumptions of the model (see section 6.2.2). I is the second moment of area and z^{II} is the second derivative of $z(x)$, the vertical deflection.

It is necessary to take into account the corrections of the beam inhomogeneity through $E_{\mathrm{Y},eff}$ and I_{eff} (Equation (6.5)) and of its disproportionate width (Equation (6.6)). Therefore, Equation (H.1) can be formulated as:

$$\frac{1 - {\nu_{eff}}^2}{E_{\mathrm{Y},eff} I_{eff}} z^{II} = M_b + M_f \left(1 - < x - x_m >^0\right). \tag{H.2}$$

Following the Euler-Bernoulli beam theory, Equation (H.2) should be integrated two consecutive times over the length of the bending tongue. The first integration yields:

$$\frac{1 - {\nu_{eff}}^2}{E_{\mathrm{Y},eff} I_{eff}} z^{I} = (M_b + M_f)\, x - M_f < x - x_m >^1 + cst_5, \tag{H.3}$$

where z^I is the first derivative of $z(x)$ and cst_5 is an integration constant. It can be calculated using the boundary conditions given in Equation (6.11):

$$z^I(x = 0) = 0 \rightarrow cst_5 = 0. \tag{H.4}$$

By combining Equations (H.3) and (H.4), it yields:

$$\frac{1 - {\nu_{eff}}^2}{E_{\mathrm{Y},eff} I_{eff}} z = (M_b + M_f)\, \frac{x^2}{2} - \frac{M_f}{2} < x - x_m >^2 + cst_6, \tag{H.5}$$

where cst_6 is an integration constant. It can be calculated using the boundary conditions given in Equation (6.12):

$$z(x = 0) = 0 \rightarrow cst_6 = 0. \tag{H.6}$$

By combining Equations (H.5) and (H.6), it yields:

$$z(x) = \frac{1 - {\nu_{eff}}^2}{2E_{\mathrm{Y},eff} I_{eff}} \left[\left(M_b + M_f \right) x^2 - M_f < x - x_m >^2 \right], \tag{H.7}$$

corresponding to Equation (6.19).

References

[1] S. Trolier-McKinstry, "Impact of ferroelectricity," *American Ceramic Society Bulletin*, vol. 99, no. 1, pp. 22–23, 2020.

[2] G. Brennecka, R. Sherbondy, R. Schwartz, and J. Ihlefeld, "Ferroelectricity - A revolutionary century of discovery," *American Ceramic Society Bulletin*, vol. 99, no. 1, pp. 24–30, 2020.

[3] C. A. Randall, R. E. Newnham, and L. E. Cross, "History of the first ferroelectric oxide, $BaTiO_3$." Materials Research Institute, The Pennsylvania State University, University Park, PA, USA, 2004.

[4] C.-B. Eom and S. Trolier-McKinstry, "Thin-film piezoelectric MEMS," *MRS Bulletin*, vol. 37, no. 11, pp. 1007–1017, 2012.

[5] H. Kohlstedt, Y. Mustafa, A. Gerber, A. Petraru, M. Fitsilis, R. Meyer, U. Böttger, and R. Waser, "Current status and challenges of ferroelectric memory devices," *Microelectronic Engineering*, vol. 80, pp. 296–304, 2005.

[6] N. Setter, D. Damjanovic, L. Eng, G. Fox, S. Gevorgian, S. Hong, A. Kingon, H. Kohlstedt, N. Y. Park, G. B. Stephenson, I. Stolitchnov, A. K. Taganstev, D. V. Taylor, T. Yamada, and S. Streiffer, "Ferroelectric thin films: Review of materials, properties, and applications," *Journal of Applied Physics*, vol. 100, no. 5, p. 051606, 2006.

[7] S. P. Alpay, J. Mantese, S. Trolier-Mckinstry, Q. Zhang, and R. W. Whatmore, "Next-generation electrocaloric and pyroelectric materials for solid-state electrothermal energy interconversion," *MRS Bulletin*, vol. 39, no. 12, pp. 1099–1109, 2014.

[8] T. Xue, H. G. Yeo, S. Trolier-Mckinstry, and S. Roundy, "A wrist-worn rotational energy harvester utilizing magnetically plucked {001} oriented bimorph PZT thin-film beams," *2017 19th International Conference on Solid-State Sensors, Actuators and Microsystems (TRANSDUCERS)*, pp. 375–378, 2017.

[9] A. Erturk and D. J. Inman, *Piezoelectric energy harvesting*. Chichester, UK: John Wiley & Sons, Ltd, 2011.

[10] I. P. Kaminow, "Optical waveguide modulators," *IEEE Transactions on Microwave Theory and Techniques*, vol. 23, no. 1, pp. 57–70, 1975.

[11] P. Tang, D. J. Towner, A. L. Meier, and B. W. Wessels, "Low-voltage, polarization-insensitive, electro-optic modulator based on a polydomain barium titanate thin film," *Applied Physics Letters*, vol. 85, no. 20, pp. 4615–4617, 2004.

[12] N. Bishop, J. Walker, C. T. DeRoo, T. Liu, M. Tendulkar, C. Vincenzo, E. N. Hertz, V. Kradinov, E. D. Schwartz, P. B. Reid, T. N. Jackson, and S. Trolier-McKinstry, "Thickness distribution of sputtered films on curved substrates for adjustable X-ray optics," *Journal of Astronomical Telescopes, Instruments, and Systems*, vol. 5, no. 2, p. 021005, 2019.

[13] J. T. Van Beek and R. Puers, "A review of MEMS oscillators for frequency reference and timing applications," *Journal of Micromechanics and Microengineering*, vol. 22, no. 1, p. 013001, 2012.

[14] S. B. Lang, "Pyroelectricity: From ancient curiosity to modern imaging tool," *Physics Today*, vol. 58, no. 8, pp. 31–36, 2005.

[15] R. W. Whatmore, P. C. Osbond, and N. M. Shorrocks, "Ferroelectric materials for thermal IR detectors," *Ferroelectrics*, vol. 76, no. 1, pp. 351–367, 1987.

[16] N. M. Shorrocks, R. W. Whatmore, and P. C. Osbond, "Lead scandium tantalate for thermal detector applications," *Ferroelectrics*, vol. 106, no. 1, pp. 387–392, 1990.

[17] S. Trolier-McKinstry and P. Muralt, "Thin film piezoelectrics for MEMS," *Journal of Electroceramics*, vol. 12, pp. 7–17, 2004.

[18] I. Kanno, "Piezoelectric MEMS: Ferroelectric thin films for MEMS applications," *Japanese Journal of Applied Physics*, vol. 57, p. 040101, 2018.

[19] K. Uchino, *Piezoelectric actuators and ultrasonic motors*. Springer US, 1997.

[20] M. Weiser, "The computer for the 21st century," *Scientific American*, vol. 265, no. 3, pp. 94–104, 1991.

[21] European Commission, "Proposal for a regulation of the European Parliament and of the Council establishing the framework for achieving climate neutrality and amending Regulation (EU) 2018/1999 (European Climate Law) - COM/2020/80 final," 2020.

[22] K. Morimoto, I. Kanno, K. Wasa, and H. Kotera, "High-efficiency piezoelectric energy harvesters of c-axis-oriented epitaxial PZT films transferred onto stainless steel cantilevers," *Sensors and Actuators, A: Physical*, vol. 163, no. 1, pp. 428–432, 2010.

[23] G. Shirane, K. Suzuki, and A. Takeda, "Phase transitions in solid solutions of $PbZrO_3$ and $PbTiO_3$ (II) X-ray study," *Journal of the Physical Society of Japan*, vol. 7, no. 1, pp. 12–18, 1952.

[24] P. Muralt, "Ferroelectric thin films for micro-sensors and actuators: A review," *Journal of Micromechanics and Microengineering*, vol. 10, no. 2, pp. 136–146, 2000.

[25] R. N. Castellano and L. G. Feinstein, "Ion-beam deposition of thin films of ferroelectric lead zirconate titanate (PZT)," *Journal of Applied Physics*, vol. 50, no. 6, pp. 4406–4411, 1979.

[26] R. N. Castellano, "Deposition of thin films of PZT by a focused ion beam sputtering technique," *Ferroelectrics*, vol. 28, no. 1, pp. 387–390, 1980.

[27] S. B. Krupanidhi, N. Maffei, M. Sayer, and K. El-Assal, "RF planar magnetron sputtering and characterization of ferroelectric $Pb(Zr,Ti)O_3$ films," *Journal of Applied Physics*, vol. 54, no. 11, pp. 6601–6609, 1983.

[28] T. Fukami, T. Sakuma, K. Tokunaga, and H. Tsuchiya, "Ferroelectric films deposited by reactive sputtering and their properties," *Japanese Journal of Applied Physics*, vol. 22, no. S2, pp. 18–21, 1983.

[29] K. Sreenivas, M. Sayer, and P. Garrett, "Properties of D.C. magnetron-sputtered lead zirconate titanate thin films," *Thin Solid Films*, vol. 172, no. 2, pp. 251–267, 1989.

[30] S. K. Dey, K. D. Budd, and D. A. Payne, "Thin-film ferroelectrics of PZT of sol-gel processing," *IEEE Transactions on Ultrasonics, Ferroelectrics, and Frequency Control*, vol. 35, no. 1, pp. 80–81, 1988.

[31] G. Yi, M. Sayer, C. K. Jen, J. C. H. Yu, and E. L. Adler, "Coaxial thin film transducers based on PZT," *Proceedings., IEEE Ultrasonics Symposium,*, vol. 2, pp. 1231–1235, 1989.

[32] H. Kueppers, T. Leuerer, U. Schnakenberg, W. Mokwa, M. J. Hoffmann, T. Schneller, U. Boettger, and R. Waser, "PZT thin films for piezoelectric microactuator applications," *Sensors and Actuators A: Physical*, vol. 97-98, pp. 680–684, 2002.

[33] G. A. C. M. Spierings, M. J. E. Ulenaers, G. L. M. Kampschöer, H. A. M. van Hal, and P. K. Larsen, "Preparation and ferroelectric properties of $PbZr_{0.53}Ti_{0.47}O_3$ thin films by spin coating and metalorganic decomposition," *Journal of Applied Physics*, vol. 70, no. 4, p. 2290, 1991.

[34] M. Okada, K. Tominaga, T. Araki, S. Katayama, and Y. Sakashita, "Metalorganic chemical vapor deposition of c-axis oriented PZT thin films," *Japanese Journal of Applied Physics*, vol. 29, no. 4R, pp. 718–722, 1990.

[35] Y. Sakashita, O. Toshiyuki, H. Segawa, K. Tominaga, and M. Okada, "Preparation and electrical properties of MOCVD-deposited PZT thin films," *Journal of Applied Crystallography*, vol. 69, no. 12, p. 8352, 1991.

[36] H. Itoh, K. Kashihara, T. Okudaira, K. Tsukamoto, and Y. Akasaka, "MOCVD for PZT thin films by using novel metalorganic sources," *International Electron Devices Meeting 1991 [Technical Digest]*, pp. 831–834, 1991.

[37] D. Roy, S. B. Krupanidhi, and J. P. Dougherty, "Excimer laser ablated lead zirconate titanate thin films," *Journal of Applied Physics*, vol. 69, no. 11, pp. 7930–7932, 1991.

[38] H. Kidoh, T. Ogawa, A. Morimoto, and T. Shimizu, "Ferroelectric properties of lead-zirconate-titanate films prepared by laser ablation," *Applied Physics Letters*, vol. 58, no. 25, pp. 2910–2912, 1991.

[39] J. Akedo, J. H. Park, and Y. Kawakami, "Piezoelectric thick film fabricated with aerosol deposition and its application to piezoelectric devices," *Japanese Journal of Applied Physics*, vol. 57, no. 7, p. 07LA02, 2018.

[40] M. D. Nguyen, H. Nazeer, K. Karakaya, S. V. Pham, R. Steenwelle, M. Dekkers, L. Abelmann, D. H. A. Blank, and G. J. H. M. Rijnders, "Characterization of epitaxial $Pb(Zr,Ti)O_3$ thin films deposited by pulsed laser deposition on silicon cantilevers," *Journal of Micromechanics and Microengineering*, vol. 20, no. 8, p. 085022, 2010.

[41] S. Dunn and R. W. Whatmore, "Substrate effects on domain structures of PZT 30/70 sol-gel films via piezoAFM," *Journal of the European Ceramic Society*, vol. 22, no. 6, pp. 825–833, 2002.

[42] L. Ceresara, A. Iembo, F. Fuso, M. Labardi, M. Allegrini, E. Arimondo, A. Diodati, B. E. Watts, F. Leccabue, G. Bocelli, A. Diodatiz, B. E. Watts, F. Leccabue, and G. Bocelli, "Pulsed laser ablation deposition and characterization of superconductive/ferroelectric bilayers," *Superconductor Science and Technology*, vol. 9, no. 8, pp. 671–677, 1996.

[43] H. N. Al-Shareef, K. D. Gifford, S. H. Rou, P. D. Hren, O. Auciello, and A. I. Kingon, "Electrodes for ferroelectric thin films," *Integrated Ferroelectrics*, vol. 3, no. 4, pp. 321–332, 1993.

[44] H. D. Chen, K. R. Udayakumar, C. Gaskey, and L. E. Cross, "Fabrication and electrical properties of lead zirconate titanate thick films," *Journal of American Ceramic Society*, vol. 79, no. 8, pp. 2189–2192, 1996.

[45] K. Sreenivas, I. Reaney, T. Maeder, N. Setter, C. Jagadish, and R. G. Elliman, "Investigation of Pt/Ti bilayer metallization on silicon for ferroelectric thin film integration," *Journal of Applied Physics*, vol. 75, no. 1, pp. 232–239, 1994.

[46] J.-R. Cheng, W. Zhu, N. Li, and L. E. Cross, "Electrical properties of sol-gel-derived $Pb(Zr_{0.52}Ti_{0.48})O_3$ thin films on a $PbTiO_3$-coated stainless steel substrate," *Applied Physics Letters*, vol. 81, no. 25, pp. 4805–4807, 2002.

[47] Q. Zou, H. E. Ruda, B. G. Yacobi, K. Saegusa, and M. Farrell, "Dielectric properties of lead zirconate titanate thin films deposited on metal foils," *Applied Physics Letters*, vol. 77, no. 7, pp. 1038–1040, 2000.

[48] Q. Zou, H. E. Ruda, and B. G. Yacobi, "Improved dielectric properties of lead zirconate titanate thin films deposited on metal foils with $LaNiO_3$ buffer layers," *Applied Physics Letters*, vol. 78, no. 9, pp. 1282–1284, 2001.

[49] J. H. Yi, R. Seveno, and H. W. Gundel, "Sol-gel derived PZT/RuO_2 multilayer films on stainless steel substrates," *Integrated Ferroelectrics*, vol. 23, no. 1, pp. 199–214, 1999.

[50] R. Seveno and D. Averty, "Ultra light tunable capacitor based on PZT thin film deposited onto aluminium foil," *Journal of Sol-Gel Science and Technology*, vol. 68, no. 2, pp. 175–179, 2013.

[51] H. G. Yeo and S. Trolier-McKinstry, "{001} oriented piezoelectric films prepared by chemical solution deposition on Ni foils," *Journal of Applied Physics*, vol. 116, no. 1, p. 014105, 2014.

[52] H. G. Yeo, T. Xue, S. Roundy, X. Ma, C. Rahn, and S. Trolier-McKinstry, "Strongly (001) oriented bimorph PZT film on metal foils grown by *rf*-sputtering for wrist-worn piezoelectric energy harvesters," *Advanced Functional Materials*, vol. 28, no. 36, pp. 1–9, 2018.

[53] K. Coleman, J. Walker, T. Beechem, and S. Trolier-Mckinstry, "Effect of stresses on the dielectric and piezoelectric properties of $Pb(Zr_{0.52}Ti_{0.48})O_3$ thin films," *Journal of Applied Physics*, vol. 126, no. 3, p. 034101, 2019.

[54] K. Coleman, S. Shetty, B. Hanrahan, W. Zhu, and S. Trolier-McKinstry, "Extrinsic contributions to the dielectric and pyroelectric properties of $Pb_{0.99}[(Zr_{0.52}Ti_{0.48})_{0.98}Nb_{0.02}]O_3$ thin films on Si and Ni substrates," *Journal of Applied Physics*, vol. 128, no. 11, p. 114102, 2020.

[55] Y. J. Ko, D. Y. Kim, S. S. Won, C. W. Ahn, I. W. Kim, A. I. Kingon, S.-H. Kim, J.-H. Ko, and J. H. Jung, "Flexible $Pb(Zr_{0.52}Ti_{0.48})O_3$ films for a hybrid piezoelectric-pyroelectric nanogenerator under harsh environments," *ACS Applied Materials & Interfaces*, vol. 8, no. 10, pp. 6504–6511, 2016.

[56] H.-J. Tseng, W.-C. Tian, and W.-J. Wu, "Flexible PZT thin film tactile sensor for biomedical monitoring," *Sensors (Basel, Switzerland)*, vol. 13, no. 5, pp. 5478–5492, 2013.

[57] G. Magagnin, *Chemical solution processed ferroelectric thick films on metal foil*. Final year internship thesis (Supervisor: N. Bassiri-Gharb), Ecole Centrale de Lyon (France) - Georgia Tech (USA), 2019.

[58] H. Li, S. Wang, J. Jian, H. Dong, J. Chen, D. Jin, and J. Cheng, "Improved ferroelectric properties of (100)-oriented PZT thin films deposited on stainless steel substrates with $La_{0.5}Sr_{0.5}CoO_3$ buffer layers," *Journal of Materials Science: Materials in Electronics*, vol. 29, no. 17, pp. 14651–14656, 2018.

[59] S. S. Won, H. Seo, M. Kawahara, S. Glinsek, J. Lee, Y. Kim, C. K. Jeong, A. I. Kingon, and S. H. Kim, "Flexible vibrational energy harvesting devices using strain-engineered perovskite piezoelectric thin films," *Nano Energy*, vol. 55, pp. 182–192, 2019.

[60] M. Oikawa and K. Toda, "Preparation of $Pb(Zr,Ti)O_3$ thin films by an electron beam evaporation technique," *Applied Physics Letters*, vol. 29, no. 8, pp. 491–492, 1976.

[61] M. Koinuma, H. Ohmura, Y. Fujioka, Y. Matsumoto, and S. Yamada, "Preparation of PZT thin films on stainless steel using electrochemical reduction," *Journal of Solid State Chemistry*, vol. 136, no. 2, pp. 293–297, 1998.

[62] T. Suzuki, I. Kanno, J. J. Loverich, H. Kotera, and K. Wasa, "Characterization of $Pb(Zr,Ti)O_3$ thin films deposited on stainless steel substrates by RF-magnetron sputtering for MEMS applications," *Sensors and Actuators A: Physical*, vol. 125, no. 2, pp. 382–386, 2006.

[63] T. Nishi, T. Ito, H. Hida, and I. Kanno, "Shoe-mounted vibration energy harvester of PZT piezoelectric thin films on metal foils," *Journal of Physics: Conference Series*, vol. 773, no. 1, p. 012062, 2016.

[64] T. Ito, T. Nishi, T. Umegaki, H. Hida, and I. Kanno, "The piezoelectric PZT thin films deposited on metal substrates," *Journal of Physics: Conference Series*, vol. 1052, no. 1, p. 012094, 2018.

[65] Y. Tsujiura, E. Suwa, F. Kurokawa, H. Hida, and I. Kanno, "Reliability of vibration energy harvesters of metal-based PZT thin films," *Journal of Physics: Conference Series*, vol. 557, no. 1, pp. 3–8, 2014.

[66] Y. Tsujiura, E. Suwa, T. Nishi, F. Kurokawa, H. Hida, and I. Kanno, "Airflow energy harvester of piezoelectric thin-film bimorph using self-excited vibration," *Sensors and Actuators A: Physical*, vol. 261, pp. 295–301, 2017.

[67] A. Bose, M. Sreemany, and S. Bysakh, "Influence of processing parameters on the growth characteristics and ferroelectric properties of sputtered PZT thin films on stainless steel substrates," *Applied Surface Science*, vol. 282, pp. 202–210, 2013.

[68] T. Fujii, Y. Hishinuma, T. Mita, and T. Naono, "Characterization of Nb-doped $Pb(Zr,Ti)O_3$ films deposited on stainless steel and silicon substrates by RF-magnetron sputtering for MEMS applications," *Sensors and Actuators A: Physical*, vol. 163, no. 1, pp. 220–225, 2010.

[69] R. G. Ballas, H. F. Schlaak, and A. J. Schmid, "The constituent equations of piezoelectric multilayer bending actuators in closed analytical form and experimental results," *Sensors and Actuators A: Physical*, vol. 130-131, pp. 91–98, 2006.

[70] R. G. Ballas, *Piezoelectric multilayer beam bending actuators*. Springer-Verlag Berlin Heidelberg, 2007.

[71] K. G. Webber, D. J. Franzbach, and J. Koruza, "Determination of the true operational range of a piezoelectric actuator," *Journal of the American Ceramic Society*, vol. 97, no. 9, pp. 2842–2849, 2014.

[72] K. G. Webber, "Application of a classical lamination theory model to the design of piezoelectric composite unimorph actuators," *Journal of Intelligent Material Systems and Structures*, vol. 17, no. 1, pp. 29–34, 2006.

[73] L. Q. Chen, "Phase-field method of phase transitions/domain structures in ferroelectric thin films: A review," *Journal of the American Ceramic Society*, vol. 91, no. 6, pp. 1835–1844, 2008.

[74] Y. Su and C. M. Landis, "Continuum thermodynamics of ferroelectric domain evolution: Theory, finite element implementation, and application to domain wall pinning," *Journal of the Mechanics and Physics of Solids*, vol. 55, no. 2, pp. 280–305, 2007.

[75] B. X. Xu, D. Schrade, R. Müller, D. Gross, T. Granzow, and J. Rödel, "Phase field simulation and experimental investigation of the electro-mechanical behavior of ferroelectrics," *ZAMM Zeitschrift fur Angewandte Mathematik und Mechanik*, vol. 90, no. 7-8, pp. 623–632, 2010.

[76] J. E. Huber, N. A. Fleck, C. M. Landis, and R. M. McMeeking, "A constitutive model for ferroelectric polycrystals," *Journal of the Mechanics and Physics of Solids*, vol. 47, no. 8, pp. 1663–1697, 1999.

[77] S. C. Hwang, C. S. Lynch, and R. M. McMeeking, "Ferroelectric/ferroelastic interactions and a polarization switching model," *Acta Metallurgica et Materialia*, vol. 43, no. 5, pp. 2073–2084, 1995.

[78] S. Hwang, J. Huber, R. McMeeking, and N. Fleck, "The simulation of switching in polycrystalline ferroelectric ceramics," *Journal of Applied Physics*, vol. 84, no. 3, pp. 1530–1540, 1998.

[79] R. M. McMeeking and S. C. Hwang, "On the potential energy of a piezoelectric inclusion and the criterion for ferroelectric switching," *Ferroelectrics*, vol. 200, no. 1-4, pp. 151–173, 1997.

[80] X. Chen, D. N. Fang, and K. C. Hwang, "Micromechanics simulation of ferroelectric polarization switching," *Acta Materialia*, vol. 45, no. 8, pp. 3181–3189, 1997.

[81] W. Chen and C. S. Lynch, "A micro-electro-mechanical model for polarization switching of ferroelectric materials," *Acta Materialia*, vol. 46, no. 15, pp. 5303–5311, 1998.

[82] S. Hwang and R. Waser, "Study of electrical and mechanical contribution to switching in ferroelectric/ferroelastic polycrystals," *Acta Materialia*, vol. 48, no. 12, pp. 3271–3282, 2000.

[83] Y. Fotinich and G. P. Carman, "Stresses in piezoceramics undergoing polarization switchings," *Journal of Applied Physics*, vol. 88, no. 11, pp. 6715–6725, 2000.

[84] J. Li and G. J. Weng, "A micromechanics-based hysteresis model for ferroelectric ceramics," *Journal of Intelligent Materials Systems and Structures*, vol. 12, no. 2, pp. 79–91, 2001.

[85] F. Narita, Y. Shindo, and K. Hayashi, "Bending and polarization switching of piezoelectric laminated actuators under electromechanical loading," *Computers & Structures*, vol. 83, no. 15-16, pp. 1164–1170, 2005.

[86] M. E. Lines and A. M. Glass, "Basic concepts," in *Principles and applications of ferroelectrics and related materials*, ch. 1, pp. 1–23, Oxford, UK: Oxford University Press, 1977.

[87] J. Tichý, J. Erhart, E. Kittinger, and J. Přívratská, "Introduction to phenomenological crystal structure," in *Fundamentals of piezoelectric sensorics*, ch. 2, pp. 15–29, Springer Heidelberg Dordrecht London New York, 2010.

[88] J. F. Nye, "The groundwork of crystal physics," in *Physical properties of crystals*, ch. 1, pp. 3–32, Oxford, UK: Clarendon Press, 1957.

[89] J. F. Nye, "Piezoelectricity. Third-rank tensors," in *Physical properties of crystals*, ch. 7, pp. 110–130, Oxford, UK: Clarendon Press, 1957.

[90] J. Tichý, J. Erhart, E. Kittinger, and J. Přívratská, "Basic thermodynamics of piezoelectric crystals," in *Fundamentals of piezoelectric sensorics*, ch. 4, pp. 55–68, Springer Heidelberg Dordrecht London New York, 2010.

[91] S. M. Pilgrim, "Electrostrictive ceramics for low-frequency active transducers," *IEEE Transactions on Ultrasonics, Ferroelectrics, and Frequency Control*, vol. 47, no. 4, pp. 861–876, 2000.

[92] M. Mehdizadeh, "The impact of fields on materials at RF/microwave frequencies," in *Microwave/RF Applicators and Probes*, ch. 1, pp. 1–34, Elsevier, 2010.

[93] J. F. Nye, "Natural and artificial double refraction. Second-order effects," in *Physical properties of crystals*, ch. 13, pp. 235–259, Oxford, UK: Clarendon Press, 1957.

[94] G. Gautschi, "Background of piezoelectric sensors," in *Piezoelectric sensorics*, ch. 2, pp. 5–11, Springer-Verlag Berlin Heidelberg, 2002.

[95] J. Tichý, J. Erhart, E. Kittinger, and J. Přívratská, "Principles of piezoelectricity," in *Fundamentals of piezoelectric sensorics*, ch. 1, pp. 1–14, Springer Heidelberg Dordrecht London New York, 2010.

[96] J. Curie and P. Curie, "Développement par compression de l'électricité polaire dans les cristaux hémièdres à faces inclinées," *Bulletin de Minéralogie*, vol. 3-4, pp. 90–93, 1880.

[97] P. Curie, "Sur la symétrie dans les phénomènes physiques, symétrie d'un champ électrique et d'un champ magnétique," *Journal de Physique Théorique et Appliquée*, vol. 3, no. 1, pp. 393–415, 1894.

[98] D. Damjanovic, "Ferroelectric, dielectric and piezoelectric properties of ferroelectric thin films and ceramics," *Reports on Progress in Physics*, vol. 61, no. 11, pp. 1267–1324, 1998.

[99] H. Klapper and T. Hahn, "Point-group symmetry and physical properties of crystals," in *International tables for crystallography volume A: Space-group symmetry* (T. Hahn, ed.), ch. 10.2, pp. 804–808, Dordrecht, Netherlands: Springer, 5^{th} ed., 2006.

[100] W. G. Cady, "Principles of piezoelectricity," in *Piezoelectricity - Volume one*, ch. 8, pp. 177–199, Mineola, NY, USA: Courier Dover Publications, revised ed., 2018.

[101] D. A. Hall, "Nonlinearity in piezoelectric ceramics," *Journal of Materials Science*, vol. 36, no. 19, pp. 4575–4601, 2001.

[102] A. J. Moulson and J. M. Herbert, "Piezoelectric ceramics," in *Electroceramics*, ch. 6, pp. 339–410, Chichester, UK: John Wiley & Sons, Inc., 2^{nd} ed., 2003.

[103] J. Tichý, E. Jiří, E. Kittinger, and J. Přívratská, "Piezoelectric properties," in *Fundamentals of piezoelectric sensorics*, ch. 5, pp. 69–100, Springer Heidelberg Dordrecht London New York, 2010.

[104] D. Horsley, Y. Lu, and O. Rozen, "Flexural piezoelectric resonators," in *Piezoelectric MEMS resonators* (H. Bhugra and G. Piazza, eds.), ch. 6, pp. 153–173, Springer Berlin Heidelberg, 2017.

[105] F. Jona and G. Shirane, "Introduction," in *Ferroelectric crystals*, ch. 1, pp. 1–27, New York City, NY, USA: Dover Publications, 1993.

[106] K. M. Rabe, M. Dawber, C. Lichtensteiger, C. H. Ahn, and J.-M. Triscone, "Modern physics of ferroelectrics: Essential background," in *Physics of ferroelectrics* (K. M. Rabe, C. H. Ahn, and J.-M. Triscone, eds.), ch. 1, pp. 1–30, Springer-Verlag Berlin Heidelberg, 2007.

[107] The American Physical Society, "Minutes of the Washington meeting, April 23 and 24, 1920," *Physical Review*, vol. 15, no. 6, p. 505, 1920.

[108] J. Valasek, "Piezo-electric and allied phenomena in Rochelle salt," *Physical Review*, vol. 17, no. 4, p. 475, 1921.

[109] R. Resta and D. Vanderbilt, "Theory of polarization: A modern approach," in *Physics of ferroelectrics* (K. M. Rabe, C. H. Ahn, and J.-M. Triscone, eds.), ch. 2, pp. 31–68, Springer-Verlag Berlin Heidelberg, 2007.

[110] N. A. Spaldin, "A beginners guide to the modern theory of polarization," *Journal of Solid State Chemistry*, vol. 195, pp. 2–10, 2012.

[111] R. Resta, "Theory of the electric polarization in crystals," *Ferroelectrics*, vol. 136, no. 1, pp. 51–55, 1992.

[112] R. D. King-Smith and D. Vanderbilt, "Theory of polarization of crystalline solids," *Physical Review B*, vol. 47, no. 3, pp. 1651–1654, 1993.

[113] R. Resta, "Macroscopic polarization in crystalline dielectrics: The geometric phase approach," *Reviews of Modern Physics*, vol. 66, no. 3, pp. 889–915, 1994.

[114] D. Vanderbilt and R. D. King-Smith, "Electric polarization as a bulk quantity and its relation to surface charge," *Physical Review B*, vol. 48, no. 7, pp. 4442–4455, 1993.

[115] R. Resta, "Macroscopic electric polarization as a geometric quantum phase," *Europhysics Letters*, vol. 22, no. 2, pp. 133–138, 1993.

[116] K. M. Rabe and P. Ghosez, "First-principles studies of ferroelectric oxides," in *Physics of ferroelectrics* (K. M. Rabe, C. H. Ahn, and J.-M. Triscone, eds.), ch. 4, pp. 117–174, Springer-Verlag Berlin Heidelberg, 2007.

[117] M. E. Lines and A. M. Glass, "Statistical theory, soft modes, and phase transitions," in *Principles and applications of ferroelectrics and related materials*, ch. 2, pp. 24–58, Oxford, UK: Oxford University Press, 1977.

[118] P. Chandra and P. B. Littlewood, "A Landau primer for ferroelectrics," in *Physics of ferroelectrics* (K. M. Rabe, C. H. Ahn, and J.-M. Triscone, eds.), ch. 3, pp. 69–115, Springer-Verlag Berlin Heidelberg, 2007.

[119] M. E. Lines and A. M. Glass, "Macroscopics and phenomenology," in *Principles and Applications of Ferroelectrics and Related Materials*, ch. 3, pp. 59–86, Oxford, UK: Oxford University Press, 1977.

[120] "An american national standard IEEE standard definitions of terms associated with ferroelectric and related materials," *IEEE Transactions on Ultrasonics, Ferroelectrics, and Frequency Control*, vol. 50, no. 12, pp. 1–32, 2003.

[121] J. Tichý, E. Jiří, E. Kittinger, and J. Přívratská, "Piezoelectric materials," in *Fundamentals of piezoelectric sensorics*, ch. 7, pp. 119–185, Springer Heidelberg Dordrecht London New York, 2010.

[122] S. Trolier-McKinstry, N. Bassiri Gharb, and D. Damjanovic, "Piezoelectric nonlinearity due to motion of 180° domain walls in ferroelectric materials at subcoercive fields: A dynamic poling model," *Applied Physics Letters*, vol. 88, no. 20, p. 202901, 2006.

[123] T. Mitsui and J. Furuichi, "Domain structure of rochelle salt and KH_2PO_4," *Physical Review*, vol. 90, no. 2, pp. 193–202, 1953.

[124] G. Arlt and P. Sasko, "Domain configuration and equilibrium size of domains in $BaTiO_3$ ceramics," *Journal of Applied Physics*, vol. 51, no. 9, pp. 4956–4960, 1980.

[125] S. Trolier-McKinstry and P. Muralt, "Thin film piezoelectrics for MEMS," in *Electroceramic-Based MEMS* (N. Setter, ed.), ch. 10, pp. 199–216, Springer US, 2005.

[126] A. K. Tagantsev, L. E. Cross, and J. Fousek, "Switching phenomena and small-signal response," in *Domains in ferroic crystals and thin films*, ch. 8, pp. 351–520, Springer-Verlag New York, 2010.

[127] D. Damjanovic and M. Demartin, "The Rayleigh law in piezoelectric ceramics," *Journal of Physics D: Applied Physics*, vol. 29, no. 7, pp. 2057–2060, 1996.

[128] B. Lewis, "Energy loss processes in ferroelectric ceramics," *Proceedings of the Physical Society (1958-1967)*, vol. 73, no. 1, pp. 17–24, 1959.

[129] J.-H. Bae and S.-H. Chang, "PVDF-based ferroelectric polymers and dielectric elastomers for sensor and actuator applications: A review," *Functional Composites and Structures*, vol. 1, no. 1, p. 012003, 2019.

[130] J. Walker, S. Scherrer, N. S. Løndal, T. Grande, and M. A. Einarsrud, "Electric field dependent polarization switching of tetramethylammonium bromotrichloroferrate(III) ferroelectric plastic crystals," *Applied Physics Letters*, vol. 116, no. 24, p. 242902, 2020.

[131] W. Wersing, W. Heywang, H. Beige, and H. Thomann, "The role of ferroelectricity for piezoelectric materials," in *Piezoelectricity* (W. Heywang, K. Lubitz, and W. Wersing, eds.), ch. 3, pp. 37–87, Springer-Verlag Berlin Heidelberg, 2008.

[132] S.-E. Park and T. R. Shrout, "Ultrahigh strain and piezoelectric behavior in relaxor based ferroelectric single crystals," *Journal of Applied Physics*, vol. 82, no. 4, pp. 1804–1811, 1997.

[133] M. E. Lines and A. M. Glass, "Oxygen octahedra," in *Principles and applications of ferroelectrics and related materials*, ch. 8, pp. 241–292, Oxford, UK: Oxford University Press, 1977.

[134] N. A. Benedek and C. J. Fennie, "Why are there so few perovskite ferroelectrics?," *Journal of Physical Chemistry C*, vol. 117, no. 26, pp. 13339–13349, 2013.

[135] J. M. Rondinelli and C. J. Fennie, "Octahedral rotation-induced ferroelectricity in cation ordered perovskites," *Advanced Materials*, vol. 24, no. 15, pp. 1961–1968, 2012.

[136] V. M. Goldschmidt, "Die Gesetze der Krystallochemie," *Naturwissenschaften*, vol. 14, no. 21, pp. 477–485, 1926.

[137] G. Shirane and A. T. Tokyo, "Phase transitions in solid solutions of $PbZrO_3$ and $PbTiO_3$ (I) Small concentrations of $PbTiO_3$," *Journal of the Physical Society of Japan*, vol. 7, no. 1, pp. 5–11, 1952.

[138] B. Jaffe, J. Cook, William R., and H. Jaffe, "Solid solutions of Pb(Ti, Zr, Sn, Hf)O_3," in *Piezoelectric ceramics*, ch. 7, pp. 135–184, London, UK: Academic Press, 1971.

[139] International Centre for Diffraction (ICDD), "Powder Diffraction File (PDF): 04-011-7309," *$Pb(Zr_{0.52}Ti_{0.48})O_3$ @ 850 K*, 2013.

[140] International Centre for Diffraction (ICDD), "Powder Diffraction File (PDF): 01-072-7167," *$Pb(Zr_{0.52}Ti_{0.48})O_3$ @ 298 K*, 2013.

[141] N. Zhang, H. Yokota, A. M. Glazer, Z. Ren, D. A. Keen, D. S. Keeble, P. A. Thomas, and Z. G. Ye, "The missing boundary in the phase diagram of $PbZr_{1-x}Ti_xO_3$," *Nature Communications*, vol. 5, pp. 1–9, 2014.

[142] A. Bouzid, E. M. Bourim, M. Gabbay, and G. Fantozzi, "PZT phase diagram determination by measurement of elastic moduli," *Journal of the European Ceramic Society*, vol. 25, no. 13, pp. 3213–3221, 2005.

[143] B. Noheda, J. A. Gonzalo, A. C. Caballero, C. Moure, D. E. Cox, and G. Shirane, "New features of the morphotropic phase boundary in the $Pb(Zr_{1-x}Ti_x)O_3$ system," *Ferroelectrics*, vol. 237, no. 1-4, pp. 237–244, 2000.

[144] N. J. Donnelly and C. A. Randall, "Pb loss in $Pb(Zr,Ti)O_3$ ceramics observed by *in situ* ionic conductivity measurements," *Journal of Applied Physics*, vol. 109, no. 10, p. 104107, 2011.

[145] K. H. Härdtl and H. Rau, "PbO vapour pressure in the $Pb(Ti_{1-x}Zr_x)O_3$ system," *Solid State Communications*, vol. 7, no. 1, pp. 41–45, 1969.

[146] R. D. Klissurska, K. G. Brooks, I. M. Reaney, C. Pawlaczyk, M. Kosec, and N. Setter, "Effect of Nb doping on the microstructure of sol-gel-derived PZT thin films," *Journal of the American Ceramic Society*, vol. 78, no. 6, pp. 1513–1520, 1995.

[147] C. K. Kwok and S. B. Desu, "Formation kinetics of $PbZr_xTi_{1-x}O_3$ thin films," *Journal of Materials Research*, vol. 9, no. 7, pp. 1728–1733, 1994.

[148] B. A. Tuttle, J. A. Voigt, T. J. Garino, D. C. Goodnow, R. W. Schwartz, D. L. Lamppa, T. J. Headley, and M. O. Eatough, "Chemically prepared $Pb(Zr,Ti)O_3$ thin films: The effects of orientation and stress," *ISAF '92: Proceedings of the Eighth IEEE International Symposium on Applications of Ferroelectrics*, pp. 344–348, 1992.

[149] M. R. Soares, A. M. Senos, and P. Q. Mantas, "Phase coexistence region and dielectric properties of PZT ceramics," *Journal of the European Ceramic Society*, vol. 20, no. 3, pp. 321–334, 2000.

[150] R. A. Wolf and S. Trolier-McKinstry, "Temperature dependence of the piezoelectric response in lead zirconate titanate films," *Journal of Applied Physics*, vol. 95, no. 3, pp. 1397–1406, 2004.

[151] V. Kayasu and M. Ozenbas, "The effect of Nb doping on dielectric and ferroelectric properties of PZT thin films prepared by solution deposition," *Journal of the European Ceramic Society*, vol. 29, no. 6, pp. 1157–1163, 2009.

[152] E. C. Souza, A. Z. Simões, M. Cilense, E. Longo, and J. A. Varela, "The effect of Nb doping on ferroelectric properties of PZT thin films prepared from polymeric precursors," *Materials Chemistry and Physics*, vol. 88, no. 1, pp. 155–159, 2004.

[153] M. D. Nguyen, T. Q. Trinh, M. Dekkers, E. P. Houwman, H. N. Vu, and G. Rijnders, "Effect of dopants on ferroelectric and piezoelectric properties of lead zirconate titanate thin films on Si substrates," *Ceramics International*, vol. 40, no. 1, pp. 1013–1018, 2014.

[154] H. Sun, Y. Zhang, X. Liu, S. Guo, Y. Liu, and W. Chen, "The effect of Mn/Nb doping on dielectric and ferroelectric properties of PZT thin films prepared by sol–gel process," *Journal of Sol-Gel Science and Technology*, vol. 74, no. 2, pp. 378–386, 2015.

[155] T. Haccart, E. Cattan, D. Remiens, S. Hiboux, and P. Muralt, "Evaluation of niobium effects on the longitudinal piezoelectric coefficients of $Pb(Zr, Ti)O_3$ thin films," *Applied Physics Letters*, vol. 76, no. 22, pp. 3292–3294, 2000.

[156] W. Zhu, I. Fujii, W. Ren, and S. Trolier-Mckinstry, "Domain wall motion in A and B site donor-doped $Pb(Zr_{0.52}Ti_{0.48})O_3$ films," *Journal of the American Ceramic Society*, vol. 95, no. 9, pp. 2906–2913, 2012.

[157] D. F. Ryder and N. K. Raman, "Sol-gel processing of Nb-doped $Pb(Zr, Ti)O_3$ thin films for ferroelectric memory applications," *Journal of Electronic Materials*, vol. 21, no. 10, pp. 971–975, 1992.

[158] M. Zhu, P. Komissinskiy, A. Radetinac, M. Vafaee, Z. Wang, and L. Alff, "Effect of composition and strain on the electrical properties of $LaNiO_3$ thin films," *Applied Physics Letters*, vol. 103, no. 14, p. 141902, 2013.

[159] X. Guo, C. Li, Y. Zhou, and Z. Chen, "High-quality $LaNiO_3$ thin-film electrode grown by pulsed laser deposition," *Journal of Vacuum Science & Technology A: Vacuum, Surfaces, and Films*, vol. 17, no. 3, pp. 917–920, 1999.

[160] G. Gou, I. Grinberg, A. M. Rappe, and J. M. Rondinelli, "Lattice normal modes and electronic properties of the correlated metal $LaNiO_3$," *Physical Review B - Condensed Matter and Materials Physics*, vol. 84, no. 14, pp. 1–13, 2011.

[161] L. Sun, T. Yu, Y.-F. Chen, J. Zhou, and N.-B. Ming, "Conductive $LaNiO_3$ electrode grown by pulsed laser ablation on Si substrate," *Journal of Materials Research*, vol. 12, no. 4, pp. 931–935, 1997.

[162] Y. H. Yu, M. O. Lai, and L. Lu, "Highly (100) oriented $Pb(Zr_{0.52}Ti_{0.48})O_3/LaNiO_3$ films grown on amorphous substrates by pulsed laser deposition," *Applied Physics A: Materials Science and Processing*, vol. 88, no. 2, pp. 365–370, 2007.

[163] D. Galusek and K. Ghillányová, "Ceramic oxides," in *Ceramics science and technology - Volume 2* (R. Riedel and I.-W. Chen, eds.), ch. 1, pp. 3–58, Wheinheim, Germany: Wiley-VCH, 2010.

[164] M. Venkatraman and J. P. Neumann, "The Cr-Pt (chromium-platinum) system," *Bulletin of Alloy Phase Diagrams*, vol. 11, no. 1, pp. 16–21, 1990.

[165] W. C. Leslie, "Stainless steels," in *The physical metallurgy of steels*, ch. 12, pp. 326–357, London, UK: Hemisphere Publishing Corporation, 1981.

[166] R. Honeycombe and H. K. D. H. Bhadeshia, "Stainless steel," in *Steels: Microstructure and properties*, ch. 12, pp. 250–279, London, UK: Edward Arnold, 2 ed., 1995.

[167] W. C. Young and R. G. Budynas, "Beams; Flexure of straight bars," in *Roark's Formulas for Stress and Strain*, ch. 8, pp. 125–266, New York City: McGraw-Hill Book Company, 7 ed., 2002.

[168] W. C. Leslie, "Properties of high-purity iron," in *The physical metallurgy of steels*, ch. 1, pp. 1–67, London, UK: Hemisphere Publishing Corporation, 1981.

[169] K. Sree Harsha, "Structure and properties of films," in *Principles of vapor deposition of thin films*, ch. 12, pp. 961–1072, Oxford, UK: Elsevier, 2006.

[170] K. Sree Harsha, "Introduction," in *Principles of vapor deposition of thin films*, ch. 1, pp. 1–10, Oxford, UK: Elsevier, 2006.

[171] M. Ohring, "Substrate surfaces and thin-film nucleation," in *Materials science of thin films*, ch. 7, pp. 357–415, San Diego, CA, USA: Academic Press, 2^{nd} ed., 2002.

[172] A. Rockett, "Thin film growth processes," in *The materials science of semiconductors*, ch. 10, pp. 455–503, Springer US, 2008.

[173] A. Rockett, "Physical vapor deposition," in *The materials science of semiconductors*, ch. 11, pp. 505–572, Springer US, 2008.

[174] H. Ibach, "Adsorption," in *Physics of surfaces and interfaces*, ch. 6, pp. 245–308, Springer-Verlag Berlin Heidelberg, 2006.

[175] Z. Zhang and M. G. Lagally, "Atomistic processes in the early stages of thin-film growth," *Science*, vol. 276, no. 5311, pp. 377–383, 1997.

[176] U. W. Pohl, "Thermodynamics of epitaxial layer-growth," in *Epitaxy of semiconductors*, ch. 4, pp. 131–170, Springer-Verlag Berlin Heidelberg, 2013.

[177] K. Sree Harsha, "Nucleation and growth of films," in *Principles of vapor deposition of thin films*, ch. 9, pp. 685–829, Oxford, UK: Elsevier, 2006.

[178] H. Ibach, "Equilibrium thermodynamics," in *Physics of surfaces and interfaces*, ch. 4, pp. 149–206, Springer-Verlag Berlin Heidelberg, 2006.

[179] F. Bechstedt, "Thermodynamics," in *Principles of surface physics*, ch. 2, pp. 45–80, Springer-Verlag Berlin Heidelberg, 2003.

[180] F. K. Lotgering, "Topotactical reactions with ferrimagnetic oxides having hexagonal crystal structures - I," *Journal of Inorganic and Nuclear Chemistry*, vol. 9, no. 2, pp. 113–123, 1959.

[181] R. Furushima, S. Tanaka, Z. Kato, and K. Uematsu, "Orientation distribution-Lotgering factor relationship in a polycrystalline material - As an example of bismuth titanate prepared by a magnetic field," *Journal of the Ceramic Society of Japan*, vol. 118, no. 10, pp. 921–926, 2010.

[182] L. Alff, A. Klein, P. Komissinskiy, and J. Kurian, "Vapor-phase deposition of oxides," in *Ceramics science and technology - Volume 1* (R. Riedel and I.-W. Chen, eds.), vol. 3, ch. 11, pp. 269–290, Wheinheim, Germany: Wiley-VCH, 2012.

[183] M. Ohring, "Discharges, plasmas, and ion-surface interactions," in *Materials science of thin films*, ch. 4, pp. 145–202, San Diego, CA, USA: Academic Press, 2^{nd} ed., 2002.

[184] D. P. Norton, "Pulsed laser deposition of complex materials: Progress towards applications," in *Pulsed laser deposition of thin films* (R. Eason, ed.), ch. 1, pp. 3–31, Hoboken, NJ, USA: John Wiley & Sons, Inc., 2007.

[185] D. P. Norton, "Synthesis and properties of epitaxial electronic oxide thin-film materials," *Materials Science and Engineering: R: Reports*, vol. 43, no. 5-6, pp. 139–247, 2004.

[186] D. W. Bäuerle, "Thin-film formation by pulsed-laser deposition and laser-induced evaporation," in *Laser processing and chemistry*, ch. 22, pp. 397–421, Springer-Verlag Berlin Heidelberg, 2^{nd} ed., 1996.

[187] G. J. H. M. Rijnders, G. Koster, D. H. A. Blank, H. Rogalla, G. Koster, and H. Rogalla, "In situ monitoring during pulsed laser deposition of complex oxides using reflection high energy electron diffraction under high oxygen pressure," *Applied Physics Letters*, vol. 70, no. 14, pp. 1888–1890, 1997.

[188] G. J. H. M. Rijnders and D. H. A. Blank, "In situ diagnostics by high-pressure RHEED during PLD," in *Pulsed laser deposition of thin films* (R. Eason, ed.), ch. 4, pp. 85–97, Hoboken, NJ, USA: John Wiley & Sons, Inc., 2007.

[189] M. Wehner and J. Ihlemann, "Ablative micro-fabrication," in *Excimer laser technology* (D. Basting and G. Marowsky, eds.), ch. 11, pp. 158–186, Springer-Verlag Berlin Heidelberg, 2005.

[190] E. G. Gamaly, A. V. Rode, and B. Luther-Davies, "Ultrafast laser ablation and film deposition," in *Pulsed laser deposition of thin films* (R. Eason, ed.), ch. 5, pp. 99–130, Hoboken, NJ, USA: John Wiley & Sons, Inc., 2007.

[191] J. Greer, "Large-area commercial pulsed laser deposition," in *Pulsed laser deposition of thin films* (R. Eason, ed.), ch. 9, pp. 191–213, Hoboken, NJ, USA: John Wiley & Sons, Inc., 2007.

[192] E. G. Gamaly, A. V. Rode, and B. Luther-Davies, "Ultrafast ablation with high-pulse-rate lasers. Part I: Theoretical considerations," *Journal of Applied Physics*, vol. 85, no. 8, pp. 4213–4221, 1999.

[193] D. J. Keeble, S. Wicklein, R. Dittmann, L. Ravelli, R. A. MacKie, and W. Egger, "Identification of A- and B-site cation vacancy defects in perovskite oxide thin films," *Physical Review Letters*, vol. 105, no. 22, p. 226102, 2010.

[194] D. Preziosi, A. Sander, A. Barthélémy, and M. Bibes, "Reproducibility and off-stoichiometry issues in nickelate thin films grown by pulsed laser deposition," *AIP Advances*, vol. 7, no. 1, p. 015210, 2017.

[195] A. V. Gusarov, A. G. Gnedovets, and I. Smurov, "Gas dynamics of laser ablation : Influence of ambient atmosphere," *Journal of Applied Physics*, vol. 88, no. 7, pp. 4352–4364, 2000.

[196] International Centre for Diffraction (ICDD), "Powder Diffraction File (PDF): 04-007-6256," *$LaNiO_3$ @ 298 K*, 2013.

[197] M. Ohring, "Plasma and ion beam processing of thin films," in *Materials science of thin films*, ch. 5, pp. 203–275, San Diego, CA, USA: Academic Press, 2^{nd} ed., 2002.

[198] Y. Waseda, E. Matsubara, and K. Shinoda, "Fundamental properties of X-rays," in *X-Ray diffraction crystallography*, ch. 1, pp. 1–20, Springer-Verlag Berlin Heidelberg, 2011.

[199] K. Inaba, "X-ray thin-film measurement techniques I. Overview," *The Rigaku Journal*, vol. 24, no. 1, pp. 10–15, 2008.

[200] T. Mitsunaga, "X-ray thin-film measurement techniques II. Out-of-plane diffraction measurements," *The Rigaku Journal*, vol. 25, no. 1, pp. 7–12, 2009.

[201] W. H. Bragg and W. L. Bragg, "The reflection of X-rays by crystals," *Proceedinds of the Royal Society A - Mathematical, Physical and Engineeting Sciences*, vol. 88, no. 605, pp. 428–438, 1913.

[202] M. Maul, B. Schulte, P. Häussler, G. Frank, T. Steinborn, H. Fuess, and H. Adrian, "Epitaxial CeO_2 buffer layers for $YBa_2Cu_3O_{7-\delta}$ films on sapphire," *Journal of Applied Physics*, vol. 74, no. 4, p. 2942, 1993.

[203] P. Scherrer, "Bestimmung der inneren Struktur und der Größe von Kolloidteilchen mittels Röntgenstrahlen," in *Kolloidchemie ein Lehrbuch*, pp. 387–409, Springer Berlin Heidelberg, 1912.

[204] W. H. Hall, "X-ray line broadening in metals," *Proceedings of the Physical Society. Section A*, vol. 62, no. 11, pp. 741–743, 1949.

[205] M. Yasaka, "X-ray thin-film measurement techniques V. X-ray reflectivity measurement," *The Rigaku Journal*, vol. 26, no. 2, pp. 1–9, 2010.

[206] J. I. Goldstein, D. E. Newbury, D. C. Joy, C. E. Lyman, P. Echlin, E. Lifshin, L. Sawyer, and J. R. Michael, *Scanning electron microscopy and X-ray microanalysis*. New York City, NY, USA: Springer Nature, 3^{rd} ed., 2003.

[207] L. Stauffer, *C-V measurement tips, tricks, and traps - Keithley Instruments white paper*. 2011.

[208] Keysight Technologies, *Impedance measurement handbook - A guide to measurement technology and techniques*. 6^{th} ed., 2020.

[209] A. E. Kennelly, "Impedance," *Transactions of the American Institute of Electrical Engineers*, vol. X, pp. 172–232, 1893.

[210] Finnish Forest Industries Federation, *Handbook of Finnish plywood*. 2002.

[211] K. Prume, T. Schmitz, and S. Tiedke, "Electrical characterization of ferroelectrics," in *Polar oxides* (R. Waser, U. Böttger, and S. Tiedke, eds.), ch. 3, pp. 53–75, Weinheim, Germany: Wiley-VCH, 2005.

[212] C. B. Sawyer and C. H. Tower, "Rochelle salt as a dielectric," *Physical Review*, vol. 35, no. 3, pp. 269–273, 1930.

[213] B. Jaffe, J. Cook, William R., and H. Jaffe, "Measurement techniques," in *Piezoelectric ceramics*, ch. 3, pp. 23–47, London, UK: Academic Press, 1971.

[214] D. Bolten, O. Lohse, M. Grossmann, and R. Waser, "Reversible and irreversible domain wall contributions to the polarization in ferroelectric thin films," *Ferroelectrics*, vol. 221, no. 1-4, pp. 251–257, 1999.

[215] R. G. Polcawich and S. Trolier-McKinstry, "Piezoelectric and dielectric reliability of lead zirconate titanate thin films," *Journal of Materials Research*, vol. 15, no. 11, pp. 2505–2513, 2000.

[216] B. Akkopru-Akgun, W. Zhu, M. T. Lanagan, and S. Trolier-McKinstry, "The effect of imprint on remanent piezoelectric properties and ferroelectric aging of $PbZr_{0.52}Ti_{0.48}O_3$ thin films," *Journal of the American Ceramic Society*, vol. 102, no. 9, pp. 5328–5341, 2019.

[217] N. Bassiri Gharb, *Dielectric and piezoelectric nonlinearities in oriented $Pb(Yb_{1/2}Nb_{1/2})O_3$-$PbTiO_3$ thin films*. Ph.D. thesis, The Pennsylvania State University, Department of Materials Science and Engineering, 2005.

[218] H. G. Yeo, X. Ma, C. Rahn, and S. Trolier-McKinstry, "Efficient piezoelectric energy harvesters utilizing (001) textured bimorph PZT films on flexible metal foils," *Advanced Functional Materials*, vol. 26, no. 32, pp. 5940–5946, 2016.

[219] Q. M. Zhang, W. Y. Pan, and L. E. Cross, "Laser interferometer for the study of piezoelectric and electrostrictive strains," *Journal of Applied Physics*, vol. 63, no. 8, pp. 2492–2496, 1988.

[220] A. L. Kholkin, C. Wütchrich, D. V. Taylor, and N. Setter, "Interferometric measurements of electric field-induced displacements in piezoelectric thin films," *Review of Scientific Instruments*, vol. 67, no. 5, pp. 1935–1941, 1996.

[221] M. Sakata, S. Wakabayashi, H. Totani, M. Ikeda, H. Goto, M. Takeuchi, T. Yada, and W. Tsukuba-city, "Basic characteristics of a piezoelectric buckling type of actuator," *Proceedings of the International Solid-State Sensors and Actuators Conference - TRANSDUCERS '95*, pp. 422–425, 1995.

[222] M. Sakata, S. Wakabayashi, H. Goto, H. Totani, M. Takeuchi, and T. Yada, "Sputtered high $\mid d_{31} \mid$ coefficient PZT thin film for micro actuators," *Proceedings of Ninth International Workshop on Micro Electromechanical Systems*, pp. 263–266, 1996.

[223] J. L. Deschanvres, P. Rey, G. Delabouglise, M. Labeau, J. C. Joubert, and J. C. Peuzin, "Characterization of piezoelectric properties of zinc oxide thin films deposited on silicon for sensors applications," *Sensors and Actuators: A. Physical*, vol. 33, no. 1-2, pp. 43–45, 1992.

[224] M. Toyama, R. Kubo, E. Takata, K. Tanaka, and K. Ohwada, "Characterization of piezoelectric properties of PZT thin films deposited on Si by ECR sputtering," *Sensors and Actuators: A. Physical*, vol. 45, no. 2, pp. 125–129, 1994.

[225] E. Cattan, T. Haccart, and D. Rémiens, "e_{31} piezoelectric constant measurement of lead zirconate titanate thin films," *Journal of Applied Physics*, vol. 86, no. 12, pp. 7017–7023, 1999.

[226] D.-G. Kim and H.-G. Kim, "Piezoelectric properties of lead zirconate titanate thin films characterized by the pneumatic loading method," *Integrated Ferroelectrics*, vol. 24, no. 1-4, pp. 107–119, 1999.

[227] K. Lefki and G. J. Dormans, "Measurement of piezoelectric coefficients of ferroelectric thin films," *Journal of Applied Physics*, vol. 76, no. 3, pp. 1764–1767, 1994.

[228] J. E. A. Southin, S. A. Wilson, D. Schmitt, and R. W. Whatmore, "$e_{31,f}$ determination for PZT films using a conventional 'd_{33}' meter," *Journal of Physics D: Applied Physics*, vol. 34, no. 10, pp. 1456–1460, 2001.

[229] M.-A. Dubois and P. Muralt, "Measurement of the effective transverse piezoelectric coefficient $e_{31,f}$ of AlN and $Pb(Zr_x,Ti_{1-x})O_3$ thin films," *Sensors and Actuators A: Physical*, vol. 77, no. 2, pp. 106–112, 1999.

[230] L. M. Garten and S. Trolier-Mckinstry, "The field induced $e_{31,f}$ piezoelectric and Rayleigh response in barium strontium titanate thin films," *Applied Physics Letters*, vol. 105, no. 13, p. 132905, 2014.

[231] J. F. Shepard, P. J. Moses, and S. Trolier-McKinstry, "The wafer flexure technique for the determination of the transverse piezoelectric coefficient (d_{31}) of PZT thin films," *Sensors and Actuators A: Physical*, vol. 71, no. 1-2, pp. 133–138, 1998.

[232] J. F. Shepard, *The investigation of biaxial stress effects and the transverse piezoelectric (d_{31}) characterization of lead zirconate titanate thin films*. Ph.D. thesis, The Pennsylvania State University, Department of Materials Science and Engineering, 1998.

[233] J. F. Shepard, F. Chu, I. Kanno, and S. Trolier-McKinstry, "Characterization and aging response of the d_{31} piezoelectric coefficient of lead zirconate titanate thin films," *Journal of Applied Physics*, vol. 85, no. 9, pp. 6711–6716, 1999.

[234] Q. Zhou, J. M. Cannata, R. J. Meyer, D. J. Van Tol, S. Tadigadapa, W. J. Hughes, K. K. Shung, and S. Trolier-McKinstry, "Fabrication and characterization of micromachined high-frequency tonpilz transducers derived by PZT thick films," *IEEE Transactions on Ultrasonics, Ferroelectrics, and Frequency Control*, vol. 52, no. 3, pp. 350–356, 2005.

[235] F.-C. Chiu, "A review on conduction mechanisms in dielectric films," *Advances in Materials Science and Engineering*, vol. 2014, p. 578168, 2014.

[236] Keithley Instruments, *Low level measurements handbook*. 7^{th} ed., 2014.

[237] I. K. Yoo, C. J. Kim, and S. B. Desu, "Breakdown mechanisms in PZT thin film capacitors," *Integrated Ferroelectrics*, vol. 11, no. 1-4, pp. 269–275, 1995.

[238] A. K. Tagantsev, A. L. Kholkin, E. L. Colla, K. G. Brooks, and N. Setter, "Effect of ferroelectric polarization on current response of PZT thin films," *Integrated Ferroelectrics*, vol. 10, no. 1-4, pp. 189–204, 1995.

[239] Euro Inox - The European Stainless Steel Development Association, *Stainless steel: Table of technical properties*. Luxembourg: Euro Inox, 2^{nd} ed., 2007.

[240] International Centre for Diffraction (ICDD), "Powder Diffraction File (PDF): 00-004-0802," *Pt @ 298 K*, 2013.

[241] International Centre for Diffraction (ICDD), "Powder Diffraction File (PDF): 00-026-0142," *$Pb_2Ti_2O_6$ @ 298 K*, 2019.

[242] International Centre for Diffraction (ICDD), "Powder Diffraction File (PDF): 03-065-4629," *CrPt @ 298 K*, 2019.

[243] International Centre for Diffraction (ICDD), "Powder Diffraction File (PDF): 00-033-0397," $Fe_{0.49}Cr_{0.29}Ni_{0.16}C_{0.06}$ *@ 298 K*, 2019.

[244] International Centre for Diffraction (ICDD), "Powder Diffraction File (PDF): 00-034-0396," $Cr_{0.26}Fe_{1.74}$ *@ 298 K*, 2019.

[245] J. Cardoletti, P. Komissinskiy, E. Bruder, C. Morandi, and L. Alff, "{001}-textured Pb(Zr, Ti)O_3 thin films on stainless steel by pulsed laser deposition," *Journal of Applied Physics*, vol. 128, no. 10, p. 104103, 2020.

[246] G. L. Brennecka, W. Huebner, B. a. Tuttle, and P. G. Clem, "Use of stress to produce highly oriented tetragonal lead zirconate titanate (PZT 40/60) thin films and resulting electrical properties," *Journal of the American Ceramic Society*, vol. 87, no. 8, pp. 1459–1465, 2004.

[247] M. D. Nguyen, E. P. Houwman, H. Yuan, B. J. Wylie-Van Eerd, M. Dekkers, G. Koster, J. E. Ten Elshof, and G. Rijnders, "Controlling piezoelectric responses in $Pb(Zr_{0.52}Ti_{0.48})O_3$ films through deposition conditions and nanosheet buffer layers on glass," *ACS Applied Materials and Interfaces*, vol. 9, no. 41, pp. 35947–35957, 2017.

[248] N. Bassiri-Gharb, I. Fujii, E. Hong, S. Trolier-Mckinstry, D. V. Taylor, and D. Damjanovic, "Domain wall contributions to the properties of piezoelectric thin films," *Journal of Electroceramics*, vol. 19, no. 1, pp. 47–65, 2007.

[249] J. Pérez de la Cruz, E. Joanni, P. M. Vilarinho, and A. L. Kholkin, "Thickness effect on the dielectric, ferroelectric, and piezoelectric properties of ferroelectric lead zirconate titanate thin films," *Journal of Applied Physics*, vol. 108, no. 11, p. 114106, 2010.

[250] A. Rose, "Space-charge-limited currents in solids," *Physical Review*, vol. 97, no. 6, pp. 1538–1544, 1955.

[251] S. Trolier-McKinstry, J. Chen, K. Vedam, and R. E. Newnham, "In situ annealing studies of sol-gel ferroelectric thin films by spectroscopic ellipsometry," *Journal of American Ceramic Society*, vol. 78, no. 7, pp. 1907–1913, 1995.

[252] International Centre for Diffraction (ICDD), "Powder Diffraction File (PDF): 04-016-0218," *Pb @ 298 K*, 2020.

[253] A. K. Tagantsev and I. A. Stolichnov, "Injection-controlled size effect on switching of ferroelectric thin films," *Applied Physics Letters*, vol. 74, no. 9, pp. 1326–1328, 1999.

[254] T. Haccart, E. Cattan, and D. Remiens, "Dielectric, ferroelectric and piezoelectric properties of sputtered PZT thin films on Si substrates: Influence of film thickness and orientation," *Semiconductor Physics, Quantum Electronics & Optoelectronics*, vol. 5, no. 1, pp. 78–88, 2002.

[255] B. Jaffe, J. Cook, William R., and H. Jaffe, "Interpretation of some experimental results," in *Piezoelectric ceramics*, ch. 10, pp. 237–252, London, UK: Academic Press, 1971.

[256] C. A. Randall, N. Kim, J. P. Kucera, W. Cao, and T. R. Shrout, "Intrinsic and extrinsic size effects in fine-grained morphotropic-phase-boundary lead zirconate titanate ceramics," *Journal of the American Ceramic Society*, vol. 81, no. 3, pp. 677–688, 1998.

[257] T. Rojac, S. Drnovšek, A. Bencan, B. Malič, and D. Damjanovic, "Role of charged defects on the electrical and electromechanical properties of rhombohedral Pb(Zr,Ti)O_3 with oxygen octahedra tilts," *Physical Review B*, vol. 93, no. 1, p. 014102, 2016.

[258] T. M. Kamel and G. de With, "Poling of hard ferroelectric PZT ceramics," *Journal of the European Ceramic Society*, vol. 28, no. 9, pp. 1827–1838, 2008.

[259] Y. A. Genenko, J. Glaum, M. J. Hoffmann, and K. Albe, "Mechanisms of aging and fatigue in ferroelectrics," *Materials Science and Engineering B*, vol. 192, pp. 52–82, 2015.

[260] M. I. Morozov and D. Damjanovic, "Hardening-softening transition in Fe-doped Pb(Zr,Ti)O_3 ceramics and evolution of the third harmonic of the polarization response," *Journal of Applied Physics*, vol. 104, no. 3, p. 034107, 2008.

[261] G. Arlt and H. Neumann, "Internal bias in ferroelectric ceramics: Origin and time dependence," *Ferroelectrics*, vol. 87, no. 1, pp. 109–120, 1988.

[262] M. Dawber and J. F. Scott, "A model for fatigue in ferroelectric perovskite thin films," *Applied Physics Letters*, vol. 76, no. 8, p. 1060, 2000.

[263] J. Cardoletti, "FeBeTo – Ferroelectric Bending Tongues modelling program," *Technische Universität Darmstadt*, 2018.

[264] F. I. Baratta, "When is a beam a plate?," *Communications of the American Ceramic Society*, vol. 64, no. 5, pp. C–86, 1981.

[265] J. Cardoletti, A. Radetinac, D. Thiem, J. Walker, P. Komissinskiy, B. X. Xu, H. Schlaak, S. Trolier-Mckinstry, and L. Alff, "Modelling of the vertical deflection of ferroelectric bending tongues loaded at their free end," *AIP Advances*, vol. 9, no. 2, p. 025017, 2019.

[266] W. H. Macaulay, "Note on the deflection of beams," *The Messenger of Mathematics*, vol. 48, pp. 129–130, 1919.

[267] T. Bailey and J. E. Hubbard Jr., "Distributed piezoelectric-polymer active vibration control of a cantilever beam," *Journal of Guidance, Control, and Dynamics*, vol. 8, no. 5, pp. 605–611, 1985.

[268] K. Lücke, J. Pospiech, K. H. Virnich, and J. Jura, "On the problem of the reproduction of the true orientation distribution from pole figures," *Acta Metallurgica*, vol. 29, no. 1, pp. 167–185, 1981.

[269] B. Tuttle, T. Headley, C. Drewien, J. Michael, J. Voigt, and T. Garino, "Comparison of ferroelectric domain assemblages in Pb(Zr,Ti)O_3 thin films and bulk ceramics," *Ferroelectrics*, vol. 221, no. 1-4, pp. 209–218, 1999.

[270] C. B. Yeager and S. Trolier-McKinstry, "Epitaxial Pb(Zr_x,Ti_{1-x})O_3 ($0.30 \leq x \leq 0.63$) films on (100) MgO substrates for energy harvesting applications," *Journal of Applied Physics*, vol. 112, no. 7, p. 074107, 2012.

[271] Q. Sunder and Bakialakshmi, "Human energy harvesting based on piezoelectric transduction using MEMS technology," *International Journal of Advanced Research in Electrical, Electronics and Instrumentation Engineering*, vol. 3, no. 4, pp. 8958–8965, 2014.

[272] A. J. Fleming and K. K. Leang, "Piezoelectric transducers," in *Design, modeling and control of nanopositioning systems*, ch. 2, pp. 17–42, Springer International Publishing, 2014.

[273] N. A. Pertsev, J. Rodríguez Contreras, V. G. Kukhar, B. Hermanns, H. Kohlstedt, and R. Waser, "Coercive field of ultrathin $Pb(Zr_{0.52}Ti_{0.48})O_3$ epitaxial films," *Applied Physics Letters*, vol. 83, no. 16, pp. 3356–3358, 2003.

[274] M. J. Haun, E. Furman, S. J. Jang, and L. E. Cross, "Thermodynamic theory of the lead zirconate-titanate solid solution system, part V: Theoretical calculations," *Ferroelectrics*, vol. 99, no. 1, pp. 63–86, 1989.

[275] J. L. Butler and C. H. Sherman, "Appendix," in *Transducers and arrays for underwater sound*, ch. 13, pp. 637–680, Springer International Publishing, 2^{nd} ed., 2016.

[276] S. N. Kallaev, G. G. Gadzhiev, I. K. Kamilov, Z. M. Omarov, S. A. Sadykov, and L. A. Reznichenko, "Thermal properties of PZT-based ferroelectric ceramics," *Physics of the Solid State*, vol. 48, no. 6, pp. 1169–1170, 2006.

[277] Y. H. Yu, M. O. Lai, L. Lu, and G. Y. Zheng, "Measurement of Young's modulus and Poisson's ratio of thin films by synchrotron X-ray diffraction," *Advances in Synchrotron Radiation*, vol. 1, no. 2, pp. 179–187, 2008.

[278] H. Rohloff and A. Zastera, *Physikalische Eigenschaften gebräuchlicher Stähle*. Düsseldorf, Germany: Verlag Stahleisen, 1996.

[279] Y. A. Genenko, R. Khachaturyan, J. Schultheiß, A. Ossipov, J. E. Daniels, and J. Koruza, "Stochastic multistep polarization switching in ferroelectrics," *Physical Review B*, vol. 97, no. 22, p. 144101, 2018.

[280] "Directive 2002/95/EC of the European Parliament and of the Council of 27 January 2003 on the restriction of the use of certain hazardous substances in electrical and electronic equipment," *Official Journal of the European Union*, vol. L 37, no. 13.2.2003, pp. 19–23, 2003.

[281] "Directive 2011/65/EU of the European Parliament and of the Council of 8 June 2011 on the restriction of the use of certain hazardous substances in electrical and electronic equipment," *Official Journal of the European Union*, vol. L 174, no. 1.7.2011, pp. 88–110, 2011.

[282] "Commission delegated directive (EU) 2015/863 of 31 March 2015 amending Annex II to Directive 2011/65/EU of the European Parliament and of the Council as regards the list of restricted substances," *Official Journal of the European Union*, vol. L 137, no. 4.6.2015, pp. 10–12, 2015.

[283] A. J. Bell and D. Damjanovic, "Balancing hyperbole and impact in research communications related to lead-free piezoelectric materials," *Journal of Materials Science*, vol. 55, no. 25, pp. 10971–10974, 2020.

List of publications and scientific contributions

Publications

Peer-reviewed publications

J. Cardoletti, P. Komissinskiy, S. Drnovšek, B. Malič, and L. Alff, "{001}-textured Nb-doped Pb(Zr, Ti)O_3 thin films on stainless steel by pulsed laser deposition", *2021 IEEE International Symposium on Applications of Ferroelectrics (ISAF)*, pp. 1-4, 2021, DOI: 10.1109/ISAF51943.2021.9477358.

J. Cardoletti, P. Komissinskiy, E. Bruder, C. Morandi, and L. Alff , "{001}-textured Pb(Zr, Ti)O_3 thin films on stainless steel by pulsed laser deposition", *Journal of Applied Physics*, vol. 128, no. 10, p. 104103, 2020, DOI: 10.1063/5.0019967.

M. Rutsch, O. Ben Dali, A. Jäger, G. Allevato, K. Beerstecher, J. Cardoletti, A. Radetinac, L. Alff, and M. Kupnik, "Air-coupled ultrasonic bending plate transducer with piezoelectric and electrostatic transduction element combination", *2019 IEEE International Ultrasonics Symposium (IUS)*, pp. 147-150, 2019, DOI: 10.1109/ULTSYM.2019.8925701.

J. Cardoletti, A. Radetinac, D. Thiem, J. Walker, P. Komissinskiy, B. X. Xu, H. Schlaak, S. Trolier-McKinstry, and L. Alff, "Modelling of the vertical deflection of ferroelectric bending tongues loaded at their free end", *AIP Advances*, vol. 9, no. 2, p. 025017, 2019, DOI: 10.1063/1.5082392.

Other publications

J. Cardoletti, "FeBeTo - Ferroelectric Bending Tongues modelling program", *Technische Universität Darmstadt*, 2018, DOI: 10.25534/tudatalib-11.3.

D.B. Thiem, A. Carrasco, J. Cardoletti, L. Alff, and H. F. Schlaak, "Rotary planar actuator using mechanical anisotropy of tilted carbon fiber arrays", *Innovative Small Drives and Micro-Motor Systems; 11th GMM/ETG-Symposium*, 2017, pp. 1-5.

Conference contributions

Invited presentations

Deposition of $PbZr_{0.52}Ti_{0.48}O_3$ thin films on stainless steel for actuators applications, J. Cardoletti, P. Komissinskiy, and L. Alff, $F^2c\pi^2$ 2019 Joint conference - IEEE International Symposium on Applications of Ferroelectrics (ISAF) (Lausanne, Switzerland, 14-19 July 2019).

Contributed presentations

{001}-Textured Nb-Doped Pb(Zr,Ti)O_3 Thin Films on Stainless Steel by Pulsed Laser Deposition, J. Cardoletti, P. Komissinskiy, S. Drnovšek, B. Malič, and L. Alff, 2021 Joint ISAF-ISIF-PFM Virtual Conference (16-21 May 2021).

Deposition of {001}-oriented $PbZr_{0.52}Ti_{0.48}O_3$ thin films on stainless steel, J. Cardoletti, P. Komissinskiy, E. Bruder, C. Morandi, and L. Alff, Electroceramics XVII (Darmstadt, Germany, 24-28 August 2020).

Modelling of the vertical deflection of ferroelectric bending tongues, J. Cardoletti, A. Radetinac, J. Walker, P. Komissinskiy, S. Trolier-McKinstry, and L. Alff, 2018 Joint meeting of the DPG and EPS Condensed Matter Divisions (Berlin, Germany, 11-16 March 2018).

Posters

Pulsed Laser Deposition of $PbZr_{0.52}Ti_{0.48}O_3$ thin films on stainless steel, J. Cardoletti, A. Radetinac, P. Komissinskiy, and L. Alff, 2018 Joint meeting of the DPG and EPS Condensed Matter Divisions (Berlin, Germany, 11-16 March 2018).

Academic contributions

Ferroelectric thin films and their applications, lecture within the *Materials science of thin films* course, Master level (2018 – 2020, summer semester) at the Institute of Materials Science, Technische Universität Darmstadt, Germany

Curriculum Vitae

Education

09/2016 – 06/2021	Doctoral studies at Institute of Materials Science, Technische Universität Darmstadt, Germany
09/2014 – 08/2016	Double Master degree: Erasmus Mundus FAME Master of Science in Functional Advanced Materials for Engineering: - Engineer Degree (Titre d'Ingénieur diplômé de l'Institut polytechnique de Grenoble) at Grenoble INP Institute of Engineering – Phelma (École nationale supérieure de physique, électronique, matériaux), France - Master of Science in Materials Science at Institute of Materials Science, Technische Universität Darmstadt, Germany
09/2013 – 06/2014	Bachelor in Engineering Sciences (Diplôme de Bachelor en Sciences de l'Ingénieur) at Grenoble INP Institute of Engineering – Phelma (École nationale supérieure de physique, électronique, matériaux), France
09/2011 – 06/2013	University Degree in Technology – Instrumentation & Applied Physics (Diplôme Universitaire de Technology - Mesures Physiques) at Université de Savoie, Institut Universitaire de Technologie d'Annecy, France

Research experiences

03/2017 – 09/2017	Research scholar at The Materials Research Institute, The Pennsylvania State University, United States of America
03/2016 – 08/2016	Master thesis at Institute of Materials Science, Technische Universität Darmstadt, Germany
05/2015 – 08/2015	Research internship at Department of Materials, Imperial College London, United Kingdom
04/2013 – 06/2013	University Degree in Technology thesis at SYMME laboratory (SYstems and Materials for MEchatronics), Université de Savoie, France

Scholarships

2017, 2018	Mobility allowance from the International Doctoral School in Functional Materials: Research and Innovation (EIT RawMaterials) for international mobility and training schools attendance